Universität Bremen

HSB
Hochschule Bremen
City University of Applied Sciences

Characterization of freeform surfaces by reflective gradient measurement

Tobias Binkele

University of Bremen
University of Applied Sciences Bremen

The Dissertation

Characterization of freeform surfaces by reflective gradient measurement

by Tobias Binkele, M.Sc.,

has been approved by
Faculty 01: Physics/Electrical Engineering
of University of Bremen to grant
the academic title
Doctor of Engineering (Dr.-Ing.).

Assessor 1:	Prof. Dr.-Ing. Walter Lang University of Bremen
Assessor 2:	Prof. Dr.-Ing. Friedrich Fleischmann University of Appl. Sci. Bremen
Examinant:	Prof. Dr.-Ing. Michael Vellekoop University of Bremen
Examinant:	Prof. Dr. rer. nat. Thomas Henning University of Appl. Sci. Bremen

Date of submission:	21st December 2021
Date of colloquium:	14th March 2022

Abstract

In freeform surfaces, the evolution of optical components has exceeded the next level. After spherical and aspherical surfaces, freeform surfaces do not follow a certain basic shape. Therewith, they offer a much higher degree of freedom for designers and the field of possibilities of optical function is extended. Simultaneously, the designs can be more compact as multiple spherical or aspherical surfaces can be replaced by one single freeform surface.

Since verification in the fabrication process is indispensable, adequate measurement techniques for the characterization of freeform surfaces are required. For spherical and aspherical surfaces, highly developed surface measurement techniques area available. However, these techniques exceed their limits, when the basic shape of a freeform is not spherical or aspherical, but flat. To provide manufacturer with a high accurate option to measure freeform surfaces, deviating from a flat basic shape, a gradient-based measurement technique for these kind of freeform surfaces is proposed. This measurement technique is of laser deflectometry type and measures the gradient field of a freeform surface by use of a variation of Experimental Ray Tracing. Using an appropriate integration method leads to the reconstruction of the measured freeform surface from the measured gradient field.

The proposed measurement technique uses evaluation and calibration techniques, which are implemented using homogeneous coordinates. With a commercially available simulation software, the proposed measurement process and the evaluation and calibration methods are validated. The results for different surfaces models are presented and evaluated.

An experimental setup has been built up and described in this work. Using multiple different surface types, the abilities of the experimental measurement setup are shown. Comparing the results from the proposed measurement technique to results from commercially available measurement techniques, good agreement in the sub-micrometer range can be determined.

To set the measurement results in context to the expected measurement uncertainty, multiple error sources are evaluated for the experimental measurement setup. The considered error sources are described and magnitudes are given either by experimental determination or by test protocols from the manufacturers. The determined measurement uncertainties are evaluated. In relation to the measurement results from the experimental measurements, these determined uncertainties shows higher values than expected. Reasons for these deviations are discussed.

Summarizing the proposed measurement technique, optional further developments and enhancements are discussed.

Kurzfassung

Die Entwicklung optischer Komponenten hat in Freiformoberflächen ihre nächste Stufe erreicht. Anders als sphärische und asphärische Oberflächen folgen Freiformoberflächen keiner bestimmten Grundform. Dadurch bieten sie viel mehr Freiheitsgrade für Designer und erweitern die Möglichkeiten der optischen Funktionen. Gleichzeitig können deutlich kompaktere Designs erstellt werden, da mehrere sphärische und asphärische Oberflächen in nur einer einzigen Freiformoberfläche kombiniert werden können.

Da die Überprüfung im Herstellungsprozess unabdingbar ist, werden Messtechniken für die Charakterisierung von Oberflächen benötigt. Für sphärische oder asphärische Oberflächen existieren bereits weit entwickelte Messtechniken. Diese Messtechniken stoßen allerdings an ihre Grenzen, wenn die Grundform einer Freiform nicht sphärisch oder asphärisch, sondern flach ist. Um Herstellern eine hoch präzise Messtechnik zur Vermessung von Freiformen mit einer flachen Grundform zur Verfügung zu stellen, wird eine Gradienten-basierte Messtechnik für diese Art von Freiformoberflächen vorgestellt. Die Messtechnik ist im Bereich der Laser Deflektometrie anzusiedeln und misst das Gradientenfeld einer Freiformoberfläche mit Hilfe einer Abwandlung des Experimental Ray Tracing. Unter Nutzung einer geeigneten Integrationsmethode kann die Freiformoberfläche aus dem gemessenen Gradientenfeld rekonstruiert werden.

Die vorgestellte Messtechnik nutzt Auswerte- und Kalibrationsmethoden, welche mit Hilfe von homogenen Koordinaten implementiert wurden. Unter Zuhilfenahme einer kommerziell erhältlichen Simulationssoftware wurden der Messprozess, sowie die Auswerte- und Kalibrationsmethoden validiert. Die Ergebnisse verschiedener Oberflächenmodelle werden präsentiert und evaluiert.

Ein experimenteller Aufbau wurde erstellt und wird in dieser Arbeit beschrieben. Unter Verwendung mehrerer verschiedener Oberflächentypen werden die Fähigkeiten des experimentellen Aufbaus dargelegt. Im Vergleich der Messergebnisse der vorgestellten Messtechnik mit Messergebnissen kommerziell verfügbarer Messtechniken können gute Übereinstimmungen im sub-Mikrometerbereich festgestellt werden.

Um die Messergebnisse im Kontext der zu erwartenden Messunsicherheit zu betrachten, wurden relevante Fehlerquellen des experimentellen Messaufbaus evaluiert. Diese betrachteten Fehlerquellen werden beschrieben und ihre Größe entweder experimentell oder durch verfügbare Testprotokolle der Hersteller bestimmt und evaluiert. Im Vergleich zu den Ergebnissen aus den experimentellen Messungen, zeigen die festgestellten Messunsicherheiten höhere Werte. Gründe für diese Abweichungen werden diskutiert.

In der Zusammenfassung der vorgestellten Messtechnik werden optionale Weiterentwicklungen und Verbesserungen diskutiert.

Content

List of abbreviations and symbols

Abbreviations

API	application programming interface
BFS	best-fit-sphere
CGH	computer generated hologram
CS	coordinate system
DUT	device under test
ERT	experimental ray tracing
FWHM	full width half maximum
ITF	instrument transfer function
LD	laser deflectometry
LES	linear equation system
MCS	Monte-Carlo-simulation
OPD	optical path difference
PMD	phase measuring deflectometry
PSF	point spread function
PV	peak-to-valley
RBF	radial basis function
RMS	root mean square
SHS	Shack-Hartmann sensor
SUT	surface under test

Symbols

a, b	expected surface slopes at point K
$\boldsymbol{A}$	area the surface under test is investigated over
$\mathbf{A}$	interpolation matrix
c_j	coefficient of the j-th function in a set of functions
C, D	points of intersection of the reflected ray with the observation planes; their position vectors are $\boldsymbol{C}$ and $\boldsymbol{D}$
$\mathcal{C} = \{\boldsymbol{e}_u, \boldsymbol{e}_v, \boldsymbol{e}_w, \boldsymbol{O}^{\mathcal{C}}\}$	basis of the coordinate system of the camera with the axis u, v, w and the origin $\boldsymbol{O}^{\mathcal{C}}$

$d_i = h_i - s_i$	deviation between the determined surface sag h_i and the surface model s_i for the i-th sample point
$\boldsymbol{g}$	direction of the surface normal
h	surface sag determined from $\boldsymbol{i}$ and $\boldsymbol{r}$
$\mathbf{H} = \mathbf{H}(\boldsymbol{\gamma}, \boldsymbol{t})$	transformation matrix
I	point of intersection of the incident ray with position vector $\boldsymbol{I}$
$\mathcal{I} = \{\boldsymbol{e}_{\tilde{u}}, \boldsymbol{e}_{\tilde{v}}, \boldsymbol{e}_{\tilde{w}}, \boldsymbol{O}^{\mathcal{I}}\}$	basis of the coordinate system of the incident beam with the axis $\tilde{u}$, $\tilde{v}$, $\tilde{w}$ and the origin $\boldsymbol{O}^{\mathcal{I}}$
$i = 1 \dots M$	index for the i-th element within a set of elements with the length M
$\boldsymbol{i}$	direction of the incident ray
$j = 1 \dots N$	index of the j-th polynomial in a set of N polynomials
J	targeted point in the $\tilde{x}\tilde{y}$-plane of the coordinate system of the measurement plane ($\mathcal{M}$); its position vector is $\boldsymbol{J}$
K	expected point of intersection of the incident ray with the SUT; It's position vector is $\boldsymbol{K}$
l	index of Zernike polynomials
L	point of the projection of point $\boldsymbol{J}$ or $\boldsymbol{I}$ on the $\tilde{x}\tilde{y}$-plane; its position vector is $\boldsymbol{L}$
M	number of sample points
$m_i = s_x(\boldsymbol{x}_i)$, $n_i = s_y(\boldsymbol{x}_i)$	slope of the surface model in x- and y-direction at the i-th sample point
$\mathcal{M} = \{\boldsymbol{e}_{\tilde{x}}, \boldsymbol{e}_{\tilde{y}}, \boldsymbol{e}_{\tilde{z}}, \boldsymbol{O}^{\mathcal{M}}\}$	basis of the coordinate system of the measurement plane with the axis $\tilde{x}$, $\tilde{y}$, $\tilde{z}$ and the origin $\boldsymbol{O}^{\mathcal{M}}$
N	Number of polynomials in a set or number of center points for RBF integration
$\boldsymbol{O}$	origin of a coordinate system
P_l	Zernike polynomial with the index l
p_i, q_i	measured surface slope in x- and y-direction at the i-th sample point
$\boldsymbol{R}$	position vector to a point on the line representing the incident ray
$\mathbf{R}_x$, $\mathbf{R}_y$, $\mathbf{R}_z$	transformation matrix to perform rotation around indexed axis
$\hat{R}$	radius of curvature of the cylindrical surface model
$\boldsymbol{r}$	direction of the reflected ray
$\mathcal{S} = \{\boldsymbol{e}_x, \boldsymbol{e}_y, \boldsymbol{e}_z, \boldsymbol{O}^{\mathcal{S}}\}$	basis of the coordinate system of the SUT with the axis x, y, z and the origin $\boldsymbol{O}^{\mathcal{S}}$

$s(\boldsymbol{x})$	function of the surface under test
$s_{\tilde{u}}$, $s_{\tilde{v}}$	derivatives of $s(\tilde{u}, \tilde{v})$ in the coordinate system of the incident ray
s_x, s_y	derivatives of $s(x, y)$ in the coordinate system of the SUT
$\mathbf{T}$	transformation matrix to perform translation
$\boldsymbol{t} = (\Delta x, \Delta y, \Delta z)$	shifting vector to define a transformation matrix $\mathbf{H}$
t_m	measurement time to define the centroid drift
V	Projective vector space of the form $\mathbb{R}^4$
$\boldsymbol{x}$	position in the xy-plane of the coordinate system of the SUT
$\tilde{\boldsymbol{x}}$	position in the $\tilde{x}\tilde{y}$-plane of the coordinate system of the measurement plane
$\boldsymbol{X}$	set of all sample positions

Greek symbols

$\hat{\alpha}$	surface angle in the coordinate system of the SUT
$\hat{\beta}$	ray angle in the coordinate system of the camera
$\boldsymbol{\gamma} = (\alpha, \beta, \gamma)$	rotation angles to create a transformation matrix
$\boldsymbol{\zeta}(\boldsymbol{x})$	gradient field of the surface under test model
$\boldsymbol{\eta}(\boldsymbol{x})$	gradient field of the reconstructed surface
Θ	angle between incident ray and surface normal
λ	wavelength of light
λ_s	spatial wavelength
$\boldsymbol{\xi}(\boldsymbol{x})$	residual gradient field
ρ	support radius of the Wendland function
σ_q	surface slope uncertainty in y-direction
σ_{T_u}, σ_{T_v}	ray slope uncertainty in u- and v-direction
σ_u, σ_v	centroid uncertainty in u- and v-direction
$\sigma_{u,d}$, $\sigma_{v,d}$	centroid drift in u- and v-direction
σ_w	uncertainty of the detector positioning in w-direction
$\sigma_{w,cy}$, $\sigma_{w,cp}$	constant yaw and constant pitch error of the w-stage determined from its straightness and flatness error
$\sigma_{w,p}$, $\sigma_{w,y}$	pitch and yaw error of the w-stage
$\sigma_{w,s}$, $\sigma_{w,f}$	straightness and flatness error of the w-stage
$\sigma_{\tilde{x}}$, $\sigma_{\tilde{y}}$	positioning uncertainty of the $\tilde{x}\tilde{y}$-stages
$\sigma_{\tilde{x},y}$, $\sigma_{\tilde{y},y}$	yaw error of the $\tilde{x}\tilde{y}$-stages
$\sigma_{\tilde{x},s}$, $\sigma_{\tilde{y},s}$, $\sigma_{\tilde{x},f}$, $\sigma_{\tilde{y},f}$	straightness and flatness errors of the $\tilde{x}\tilde{y}$-stages

$\sigma_{\hat{\alpha}_y}$	surface angle uncertainty
$\sigma_{\overline{\Delta z}}$	surface height uncertainty
Φ	angle between reflected ray and surface normal
ψ	Wendland function as RBF

Terminology

In this work, the terminology follows a certain pattern, if not stated differently in the text. The used pattern is described here.

Direction vectors
Direction vectors are shown in lower-case bold-italic letters. Additionally, direction vectors are always considered unit vectors.

Example for a direction vector: $\boldsymbol{g} = \frac{\boldsymbol{g}}{|\boldsymbol{g}|}$

Points in space and their position vectors
Points in space are shown with italic upper-case letters. A corresponding position vector pointing to a point in space has the same upper-case letter, but shown in bold-italic.

Example for a point in space: I

Position vector to the point I: $\boldsymbol{I}$

Matrices
shown in upper-case bold letters.

Example for a direction vector: $\mathbf{H}$

Transformation matrices
Transformation matrices to transfer vectors from one coordinate system to another, are shown with the coordinate system, the transformation matrix is transferring from in subscript and the coordinate system it is transferring into in superscript.

Example for a transformation of a vector $\boldsymbol{g}$ from the coordinate system $\mathcal{C}$ into the coordinate system $\mathcal{M}$ by using the transformation matrix $\mathbf{H}$:

$$\mathbf{H}_{\mathcal{C}}^{\mathcal{M}} \boldsymbol{g}^{\mathcal{C}} = \boldsymbol{g}^{\mathcal{M}}$$

Angles in transformation matrices
Angles to define a transformation matrix follow the same terminology as the transformation matrix in terms of the sub- and superscript.

Example for the angle to define $\mathbf{H}_{\mathcal{C}}^{\mathcal{M}}$:

$$\alpha_{\mathcal{C}}^{\mathcal{M}}.$$

Discrete variables
The element $\boldsymbol{g}_i$ is the i-th element of $\boldsymbol{g}$ in a certain sequence.

Inner product of vectors
The inner product of two vectors $\boldsymbol{g}$ and $\boldsymbol{i}$ is donated $(\boldsymbol{g} \cdot \boldsymbol{i})$.

Vector product

The vector product of two vectors $\boldsymbol{g}$ and $\boldsymbol{i}$ is donated $\boldsymbol{g} \times \boldsymbol{i}$.

Least-squares sense relation

A least-squares sense relation is donated $\underset{c_j}{\widehat{=}}$, while c_j represents the optimized parameters.

Example for a least-squares sense relation:

$$s(x) \underset{c_j}{\widehat{=}} \sum_{j=0}^{N} c_j x^j$$

List of Figures

List of Tables

1. Introduction

1.1 Motivation

In optics, components like lenses and mirrors are used to redirect light to achieve a desired distribution. Surfaces on these components are shaped in certain ways to achieve this desired redirection of the light by refraction or reflection [1]. Usually, these surfaces are of flat, spherical or aspherical shape. The freeform surface marks the next step in the development of optical surfaces [2]. It opens up new abilities, while reducing packaging and weight of optical systems as shown in Figure 1.1, since the function of multiple surfaces can be combined in only one freeform surface [3, 4].

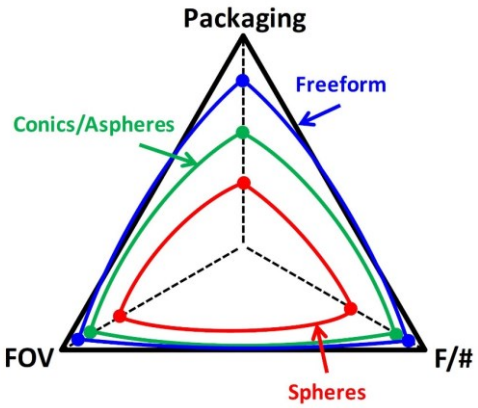

Figure 1.1: Qualitative comparison of spheres, conics/aspheres and freeform surfaces in terms of field of view (FOV), F/number (F/#) and packaging [3].

For a freeform surface, different definitions exist [4]. In this work, a surface is considered to be of freeform shape, when it cannot be described by one of the aspheric surface types described in DIN ISO 10110-12 [5]. This includes plane, sphere, asphere, cylinder, cone and toric surfaces. In DIN ISO 10110-19 general descriptions for surfaces are given [6]. Therewith, surfaces with freeform shape and freeform aperture can be described.

For freeform surfaces, a huge variety of applications is considerable [7]. In imaging optics, it offers the ability to design surfaces to suppress aberrations, even for tilted or folded optical paths. For example, using freeform mirrors, the optical path in telescopes can be folded to use space more efficiently [3, 8, 9]. This increasing efficiency in the use of space is also very helpful in technologies like head worn displays [10]. In non-imaging optics, freeform surfaces can be used to create special illumination patterns [11, 12]. They can also be used to shape the light emitting distribution of LEDs [13]. Even the improvement of the distribution of solar light onto a solar cell to increase photovoltaic efficiency can be achieved by freeform surfaces [14].

Independent on the function the freeform optical component fulfills, its surface form quality has to satisfy high demands. Therefore, metrology is needed that is able to verify the desired surface quality [15, 16]. To verify freeform surfaces deviating from a basic shape of a sphere, highly developed surface measurement techniques designed for spherical or aspherical

surfaces can be adapted. Therewith, these kind of freeform surfaces can already be measured with high accuracy [17]. However, if it comes to freeform surfaces deviating from a flat basic shape, these measurement techniques exceed their limits.

For flat surfaces, like wafers, techniques for flatness measurement exist. These measurement techniques are able to determine the flatness with high accuracy, but also exceed their limits, if the deviation from the flat is too high.

The gap in between the measurement of surfaces with spherical basic shape and the measurement of surfaces with flat basic shape can only be filled with high effort using the existing measurement techniques. The measurement technique proposed in this thesis is intended to fill this gap. It has been developed to characterize freeform shaped surfaces deviating from a flat with high accuracy using a straightforward measurement setup without cost-intensive optical components.

1.2 State of the art

1.2.1 Introduction

Exact requirements on accuracy to verify an optical component are not defined. However, if requirements for a surface quality are given, the measurement technique has to be accurate enough to confirm the surface quality or to give data to correct the surface. Otherwise, a confirmation or a correction of the surface quality is not possible [15].

In the field of metrology of aspheric surfaces, the measurement techniques have evolved in recent years, as aspheric components got common more and more in optical applications. A round robin test of aspheric surfaces using different measurement techniques revealed deviations in between the measurement techniques of up to $\pm 50\,\mathrm{nm}$ [18]. A round robin test including freeform surfaces deviating from a spherical basic shape showed deviations of up to $\pm 110\,\mathrm{nm}$ for the different measurements performed [17]. Since these round robin measurements included up-to-date measurement techniques, an accuracy in the same range is targeted.

In the following, state of the art measurement techniques are described. These techniques are basically distinguished in two types: surface sag measurement techniques and gradient based measurement techniques. While surface sag measurement techniques directly measure the surface height, gradient-based measurement techniques measure the surface gradient first and reconstruct the surface sag by integration of the measured surface gradient data [19].

Both measurement techniques have advantages and disadvantages. While surface sag measurement techniques directly create a point cloud with the determined positions, they need to offer the same accuracy over the full measurement range, including a standoff representing the SUT's distance from the measure's origin [20]. Therewith, even if the SUT is flat, redundant data is gathered by measuring the standoff with high accuracy. With gradient-based measurement techniques, this standoff is irrelevant, as not the surface sag, but the surface's gradient field is measured. This gradient field can be determined with a higher information efficiency, as it only represents the change of the sag and not the sag itself and its standoff [19]. Although, to reconstruct the surface sag from the determined gradient field, an appropriate integration method has to be used [21].

To utilize the advantages of gradient-based measurements, the measurement technique presented in this work is of this type and designed to measure specular surfaces in reflection. In the state of the art, both surface sag and gradient-based measurement techniques are presented, as both types are used for surface characterization measurements.

1.2.2 Surface sag measurement

Tactile coordinate measurement

The basic principle of tactile coordinate measurements is very descriptive. A stylus is moved over the surface under test (SUT). According to the sag of the SUT, the stylus is elevated [22]. This elevation can be measured in different ways. Dependent on the stylus type and size, different surface characteristics can be measured. Tactile coordinate measurement machines can achieve high accuracies even for large SUT sizes [18]. Examples for tactile coordinate measurement machines are *UA3P* series by Panasonic Corp., *ISARA 400* by IBS Precision Engineering GmbH or *MarSurf LD 130 / LD 260* by Mahr GmbH [23, 24, 25]. Since tactile coordinate measurement relies on a contact between the stylus and the SUT, damage at the SUT may occur. To overcome this problem the stylus can be replaced by an optical probe, leading to the following category of measurement technique.

Confocal/interferometric coordinate measurement

In confocal or interferometric coordinate measurement techniques, an optical probe determining the distance to the SUT replaces the tactile stylus. With this, higher scanning rates can be achieved [26]. Confocal probes can detect the distance of the probe from the SUT by determining the defocus of a test beam focused onto the SUT [27]. Interferometric probes determine height information from the phase difference between a reference and the SUT [22]. Therewith, the coordinates of the sampled point can be determined. However, both probe types have to stick to optical limitations. Especially when surfaces with higher slopes are faced, sufficient light has to return to the probe to work properly. This can be ensured by tilting the probe to be always perpendicular to the SUT at all sample points. If the mechanical and optical limitations are met, freeform surfaces can be measured with this measurement technique [28]. Examples for coordinate measurement machines with optical probes are *LuphoScan 260 HD* manufactured by AMETEK Inc., *CT 300* by cyberTECHNOLOGIES GmbH, *MarForm MFU 200 Aspheric 3D* by Mahr GmbH and *NMF350 S / NMF600 S* by Dutch United Instruments [29, 30, 31, 32].

Interferometry

The phenomenon of interference occurs, when two or more waves superpose and create regions of constructive and destructive superposition [1, 33]. For the purpose of optical metrology, this includes the superposition of two coherent waves, usually derived from splitting the light of one coherent beam into two separate beams [22, 27]. One of the beams, the test beam, can now be altered by the DUT, while the other beam, the reference beam, serves as a reference. Superposing the two beams, interference occurs. Since both beams have the same origin, differences in the optical path length, the optical path difference (OPD), defines the regions where constructive and destructive superposition occurs. In constructive regions, the OPD is an integer multiple of the light's wavelength [33]. These regions occur bright on a detector. In destructive regions, the OPD is an odd integer multiple of half of the lights wavelength. These regions occur dark. The patterns of dark and bright regions are called interferograms [1]. From these patterns, conclusions about the OPD and therewith about the altering of the test beam by the DUT can be drawn. In terms of a configuration, where the test beam is reflected by a SUT, its topography can be determined from the interferogram. In contrast to the coordinate measurement techniques shown before, interferometers have the advantage that the standoff is not measured, since only the OPD to the reference object is determined. However, this may not be confused with gradient-based measurement techniques, which determine the slope of a beams wavefront as described later.

Many different configuration types of interferometers have been developed. Well-known configurations are the Fizeau, Twyman-Green and Mach-Zehnder interferometer [33]. An

example for an interferometric metrology system is the *Verifire* series by Zygo [34]. It applies phase-shift interferometry on a Fizeau configuration [27].

Interferometers can provide high accuracies, but need very accurate alignment and positioning to achieve these potentials. Thus, high precision optical components and usually specialized staff is needed to operate an interferometer. The result of an inaccurate setup of an interferometer has painfully been determined in the Hubble Space Telescope program of NASA [35]. Due to the inaccurate setup, a form error has been manufactured into the aspheric primary mirror resulting in blurred images of the telescope.

Stitching interferometry

Certain limits apply when it comes to the evaluation of an interferogram. Considering a configuration where the test beam is reflected from a SUT and the reference beam is reflected from a reference surface, the interferogram's dark and bright regions indicates changes of the SUT's from the reference surface's topography. If this change is too fast, the bright and dark regions also alternate too fast and cannot be distinguished anymore. This problem can be overcome using stitching interferometry [36]. In this technique, the full aperture of a SUT, which cannot be investigated in one interferometric measurement due to limitations, is split into overlapping subapertures of smaller dimensions being within the limits. To investigate the subapertures according to the limits, the SUT is positioned and oriented within the interferometers scope. After investigating the subapertures separately, they are stitched together using the overlapping areas to reconstruct the full aperture's topography. Therewith, the limits of interferometric measurements are extended [37]. An example for a stitching interferometry measurement machine is the *ASI(Q)* by QED Technologies International, Inc. [38].

Interferometry with computer generated holograms

Using a computer-generated hologram (CGH) in an interferometer is not defining a new configuration of interferometer. It introduces a way to alter a beam in the interferometer by applying the wavefront stored in the CGH to one of the beams [22, 39]. Therewith, either a reference beam with a certain wavefront can be created that compensates the expected test wavefront, or the test wavefront can be altered to be comparable to a certain known reference wavefront. Either way, using a CGH extends the limits of interferometers of different configurations [40, 41]. This can even be applied to non-rotational apertures and freeform optics [8, 42]. A provider of CGHs is DIOPTIC GmbH. They offer CGHs for spherical, aspherical, cylindrical and even freeform surfaces [43]. A drawback of CGHs is that for every new SUT shape, a new CGH has to be manufactured, what can be time consuming and expensive [26].

Tilted wave interferometry

The technique of tilted wave interferometry is based on the extension of one spherical wavefront to create an array of tilted wavefronts propagating towards the SUT [15]. This array of tilted wavefronts is created using an aperture array in a collimated beam. Therewith, wavefronts are sent towards the SUT with different angles enabling the observation of the whole SUT from different directions simultaneously. As long as at least one of the wavefronts meet the limitations for a certain region on the SUT, this region can be observed. The basic shape to be measured with this technique is a sphere. With rather large departures from a sphere that can be measured, the technique is able to measure even large freeform surfaces deviating from a sphere as well [44]. However, when it comes to freeform surfaces deviating from a flat, this technique exceeds its limitations fast. This measurement technique has been implemented in the *MarOpto TWI 60* by Mahr GmbH [45].

1.2.3 Gradient-based measurement

Shack-Hartmann senor

Measuring the wavefront of a beam, a Shack-Hartmann sensor (SHS) offers a fast and handy solution. The functional principle is derived from the Hartmann-test [46]. It is based on splitting the wavefront to be measured in multiple small segments using a micro-lens array and focusing these smaller wavefront segments onto a 2D detector array [1]. Comparing the spot's locations to the locations when a collimated beam is introduced into the system, conclusions about the wavefront's slope can be drawn. Integrating the slope data, the wavefront can be reconstructed. Using such a sensor to investigate the wavefront reflected from a SUT, its topography can be reconstructed from the determined wavefront data [47]. However, the resolution of these sensors is limited and fixed by the micro-lens array. Additionally, the detectable wavefront slope is limited by the micro-lens pitch as ambiguities in the detected spots occur, when the wavefront slopes vary to fast. SHSs are available from multiple companies. Exemplary, the company OPTOCRAFT GmbH can be named, as this company is specialized in the manufacturing of SHSs in form of their *SHSCam* sensors [48, 49].

Lateral shearing interferometry

In the sections before, interferometry has been introduced as the superposing of a test wavefront with a reference wavefront. In lateral shearing interferometry, the test wavefront is superposed with itself by a small lateral shear [22, 50]. Therewith the OPD, creating the interferogram, is dependent on the wavefront's slope in the direction of the lateral shear. For the interferogram, one can say that a higher wavefront slope creates a larger OPD, while a lower wavefront slope creates a smaller OPD. After deriving the OPD from the interferogram and knowing the lateral shear, the wavefront's slope can be determined. Integrating this slope data, the wavefront can be reconstructed. May the wavefront be reflected from a SUT and the initial wavefront targeted onto the SUT is known, the SUT's topography can be reconstructed using lateral shearing interferometry. An example for a wavefront sensor using lateral shearing interferometry is the *SID4-HR* manufactured by Phasics SA [51, 52].

Phase measuring deflectometry

The technique known as phase measuring deflectometry (PMD) is also known as fringe reflection. It must not be confused with structured light projection, which is not applicable for specular surfaces. In PMD, a screen with a certain pattern is placed near by the SUT. The screens position and orientation is chosen in a way that its emitted light is reflected from the SUT into a camera [53, 54]. From the distortion of the reflected pattern, slope data of the SUT can be resolved. Since an ambiguity between the surface slope and the investigated point on the surface exists, absolute measurements are not possible. This ambiguity can be overcome by either using the surface model function to determine the differences from this model or by using a second camera for applying stereo deflectometry [55]. With this technique, even large objects can be measured [56]. An example for a measurement machine based on PMD is the *SpecGAGE3D* series, by ISRA VISION AG [57].

Laser deflectometry

The technique of laser deflectometry (LD), sometimes also called scanning beam deflectometry, is the technique of scanning a SUT with a single laser beam while determining the surface's slope from the deflected beams direction. The measurement technique presented in this thesis is a variation of the LD.

For LD multiple different implementations have been proposed. They can be categorized in implementations with imaging optics and techniques without imaging optics. Implementations including imaging optics use these optics to convert the direction of the reflected beam into a

position in the focal plane. Determining the position of the beam with an areal sensor and knowing the focal length of the imaging optic, the beams direction can be determined.

A measurement technique for almost flat surfaces has been proposed using a tilting mirror to scan the surface [58]. With this technique, high measurement speeds can be achieved, while the number of moving objects in the setup is very low.

Another measurement technique introduced for almost flat surfaces uses a pentaprism and an autocollimator [59]. The pentaprism is used to scan the surface, while the autocollimator is used to send out the test beam and to determine the reflected ray's direction. Variations of this measurement technique exist, including the separation of the measurement of the reflected beam's direction from the surface angle determination, a new sensor to determine the reflected rays direction or the ability to determine the surface curvature instead of slope to overcome inaccuracies in positioning stages [59, 60, 61].

To measure spherical SUTs, a technique has been introduced including a beamsplitter to generate a reference beam reflected from a flat mirror, while the test beam is targeted onto and reflected from the spherical SUT [62]. Using a collimating lens and an areal detector in the focal plane of the lens, the position of the test beam and the reference beam is determined. From the distance in between the two positions, the test beam's direction is determined. To scan the spherical surface, it is rotated around its center of curvature.

Another technique to measure surfaces with higher surface angles combines the laser deflectometry with principles from the confocal or interferometric coordinate measurement techniques [63]. A sensor head based on an autocollimator has been introduced. Rotating this sensor head around a virtual reference sphere, the investigated surface angle is kept in the range of the sensor for spherical and many typical aspheric surfaces. Measuring the surface slope as a difference to the virtual reference sphere and integrating this difference determines the surface deviation perpendicular to the virtual reference sphere.

Implementations of LD without imaging optics suffer from an ambiguity when determining a beams direction from one beam position on an areal sensor. Two methods to overcome this problem have been proposed using basically the same setup. The test beam is targeted onto the SUT vertically through a beamsplitter. The beamsplitter redirects the reflected beam onto an areal sensor, which determines the beam's position [64, 65]. Scanning the surface, the reflected beam's position is determined for multiple sample points on the SUT. To reconstruct the SUT from these positions, an approach based on solving a partial differential equation was proposed [64]. However, in this approach the reflected beam's position on the areal sensor is only defined by its distance to a reference given by a flat SUT. This leads to difficulties in reconstructing non-rotational symmetric surface or if the SUT model function is not known properly. Another approach has been proposed for the reconstruction of spherical or aspherical surfaces for the same setup. Using a spherical surface as initial guess, the reconstructed surface is approximated iteratively from the determined reflected beams positions on the detector [65]. However, both approaches rely on an exact definition of the distance between the sensor and the SUT for one position. Otherwise, the initial ambiguity cannot be resolved.

1.2.4 Discussion

The measurement techniques described before are especially for specular surfaces. Before going into the discussion of these techniques, it has to be mentioned that also techniques for the measurement of non-specular surfaces exist. Well-known examples for these techniques are shape from shading and structured light projection. Shape from shading is based on the evaluation of one or multiple photos of the SUT with a known light source and has, for example, been used to determine the shape of the lunar surface and is now also used to determine the

shapes of human faces [66, 67]. Structured light projection is based on the projection of one or multiple known patterns on the SUT and determining the SUT's topography from the distortion of the pattern, photographed with a camera under a certain angle [68, 69]. Implementations with multiple cameras have been developed as well as miniaturized setups with very small dimensions [70, 71].

The measurement technique proposed in this thesis is a gradient-based measurement technique and a variation of laser deflectometry. It measures the surface topography without tactile contact. This prevents surface damage. In contrast to confocal or interferometric coordinate measurement techniques or surface sag measuring interferometric measurement techniques, it measures the surface gradients. Thus, it obtains the advantages of gradient-based measurement techniques described before. In contrast to measurement techniques using a SHS or lateral shearing interferometry, the proposed measurement technique is not based on the measurement of a wavefront being reflected from the SUT, but on the measurement of the direction of a single narrow beam, reflected from the SUT. Therewith, it does not rely on the accuracy of certain optical components, like lenses, beamsplitters or lenslet-arrays. PMD retrieves the SUT's gradients from the distortion of a certain pattern on a screen. Therewith, it is not a scanning technique, since all sample points can be measured in one shot. However, PMD has an ambiguity between the surface sag and the surface slope that has to be resolved by introducing multiple camera systems or by knowing the SUT's model function in advance. Comparing the proposed measurement technique to other techniques based on laser deflectometry, one can say that the proposed method is a technique without imaging optics. This prevents the introduction of errors by these optics, which either influence the measurement result or have to be calibrated extensively for compensation. Comparing the proposed method to other laser deflectometry techniques without imaging optics, it has to be noticed that the techniques presented before still use an optical component in between the SUT and the areal detector: a beamsplitter. This is not necessary in the proposed technique. More clearly, no optical component in between the SUT and the areal detector is used. Furthermore, the ambiguity of the surface sag and the surface angle, which is overcome in the techniques described before by knowing the exact distance in between the SUT and the areal sensor, is resolved in the proposed method by using a variation of Experimental Ray Tracing (ERT) to determine the beam's direction [72]. Thus, the proposed measurement technique is a novel approach on the measurement of specular freeform surfaces. It overcomes ambiguities in the measurement data faced by other gradient-based measurement techniques, while making use of their advantages. Additionally, it does not rely on high precision optical components that have to be calibrated. It offers a smart and cost-efficient solution to the measurement of freeform specular surfaces.

1.3 Outline

The presented thesis is structured as follows. As seen before, the first chapter gives an introduction into the topic of surface metrology and an overview of the state of the art metrology systems. In the second chapter, the proposed measurement concept is presented and described. Techniques and methods used are introduced. Chapter two ends in an analytical model about the measurement methodology. This analytical model is transferred into a numerical model in chapter three. This numerical model is characterized by the discretization of the analytical model. The problems introduced by this discretization are described and the approaches to overcome these problems are described. This also includes the numerical integration of the determined gradient data and the handling of non-integrable data. In chapter four the numerical model is verified by simulation. A simulation model is presented including various parameters to simulate misalignments in the measurement setup. Using different

surface models, the flexibility of the proposed measurement technique is shown. In chapter five, the transfer of the simulation model into a real measurement setup is presented. The components, used in the experimental setup, as well as the measurement procedure are described. Using four different samples, the abilities of the proposed measurement technique are verified experimentally. Chapter six is dedicated to the error analysis. Several error sources are described and evaluated. The results from the error analysis are compared to experimental repeatability measurements. In chapter seven, the proposed measurement technique and the results presented are discussed. The thesis is concluded in chapter eight and an outlook is given for further developments and improvements of the proposed measurement technique.

2. Methodology

2.1 Concept of measurement

2.1.1 Introduction of optical model and basic optical principle

The basic optical model used for the conceptual development of the proposed measurement technique is known as geometrical optics [33, 73]. In this model, the wavelength is considered in the limit case of $\lambda \to 0$. Therewith, optical phenomena based on the description of light as waves, like diffraction and interference, are not considered. This opens up the possibility to use geometrical and algebraic tools to describe the behavior of light, as this has already been applied in ray tracing procedures [74]. For example, rays, representing the direction of the propagation of the flow of the radiant energy, can be described by geometrical lines [1]. This must not be confused with the model of paraxial optics. In this model, the concept of geometrical optics is also applied, but further simplifications are used to describe the optical behaviors in small angles and distances from the optical axis. As this does not apply to the proposed measurement method here, the paraxial model is not applicable.

A well-known optical principle is the law of reflection: “angle of incidence is equal to angle of reflectance” [1]. This law describes the relation of the angle Θ for the incidence ray and the angle Φ for the reflected ray to the normal of the surface at the point where the incident ray intersects with the surface [1, 73]. This relation is illustrated in Figure 2.1. The law says that the angles $\Theta = \Phi$ are equal, while the incident ray and the reflected ray have to be coplanar with the surface normal.

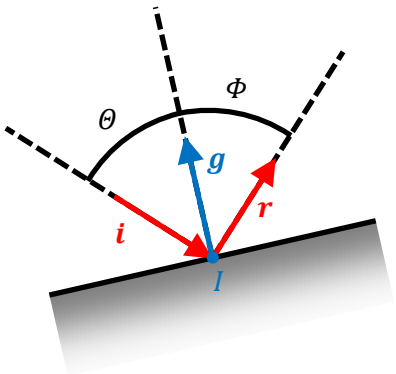

Figure 2.1: Sketch of the reflection of a ray with an incident angle Θ and an incident direction $\boldsymbol{i}$ at the point I of surface with the normal $\boldsymbol{g}$. After the reflection, the ray has the direction $\boldsymbol{r}$ with the reflectance angle Φ.

As described before, geometrical tools can be used to describe the behavior of light. Here, direction vectors are used to describe the direction of light rays while position vectors are used to describe points in space. To describe a light ray as a geometrical line in space completely, a point in space and a direction are needed [75]. However, mostly this is not necessary here. Regarding Figure 2.1, one can see that the directions of $\boldsymbol{i}$, $\boldsymbol{r}$ and $\boldsymbol{g}$ are not dependent on their

position in space, but only on their directional relation to each other. This means, the incident ray $\boldsymbol{i}$, the reflected ray $\boldsymbol{r}$ and the surface normal $\boldsymbol{g}$ can be represented by direction vectors, while the point I of intersection of the incident ray with the surface can be represented by a point in space with its position vector $\boldsymbol{I}$.

To define the geometrical relation between $\boldsymbol{i}$, $\boldsymbol{r}$ and $\boldsymbol{g}$, the vectors are considered unit vectors. This means they all have the same norm $|\boldsymbol{i}| = |\boldsymbol{r}| = |\boldsymbol{g}| = 1$. Having this, the surface normal

$$\boldsymbol{g} = \frac{\boldsymbol{r} - \boldsymbol{i}}{\sqrt{2\big(1 - (\boldsymbol{r} \cdot \boldsymbol{i})\big)}} \tag{2.1}$$

can be determined from $\boldsymbol{i}$ and $\boldsymbol{r}$ using vector geometry [76]. Thus, having the incident ray direction $\boldsymbol{i}$ and the reflected ray direction $\boldsymbol{r}$ for a point I, the surface normal $\boldsymbol{g}$ of the surface at this point can be determined.

2.1.2 Introduction of homogeneous coordinates, transformation matrices and coordinate systems

For the representation of direction vectors and position vectors in figures, a Cartesian vector space of the form $\mathbb{R}^3$ with the axis x, y and z is introduced. Cartesian coordinates are very descriptive and easily comprehensible. However, transformations in Cartesian coordinates, like translations or rotations, are cumbersome, as direction and position vectors have to be treated differently. Unfortunately, direction and position vectors cannot be distinguished by their structure in Cartesian coordinates. This is a problem as different coordinate systems (CSs) have to be defined within the Cartesian vector space including transformations of position and direction vectors between these CSs. To overcome this problem, homogeneous coordinates in a projective vector space are used [75].

In homogeneous coordinates, transformations and operations can be applied equally to position and direction vectors [77]. Additionally, problems regarding the far point of lines can be overcome [75]. These advantages have extensively been used in computer graphics, where three-dimensional scenes, even including infinitely far distant points, are transformed onto a two-dimensional screen plane [77]. These advantages are achieved by using one additional dimension resulting in a vector space of the form $\mathbb{R}^4$, the projective vector space V.

In V, a vector can be represented by

$$\boldsymbol{I} = \begin{pmatrix} I_X \\ I_Y \\ I_Z \\ I_W \end{pmatrix} \tag{2.2}$$

using the four homogeneous components I_X, I_Y, I_Z and I_W. As vectors in these homogeneous coordinates represent vectors from the Cartesian coordinates, transferred to another higher dimensional vector space, the set of all their vectors is also called projective space of the form $\mathbb{P}^3$ [75, 78]. In V, all points on a line through origin, except the origin itself, represent one and the same position vector in Cartesian coordinates. As one point of the line is the origin, a second point is needed to define the direction of the line. May I_x, I_y and I_z be the Cartesian coordinates of a position vector, one point on the line in homogeneous coordinates can be defined as

$$\boldsymbol{I} = \begin{pmatrix} I_x \\ I_y \\ I_z \\ 1 \end{pmatrix} = \begin{pmatrix} I_X \\ I_Y \\ I_Z \\ I_W \end{pmatrix} \Bigg|_{I_W=1} \tag{2.3}$$

using the Cartesian coordinates. To transfer any point on this line except the origin from homogeneous coordinates to the Cartesian coordinates, the equations

$$I_x = \frac{I_X}{I_W},\ I_y = \frac{I_Y}{I_W},\ I_z = \frac{I_Z}{I_W},\ \text{with } I_W \neq 0 \tag{2.4}$$

are used. In other words, one can say

$$I_x = I_X,\ I_y = I_Y,\ I_z = I_Z \text{ for } I_W = 1. \tag{2.5}$$

As in this work all position vectors are defined by the W-component being equal to 1, the equations given in Equation (2.5) apply to all position vectors.

In contrast to a position vector, a direction vector is not represented by a line through origin in homogeneous coordinates, but by a plane through origin. This plane has a unique line through origin where all points on this line have its W-component equal to 0. All lines lying in one plane in homogeneous coordinates have this same unique intersecting line and therewith represent the same direction vector in Cartesian coordinates. Thus, a direction vector pointing in a certain direction in Cartesian coordinates, no matter of its length, can be represented in homogeneous coordinates as a vector

$$\boldsymbol{g} = \begin{pmatrix} g_x \\ g_y \\ g_z \\ 0 \end{pmatrix} = \begin{pmatrix} g_X \\ g_Y \\ g_Z \\ g_W \end{pmatrix} \Bigg|_{g_W=0} \tag{2.6}$$

for $g_W = 0$. Or in other words,

$$g_x = g_X,\ g_y = g_Y,\ g_z = g_Z \text{ for } g_W = 0. \tag{2.7}$$

As in this work all direction vectors are defined by the W-component being equal to 0, Equation (2.7) applies to all direction vectors.

Thereby, position and direction vectors can now be distinguished in their homogeneous representation by the W-component. The wording of “homogeneous” comes from the fact that transformation can now be homogeneously applied to direction vectors and position vectors while their indication and characteristics are preserved [75].

A CS in the Cartesian space is defined by a basis in the vector space V. This basis represents the Cartesian CS with position and orientation. To represent vectors in different CSs, linear transformations in V in form of a change of basis are used [75, 78, 79]. These transformations are performed by multiplication of a homogeneous transformation matrix with the homogeneous vector to be transformed. If a shift of a Cartesian CS by Δx, Δy and Δz along the three axis x, y and z is desired, the transformation matrix

$$\mathbf{T}(\boldsymbol{t}) = \begin{pmatrix} 1 & 0 & 0 & -\Delta x \\ 0 & 1 & 0 & -\Delta y \\ 0 & 0 & 1 & -\Delta z \\ 0 & 0 & 0 & 1 \end{pmatrix}, \tag{2.8}$$

using the translation vector $\boldsymbol{t} = (\Delta x, \Delta y, \Delta z)$, can be defined. When this transformation matrix is applied to the homogeneous representation of a Cartesian position or direction vector, the new values of the homogeneous vector represent the Cartesian position or direction vector

accordingly to the desired shift. The negative sign here comes from the fact that a movement of the CS according to $\boldsymbol{t}$ results in an inverse movement of the vectors.

If differences in the orientation of Cartesian CSs exist, the matrices

$$\mathbf{R}_x(\alpha) = \begin{pmatrix} 1 & 0 & 0 & 0 \\ 0 & \cos(\alpha) & -\sin(\alpha) & 0 \\ 0 & \sin(\alpha) & \cos(\alpha) & 0 \\ 0 & 0 & 0 & 1 \end{pmatrix}, \tag{2.9}$$

$$\mathbf{R}_y(\beta) = \begin{pmatrix} \cos(\beta) & 0 & \sin(\beta) & 0 \\ 0 & 1 & 0 & 0 \\ -\sin(\beta) & 0 & \cos(\beta) & 0 \\ 0 & 0 & 0 & 1 \end{pmatrix} \tag{2.10}$$

and

$$\mathbf{R}_z(\gamma) = \begin{pmatrix} \cos(\gamma) & -\sin(\gamma) & 0 & 0 \\ \sin(\gamma) & \cos(\gamma) & 0 & 0 \\ 0 & 0 & 1 & 0 \\ 0 & 0 & 0 & 1 \end{pmatrix} \tag{2.11}$$

can be defined using the angles in the rotation vector $\boldsymbol{\gamma} = (\alpha, \beta, \gamma)$ [75]. These angles represent the rotations around the axis x, y and z in a Cartesian CS. Applying the transformation matrices defined in Equation (2.9), (2.10) and (2.11) to a homogeneous vector representing a Cartesian position or direction vector, the resulting homogeneous vector represents the Cartesian position or direction vector accordingly to the rotations defined by $\boldsymbol{\gamma}$. As these transformations can be performed homogeneously to homogeneous vectors, they can easily be combined using matrix multiplication. Thus, the matrix

$$\mathbf{H}(\boldsymbol{\gamma}, \boldsymbol{t}) = \mathbf{R}_z(\gamma)\mathbf{R}_y(\beta)\mathbf{R}_x(\alpha)\mathbf{T}(\boldsymbol{t}) \tag{2.12}$$

performs all transformations in one step while the order of the transformation is backwards in terms of the order shown in Equation (2.12). This means that the translation is performed first. After that, the rotations in the order xyz are performed. These rotations are intrinsic rotations with Cardan angles. Thus, the next rotation is always performed in reference to the orientation of the CS after the previous one [80]. To prevent misleading interpretations here, it has to be mentioned that these transformations are defined to change the CSs around fixed vectors and not to rotate vectors within a fixed CS. A rotation with $\alpha > 0$ leads to a rotation of the z-axis towards the y-axis of a CS. A rotation around the y-axis with $\beta > 0$ leads to a rotation of the x-axis towards the z-axis of a CS. Finally, a rotation around the z-axis with $\gamma > 0$ leads to a rotation of the y-axis towards the x-axis of a CS.

The location and orientation of a Cartesian CS projected in V can be described by a basis in V. May $\mathcal{S}$ be such a basis, it is defined by four vectors. Three vectors represent the direction vectors of the Cartesian CS projected to homogeneous coordinates. The fourth vector is a position vector describing the origin of this Cartesian CS projected to homogeneous coordinates. Thus, one can say $\mathcal{S} = \{\boldsymbol{e}_X, \boldsymbol{e}_Y, \boldsymbol{e}_Z, \boldsymbol{O}^{\mathcal{S}}\}$, where $\boldsymbol{e}_X, \boldsymbol{e}_Y, \boldsymbol{e}_Z \in V$ are orthonormal and describe the orientation of the CS while $\boldsymbol{O}^{\mathcal{S}} = \left(B_X^{\mathcal{S}}, B_Y^{\mathcal{S}}, B_Z^{\mathcal{S}}, 1\right)^T \in V$ describes its origin. Therewith, all elements of V can be described as a linear combination of $\mathcal{S}$ [79]. Since this description is unique and the elements of $\mathcal{S}$ are linear independent, $\mathcal{S}$ is a basis of V. Having this basis, the relation between the canonical basis of V and $\mathcal{S}$ can be described by the transformation matrix $\mathbf{H}_V^{\mathcal{S}}$ performing the mapping $V \rightarrow \mathcal{S}$. To reverse this transformation, the invers $\mathbf{H}_V^{\mathcal{S}\,-1} = \mathbf{H}_{\mathcal{S}}^V$ can be used. Having another Cartesian CS which can be defined in homogeneous coordinates by the basis $\mathcal{M}$, the transformation matrix $\mathbf{H}_V^{\mathcal{M}}$ can be defined to

transfer vectors into this CS. In this work, the canonical basis of V is irrelevant, as only the relation of the bases defined in V to each other is used. This relation

$$\mathbf{H}\left(\boldsymbol{\gamma}_{\mathcal{S}}^{\mathcal{M}}, \boldsymbol{t}_{\mathcal{S}}^{\mathcal{M}}\right) = \mathbf{H}_{\mathcal{S}}^{\mathcal{M}} = \mathbf{H}_{V}^{\mathcal{M}}\mathbf{H}_{\mathcal{S}}^{V} \tag{2.13}$$

is defined using the canonical basis, but can be bypassed if $\mathbf{H}_{\mathcal{S}}^{\mathcal{M}}$ can be defined independently. Having a transformation matrix, the transformation of direction and position vectors

$$\boldsymbol{g}^{\mathcal{S}} = \mathbf{H}_{\mathcal{M}}^{\mathcal{S}}\boldsymbol{g}^{\mathcal{M}} \text{ and } \boldsymbol{I}^{\mathcal{S}} = \mathbf{H}_{\mathcal{M}}^{\mathcal{S}}\boldsymbol{I}^{\mathcal{M}} \tag{2.14}$$

can be applied homogeneously.

The CSs used in this work are illustrated in the sketched measurement setup in Figure 2.2.

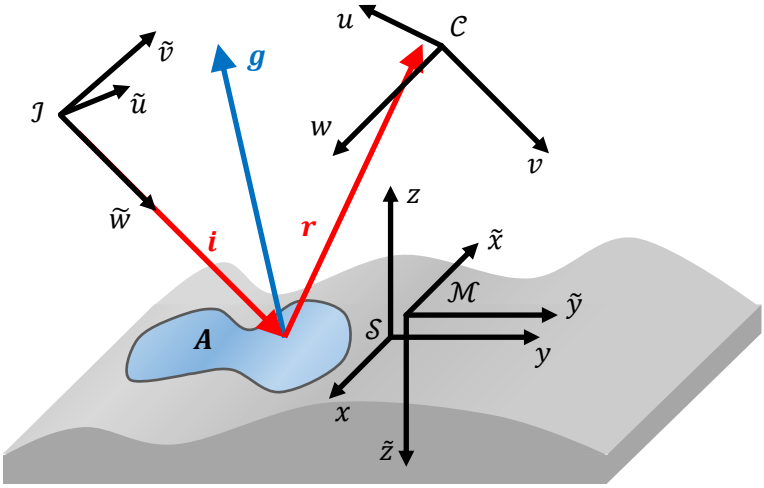

Figure 2.2: Sketch of the measurement setup with the four CSs: incident ray $\mathcal{I}$, camera $\mathcal{C}$, measurement plane $\mathcal{M}$ and the surface under test $\mathcal{S}$. $\boldsymbol{A}$ represents the investigated area.

Incident ray $\mathcal{I}$

This CS with the basis $\mathcal{I}$ represents the CS, wherein the incident ray is introduced into the measurement setup. Its axes are named $\tilde{u}$, $\tilde{v}$, $\tilde{w}$. Within this CS, the incident ray is directed along the $\tilde{w}$-axis.

Camera $\mathcal{C}$

The name of this CS with the basis $\mathcal{C}$ already identifies the experimental implementation of one of the components of the measurement setup. However, this does not change the meaning of the CS, as it is the one the reflected ray's direction is determined in. The axes of this CS are u, v, w.

Measurement plane $\mathcal{M}$

The measurement plane identifies the direction of the sampling of the SUT. As the proposed measurement technique does not detect the surface's orientation and alignment in relation to the complete device under test (DUT), this may not be mistaken with the orientation and location of the DUT itself. This gets clearer, when the measurement principle is described in Chapter 2.1.3. The CS has the basis $\mathcal{M}$ and the axes are $\tilde{x}$, $\tilde{y}$, $\tilde{z}$.

Surface under test $\mathcal{S}$

If the model function of the SUT is known, this function is described in this CS with the basis $\mathcal{S}$ and the axes x, y, z. The SUT is represented by the function

$$z = s(\boldsymbol{x}): \mathbb{R}^2 \rightarrow \mathbb{R}, \text{ with } \boldsymbol{x} = (x, y)^T \in \boldsymbol{A}, \tag{2.15}$$

which has to be defined over the investigated area $\boldsymbol{A}$ in the xy-plane. With this, one can see that the position vector to I has to fulfil

$$\boldsymbol{I}(\boldsymbol{x}) = \begin{pmatrix} x \\ y \\ s(\boldsymbol{x}) \\ 1 \end{pmatrix}. \tag{2.16}$$

The SUT has to satisfy the requirements to be continuous and continuously differentiable over $\boldsymbol{A}$, as steps in the surface cannot be detected. In addition, the surface must not exceed incidence angles of $\Theta \geq 90°$ as this leads to ambiguous points of intersection or dark spots on the SUT, which cannot be investigated. This can easily been recognized regarding Figure 2.1 and imagining an increase of Θ to $90°$. Furthermore, as this is a gradient-based measurement technique, it has to be said that a constant in $s(\boldsymbol{x})$ cannot be reconstructed.

From here on, all calculations related to direction or position vectors are performed using their homogeneous representation, while their presentation in figures is in Cartesian coordinates. The CSs are named by their basis defined in homogeneous coordinates. Thus, if the CS $\mathcal{I}$ is named, this relates to the Cartesian CS, represented by the basis $\mathcal{I}$ in homogeneous coordinates.

2.1.3 Measurement principle

Using the CSs described before, a measurement principle can be settled that scans the SUT and determines the normal $\boldsymbol{g}$ for any point I of the SUT within $\boldsymbol{A}$. Therefore, the incident ray is targeted onto the SUT with a certain direction that is along the $\tilde{w}$-axis of the CS $\mathcal{I}$ as shown in Figure 2.2. The direction of the reflected ray is determined in the CS $\mathcal{C}$. This will further be described in Chapter 2.2. From here on, the CSs $\mathcal{I}$ and $\mathcal{C}$ are considered to be fixed in relation to each other. In addition, the CS $\mathcal{S}$ is considered to be fixed in relation to the CS $\mathcal{M}$ within one measurement. To scan the surface, the CSs $\mathcal{S}$ and $\mathcal{M}$ can be translated arbitrarily within the $\tilde{x}\tilde{y}$-plane. Therefore the basis

$$\boldsymbol{O}^{\mathcal{M}} = \begin{pmatrix} B_{\tilde{x}}^{\mathcal{M}} - \tilde{x} \\ B_{\tilde{y}}^{\mathcal{M}} - \tilde{y} \\ B_{\tilde{z}}^{\mathcal{M}} \\ 1 \end{pmatrix} \tag{2.17}$$

of the CS $\mathcal{M}$ is shifted to target a certain position $\tilde{\boldsymbol{x}} = (\tilde{x}, \tilde{y})^T$. The incident ray can now be targeted onto any point on the SUT according to $\boldsymbol{I}$ in Equation (2.16).

As the direction of the reflected ray is dependent on the point I on the surface and is determined in the CS $\mathcal{C}$, it can be described as $\boldsymbol{r}^{\mathcal{C}}(\boldsymbol{I})$. To determine the surface normal using Equation (2.1), also the direction of the incident ray has to be known in $\mathcal{C}$. Having the relation between $\mathcal{I}$ and $\mathcal{C}$, the incident ray's direction $\boldsymbol{i}^{\mathcal{C}} = \mathbf{H}_{\mathcal{I}}^{\mathcal{C}}\, \boldsymbol{i}^{\mathcal{I}}$ in the CS $\mathcal{C}$ can be defined according to Equation (2.14). Applying Equation (2.1) one can get the surface normal direction

$$\boldsymbol{g}^{\mathcal{C}}(\boldsymbol{I}) = \frac{\boldsymbol{r}^{\mathcal{C}}(\boldsymbol{I}) - \boldsymbol{i}^{\mathcal{C}}}{\sqrt{2\left(1 - (\boldsymbol{r}^{\mathcal{C}}(\boldsymbol{I}) \cdot \boldsymbol{i}^{\mathcal{C}})\right)}} \tag{2.18}$$

for any $\boldsymbol{I}$.

With $\boldsymbol{g}^{\mathcal{S}}(\boldsymbol{I}) = \mathbf{H}_{\mathcal{S}}^{\mathcal{C}} \boldsymbol{g}^{\mathcal{C}}(\boldsymbol{I})$, this can now be transferred into the CS $\mathcal{S}$ where $s(\boldsymbol{x})$ is defined. According to Equation (2.6) and (2.16), the vector components

$$\boldsymbol{g}^{\mathcal{S}}(\boldsymbol{I}) = \begin{pmatrix} g_x^{\mathcal{S}}(\boldsymbol{I}) \\ g_y^{\mathcal{S}}(\boldsymbol{I}) \\ g_z^{\mathcal{S}}(\boldsymbol{I}) \\ 0 \end{pmatrix} = \boldsymbol{g}^{\mathcal{S}}(\boldsymbol{x}) \tag{2.19}$$

can be derived from $\boldsymbol{g}^{\mathcal{S}}(\boldsymbol{I})$ dependent on $\boldsymbol{x}$. This means that the direction of a normal on the surface $s(\boldsymbol{x})$ is only dependent on $\boldsymbol{x}$. Having the surface normal, the slopes

$$s_x(\boldsymbol{x}) = \frac{\partial s(\boldsymbol{x})}{\partial x} = -\frac{g_x^{\mathcal{S}}(\boldsymbol{x})}{g_z^{\mathcal{S}}(\boldsymbol{x})} \tag{2.20}$$

and

$$s_y(\boldsymbol{x}) = \frac{\partial s(\boldsymbol{x})}{\partial y} = -\frac{g_y^{\mathcal{S}}(\boldsymbol{x})}{g_z^{\mathcal{S}}(\boldsymbol{x})} \tag{2.21}$$

can be determined. These slopes also represent the first derivatives of $s(\boldsymbol{x})$ in x- and y-direction at the position $\boldsymbol{x}$ [79, 81].

Using the Nabla vector $\boldsymbol{\nabla} = \left(\frac{\partial}{\partial x}, \frac{\partial}{\partial y}, \frac{\partial}{\partial z}\right)^T$, a gradient field

$$\boldsymbol{\zeta}(\boldsymbol{x}) = \boldsymbol{\nabla} s(\boldsymbol{x}) = \begin{pmatrix} \dfrac{\partial s(\boldsymbol{x})}{\partial x} \\ \dfrac{\partial s(\boldsymbol{x})}{\partial y} \\ \dfrac{\partial s(\boldsymbol{x})}{\partial z} \end{pmatrix} = \begin{pmatrix} s_x(\boldsymbol{x}) \\ s_y(\boldsymbol{x}) \\ 0 \end{pmatrix} \tag{2.22}$$

can be defined in the CS $\mathcal{S}$. As the surface function is continuous and continuously differentiable over $\boldsymbol{A}$, the integral

$$\int_{\boldsymbol{x}_0}^{\boldsymbol{x}_1} \boldsymbol{\zeta}(\boldsymbol{x}) d\boldsymbol{x} \tag{2.23}$$

for two arbitrary positions $\boldsymbol{x}_0$ and $\boldsymbol{x}_1$, with $\boldsymbol{x}_0, \boldsymbol{x}_1 \in \boldsymbol{A}$, is independent on the path of the integration within $\boldsymbol{A}$ on the gradient field $\boldsymbol{\zeta}(\boldsymbol{x})$ [78]. May $\boldsymbol{x}_0 = (0,0)$ and $s(\boldsymbol{x}_0) = A$, the surface function can be defined for any arbitrary position $\boldsymbol{x}$ as

$$s(\boldsymbol{x}) = \int_{\boldsymbol{x}_0}^{\boldsymbol{x}} \boldsymbol{\zeta}(\boldsymbol{x}) d\boldsymbol{x} + A \tag{2.24}$$

from the gradient field.

2.2 Experimental Ray Tracing

The detection of the direction $\boldsymbol{r}$ of the reflected ray is determined in the CS $\mathcal{C}$. Within this CS a variation of a technique called ERT is used. ERT has initially been introduced to characterize optical components in transmission [72]. The idea is based on a measurement technique for collimating optics called Hartmann test [46]. In this measurement technique, a plate with pinholes is placed in front of an optical component. Having a collimated beam directed onto this plate, single sub beams, considered as rays, are created. These rays propagate through the optical component independently. Behind the optical component, the positions of the rays are detected around the focus using two parallel photo plates being exposed separately. From

the spots the rays create on the photo plate, information about the optical component can be determined. However, this technique was time-consuming as it took a long time to investigate the photo plates using a microscope. To overcome this problem, a laser diode with a pinhole and a movable scanning mirror replaced the pinhole plate. In addition, a position sensitive detector on a linear positioning stage has replaced the two photo plates [72]. Therewith, arbitrary positions on the optical component can be investigated, while the fast detection of the ray's position using the position sensitive detector can be performed in two parallel planes using the linear stage. A connection between the world of simulations using ray tracing and the experimental measurements has been built as ray tracing can now also be performed experimentally. In a next step, this technique has been developed further by using a fiber-coupled laser diode on linear stages for the positioning of the incident beam and a camera for the beam position detection. This led to a higher accuracy and repeatability of the measurement results [82].

In the measurement technique proposed here, the part of the setup of ERT to detect the ray's direction is used. The principle can be described by using the sketch shown in Figure 2.3.

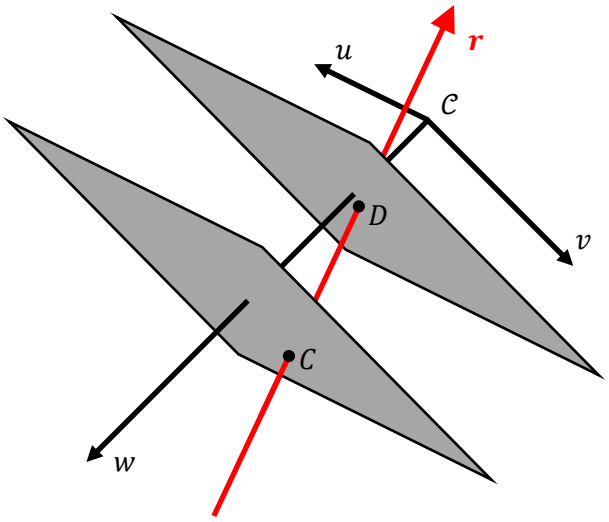

Figure 2.3: Sketch of the technique used for the detection of the direction of the reflected ray $\boldsymbol{r}$ by determining its intersection points C and D with two parallel planes.

As shown in Figure 2.3, two parallel planes are used to detect the reflected rays direction $\boldsymbol{r}$. These two parallel planes are perpendicular to the w-axes of the CS $\mathcal{C}$ and must not be identical. With this, two points C and D can be defined, where the reflected ray intersects with these planes. With the two position vectors $\boldsymbol{C}$ and $\boldsymbol{D}$ to the points C and D, the direction of the reflected ray

$$\boldsymbol{r} = \frac{\boldsymbol{D} - \boldsymbol{C}}{|\boldsymbol{D} - \boldsymbol{C}|} \tag{2.25}$$

can be determined. From this equation, one can see that the direction of $\boldsymbol{r}$ is dependent on the position of the two parallel planes. However, the orientation of the positive direction of $\boldsymbol{r}$ is dependent on these positions. Thus, it has to be assured that the positions are chosen that $C_w^{\mathcal{C}} > D_w^{\mathcal{C}}$ to preserve the validity of Equation (2.1).

2.3 Determination of surface gradients and surface reconstruction

2.3.1 Shift of sample points

As shown in Equation (2.16), the point of intersection is not only dependent on x and y but also on the function $s(\boldsymbol{x})$ that represents the point's position in z-direction. This is problematic, as the surface function $s(\boldsymbol{x})$ is intended to be determined with this measurement technique. Assuming $\boldsymbol{i}$ is parallel to the yz-plane, has an incident angle of $45°$ to the xy-plane and points onto a point J in the $\tilde{x}\tilde{y}$-plane, one can see that a change of the surface in z-direction results in a shift of I as illustrated in Figure 2.4. Additionally, this shift is dependent on the z-position and therewith on $s(\boldsymbol{x})$. Thus, a mapping from J to $\boldsymbol{x}$ independent on $s(\boldsymbol{x})$ is not possible.

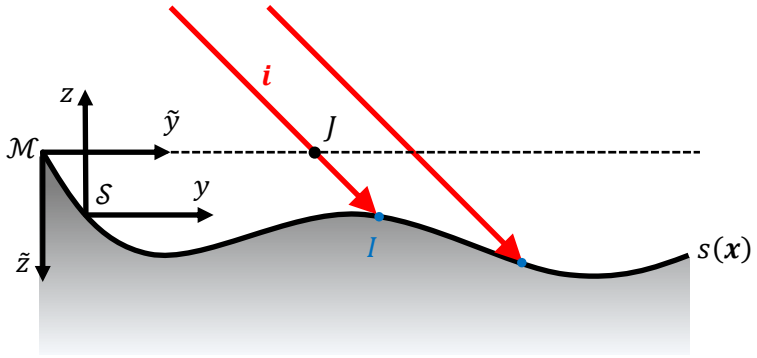

Figure 2.4: Sketch to show the difference between J and I. The partially transparent line shows an alternative position, to illustrate the change of I dependent on a shift of J in $\tilde{y}$-direction.

Although, having $s(\boldsymbol{x})$ and the transformation matrix $\mathbf{H}_{\mathcal{M}}^{\mathcal{S}}$, one can get a relation between the targeted position J with its position vector

$$\boldsymbol{J} = \boldsymbol{J}(\tilde{\boldsymbol{x}}) = \begin{pmatrix} \tilde{x} \\ \tilde{y} \\ 0 \\ 1 \end{pmatrix}, \tag{2.26}$$

and the point I, where $\tilde{\boldsymbol{x}} = (\tilde{x}, \tilde{y})$ is the targeted position in the $\tilde{x}\tilde{y}$-plane. To find this relation, the incident ray direction is used to create a set of position vectors

$$\boldsymbol{R}^{\mathcal{M}} = \boldsymbol{J} + \kappa \boldsymbol{i}^{\mathcal{M}},\ \kappa \in \mathbb{R} \tag{2.27}$$

on a line in the direction of $\boldsymbol{i}$ through the point J [83]. With $\mathbf{H}_{\mathcal{M}}^{\mathcal{S}}$ the position vectors

$$\boldsymbol{R}^{\mathcal{S}} = \boldsymbol{J}^{\mathcal{S}} + \kappa \boldsymbol{i}^{\mathcal{S}} \tag{2.28}$$

are also known. Determining the factor κ to fulfill

$$\boldsymbol{R}^{\mathcal{S}} = \boldsymbol{I}^{\mathcal{S}}, \tag{2.29}$$

a relation between the targeted position $\tilde{\boldsymbol{x}}$ and the position $\boldsymbol{I}(\boldsymbol{x})$ is found. Regarding Figure 2.4, one can say that this means that the point I is the point of intersection of $\boldsymbol{i}$, extended through the point J, and the surface $s(\boldsymbol{x})$.

2.3.2 Solution for known surfaces

Having the transformation matrix $\mathbf{H}_{\mathcal{M}}^{\mathcal{S}}$ and knowing the surface function $s(\boldsymbol{x})$, a relation between the targeted position $\boldsymbol{J}$ and the surface can be determined. However, one has to assume the base of the coordinate system $\mathcal{S}$ and therewith $\mathbf{H}_{\mathcal{M}}^{\mathcal{S}}$ is unknown. This could be the

case if, for example, the SUT is not placed perfectly centered and perfectly oriented. Thus, $\mathbf{H}_{\mathcal{M}}^{\mathcal{S}}$ has to be determined from the detected surface data.

As the integration according to Equation (2.24) can only be performed if the coordinates $\boldsymbol{x}$ are known, the determination of $\mathbf{H}_{\mathcal{M}}^{\mathcal{S}}$ is performed using the slope information. Assuming the SUT is positioned and oriented perfectly, $\mathbf{H}_{\mathcal{M}}^{\mathcal{S}}$ can be determined from the expected relation given by the measurement setup. With this assumption, one can determine the expected point of intersection K by finding its position vector $\boldsymbol{K}\left(\mathbf{H}_{\mathcal{M}}^{\mathcal{S}}, \tilde{\boldsymbol{x}}\right)$ as the intersection of $\boldsymbol{R}^{\mathcal{S}}$ with the SUT using Equation (2.29). Using Equation (2.20) and (2.21), one can calculate the expected surface slopes $a\left(\mathbf{H}_{\mathcal{M}}^{\mathcal{S}}, \tilde{\boldsymbol{x}}\right)$ and $b\left(\mathbf{H}_{\mathcal{M}}^{\mathcal{S}}, \tilde{\boldsymbol{x}}\right)$ in x- and y-direction for the position $\boldsymbol{K}\left(\mathbf{H}_{\mathcal{M}}^{\mathcal{S}}, \tilde{\boldsymbol{x}}\right)$. However, as it is assumed that the SUT is not placed perfectly, it has also to be expected that $\boldsymbol{K} \neq \boldsymbol{I}$ and therewith also $a\left(\mathbf{H}_{\mathcal{M}}^{\mathcal{S}}, \tilde{\boldsymbol{x}}\right) \neq s_x(\boldsymbol{x})$ and $b\left(\mathbf{H}_{\mathcal{M}}^{\mathcal{S}}, \tilde{\boldsymbol{x}}\right) \neq s_y(\boldsymbol{x})$. To find the relation between $\mathcal{S}$ and $\mathcal{M}$, one has to set

$$a\left(\mathbf{H}_{\mathcal{M}}^{\mathcal{S}}, \tilde{\boldsymbol{x}}\right) = s_x(\boldsymbol{x}) \text{ and } b\left(\mathbf{H}_{\mathcal{M}}^{\mathcal{S}}, \tilde{\boldsymbol{x}}\right) = s_y(\boldsymbol{x}) \tag{2.30}$$

and find a solution for $\mathbf{H}_{\mathcal{M}}^{\mathcal{S}}$ to fulfill this equation.

2.3.3 Solution for unknown surfaces

In contrast to the chapter before, the surface function $s(\boldsymbol{x})$ is here considered unknown. Thus, neither the expected point of intersection $\boldsymbol{K}$ nor expected surface slopes a and b can be determined as κ in Equation (2.29) cannot be found. This leads to the problem that with an unknown position $\boldsymbol{x}$ of the surface slopes, an integration cannot be performed. However, observing the situation from another CS, these problems can be overcome.

Observing the situation from the CS $\mathcal{I}$, this CS is considered to be fixed in relation to $\mathcal{M}$. Instead of moving the origin of $\mathcal{M}$ according to Equation (2.17), the incident ray is assumed to target a certain position $\tilde{\boldsymbol{x}}$ by moving within the $\tilde{u}\tilde{v}$-plane in $\mathcal{I}$. To overcome the dubiety about the factor κ, the position $\boldsymbol{J}^{\mathcal{M}}$ is transferred into the CS $\mathcal{I}$. As $\boldsymbol{i}$ is parallel to the $\tilde{w}$-axis in the CS $\mathcal{I}$, the position $\boldsymbol{J}^{\mathcal{M}}$ can be transferred into the CS $\mathcal{I}$ and projected onto the $\tilde{u}\tilde{v}$-plane without translations in $\tilde{u}$- or $\tilde{v}$-direction. As homogeneous coordinates are used, this can also be performed using a transformation matrix. Thus, one can say that the position vector

$$\boldsymbol{L}^{\mathcal{I}} = \begin{pmatrix} 1 & 0 & 0 & 0 \\ 0 & 1 & 0 & 0 \\ 0 & 0 & 0 & 0 \\ 0 & 0 & 0 & 1 \end{pmatrix} \mathbf{H}_{\mathcal{M}}^{\mathcal{I}} \boldsymbol{J}^{\mathcal{M}} \tag{2.31}$$

points to L in the $\tilde{u}\tilde{v}$-plane as shown in Figure 2.5. Therewith, the line of the incident beam

$$\boldsymbol{R}^{\mathcal{I}} = \boldsymbol{L}^{\mathcal{I}} + \kappa \boldsymbol{i}^{\mathcal{I}} \tag{2.32}$$

can be defined in the CS $\mathcal{I}$. Transferring the surface normal $\boldsymbol{g}^{\mathcal{I}} = \mathbf{H}_{\mathcal{C}}^{\mathcal{I}} \boldsymbol{g}^{\mathcal{C}}$ to the CS $\mathcal{I}$, it can be mapped to the position $\boldsymbol{L}^{\mathcal{I}}$ directly as the position of $\boldsymbol{L}^{\mathcal{I}}$ in the $\tilde{u}\tilde{v}$-plane is independent on the factor κ. This can also be seen regarding Figure 2.5. The point L is independent on I even if $s(\boldsymbol{x})$ is changing since J is fixed.

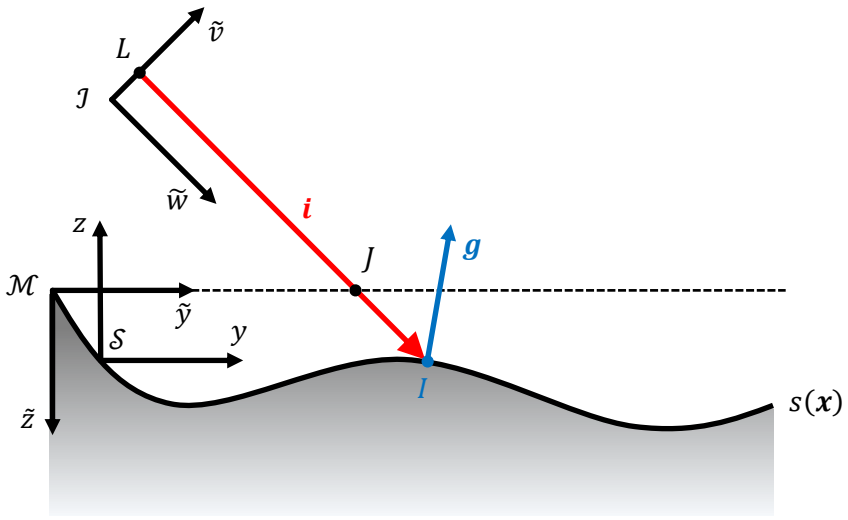

Figure 2.5: Sketch of the incident ray location in the CS $\mathcal{I}$ after the transformation of the targeted point J.

Using Equation (2.20) and (2.21) one can determine the surface slopes $s_{\tilde{u}}(\tilde{u},\tilde{v}) = -\frac{g^{\mathcal{I}}_{\tilde{u}}}{g^{\mathcal{I}}_{\tilde{w}}}$ and $s_{\tilde{v}}(\tilde{u},\tilde{v}) = -\frac{g^{\mathcal{I}}_{\tilde{v}}}{g^{\mathcal{I}}_{\tilde{w}}}$ from the normal in the CS $\mathcal{I}$. Applying Equation (2.24) accordingly in $\mathcal{I}$, the surface function can be determined. However, the surface $s(\tilde{u},\tilde{v})$ will then be represented in the CS $\mathcal{I}$. Thus, one can define the position of intersection

$$\boldsymbol{I}^{\mathcal{S}} = \mathbf{H}^{\mathcal{S}}_{\mathcal{I}}\boldsymbol{I}^{\mathcal{I}} = \mathbf{H}^{\mathcal{S}}_{\mathcal{I}}\begin{pmatrix}\tilde{u}\\ \tilde{v}\\ s(\tilde{u},\tilde{v})\\ 1\end{pmatrix} \tag{2.33}$$

that also represents the surface shape in the CS $\mathcal{S}$, from the integration performed in the CS $\mathcal{I}$. It has to be mentioned here that this is a theoretical construct as the rotation of analytical functions is not trivial and can easily lead to ambiguities. In the numerical model, this is more applicable.

3. Numerical model

3.1 Introduction

As this measurement technique is a scanning technique, it includes two major characteristics. First, the surface cannot be investigated continuously, but only on certain discrete points. Second, these discrete points cannot be investigated at the same moment, but have to be scanned serially. This chapter's focus is set onto the first point mentioned, as this introduces a new perspective on the methodology described before. The effects of the second point mentioned are further described in Chapter 5.1.

As described in the beginning of this thesis, the terminology of the discrete sampling is that the symbols stay the same, but get an index showing their discrete character. The meaning of the index is shown in the following chapter.

3.2 Sample points, surface normal and gradient field detection

As described before, the investigation of the SUT is performed by the observation of discrete points on SUT. In Chapter 2.3.1 it has been shown that the actual investigated point on the SUT is dependent on the shape of the SUT and its positioning in the setup. Thus, defining points to be investigated on the SUT directly is not possible. However, it is possible to define a number M of discrete sample points

$$\tilde{\boldsymbol{x}}_i = \begin{pmatrix} \tilde{x}_i \\ \tilde{y}_i \end{pmatrix}, \text{ with } i = 1 \dots M, \tag{3.1}$$

in the measurement plane, as described in Chapter 2.1.3. In Equation (2.17), these points represent a negative shift of the origin of the CS $\mathcal{M}$. As the CS $\mathcal{S}$ is fixed to the CS $\mathcal{M}$, one can also interpret this shift of the origin as a positive shift of the CSs $\mathcal{I}$ and $\mathcal{C}$ so that the incident ray is positioned to $\tilde{\boldsymbol{x}}_i$ in the $\tilde{x}\tilde{y}$-plane. This situation is shown in Figure 3.1. Since the sample points are now discrete, this leads also to the discrete points I_i and the discrete reflected ray directions $\boldsymbol{r}_i$. Still, it has to be fulfilled that the projection of $\boldsymbol{I}_i$ on the xy-plane has to be an element of $\boldsymbol{A}$. In Figure 3.1, a possible sequence of sample points is illustrated. However, this is only an example as the shape of the sampled area can be changed individually for any SUT.

Additionally to the shape of the area, the sample distances $\Delta\tilde{y}$ in $\tilde{y}$-direction and $\Delta\tilde{x}$ in $\tilde{x}$-direction can be chosen individually. Having one sample point at $(0,0)$, one can define all other sample points

$$\tilde{\boldsymbol{x}}_i = (f_i \Delta\tilde{x}, g_i \Delta\tilde{y})^T \text{ with } f_i, g_i \in \mathbb{Z} \text{ and } i = 1 \dots M \tag{3.2}$$

as a vector of integer multiples f_i and g_i of the sample distance. Adding constants to the two elements of $\tilde{\boldsymbol{x}}_i$ one can introduce a shift of all sample points in $\tilde{x}$- or $\tilde{y}$-direction.

For the principle of the measurement technique, the sample grid does not have to be even and can also be of arbitrary shape. However, in this work only even grids with a constant sample distance are considered. The shape of the sample grids in this work are either square, circular or a single line for a cross-section measurement.

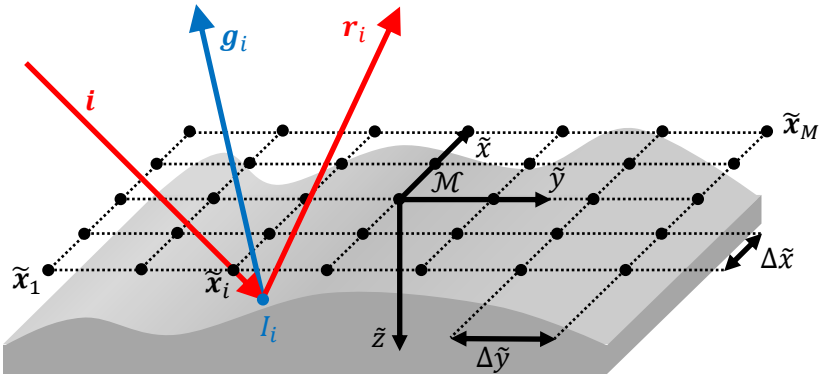

Figure 3.1: Illustration of a possible sample grid represented by the points $\tilde{\boldsymbol{x}}_1 \dots \tilde{\boldsymbol{x}}_M$ in the $\tilde{x}\tilde{y}$-plane. Additionally, the sampling of the discrete position $\tilde{\boldsymbol{x}}_i$ is leading to the discrete reflected ray's direction $\boldsymbol{r}_i$ and the discrete surface normal $\boldsymbol{g}_i$.

As the incident beam direction $\boldsymbol{i}$ is not changing dependent on the positioning of the SUT, it is the same for all sample points. With the incident beam direction and the discrete reflected ray direction $\boldsymbol{r}_i = \boldsymbol{r}(\tilde{\boldsymbol{x}}_i)$, one can determine the discrete surface normal $\boldsymbol{g}_i = \boldsymbol{g}(\tilde{\boldsymbol{x}}_i)$ using Equation (2.1).

According to Equation (2.20) and (2.21) the surface slopes m_i and n_i in x- and y-direction can be determined from the surface normal $\boldsymbol{g}_i$. Therewith, the gradient field

$$\boldsymbol{\zeta}_i = \begin{pmatrix} m_i \\ n_i \\ 0 \end{pmatrix} = \begin{pmatrix} s_x(\boldsymbol{x}_i) \\ s_y(\boldsymbol{x}_i) \\ 0 \end{pmatrix} \tag{3.3}$$

described in Equation (2.22) can now be defined numerically with the numerical surface slopes m_i and n_i.

At this point, a differentiation has to be introduced. As deviations can occur during measurement and evaluation, the determined surface slopes can deviate from those derived from the surface model. This can be introduced by uncertainties or alignment errors in the setup, by errors introduced by the integration process or by deviations of the actual SUT from the model. Since the deviations of the SUT from the model are the targeted result of this measurement technique, the other sources for deviations have to be identified and minimized. This is addressed in subsequent chapters.

In Chapter 2.1.3 one can see that the surface slopes can also be determined from the incident ray direction $\boldsymbol{i}$ and the reflected ray direction $\boldsymbol{r}_i$. In this case, it has to be considered that the deviations described above can also introduce a deviation of $\boldsymbol{r}_i$ from the expected ideal direction. Therewith, the surface normal determined from $\boldsymbol{i}$ and $\boldsymbol{r}_i$ using Equation (2.18) and consequentially the surface slopes p_i and q_i determined in x- and y-direction using Equation (2.20) and (2.21) deviate from the expected slopes of the model. Having

$$p_i = -\frac{g_{x,i}}{g_{z,i}} \tag{3.4}$$

and

$$q_i = -\frac{g_{y,i}}{g_{z,i}} \tag{3.5}$$

determined from $\boldsymbol{g}_i$, a gradient field

$$\boldsymbol{\eta}_i = \boldsymbol{\eta}(\boldsymbol{x}_i) = \begin{pmatrix} p_i \\ q_i \\ 0 \end{pmatrix} \tag{3.6}$$

representing the determined surface gradients, can be defined. This gradient field includes the surface model gradient field $\boldsymbol{\zeta}$ as well as a gradient field of deviations $\boldsymbol{\xi}$. Therewith, the relation

$$\boldsymbol{\eta} = \boldsymbol{\zeta} + \boldsymbol{\xi} \tag{3.7}$$

can be settled.

In addition to the differentiation between the model gradient field and the determined gradient field, one can also settle the differentiation between the model surface sag and the determined surface sag.

With $\lim_{\Delta\tilde{x}\to 0}$ and $\lim_{\Delta\tilde{y}\to 0}$, Equation (2.24) can be used to determine the surface sag

$$s_i = s(\boldsymbol{x}_i) = \int_{\boldsymbol{x}_0}^{\boldsymbol{x}_i} \boldsymbol{\zeta}\, d\boldsymbol{x} + A \tag{3.8}$$

from the gradient field $\boldsymbol{\zeta}$, where A is an unknown constant of the surface function. The same applies to the determined gradient field $\boldsymbol{\eta}$

$$h_i = \int_{\boldsymbol{x}_0}^{\boldsymbol{x}_i} \boldsymbol{\eta}\, d\boldsymbol{x} + A \tag{3.9}$$

and the gradient field of deviations $\boldsymbol{\xi}$

$$d_i = \int_{\boldsymbol{x}_0}^{\boldsymbol{x}_i} \boldsymbol{\xi}\, d\boldsymbol{x} \tag{3.10}$$

resulting in the determined surface sag h_i and the surface deviation d_i.

According to Equation (3.7), these sag and deviation information can be related as

$$h_i = s_i + d_i. \tag{3.11}$$

Regarding Equation (3.9), one can see that the surface can be reconstructed using the determined gradient field $\boldsymbol{\eta}$. Substituting $\boldsymbol{\eta}$ with Equation (3.7) by applying the sum rule, the surface sag

$$h_i = \int_{\boldsymbol{x}_0}^{\boldsymbol{x}_i} (\boldsymbol{\zeta} + \boldsymbol{\xi})\, d\boldsymbol{x} + A = \int_{\boldsymbol{x}_0}^{\boldsymbol{x}_i} \boldsymbol{\zeta}\, d\boldsymbol{x} + \int_{\boldsymbol{x}_0}^{\boldsymbol{x}_i} \boldsymbol{\xi}\, d\boldsymbol{x} + A \tag{3.12}$$

can also be determined from two separate integrations of the two gradient fields $\boldsymbol{\zeta}$ and $\boldsymbol{\xi}$ [79]. Using Equation (3.8) for substitution in Equation (3.12), one can see that the surface sag

$$h_i = s_i + \int_{\boldsymbol{x}_0}^{\boldsymbol{x}_i} \boldsymbol{\xi}\, d\boldsymbol{x} \tag{3.13}$$

can even be determined from the surface model and the integration of the gradient field of deviations only.

3.3 Gradient integration method and surface characterization

3.3.1 2D surface integration using Radial Basis Functions

The integral over an integrable gradient field is independent on the path of the integration. However, this is only valid, if the gradient field is continuously known. Accordingly, Equation (3.8) until (3.13) are only valid for $\lim_{\Delta\tilde{x}\to 0}$ and $\lim_{\Delta\tilde{y}\to 0}$.

Since the proposed measurement technique cannot satisfy this approach, an appropriate method for the integration of gradient data for $\Delta\tilde{x} > 0$ and $\Delta\tilde{y} > 0$, has to be used [84].

In Chapter 2.3.1, it has been shown that the actual sample points may be shifted. This leads to a non-equidistant grid of sample points. Additionally, the considered area $\boldsymbol{A}$ may has a freeform shape, according to the edge of the SUT. Thus, the integration method to be used here has to be able to handle non-equidistant grids of sample points with different shapes. An integration technique that provides these opportunities is the integration using Radial Basis Functions (RBFs). The integration using RBFs is based on positioning a certain function, the RBF, multiple times over the considered area. These positions are further called center points and are depicted $\boldsymbol{x}_j$, with $j = 1 \dots N$. In this work, the number of center points N is always chosen to be equal to the number of sample points M. Additionally, the positions of the center points are chosen to be identical with the positions of the sample points. Thus, one RBF is placed at each sample point.

The 2D integration case faced here is of Southwell configuration. This means that two slope data are available per sample point [85]. To adapt the interpolant to this situation, Ettl et al. proposed an integration method where the interpolant function is given as

$$h(\boldsymbol{x}) = \sum_{j=1}^{N} c_j \frac{\partial \psi}{\partial x}(\boldsymbol{x} - \boldsymbol{x}_j) + \sum_{j=1}^{N} c_{N+j} \frac{\partial \psi}{\partial y}(\boldsymbol{x} - \boldsymbol{x}_j) \tag{3.14}$$

with

$$\psi(\boldsymbol{x}) = \begin{cases} \frac{1}{3}(1-\hat{r})^6(35\hat{r}^2 + 18\hat{r} + 3) & \text{for } \hat{r} = \frac{1}{\rho}\sqrt{x^2+y^2} \leq 1 \text{ and } \rho > 0 \\ 0 & \text{otherwise} \end{cases} \tag{3.15}$$

being the Wendland function, where ρ is the support radius of the RBF and c_j is the coefficient for the j-th RBF [21, 86, 87]. The derivatives of the function can be found in Appendix A. The Wendland function is a positive-definite function with a limited support radius. In contrast to the also often used Gaussian function, the Wendland function and its derivatives become 0 at the position $\hat{r} = \rho$. For comparison, the Gaussian function and the Wendland function are illustrated in Figure 3.2.

As described in Equation (3.15) the Wendland function is defined to be 0 outside the support radius ρ. Therewith, the supported area of one RBF is exactly defined to be within ρ. Regarding Figure 3.2, one can see that the Gaussian function becomes close to 0 at $\hat{r} = 2.0$, too. However, applying a limited support radius to the Gaussian functions leads to a step in the function, as the Gaussian function does not become 0 before $\hat{r} = \infty$.

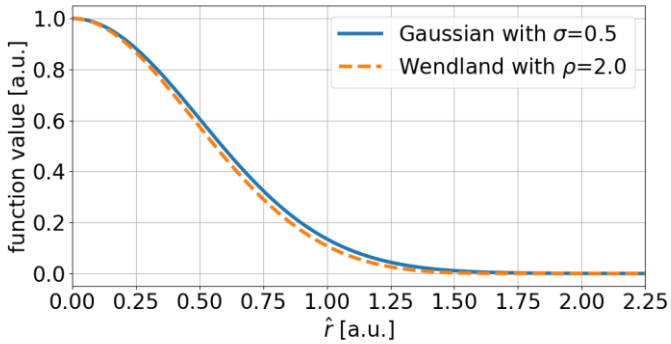

Figure 3.2: Comparison of the Gaussian function with $\sigma = 0.5$ and the Wendland function with $\rho = 2.0$.

Having Equation (3.14) as the interpolant function, the equations

$$\left(\frac{\partial h}{\partial x}\right)_i = \sum_{j=1}^{N} c_j \frac{\partial^2 \psi}{\partial x^2}(\boldsymbol{x}_i - \boldsymbol{x}_j) + \sum_{j=1}^{N} c_{N+j} \frac{\partial^2 \psi}{\partial y \partial x}(\boldsymbol{x}_i - \boldsymbol{x}_j) = p_i \tag{3.16}$$

and

$$\left(\frac{\partial h}{\partial y}\right)_i = \sum_{j=1}^{N} c_j \frac{\partial^2 \psi}{\partial x \partial y}(\boldsymbol{x}_i - \boldsymbol{x}_j) + \sum_{j=1}^{N} c_{N+j} \frac{\partial^2 \psi}{\partial y^2}(\boldsymbol{x}_i - \boldsymbol{x}_j) = q_i \tag{3.17}$$

can be derived for the slopes of the interpolant. Therewith, the interpolation is only supported by gradient data and therewith is of Hermite type [88]. With this, the linear equation system (LES)

$$\boldsymbol{S} = \mathbf{A}\boldsymbol{c} \tag{3.18}$$

can be defined, where

$$\boldsymbol{S} = \underbrace{\begin{pmatrix} p_1 \\ \vdots \\ p_M \\ q_1 \\ \vdots \\ q_M \end{pmatrix}}_{2M \times 1} \tag{3.19}$$

holds all slope values,

$$\mathbf{A} = \underbrace{\begin{pmatrix} \frac{\partial^2 \psi}{\partial x^2}(\boldsymbol{x}_i - \boldsymbol{x}_j) & \cdots & \frac{\partial^2 \psi}{\partial y \partial x}(\boldsymbol{x}_i - \boldsymbol{x}_j) \\ \vdots & \ddots & \vdots \\ \frac{\partial^2 \psi}{\partial x \partial y}(\boldsymbol{x}_i - \boldsymbol{x}_j) & \cdots & \frac{\partial^2 \psi}{\partial y^2}(\boldsymbol{x}_i - \boldsymbol{x}_j) \end{pmatrix}}_{2M \times 2N} \tag{3.20}$$

represents the interpolant matrix and

$$\boldsymbol{c} = \underbrace{\begin{pmatrix} c_1 \\ \vdots \\ c_N \\ c_{N+1} \\ \vdots \\ c_{2\cdot N} \end{pmatrix}}_{2N \times 1} \tag{3.21}$$

depicts the coefficient vector.

With $M = N$, the interpolation matrix $\mathbf{A}$ becomes symmetric and therewith a unique solution to the LES exists [21]. The determined coefficient vector $\boldsymbol{c}$ can now be used to reconstruct the surface using Equation (3.14). For easier readability, the usage of this integration method is from now on donated by

$$\boldsymbol{h} = \mathrm{rbf}(\boldsymbol{X}, \boldsymbol{\eta}; \rho), \tag{3.22}$$

where $\boldsymbol{h}$ is a set holding the integrated values, $\boldsymbol{X} = \{\boldsymbol{x}_i \dots \boldsymbol{x}_M\}$ is a set including all sample positions, $\boldsymbol{\eta}$ is the gradient field to be integrated and ρ is the support radius of the Wendland function.

This method for surface reconstruction can be adapted for noisy data of different levels. To handle data with higher noise levels, two adaptions are available: either the support radius ρ of ψ can be increased or the number of center points N can be reduced. However, it has to be kept in mind that with increasing the ρ, the rank of the interpolation matrix $\mathbf{A}$ is decreased until the matrix becomes singular. Thus, ρ has to be chosen properly to conserve local characteristics while ensure reconstruction stability, even if the given data is noisy [87]. Reducing the number of center points N, a smoothening of the noisy data can also be achieved. Regarding Equation (3.18), one can see that this leads to overdetermined LES and a non-symmetrical interpolation matrix $\mathbf{A}$. Thus, the LES has to be solved in a least-squares sense, leading to higher calculations times [89]. In this work, only the case of equal number of sample points and center points is considered. With this said, the memory usage of this method has to be considered. In the proposition of this method, Ettl et al. split a given data set of 60×60 sample points into a grid of 6×6 patches for being able to handle the solving of the LES given in Equation (3.18) [21]. The patches were later on combined to recover the reconstructed surface. This stitching method lead to the question of how much memory is needed to hold the data required by Equation (3.18). The number of elements needed

$$(4MN) + (2N) + (2M) \tag{3.23}$$

can be calculated from the given matrix and vector sizes. For $M = N$ this can be reduced to $4N^2 + 4N$. May the size of one element in a computer be $64\ \mathrm{Bit} = 8\ \mathrm{Byte}$, the evolution of the needed memory to hold the data can be calculated as illustrated in Figure 3.3.

One can clearly see that the amount of memory needed is increasing rapidly. It has also to be considered that this is only the amount needed to hold the data. Memory needed to perform the calculations, as well as for other programs or the operation system are not included. However, the increase in the sizes of memory available for computers as well as the availability of solid-state-drives to extend the memory using a swap file, make memory sizes of up to $512\ \mathrm{GB}$ or even more realizable. Thus, the need for splitting the data into patches is no longer given.

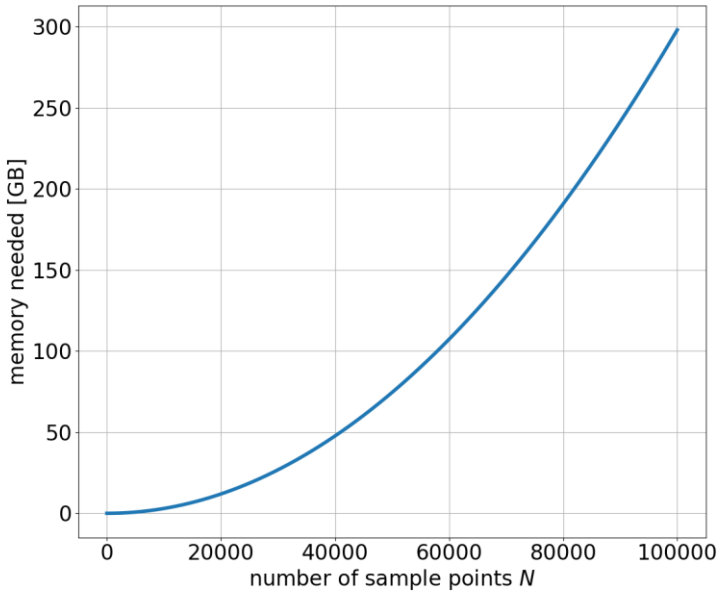

Figure 3.3: Memory needed to hold the data required by Equation (3.18) for $N = M$ and the size of one element being $8\ \mathrm{Byte}$.

3.3.2 Integrability considerations

As said before, the integrability of a discrete gradient field can be dissolved by the introduction of noise to the gradient data or even by the discretization itself. Both factors can introduce curls to the gradient field resolving in a non-integrable gradient field.

The curl of a gradient field is also a vector field describing if the gradient field contains positions, where a line following the gradient field creates a closed line [79]. In Chapter 2.1.3, it has been said if a gradient field was integrable, integration from one point to another is independent on the path. If a closed line along the gradient field exists, this path independency does not exist anymore. The curl of a gradient field

$$\operatorname{curl} \boldsymbol{\eta} = \boldsymbol{\nabla} \times \boldsymbol{\eta} \tag{3.24}$$

is calculated using the Nabla vector [79]. Introducing the discretization of the vector field $\boldsymbol{\eta}$ as described in Equation (3.6), the discrete curl can be defined as

$$\operatorname{curl} \boldsymbol{\eta}_i = \boldsymbol{\nabla} \times \boldsymbol{\eta}_i = \begin{pmatrix} \frac{\partial}{\partial x} \\ \frac{\partial}{\partial y} \\ \frac{\partial}{\partial z} \end{pmatrix} \times \begin{pmatrix} p_i \\ q_i \\ 0 \end{pmatrix} = \begin{pmatrix} \frac{\partial 0}{\partial y} - \frac{\partial q_i}{\partial z} \\ \frac{\partial p_i}{\partial z} - \frac{\partial 0}{\partial x} \\ \frac{\partial q_i}{\partial x} - \frac{\partial p_i}{\partial y} \end{pmatrix} = \begin{pmatrix} 0 \\ 0 \\ \frac{\partial q_i}{\partial x} - \frac{\partial p_i}{\partial y} \end{pmatrix}. \tag{3.25}$$

Thus, for a 2D gradient field, as given here, the curl vector field is a field of vectors parallel to the z-axis, while the length of the vectors is giving information about the magnitude of the curl at the considered position. For further considerations, it is assumed to have the situation shown in Figure 3.4 for one certain point in a gradient field.

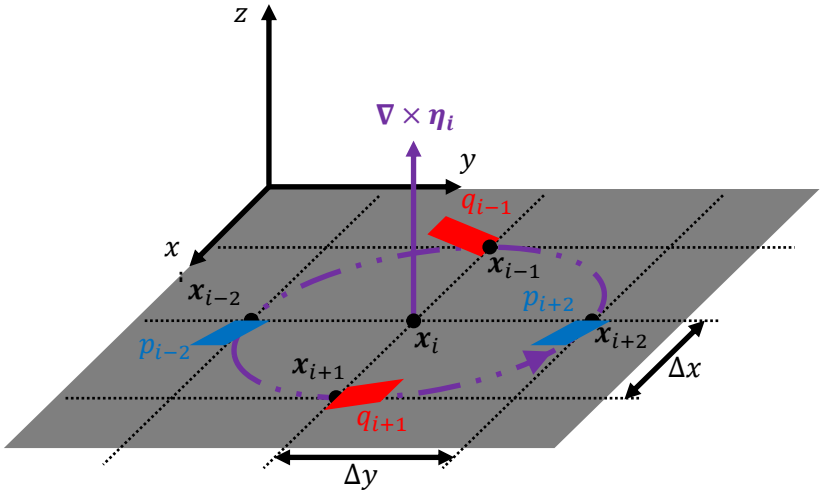

Figure 3.4: Illustration of a curl vector $\nabla \times \boldsymbol{\eta}_i$ at $\boldsymbol{x}_i$ derived from surface slopes given at the sample points $\boldsymbol{x}_{i-2}$, $\boldsymbol{x}_{i-1}$, $\boldsymbol{x}_{i+1}$ and $\boldsymbol{x}_{i+2}$ connected to $\boldsymbol{x}_i$. The red slopes q_{i-1} and q_{i+1} represent slopes in y-direction, while the blue slopes p_{i-2} and p_{i+2} represent slopes in x-direction.

To determine the derivatives needed to calculate the curl according to Equation (3.25), symmetric derivative calculation is used [90]. Therewith, the z-component of the curl vector as illustrated in Figure 3.4 can be calculated by

$$\frac{\partial q_i}{\partial x} - \frac{\partial p_i}{\partial y} = \frac{q_{i+1} - q_{i-1}}{2\Delta x} - \frac{p_{i+2} - p_{i-2}}{2\Delta y}. \tag{3.26}$$

Thus, the length of the curl vector gives information about the slope's sum along the purple circle illustrated in Figure 3.4. May the illustrated slopes in this figure have the values $p_{i-2} = 1$, $q_{i-1} = -1$, $q_{i+1} = 1$ and $p_{i+2} = 1$ and may $\Delta x = \Delta y$, the length of the curl vector

$$\frac{q_{i+1} - q_{i-1}}{2\Delta x} - \frac{p_{i+2} - p_{i-2}}{2\Delta y} = \frac{2}{2\Delta x} \tag{3.27}$$

for the sample point $\boldsymbol{x}_i$ can be determined. Multiplying this with $2\Delta x$, the slope increase or decrease along the curl can be determined. Assuming to have this increase or decrease along the circle, a height deviation

$$h_{curl,i} = \left(\frac{\partial q_i}{\partial x} - \frac{\partial p_i}{\partial y}\right) 4\pi \Delta x^2 \tag{3.28}$$

introduced by the curl can be determined. This height deviation cannot be represented in the reconstruction of the surface as it is not integrable. The RBF method used for the integration in this work is able to find a least-squares solution for non-integrable gradient fields. However, it has also been shown that this integration method shows integration instabilities, when large curl fields are applied [91]. To overcome this problem, the integrability has to be enforced [92]. Regarding Figure 3.4, one can see that one slope information influences two curl vectors: one in the positive and one in the negative direction. Thus, there is no direct mapping of the slope values from the determined curl vectors. To solve this, a LES

$$\boldsymbol{b} = \mathbf{B}\boldsymbol{S} \tag{3.29}$$

based on Equation (3.26) is defined, where $\boldsymbol{b}$ is a vector holding all curl values $\nabla \times \boldsymbol{\eta}_i$, $\boldsymbol{S}$ is a vector holding all slope data and $\mathbf{B}$ is a sparse matrix mapping the slope values to the corresponding curl. As the calculation of the curl underlies the sum rule, the given gradient field can be imagined to be the sum of a curl-free gradient field and a non-curl-free gradient

field. Using the given gradient field in Equation (3.29), the curl of the gradient field is retrieved. Reversing the process and solving the LES for $\boldsymbol{S}$ using the calculated curl values, the slopes of a non-curl-free gradient field are retrieved. Subtracting these from the given gradient field results in an integrable curl-free gradient field [92].

As described before, curls can also occur due to discretization of the continuous surface function. In Chapter 3.2, it has been shown that if the surface model function is known, only the gradient field of deviations $\boldsymbol{\xi}_i$ had to be integrated. May the discretization of the model function introduce a non-curl-free gradient field $\boldsymbol{\zeta}_{c,i}$ to the model gradient field

$$\boldsymbol{\zeta}_i = \boldsymbol{\zeta}_{0,i} + \boldsymbol{\zeta}_{c,i}, \tag{3.30}$$

this non-curl-gradient field also appears in the determined gradient field

$$\boldsymbol{\eta}_i = \boldsymbol{\eta}_{0,i} + \boldsymbol{\zeta}_{c,i}, \tag{3.31}$$

due to Equation (3.7), while $\boldsymbol{\zeta}_{0,i}$ and $\boldsymbol{\eta}_{0,i}$ represent curl-free gradient fields. Rearranging Equation (3.7) and inserting Equation (3.30) and (3.31) to

$$\boldsymbol{\xi}_i = \boldsymbol{\eta}_i - \boldsymbol{\zeta}_i = \left(\boldsymbol{\eta}_{0,i} + \boldsymbol{\zeta}_{c,i}\right) - \left(\boldsymbol{\zeta}_{0,i} + \boldsymbol{\zeta}_{c,i}\right) = \left(\boldsymbol{\eta}_i - \boldsymbol{\zeta}_i\right) + \left(\boldsymbol{\zeta}_{c,i} - \boldsymbol{\zeta}_{c,i}\right), \tag{3.32}$$

one can see that the curls introduced by discretization of the model function do not appear in the deviation gradient field $\boldsymbol{\xi}_i$. It has to be mentioned that this consideration does not cover curls appearing in the deviation gradient field $\boldsymbol{\xi}_i$ introduced by noise or the deviations from the model function itself.

The considerations described before are only valid for the reconstruction of a surface, where the model function is known. If the model function is not known, enforcing the integrability on the determined gradient field $\boldsymbol{\eta}_i$ can lead to deviations in the reconstructed surface. Regarding Equation (3.31) and assuming $\boldsymbol{\zeta}_{c,i}$ be a non-curl-free gradient field introduced by discretization of the ground truth of the SUT, this non-curl-free gradient field includes information about the ground truth that is actually correct. Thus, subtracting these curls from the determined gradient field, leads to the curl-free gradient field

$$\boldsymbol{\eta}_{0,i} = \boldsymbol{\eta}_i - \boldsymbol{\zeta}_{c,i}, \tag{3.33}$$

that might deviate from the actually correct gradient field $\boldsymbol{\eta}_i$ and therewith represents the gradient field of a surface deviating from the ground truth. As described in Chapter 3.3.1, the 2D integration using RBFs finds a least-squares solution for the deviation of the reconstructed surface's slopes to the given slopes from the determined gradient field $\boldsymbol{\eta}_i$. Thus, even if a discrete non-curl-free gradient field of a continuous surface is given, this method can be able to find a solution for a continuous reconstructed surface [93]. Therefore, the enforcement of the integrability is not performed for the reconstruction of unknown surfaces, as a high chance exists that relevant information is subtracted by the enforcement. This will further be shown by simulations in Chapter 4.2.3.

3.3.3 Surface characterization

As surfaces have different properties and characteristics, a common language for the transfer of information has to be defined. In general, a definition for surface description and characterization is given by the DIN ISO standard 10110. This standard is intended to have a common language of drawings of optical surfaces. From part 5 of this standard, it has been adopted to represent all deviations here in sagittal deviation [94]. This means all deviations are represented as distances parallel to the z-axis of the CS $\mathcal{S}$. Furthermore, this part of the DIN

ISO standard 10110 gives specifications about the units used for different parameters, which has been adopted here.

The topic of surface characterization is targeted in this work from two perspectives. One is the perspective of the influence of certain surface characteristics on the optical performance of a DUT. The second perspective is to observe which surface characteristics determined by the measurement setup may be introduced from misalignment, stage non-linearity and errors in the calibration in the measurement setup.

For the perspective of optical performance, one has to consider the influence of different surface characteristics on the light propagating through the optical component. Therefore, the spatial wavelength λ_s of the surface structure is considered. This wavelength is separated into three different bandwidths: form, waviness and roughness [95]. As shown in Figure 3.5 all three of these bandwidths have different influence on the interaction with incident light.

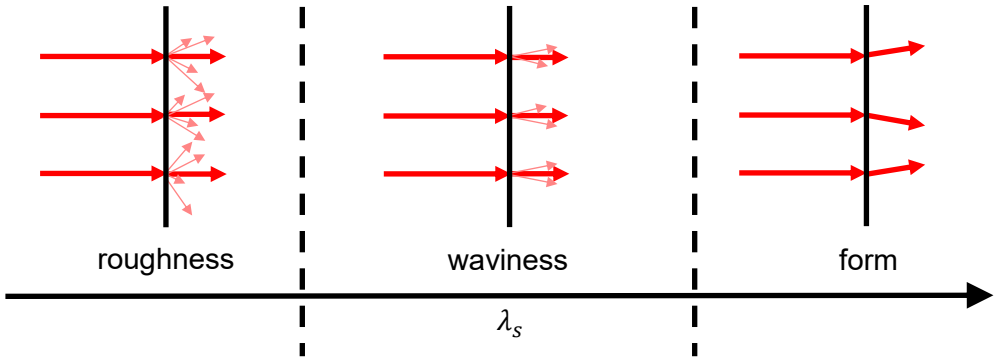

Figure 3.5: Scattering of incident light by surface errors of different bandwidths.

While form deviations are introducing a slight scattering of the light resulting in the conventional aberrations, waviness and roughness introduce scattering in medium and higher angles [96]. This introduces different effects on the optical performance. To show these effects, they are illustrated in Figure 3.6 in terms of influence on the Point Spread Function (PSF) of an imaging system.

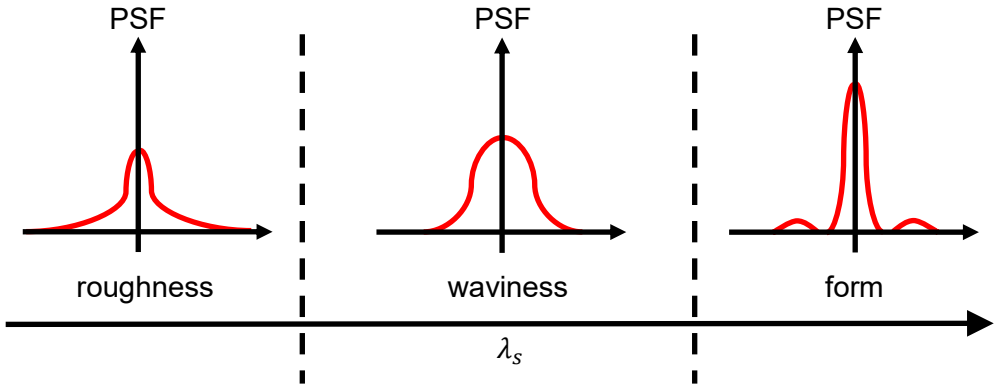

Figure 3.6: Influence of surface structures of different bandwidths on the point spread function of an imaging system [96].

While form deviations do not influence the center peak of the point spread function significantly, the introduced aberrations generate an increase of the energy in the first diffraction rings. In contrast to that, waviness widens the center peak of the PSF, resulting in a blurring of the image generated by the system. Therefore, this bandwidth is very important for the imaging quality. While roughness also scatters light in higher angles, the scattering is not widening the

center peak significantly, but distributing light in the area around the center peak. This results in a reduction of the contrast of the image, while preserving the sharpness. These effects are not only dependent on the spatial wavelength λ_s of the surface structure, but also in the wavelength λ of the introduced light. However, the wavelength λ used for the incident light in the measurement method proposed in this work does not have to be equal to the wavelength, the investigated surface is intended for. Thus, specific limits for the bandwidths cannot be given. When specific limits are not given, a general specification is given by DIN ISO 10110-8 [95]. This general specification defines the form deviation for $\lambda_s > 2.5\ \mathrm{mm}$, the waviness for $2.5\ \mathrm{mm} > \lambda_s > 80\ \mu\mathrm{m}$ and the roughness for $\lambda_s < 80\ \mu\mathrm{m}$.

For the perspective of surface characterization in terms of influences from misalignment, stage non-linearity and errors in the calibration, the reconstructed surface from a measured gradient field is considered. This gradient field, and therewith the reconstructed surface, includes deviations introduced by the factors mentioned above. In contrast to form, waviness and roughness, these deviations are not bound to the SUT, but are introduced by the measurement system itself. These errors can change in magnitude and spatial frequency when changing the size or location of the investigated area and mostly appear in global structures covering the whole investigated area. To describe these global structures, Zernike polynomials are suitable [95, 97].

Zernike polynomials have been introduced by Fritz Zernike and are defined over the unit disc [98]. They are suitable for optical applications with circular apertures. Especially for the representation of wavefronts and their aberrations, Zernike polynomials are applied broadly, as some single polynomials represent certain types of aberrations of the wavefront [99].

The Zernike polynomials are a complete set of polynomials. This means that any arbitrary function can be represented by the sum of the complete set of polynomials each multiplied with an appropriate coefficient. The polynomials are originally assigned by two indices. For applications in linear algebra, as it is supposed to be used here, a single index notation is advantageous. Therefore, the single index l of natural ordering of the polynomials is used in this work [100].

Initially, the Zernike polynomials have been defined in polar coordinates. However, they can also be transferred to Cartesian coordinates [100]. As Cartesian coordinates are used in this work, the Zernike polynomials will also be used in this definition. The first 15 Zernike polynomials P_l in the natural order are explicitly presented in Cartesian Coordinates in Table 3.1.

Interpreting the polynomials as surface structures of a reconstructed surface with normalized aperture, these polynomials represent global structures within this surface. To find the corresponding coefficients for the polynomials to fit these to a reconstructed surface, the Equation

$$h(\boldsymbol{x}_i) \mathrel{\widehat{=}}_{c_j} \sum_{j=1}^{N} c_j\, P_{j-1}(\boldsymbol{x}_i) \tag{3.34}$$

has to be solved in a least-squares sense, where $P_{j-1} = P_l$ represents the l-th Zernike polynomial.

Table 3.1: First 15 Zernike polynomials in Cartesian Coordinates in natural order.

l	$P_l(x,y)$
0	1
1	y
2	x
3	$2xy$
4	$2x^2+2y^2-1$
5	x^2-y^2
6	$3x^2y-y^3$
7	$3x^2y+3y^3-2y$
8	$3x^3+3xy^2-2x$
9	x^3-3xy^2
10	$4x^3y-4xy^3$
11	$8x^3y+8xy^3-6xy$
12	$6x^4+12x^2y^2-6x^2+6y^4-6y^2+1$
13	$4x^4-3x^2-4y^4+3y^2$
14	$x^4-6x^2y^2+y^4$

For this, Equation (3.34) can also be written in matrix form

$$\boldsymbol{h} = \mathbf{A}\boldsymbol{c} \tag{3.35}$$

where

$$\boldsymbol{h} = \underbrace{\begin{pmatrix} h_1 \\ \vdots \\ h_M \end{pmatrix}}_{M \times 1}, \tag{3.36}$$

$$\mathbf{A} = \underbrace{\begin{pmatrix} P_0(\boldsymbol{x}_1) & \cdots & P_{N-1}(\boldsymbol{x}_1) \\ \vdots & \ddots & \vdots \\ P_0(\boldsymbol{x}_M) & \cdots & P_{N-1}(\boldsymbol{x}_M) \end{pmatrix}}_{M \times N} \tag{3.37}$$

and

$$\boldsymbol{c} = \underbrace{\begin{pmatrix} c_1 \\ \vdots \\ c_N \end{pmatrix}}_{N \times 1} \tag{3.38}$$

defining a LES to be solved. Solving this LES for a low number of N, for example $N = 36$, global structures in the reconstructed surface can be detected independent on the size of the surface itself. Using different numbers for N or even a range for j, different structures can be retrieved and, if desired, subtracted from the given height data [101]. In this work, the first 36 Zernike polynomials are considered representing global structures, since these polynomials represent low radial and azimuthal degrees and therewith low-frequency structures. Thus, the sum of these polynomials can be called low-frequency structures. Subtracting these low-frequency structures from given height data, high-frequency structures can be derived, which could be disguised by the mostly more prominent global structures.

For the presentation and transfer of general surfaces, like freeform surfaces, the DIN ISO 10110-19 gives several options [6]. In this work, all presented data are in the form of point clouds. If not stated differently, the corresponding CS is $\mathcal{S}$.

3.4 Reconstruction of known surfaces

The reconstruction of known surfaces has been described analytically in Chapter 2.3.2. Here, the numerical tools described before are used to describe the evaluation steps as they are performed in the simulation and the experimental setup.

Having the desired sample points $\tilde{\boldsymbol{x}}_i$ defined, the detected surface normals can be determined according to the descriptions in Chapter 2 and 3.2. As the surface normals are determined in the CS $\mathcal{C}$, the surface normals are defined as $\boldsymbol{g}_i^{\mathcal{C}}$ and can be transferred into the CS $\mathcal{M}$ using the transformation matrix $\mathbf{H}_{\mathcal{C}}^{\mathcal{M}}$ according to Equation (2.14). As the surface model is known, the relation of the origin of the function describing the surface model and the origin of the CS $\mathcal{M}$, the transformation matrix $\mathbf{H}_{\mathcal{M}}^{\mathcal{S}}$, has to be found. According to Equation (2.12), the transformation matrix is defined using the rotation vector $\boldsymbol{\gamma}_{\mathcal{M}}^{\mathcal{S}}$ and the translation vector $\boldsymbol{t}_{\mathcal{M}}^{\mathcal{S}}$. The process to appropriate values for the rotation and the translation vector are described in Chapter 2.3.2 and lead to the requirement given by Equation (2.30). Since it is now expected that the detected surface normals are not error-free, these Equations have to be solved in least-squares sense. Therefore, the non-linear cost function

$$\chi^2 = \sqrt{\frac{1}{2M}\sum_{i=1}^{M}\left(\left(p_i^{\mathcal{S}}\left(\mathbf{H}_{\mathcal{M}}^{\mathcal{S}}\right) - s_x(\boldsymbol{x}_i)\right) + \left(q_i^{\mathcal{S}}\left(\mathbf{H}_{\mathcal{M}}^{\mathcal{S}}\right) - s_y(\boldsymbol{x}_i)\right)\right)} \tag{3.39}$$

is defined, which has to be minimized by optimizing $\mathbf{H}_{\mathcal{M}}^{\mathcal{S}}$. The position $\boldsymbol{x}_i$ is hereby assumed to be the position determined from the shift of sample points as described in Chapter 2.3.1. The cost function is derived from the root mean square (RMS) slope deviation as defined in the DIN ISO 10110-8 standard [95]. Regarding the intended setup and the meaning of the components of the translation vector $\boldsymbol{t}_{\mathcal{M}}^{\mathcal{S}} = \left(\Delta\tilde{x}_{\mathcal{M}}^{\mathcal{S}}, \Delta\tilde{y}_{\mathcal{M}}^{\mathcal{S}}, \Delta\tilde{z}_{\mathcal{M}}^{\mathcal{S}}\right)$, one can see that an ambiguity between the shifts $\Delta\tilde{x}_{\mathcal{M}}^{\mathcal{S}}$ and $\Delta\tilde{y}_{\mathcal{M}}^{\mathcal{S}}$ and the shift $\Delta\tilde{z}_{\mathcal{M}}^{\mathcal{S}}$ exists. Any shift in $\tilde{z}$-direction can also be represented by a shift in $\tilde{x}$- and $\tilde{y}$-direction, due to the direction $\boldsymbol{i}$ of the incident ray. Thus, the degree of freedom can be reduced and only the parameters $\alpha_{\mathcal{M}}^{\mathcal{S}}, \beta_{\mathcal{M}}^{\mathcal{S}}, \gamma_{\mathcal{M}}^{\mathcal{S}}, \Delta\tilde{x}_{\mathcal{M}}^{\mathcal{S}}$ and $\Delta\tilde{y}_{\mathcal{M}}^{\mathcal{S}}$ have to be optimized [102]. The transformation matrix will therefore be of the form $\mathbf{H}_{\mathcal{M}}^{\mathcal{S}} = \mathbf{H}\left(\left(\alpha_{\mathcal{M}}^{\mathcal{S}}, \beta_{\mathcal{M}}^{\mathcal{S}}, \gamma_{\mathcal{M}}^{\mathcal{S}}\right), \left(\Delta\tilde{x}_{\mathcal{M}}^{\mathcal{S}}, \Delta\tilde{y}_{\mathcal{M}}^{\mathcal{S}}, 0\right)\right)$.

Having $\mathbf{H}_{\mathcal{M}}^{\mathcal{S}}$ found from the non-linear optimization, the detected normals

$$\boldsymbol{g}_i^{\mathcal{S}} = \mathbf{H}_{\mathcal{M}}^{\mathcal{S}}\boldsymbol{g}_i^{\mathcal{M}} \tag{3.40}$$

can be transferred into the CS $\mathcal{S}$ and the detected surface slopes $p_i^{\mathcal{S}}$ and $q_i^{\mathcal{S}}$ can be calculated generating the gradient field $\boldsymbol{\eta}^{\mathcal{S}}$. Applying Equation (3.7), the gradient field of deviations $\boldsymbol{\xi}^{\mathcal{S}}$ can be calculating subtracting the model gradient field $\boldsymbol{\zeta}^{\mathcal{S}}$ from $\boldsymbol{\eta}^{\mathcal{S}}$. On this gradient field of deviations, the integrability can now be enforced. In Equation (3.13), it has been shown that it is sufficient to integrate the gradient field of deviations only. Thus, the integration

$$d_i^{\mathcal{S}} = \mathrm{rbf}\left(\boldsymbol{X}, \boldsymbol{\xi}^{\mathcal{S}}; \rho\right)_i \tag{3.41}$$

can now be performed to reconstruct the surface deviations. The surface can now be reconstructed using the model data as shown in Equation (3.11).

A flowchart illustrating the process of the reconstruction of known surfaces is shown in Figure 3.7.

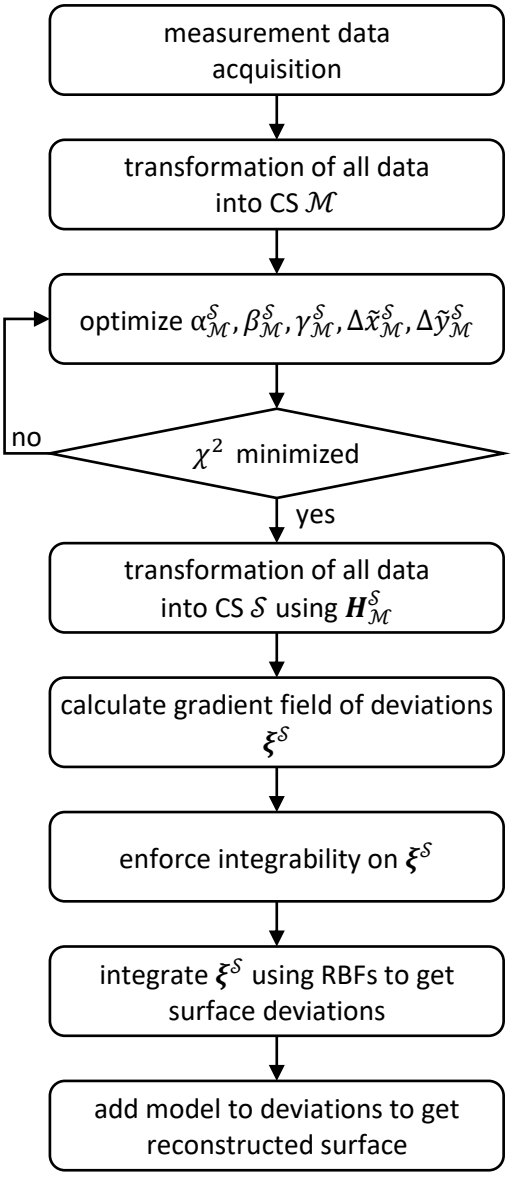

Figure 3.7: Flowchart of the reconstruction of known surfaces from measurement data acquisition until the reconstructed surface.

3.5 Reconstruction of unknown surfaces

Equivalently to the reconstruction of known surfaces, the reconstruction of unknown surfaces has already been described analytically. This description can be found in Chapter 2.3.3. Also, the process for the surface reconstruction of unknown surfaces is described here in the same way as it is performed in the simulations and the experimental setup.

Having the detected surface normals $\boldsymbol{g}_i^{\mathcal{C}}$ in the CS $\mathcal{C}$, the target sample points $\boldsymbol{J}^{\mathcal{M}}$ in the CS $\mathcal{M}$ and the transformation matrics $\mathbf{H}_{\mathcal{C}}^{\mathcal{M}}$ and $\mathbf{H}_{\mathcal{C}}^{\mathcal{I}}$, the detected surface normals

$$\boldsymbol{g}_i^{\mathcal{I}} = \mathbf{H}_{\mathcal{C}}^{\mathcal{I}} \boldsymbol{g}_i^{\mathcal{C}} \tag{3.42}$$

as well as the targeted sample points

$$\boldsymbol{J}_i^{\mathcal{I}} = \mathbf{H}_{\mathcal{C}}^{\mathcal{I}} \mathbf{H}_{\mathcal{M}}^{\mathcal{C}} \boldsymbol{J}_i^{\mathcal{M}} \tag{3.43}$$

can be transferred in the CS $\mathcal{I}$. Performing the projection of $\boldsymbol{J}_i^{\mathcal{I}}$ into the $\tilde{u}\tilde{v}$-plane as described in Equation (2.31) the position vectors $\boldsymbol{L}_i = (\tilde{u}_i, \tilde{v}_i, 0,1)^T$ can be determined. May

$$\boldsymbol{U} = \{(\tilde{u}_1, \tilde{v}_1)^T, (\tilde{u}_2, \tilde{v}_2)^T, \dots, (\tilde{u}_M, \tilde{v}_M)^T\} \tag{3.44}$$

be a vector holding all positions of $\boldsymbol{L}$ in the $\tilde{u}\tilde{v}$-plane and $\boldsymbol{\eta}^{\mathcal{I}}$ be the gradient field determined from the detected vectors $\boldsymbol{g}_i^{\mathcal{I}}$, the integration in the CS $\mathcal{I}$ can now be performed to reconstruct the surface

$$h_i^{\mathcal{I}} = \mathrm{rbf}\big(\boldsymbol{U}, \boldsymbol{\eta}^{\mathcal{I}}; \rho\big)_i. \tag{3.45}$$

The determined points of intersection, also describing the surface shape in the CS $\mathcal{I}$,

$$\boldsymbol{I}_i^{\mathcal{I}} = \begin{pmatrix} \tilde{u}_i \\ \tilde{v}_i \\ h_i^{\mathcal{I}} \\ 1 \end{pmatrix} \tag{3.46}$$

are defined as position vectors. As the model is not known here, the relation between the CS $\mathcal{M}$ and the CS $\mathcal{S}$ can be chosen arbitrarily. However, in this work, it is assumed to have the relation as shown in Figure 2.2 for unknown surfaces, resulting in

$$\mathbf{H}_{\mathcal{M}}^{\mathcal{S}} = \mathbf{H}\big((0, 180°, 0), (0, 0, 0)\big) \tag{3.47}$$

for the corresponding transformation matrix. Thus, the position vectors in the CS $\mathcal{S}$ can be calculated by

$$\boldsymbol{I}_i^{\mathcal{S}} = \begin{pmatrix} x_i \\ y_i \\ h_i^{\mathcal{S}} \\ 1 \end{pmatrix} = \mathbf{H}_{\mathcal{M}}^{\mathcal{S}} \mathbf{H}_{\mathcal{C}}^{\mathcal{M}} \mathbf{H}_{\mathcal{I}}^{\mathcal{C}} \boldsymbol{I}_i^{\mathcal{I}}, \tag{3.48}$$

where $h_i^{\mathcal{S}}$ represents the reconstructed surface topography value at the point $\boldsymbol{x}_i$. A flowchart illustrating the process of the surface reconstruction of unknown surfaces is shown in Figure 3.8.

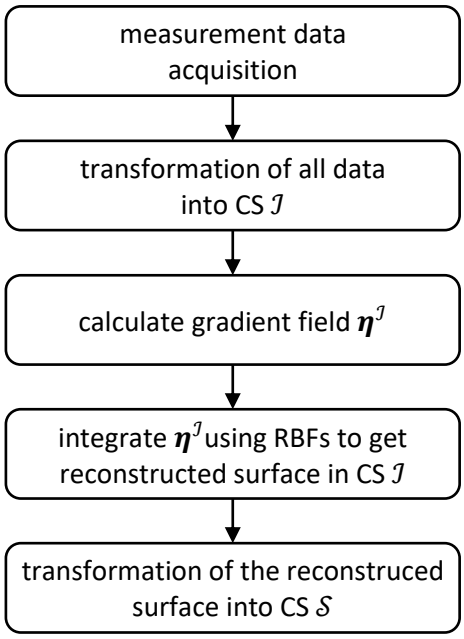

Figure 3.8: Flowchart of the reconstruction of unknown surfaces from measurement data acquisition until the reconstructed surface.

3.6 Calibration methods

3.6.1 Combined calibration including camera rotation

It is expected that an experimental setup is not built up perfectly. Alignment errors occur due to these imperfections. For high accurate measurements, the alignments have to be known accurately, too. To get the relevant information, a calibration method has to be found determining the values $\alpha_{\mathcal{C}}^{\mathcal{I}}$ and $\beta_{\mathcal{C}}^{\mathcal{I}}$ for $\mathbf{H}_{\mathcal{C}}^{\mathcal{I}}$, the values $\alpha_{\mathcal{C}}^{\mathcal{M}}$ and $\beta_{\mathcal{C}}^{\mathcal{M}}$ for $\mathbf{H}_{\mathcal{C}}^{\mathcal{M}}$ and the value $\gamma_{\mathcal{C}}^{\mathcal{C}}$ describing the rotation of the camera around the w-axis as shown in Figure 3.9.

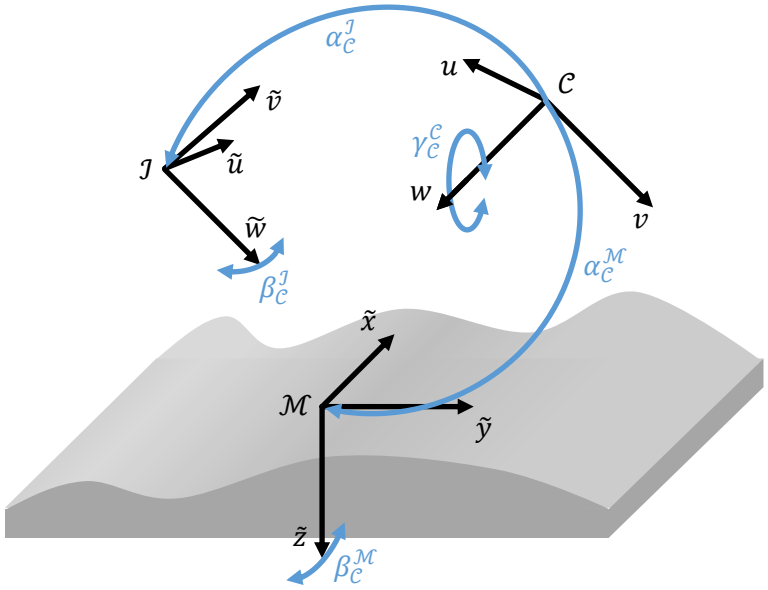

Figure 3.9: Illustration of the parameters $\alpha_{\mathcal{C}}^{\mathcal{I}}$, $\beta_{\mathcal{C}}^{\mathcal{I}}$, $\alpha_{\mathcal{C}}^{\mathcal{M}}$, $\beta_{\mathcal{C}}^{\mathcal{M}}$ and $\gamma_{\mathcal{C}}^{\mathcal{C}}$ determined by the combined calibration method.

One can see in Figure 3.9 that angles are determined with this calibration method only, as positions are not relevant to know for both the measurement of known and unknown surfaces.

The calibration method is based on the evaluation of a known surface in combination with a non-linear minimization. The basic idea is to find the optimal parameters described above from the results of the measurement of a known object by minimizing the deviation of the reconstructed surface from the given model. Observing the influence of misalignments in the considered parameters lead to the assumption that these misalignments introduce global structures in the deviations of the reconstructed surface from the model. These global structures can be represented by Zernike polynomials as described in Chapter 3.3.3. From the observations, it has been determined that global structures introduced by misalignments in the considered parameters, can be represented by the first 15 Zernike polynomials, ordered as described in Table 3.1. Minimizing the RMS of the sum of these fitted polynomials over the considered sample points, by varying the angles described before, leads to the desired parameters [102]. It has to be mentioned here that the considered SUT used for the calibration must have changing surface sag values and surface slope values. Using just a flat mirror is not meaningful for this calibration method. Also, the SUT used should not deviate to far from its model. This will be further investigated in Chapter 6.4.

Abstracting the process of a measurement of a known surface as described in Figure 3.7 as “reconstruction of known surface”, the combined calibration process can be illustrated by the flowchart shown in Figure 3.10.

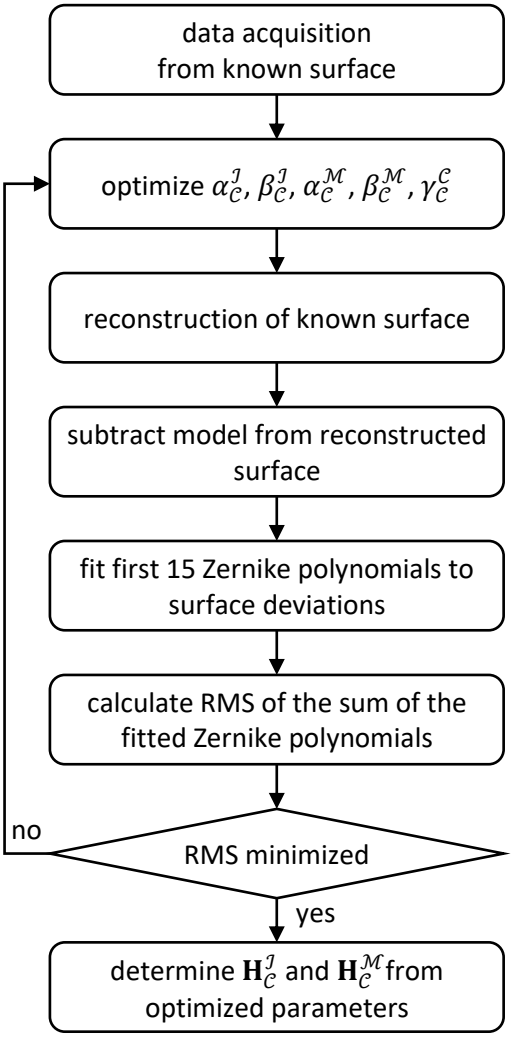

Figure 3.10: Flowchart of the combined calibration of the two transformation matrices $\mathbf{H}_C^{\mathcal{I}}$ and $\mathbf{H}_C^{\mathcal{M}}$ and the camera rotation $\gamma_C^{\mathcal{C}}$.

For easy application, the parameter $\gamma_C^{\mathcal{C}}$ can be used to define a transformation matrix $\mathbf{H}_C^{\mathcal{C}}$ as described in Equation (2.12). This transformation matrix can be applied to the position vectors $\boldsymbol{C}_i$ and $\boldsymbol{D}_i$ directly to perform the rotation of the camera around the w-axis determined by the combined calibration.

3.6.2 Pitch of DUT positioning

The stages used for the positioning of the DUT are not perfectly even in their movement. They introduce a pitch and roll due to imperfections in the manufacturing of the bearing of the moving carriage. Since this measurement technique is based on the determination of the gradient of a SUT, angular imperfections in the positioning of the DUT are directly transferred into the measurement results. However, the pitch and roll of the positioning stages is reproducible and therewith can be measured and subtracted from the determined gradient field.

Since the stages are aligned perpendicular to each other, the pitch of one stage represents the roll of the other stage. Thus, only the pitches in $\tilde{x}$- and $\tilde{y}$-direction have to be considered. To detect these pitches, a setup where a test ray, fixed to the DUT positioning stages, is targeted onto the camera directly is considered. This ray can now be moved along the $\tilde{x}$- and $\tilde{y}$-axis while targeting onto the camera. A sketch of the considered setup is shown in Figure 3.11.

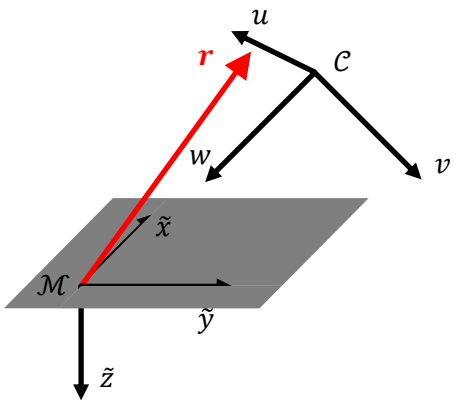

Figure 3.11: Sketch of the setup considered for the determination of the pitch of the $\tilde{x}\tilde{y}$-stage. The illustrated ray direction $\boldsymbol{r}$ is fixed in relation to the CS $\mathcal{M}$.

Considering that the direction of $\boldsymbol{r}$ is fixed in relation to the moving carriage, which moves along the $\tilde{x}$- and $\tilde{y}$-direction, any change of the direction of $\boldsymbol{r}$ can be traced back to a pitch of the $\tilde{x}$- or $\tilde{y}$-axis. The absolute relation between $\boldsymbol{r}$ and the CS $\mathcal{M}$ is not needed as only the change of $\boldsymbol{r}$ is relevant for the determination of the stages pitches. Scanning the considered area, the pitch at multiple positions can be obtained, while the average direction of $\boldsymbol{r}$ is considered as the pitch-free position of the moving carriage. Since the considered positions for this calibration do not have to be identical with the positions used in a measurement, an interpolation has to be performed. As the detected pitch of the positioning stages can also be considered being slopes introduced by the pitch, Zernike polynomials can be used for the interpolation. Fitting the first 36 Zernike polynomials to the detected pitch data, an interpolation can be performed using the determined Zernike coefficients, while high-frequency influences introduced by noise are suppressed.

May the positions $\tilde{\boldsymbol{x}}_i$ be investigated for the determination of the pitch, the ray directions $\boldsymbol{r}_i$ can be determined for each position. Using $\mathbf{H}_{\mathcal{C}}^{\mathcal{M}}$, the ray directions can be transferred into the CS $\mathcal{M}$ resulting in $\boldsymbol{r}_i^{\mathcal{M}}$. From this, the slope values $\tilde{p}_i$ and $\tilde{q}_i$ in $\tilde{x}$- and $\tilde{y}$-direction can be determined. To observe the changes only, the mean value of these slopes is subtracted to get the slopes

$$\hat{p}_i = \tilde{p}_i - \frac{\sum_{i=1}^{M} \tilde{p}_i}{M} \tag{3.49}$$

and

$$\hat{q}_i = \tilde{q}_i - \frac{\sum_{i=1}^{M} \tilde{q}_i}{M}. \tag{3.50}$$

From partial differentiation of Equation (3.34), one can derive the 2D least-squares sense fitting of the Zernike polynomials P_j as

$$\begin{pmatrix} \hat{p}_i \\ \hat{q}_i \end{pmatrix} \mathrel{\hat{=}}_{c_j} \sum_{j=1}^{N} c_j \begin{pmatrix} \frac{\partial P_{j-1}}{\partial x}(\tilde{x}_i, \tilde{y}_i) \\ \frac{\partial P_{j-1}}{\partial y}(\tilde{x}_i, \tilde{y}_i) \end{pmatrix}. \tag{3.51}$$

Solving this equation for $N = 36$, a set of 36 coefficients is derived. These coefficients can be used for the interpolation at any position $(\tilde{x}, \tilde{y})$ within the area, the fit has been performed over.

The slope deviations introduced by the pitch of the DUT positioning stages is only dependent on the targeted sample point $\tilde{\boldsymbol{x}}_i$ and not on the actual investigated position $\boldsymbol{x}_i$ on a SUT. Thus,

the correction is performed directly after the data acquisition. Regarding the flowchart shown in Figure 3.7, the process step for the correction of the slopes is added for the reconstruction of known surfaces as shown in Figure 3.12.

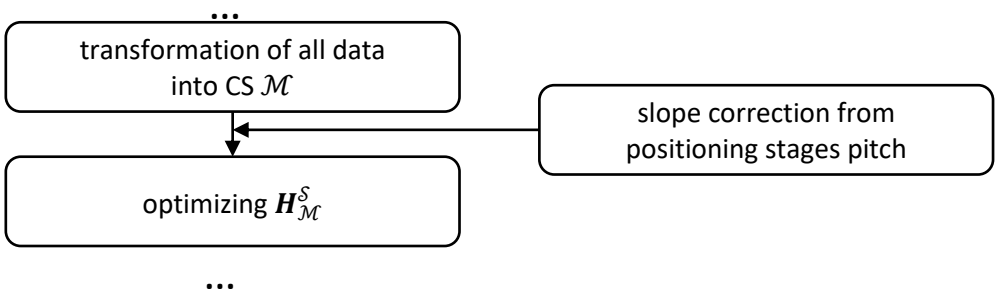

Figure 3.12: Introduction of the pitch correction of the DUT positioning stages into the flowchart for the reconstruction of known surfaces shown in Figure 3.7.

For the correction of the slopes in the reconstruction of an unknown surface, an additional step has to be added since the correction can only be performed in the CS $\mathcal{M}$. Regarding the flowchart shown in Figure 3.8, the two steps have to be added as presented in Figure 3.13.

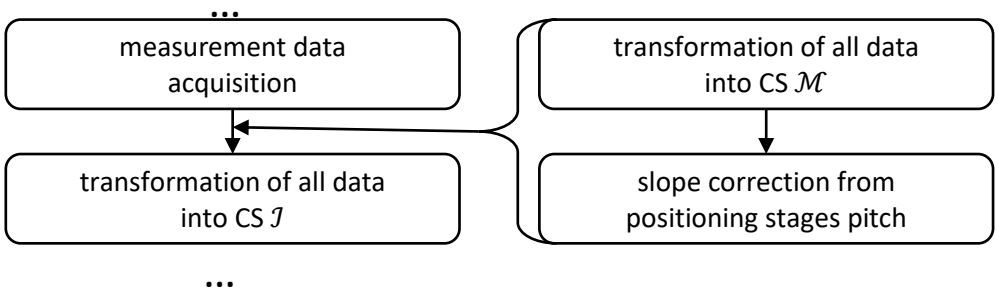

Figure 3.13: Introduction of the pitch correction of the DUT positioning stages into the flowchart for the reconstruction of unknown surfaces shown in Figure 3.8.

4. Simulations

4.1 Simulation setup and samples

4.1.1 Simulation setup

The setup for the simulations consists of three main parts: the optical simulation, the data evaluation and the process control. The setup is depicted as a block diagram in Figure 4.1. The three main parts are described below.

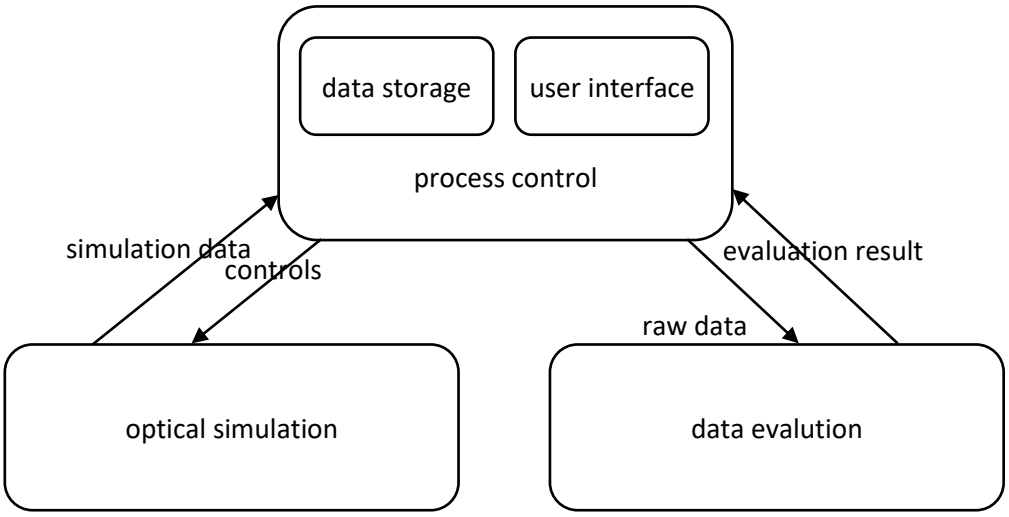

Figure 4.1: Block diagram of the simulation setup. The three main parts are the process control, the optical simulation and the data evaluation. Besides the controlling of the simulation process, the process control offers the opportunity to store data on the computers data storage and provides the user interface.

Optical simulation

For the optical simulation, the software OpticStudio by Zemax is used [103]. In this software, the intended setup is modeled and the optical simulation is performed. These simulations are mainly single ray tracing processes performed in the sequential mode of OpticStudio. The modeled setup is shown in the 3D Layout sketch created by OpticStudio shown in Figure 4.2.

The major components of the modeled setup are the incident ray, the SUT and the detector. The incident ray is a single ray source pointing towards the SUT. The SUT can represent different surface types. In Figure 4.2 it is a simple flat surface. However, it can also represent standard surface types like cylindrical, spherical or aspherical surfaces. Additionally user defined surfaces are available in which arbitrary surface functions can be defined. The third major component is the detector. It is a simple standard surface providing the ability to determine the reflected ray's position on its surface. The origin of the CS $\mathcal{C}$ is here set to be in a distance of $28\ \mathrm{mm}$ from the origin of the CS $\mathcal{M}$, while the w-axis of the CS $\mathcal{C}$ is pointing towards the origin of the CS $\mathcal{M}$. The linear stage in the experimental setup has a travel range of $100\ \mathrm{mm}$ with its origin in the origin of the CS $\mathcal{C}$. As the detector's movement is along the

w-axis, the detector has a distance of $28\ \mathrm{mm}$ from the origin of the CS $\mathcal{M}$, when the detector is positioned to $w = 100\ \mathrm{mm}$.

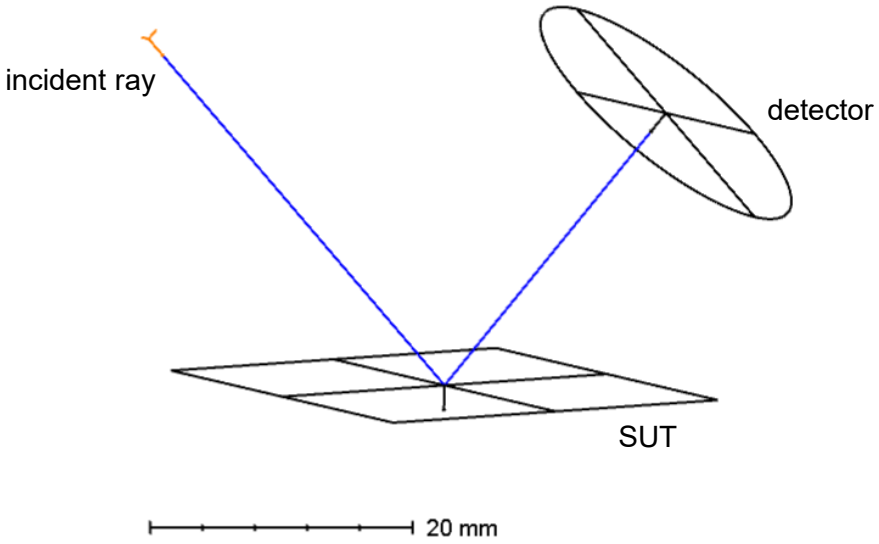

Figure 4.2: Sketch of the modeled setup in OpticStudio [103]. The three major components of the model are the incident ray, the SUT and the detector.

Additionally, multiple surfaces of the type “coordinate break” are added. These coordinate breaks perform three different tasks. First, they are used to model the rotation of the three major components to each other. This rotation is initially chosen to have $\alpha_{\mathcal{C}}^{\mathcal{I}} = 90°$, $\beta_{\mathcal{C}}^{\mathcal{I}} = 0°$, $\alpha_{\mathcal{C}}^{\mathcal{M}} = 45°$, $\beta_{\mathcal{C}}^{\mathcal{M}} = 0°$ and $\gamma_{\mathcal{C}}^{\mathcal{C}} = 0°$. Second, they are used to perform the positioning of the SUT to the desired positions $\tilde{\boldsymbol{x}}_i$. Third, these coordinate breaks are also used to introduce misalignments into the setup. These misalignments are used to check the performance of the calibration methods described before. The full list of surfaces used in the modeled setup in OpticStudio is shown and described in Table 4.1.

Table 4.1: List of all surfaces used for the modeling of the setup in OpticStudio. The background colors in the id-column are used for illustrating the surfaces in Figure 4.3.

id	type	rotation x	comment
0	standard	-	incident beam
1	coord. break	45°	incident beam direction towards SUT
2	coord. break	0°	misalignment of positioning stages
3	coord. break	0°	positioning of SUT to positions $\tilde{\boldsymbol{x}}_i$
4	coord. break	0°	rotation/deplacement of SUT
5	user defined	-	SUT
6	coord. break	0°	reverse rotation deplacement of SUT
7	coord. break	0°	reverse positioning of SUT
8	coord. break	0°	reverse misalignment of positioning stages
9	coord. break	45°	movement of detector to perform ERT
10	coord. break	0°	rotation/deplacement of detector
11	standard	-	detector

To visualize the different surfaces in the modeled setup, they are illustrated in Figure 4.3 with their id and color according to Table 4.1.

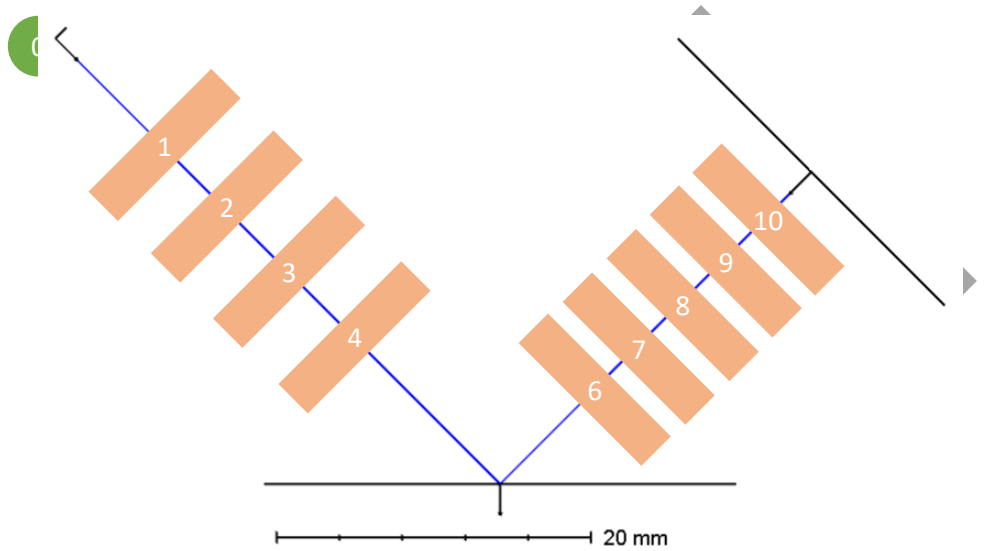

Figure 4.3: Sketch of the modeled setup in OpticStudio including the illustration of all surfaces used. The number on all surfaces corresponds to the given ids in Table 4.1. In this table, further information and descriptions about the surfaces can be found.

The coordinate breaks defined in OpticStudio have a flag to define the order of the performed transformations. By default they follow the order of translation first, rotation around the x-axis second, rotation around the new y-axis third and finally rotation around the new z-axis [104]. This is equivalent to the transformations performed by the transformation matrix defined in Chapter 2.1.2. However, if the flag is switched, the order of transformation is reversed including the order of rotations. Therewith, a coordinate break with reversed order of transformation and inverted values of another coordinate break inverts its effect. This is used for the surfaces with the ids 6, 7 and 8 described in Table 4.1, which therewith invert the effects introduced by the surfaces with the ids 2, 3 and 4.

Data evaluation

For the evaluation of the data determined from OpticStudio, algorithms have been implemented using Python. To maintain package compatibility the distribution Anaconda is used [105]. For easier usability and maintainability, several algorithms have been implemented in separate modules to be used within different scripts equivalently.

Process control

To control the full process of the simulation, a desktop software has been implemented. This software is able to communicate with the OpticStudio software over its application programming interface (API). With this API, OpticStudio can be controlled and simulated data can be exported. After performing the simulation using OpticStudio, the process control application provides the simulation data to the data evaluation and starts the evaluation process. Finally, the evaluated data is presented in the desktop software. Additionally, the data determined from the simulation, as well as the evaluated data are stored on the computers storage drive. Therewith, the data is saved and can be used for further investigation later on.

4.1.2 Sample 1 – “Franke surface”

For the simulations three different surfaces are investigated. The first surface is the so-called “Franke surface” [106]. This surface follows the function

$$s(\boldsymbol{x}) = 0.75e^{-\frac{(9x-2)^2+(9y-2)^2}{4}} + 0.75e^{-\frac{(9x+1)^2}{49}-\frac{9y+1}{10}} + 0.5e^{-\frac{(9x-7)^2+(9y-3)^2}{4}} - 0.2e^{-(9x-4)^2-(9y-7)^2} \tag{4.1}$$

and is widely used as test function in interpolation studies [97]. It consists of three peaks and one sag of exponential shape. This function is designed for an interval of $x = [-1 \dots 1]$ and $y = [-1 \dots 1]$. As it will be shown later in this work, a sample distance of $100\ \mu\mathrm{m}$ will be used for the experimental setup. Assuming the unit for the design interval mentioned above is mm and the investigated area is square, a number of only 441 sample points will be reached. To increase this number, the function given in Equation (4.1) is altered to

$$s(\boldsymbol{x}) = 0.75e^{-\frac{(0.9x-2)^2+(0.9y-2)^2}{4}} + 0.75e^{-\frac{(0.9x+1)^2}{49}-\frac{0.9y+1}{10}} + 0.5e^{-\frac{(0.9x-7)^2+(0.9y-3)^2}{4}} - 0.2e^{-(0.9x-4)^2-(0.9y-7)^2}, \tag{4.2}$$

increasing the design interval to $x = [-10 \dots 10]$ and $y = [-10 \dots 10]$ and the number of sample points to 40401. The surface sag and shape is shown in Figure 4.4 a) and b). The surface slopes in x- and y-direction are shown in Figure 4.4 c) and d). The partial derivatives of Equation (4.2) are given in the Appendix B.

From the first order derivatives, the gradient field $\boldsymbol{\zeta}(\boldsymbol{x})$ can be derived. The gradient field is shown in Figure 4.5.

As shown in Figure 4.4, this surface is a freeform, showing no axis- or rotation-symmetry. Therewith, it suits very good to show the flexibility of the proposed measurement technique. Calculating the curl and the curl height of the gradient field $\boldsymbol{\zeta}$ of the surface over the considered area with a sample distance of $100\ \mu\mathrm{m}$ leads to the values shown in Figure 4.6.

These curls shown in Figure 4.6 are introduced by the discrete sampling of the gradient field with a sampling distance of $100\ \mu\mathrm{m}$ in combination with large curvature values represented by fast changes of the slope data presented in Figure 4.4. Regarding Figure 4.6 b), one can see that the curls introduce curl heights up to $\pm 60\ \mathrm{nm}$. These curl heights are not negligible. However, they are not derived from noise or any other introduced errors, but are only introduced by the discrete sampling of the given model function. Reducing the sample distance leads to smaller curl and curl height values.

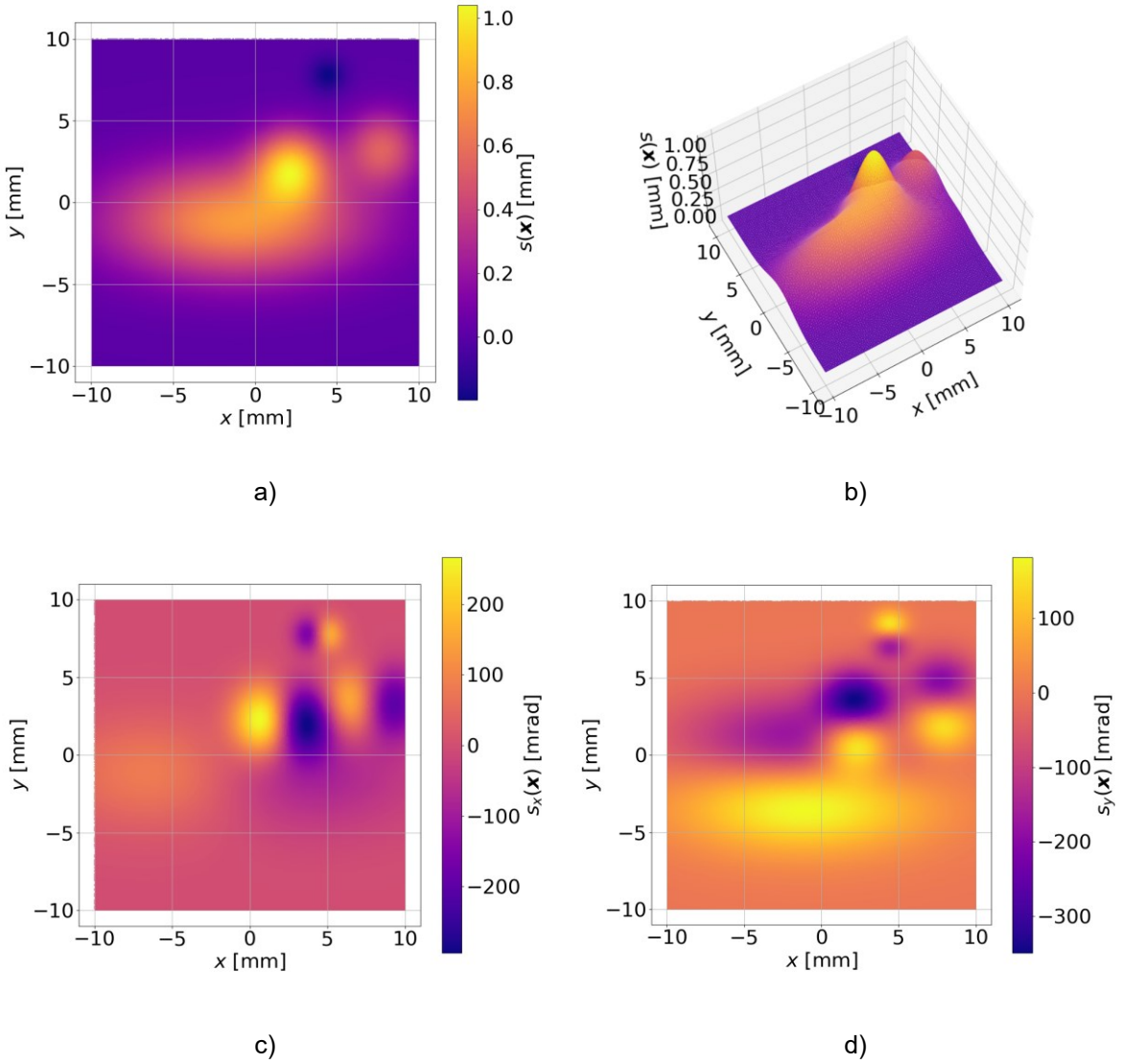

Figure 4.4: Plots presenting the Franke surface. a) and b) show the surface sag in 2D and 3D. c) and d) show the surface slopes in x- and y-direction.

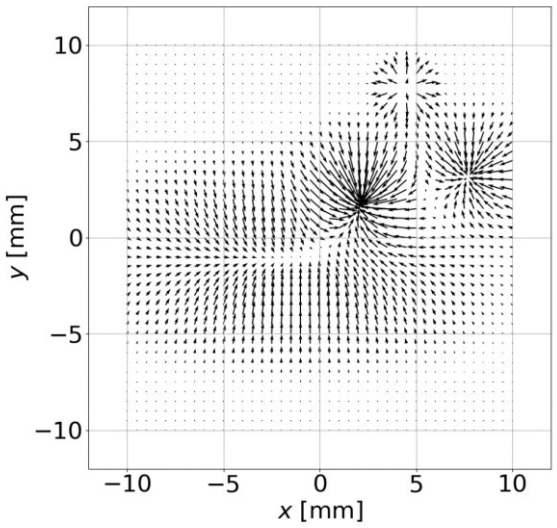

Figure 4.5: Gradient field $\boldsymbol{\zeta}(\boldsymbol{x})$ of the Franke surface.

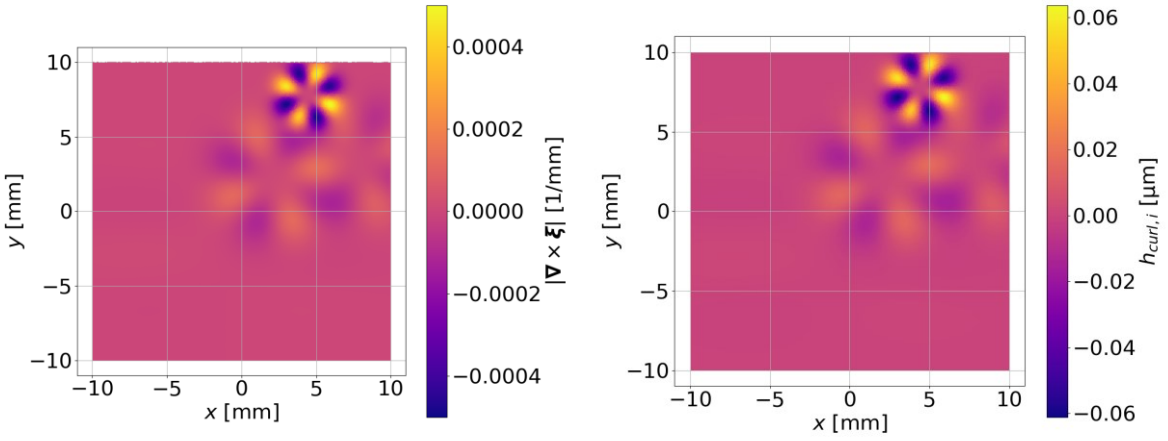

a) b)

Figure 4.6: Plots presenting a) the curl and b) the curl height of the Franke surface' discrete gradient field.

4.1.3 Sample 2 – "cylinder surface"

The second surface to be investigated is a cylinder surface. This surface type is characterized by a spherical shape in one direction, while having constant values in the other direction [5]. Here, the spherical shape is considered to be designed in y-direction. Therefore, the model function

$$s(\boldsymbol{x}) = \begin{cases} -\hat{R} + \sqrt{\hat{R}^2 - y^2} & \text{for } \hat{R} > 0 \text{ and } |y| \leq \hat{R} \\ -\hat{R} - \sqrt{\hat{R}^2 - y^2} & \text{for } \hat{R} < 0 \text{ and } |y| \leq \left|\hat{R}\right| \end{cases} \tag{4.3}$$

can be defined, where $\hat{R} \neq 0$ is the radius of the spherical surface. This surface type has the advantage that cross section investigations can be performed in y-direction, while the model function is independent on the investigated x-position. Thus, this sample is used for cross section investigations. Pre-empting the description of the experimental samples, a cylindrical surface is also available for the experimental measurements. Therefore, the design radius $\hat{R}$ for the simulation is set to $206.7\,\mathrm{mm}$ to match the $\hat{R}$ of the cylindrical sample used for experiments. Additionally, the investigated cross section range is set to $y = [-14 \,...\, 14]\,\mathrm{mm}$ according to the limits given by the dimensions of the experimental sample. The shape and slope of the cylindrical surface is shown in Figure 4.7. The partial derivative in y-direction of Equation (4.3) are given in the Appendix B.

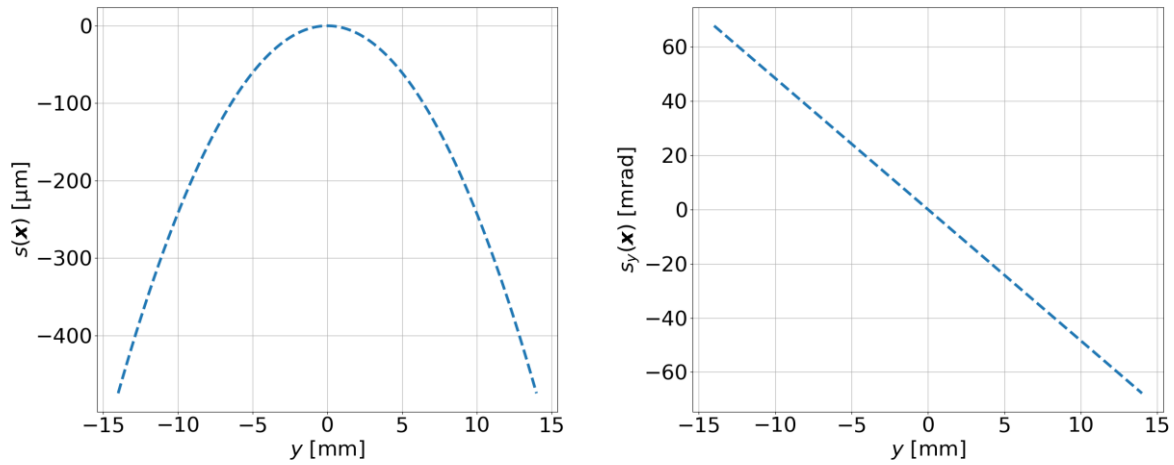

a) b)

Figure 4.7: Plots presenting the cross section of the cylinder surface with the surface radius of $\hat{R} = 206.7\ \mathrm{mm}$ in y-direction. a) shows the surface sag. b) shows the surface slopes y-direction.

In Figure 4.7, a) one can see the spherical shape in y-direction, which is independent on the x-position. In Figure 4.7 b) the surface's slope in y-direction can be seen. From these slope data, the gradient field $\boldsymbol{\zeta}(\boldsymbol{x})$ can be determined, where the gradient's component in x-direction is always 0.

4.1.4 Sample 3 – "polynomial freeform 1"

The third surface used for the simulation is a polynomial freeform. It follows the polynomial function

$$s(\boldsymbol{x}) = 3.5 \cdot 10^{-3}x^2 - 2.5 \cdot 10^{3}y^2 - 2.5 \cdot 10^{-5}x^4 + 3.5 \cdot 10^{-5}y^4 \tag{4.4}$$

and therewith is symmetrical regarding both the x- and y-direction, but is not rotational symmetric. Also, the shape in x- and y-direction is different. As another polynomial freeform will be introduced later, this polynomial freeform is called "polynomial freeform 1". A real sample having this model function is also available for the experimental measurements. Since this sample has a circular aperture and the limits of the experimental setup have to be considered, the investigated area of this sample is defined to be circular with an diameter of $22\ \mathrm{mm}$. The center of this circular area is set to the center of the function. The shape and slope of this sample for the considered area are shown in Figure 4.8. The functions $s_x(\boldsymbol{x})$ and $s_y(\boldsymbol{x})$ of the partial derivatives of Equation (4.4) are given in the Appendix B.

The gradient field derived from the slopes is shown in Figure 4.9.

Calculating the curl and the curl height from the gradient field at the desired sample positions lead to the values shown in Figure 4.10.

The curl height shown in Figure 4.10 has a RMS of less than $0.3\ \mathrm{am}$. In comparison to the curl and the curl height of the Franke surface, shown in Figure 4.6, the magnitude of the values of the polynomial freeform 1 are much lower and do not have to be considered in the reconstruction. However, if curl and curl height values in the same magnitude are determined from the simulation, they can be traced back to the discretization.

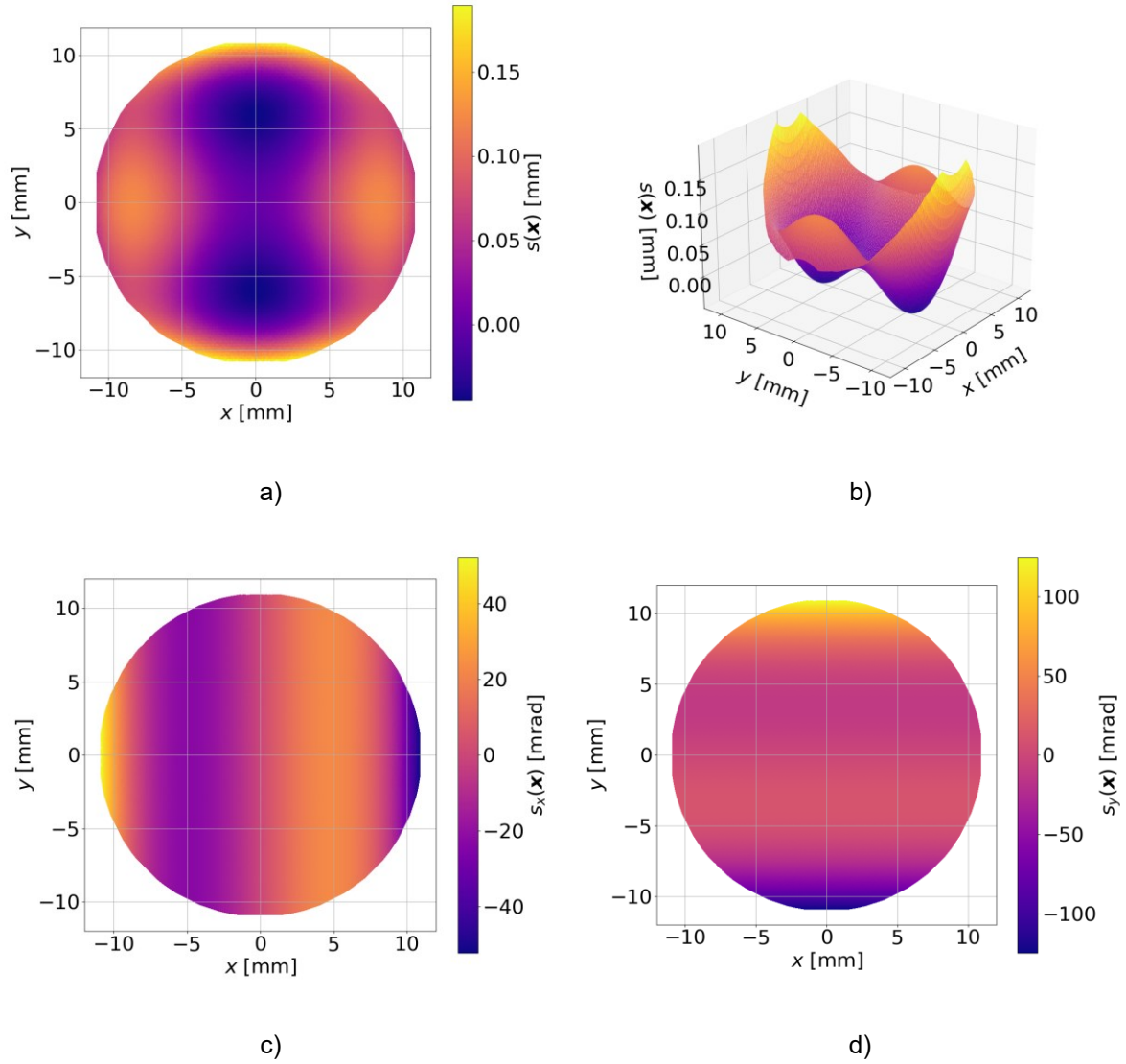

Figure 4.8: Plots presenting the polynomial freeform 1 surface. a) and b) show the surface sag in 2D and 3D. c) and d) show the surface slopes in x- and y-direction.

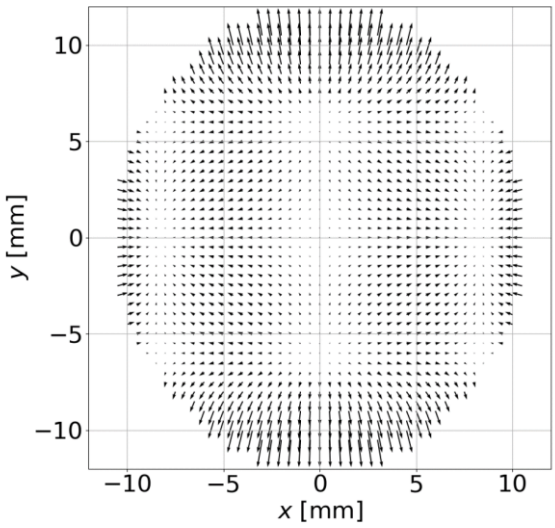

Figure 4.9: Gradient field $\boldsymbol{\zeta}(\boldsymbol{x})$ of the polynomial freeform 1.

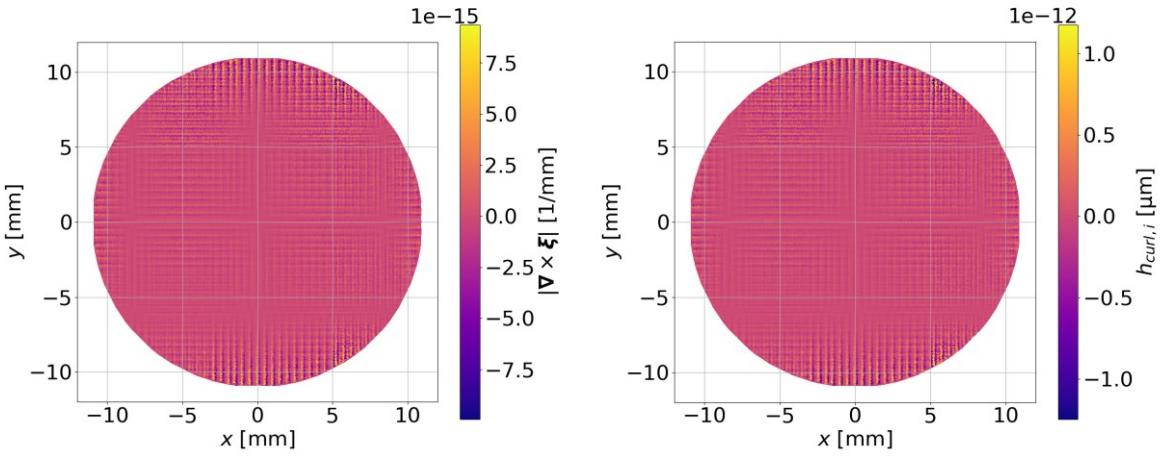

a) b)

Figure 4.10: Plots presenting a) the curl and b) the curl height of the polynomial freeform 1 sampled discrete at the desired positions $\tilde{\boldsymbol{x}}_i$.

4.2 Simulation using different surface models

4.2.1 Simulation process

As described before, the measurement process is controlled by the same application in both experimental measurement and simulation. Since the experimental measurement process has higher requirements due to limits by the hardware performance, than there are restrictions in the simulation, the process has mainly been customized for the experimental measurements. The simulation has then been adapted to this process to implement the simulation and experimental measurements in the process equally.

To start the simulation process, the sample positions $\tilde{\boldsymbol{x}}_i$ to be investigated, have to be defined. Generally, they can be arranged in arbitrary shape and arbitrary density over the area to be investigated. However, as described in the beginning of Chapter 3, only even grids are investigated here. The shape of these grids is either circular, rectangular or a cross section represented by a single line. After the definition of the sample positions $\tilde{\boldsymbol{x}}_i$, the data acquisition in the simulation is performed as illustrated in Figure 4.11.

The differences to the data acquisition in the experimental measurements are described in Chapter 5.1, where the data acquisition process of the experimental measurement is described.

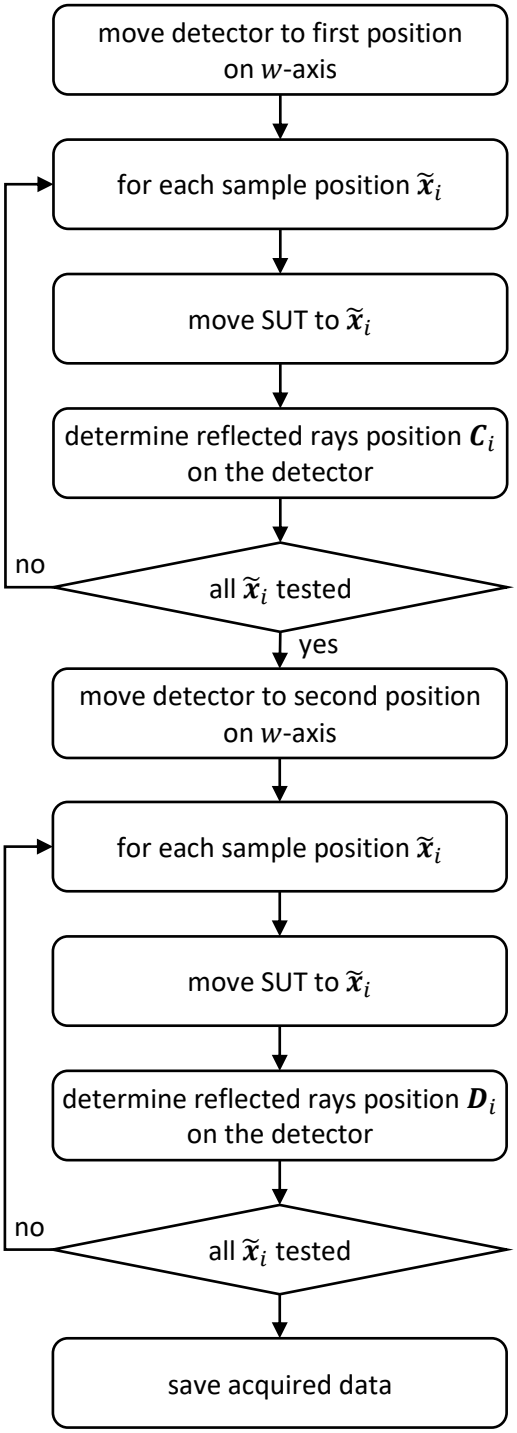

Figure 4.11: Flow chart of the simulation process.

4.2.2 Simulation results with known surface

For the simulation of all surfaces, the transformation matrices have assumed to be ideal. Thus, the angles $\alpha_{\mathcal{C}}^{\mathcal{I}} = 90°$, $\beta_{\mathcal{C}}^{\mathcal{I}} = 0°$, $\alpha_{\mathcal{C}}^{\mathcal{M}} = 45°$, $\beta_{\mathcal{C}}^{\mathcal{M}} = 0°$ and $\gamma_{\mathcal{C}}^{\mathcal{C}} = 0°$ have been chosen as set in the simulation model. The two investigated detector positions are $w = 100\ \mathrm{mm}$ to determine the positions $\boldsymbol{C}_i$ and $w = 90\ \mathrm{mm}$ to determine the positions $\boldsymbol{D}_i$. Additionally, as expected for all surfaces, the minimization process to find the SUT position found the surface to be positioned and oriented as defined in the simulation model.

For the integration, the support radius of the RBFs is set to $\rho = 20.0\,\mathrm{mm}$. The value of this is supposed to have a high influence on the accuracy of the reconstruction, when small numbers N of center points are used [107]. As stated before, the number of center points is equal to the number of sample points here. This leads to a high stability of the reconstructed surface dependent on the value of ρ. This is shown in the reconstruction of the deviations of an experimental measurement in Chapter 5.4.5.

Franke surface

From the simulation using the Franke surface, the reflected ray positions $\boldsymbol{C}_i$ and $\boldsymbol{D}_i$ have been determine as shown in Figure 4.12.

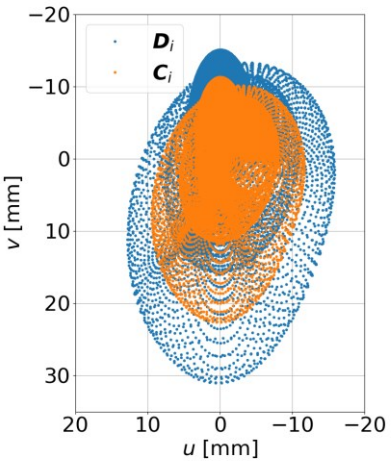

Figure 4.12: Determined positions $\boldsymbol{C}_i$, with $w = 100\,\mathrm{mm}$, and $\boldsymbol{D}_i$, with $w = 90\,\mathrm{mm}$, performing the simulation using the Franke surface as SUT.

From these reflected ray positions, the gradient field of deviations $\boldsymbol{\xi}$ is determined. As shown in the flowchart represented in Figure 3.7, the integrability is enforced over this gradient field as described in Chapter 3.3.2. Calculating the curl of $\boldsymbol{\xi}$ before enforcing the integrability, the height deviation shown in Figure 4.13, can be calculated according to Equation (3.28).

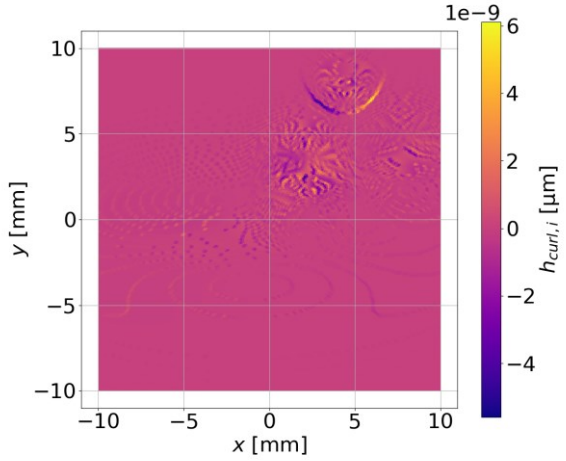

Figure 4.13: Curl height $h_{curl,i}$ of the determined resulting gradient field $\boldsymbol{\xi}$ from the simulation using the Franke surface.

Regarding Figure 4.13, one can see that the curl height is in the range of a few fm, it's RMS is $0.4\,\mathrm{fm}$. These curls are introduced by numerical errors, since curls introduced by discrete sampling are eliminated as described in Chapter 3.3.2. This can also be seen by comparing

Figure 4.13 with Figure 4.6 b) which shows the curl height introduced by the discrete sampling of the Franke surface.

After enforcing the integrability and reconstructing the surface using RBF integration, the reconstructed surface and its deviation from the surface model, as shown in Figure 4.14, are derived.

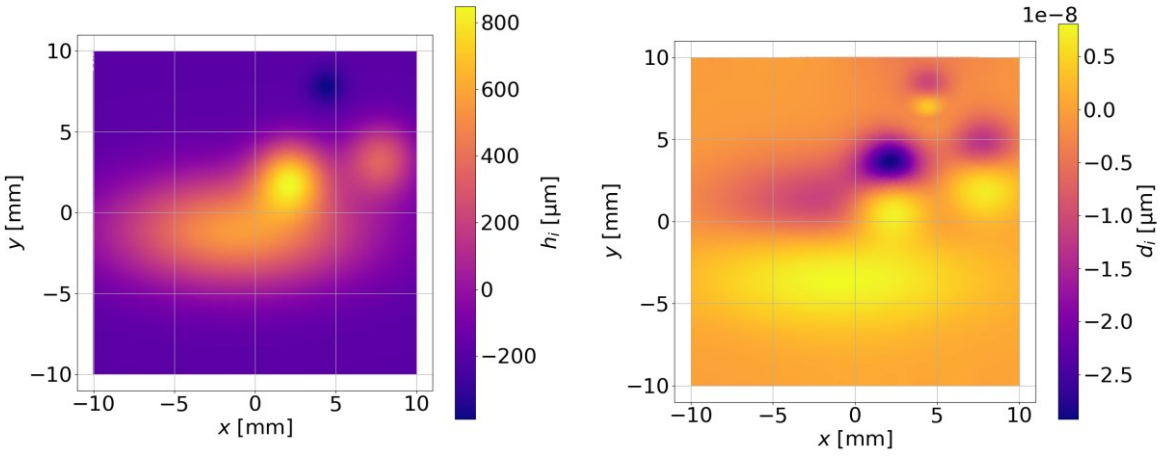

a) b)

Figure 4.14: Plots presenting a) the reconstructed surface and b) its deviation from the surface model from the simulation using the Franke surface. For the evaluation, the surface model has been considered as known.

Regarding Figure 4.14 b), one can see that deviations exit in the reconstruction of the surface. These deviations occur from numerical limits in the simulation and evaluation and the discretization of the gradient field. However, regarding the magnitude of these deviations, one can see that they are negligible. The deviations are in the range of $\pm 20\,\mathrm{fm}$. Even if a measurement accuracy of $1\,\mathrm{nm}$ may be achieved in the experimental setup, these deviations would be 25000 times smaller than the measurement accuracy. The RMS of these deviations is $4.7\,\mathrm{fm}$.

Cylinder surface – Cross section

In the simulation of a cross section measurement with the Cylinder surface with $\hat{R} = 206.7\,\mathrm{mm}$, the sample points $\tilde{\boldsymbol{x}}_i$ are chosen to have $\tilde{x} = 0$. Thus, only one line along the $\tilde{y}$-axis is investigated. Performing this using the cylinder surface, the positions $\boldsymbol{C}_i$ and $\boldsymbol{D}_i$, as shown in Figure 4.15, are determined.

In Figure 4.15, one can see that all points $\boldsymbol{C}_i$ and $\boldsymbol{D}_i$ are positioned at $u = 0\,\mathrm{mm}$. This is due to the slope values in x-direction of $s_x(\boldsymbol{x}) = 0$. Since there is no slope in x-direction, the reflected ray does not leave the center position in u-direction here.

The evaluation of a cross section is equivalent to the evaluation of a 2D area. However, since there is one dimension less, the optimization to find the SUT position can be reduced in its degrees of freedom. In the evaluation of a 2D area, the optimization performs over the parameters $\alpha_{\mathcal{M}}^{\mathcal{S}}, \beta_{\mathcal{M}}^{\mathcal{S}}, \gamma_{\mathcal{M}}^{\mathcal{S}}, \Delta\tilde{x}_{\mathcal{M}}^{\mathcal{S}}$ and $\Delta\tilde{y}_{\mathcal{M}}^{\mathcal{S}}$. In the cross section evaluation this is reduced to the parameters $\alpha_{\mathcal{M}}^{\mathcal{S}}$ and $\Delta\tilde{y}_{\mathcal{M}}^{\mathcal{S}}$. Additionally, since the model function is of cylinder form, the parameters $\alpha_{\mathcal{M}}^{\mathcal{S}}$ and $\Delta\tilde{y}_{\mathcal{M}}^{\mathcal{S}}$ are ambiguous. Thus, the parameters to be optimized can even been reduced to $\alpha_{\mathcal{M}}^{\mathcal{S}}$. Evaluating the cross section simulation leads to the reconstructed surface and the deviation from the model shown in Figure 4.16.

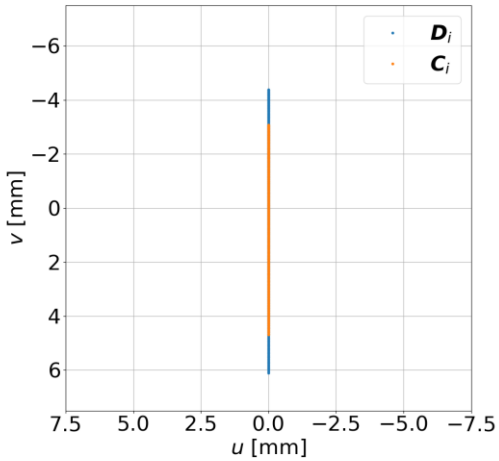

Figure 4.15: Determined positions $\boldsymbol{C}_i$, with $w = 100\,\mathrm{mm}$, and $\boldsymbol{D}_i$, with $w = 90\,\mathrm{mm}$, performing the cross section along the $\tilde{y}$-axis simulation using the Cylinder surface with $\hat{R} = 206.7\,\mathrm{mm}$ as SUT.

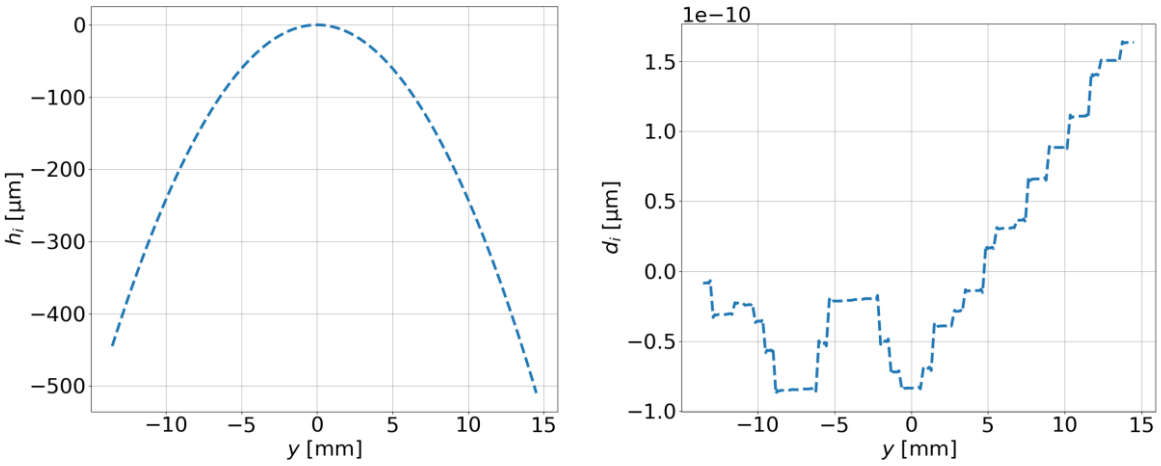

a) b)

Figure 4.16: Plots presenting a) the reconstructed surface and b) its deviation from the surface model from the cross section simulation using the cylinder surface with $\hat{R} = 206.7\,\mathrm{mm}$. For the evaluation, the surface model has been considered as known.

The deviations shown in Figure 4.16 b) show a RMS of $73\,\mathrm{am}$.

Polynomial freeform 1

Performing the simulation using the polynomial freeform 1 as SUT, the reflected ray positions are determined as shown in Figure 4.17.

In Figure 4.17, the different slope magnitudes in x- and y-direction of the polynomial freeform 1 can already be seen in the determined positions $\boldsymbol{C}_i$ and $\boldsymbol{D}_i$. Regarding Figure 4.8 c) and d), one can recognize that the slope in y-direction has higher values than the slope in x-direction. This leads to a higher distance of the determined positions $\boldsymbol{C}_i$ and $\boldsymbol{D}_i$ form the center in v-direction than in u-direction.

From the surface slopes, derived from the positions $\boldsymbol{C}_i$ and $\boldsymbol{D}_i$, the gradient field $\boldsymbol{\xi}$ can be defined. This gradient field can now be investigated regarding its integrability as described in Chapter 3.3.2. The resulting height deviation from the curl is presented in Figure 4.18.

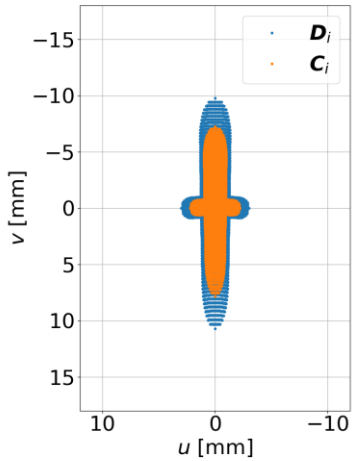

Figure 4.17: Determined positions $\boldsymbol{C}_i$, with $w = 100\,\mathrm{mm}$, and $\boldsymbol{D}_i$, with $w = 90\,\mathrm{mm}$, performing the simulation using the polynomial freeform 1 as SUT.

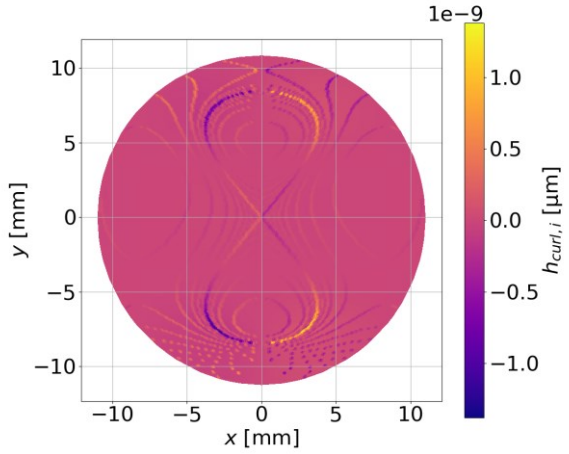

Figure 4.18: Plot of the curl height of the gradient field $\boldsymbol{\xi}$, determined from the simulation using the polynomial freeform 1.

The height deviation h_{curl} shows a RMS of only $0.1\,\mathrm{fm}$. The curls, and therewith the height deviations, are introduced by numerical limits in the simulation and evaluation. However, these deviations are within a negligible range. As the process of evaluating a known surface, illustrated in the flowchart in Figure 3.7, includes the enforcement of the integrability, this is now performed on the gradient field $\boldsymbol{\xi}$. After that, the surface is reconstructed. The reconstructed surface and its deviation from the surface model of the polynomial freeform 1 are shown in Figure 4.19.

The RMS of the deviation shown in Figure 4.19 b) is $0.9\,\mathrm{fm}$ resulting from numerical limits.

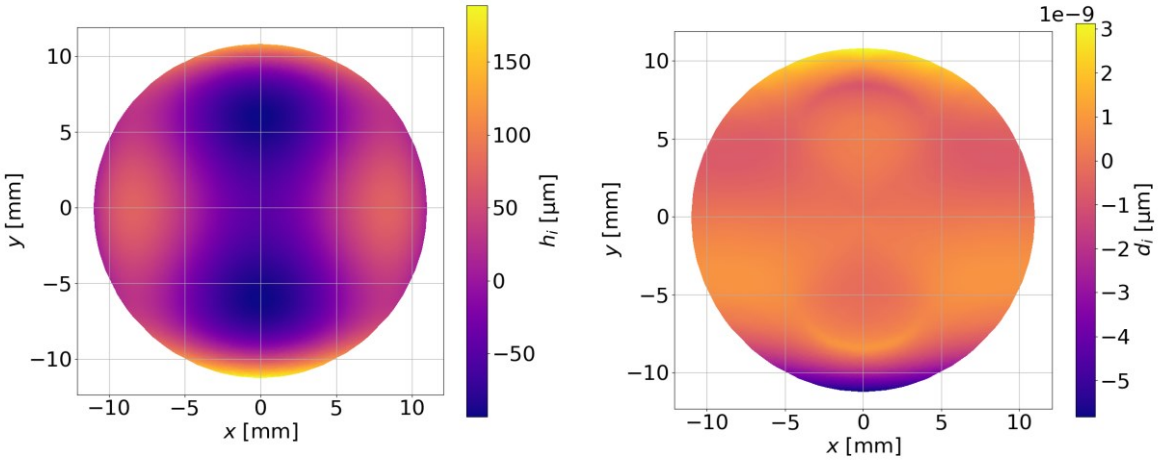

a) b)

Figure 4.19: Plots presenting a) the reconstructed surface and b) its deviation from the surface model from the simulation using the polynomial freeform 1. For the evaluation, the surface model has been considered as known.

4.2.3 Simulation results with unknown surface

The data acquisition for unknown surfaces is equivalent to the data acquisition for known surfaces. Thus, the determined positions $\boldsymbol{C}_i$ and $\boldsymbol{D}_i$ are equivalent for both methods. Only the evaluation deviates within the procedures. To avoid repetitions, the evaluation of the data assuming an unknown surface is presented here only for the Franke surface.

The positions $\boldsymbol{C}_i$ and $\boldsymbol{D}_i$ used for the evaluation are shown in Figure 4.12. Performing the evaluation as described in Chapter 3.5 leads to the reconstruction shown in Figure 4.20 a).

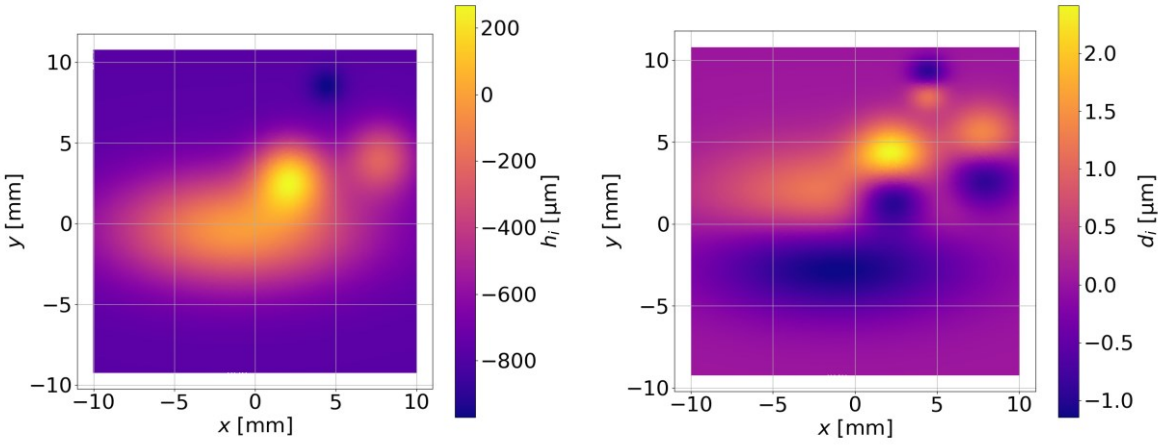

a) b)

Figure 4.20: Plots presenting a) the reconstructed surface from the simulation using the Franke surface. b) shows the deviation from the model after the reconstruction has been performed assuming the model to be unknown. From the deviation, a constant offset has been subtracted.

To evaluate the performance of the unknown surface reconstruction, the reconstructed surface shown in Figure 4.20 a) is compared to the model of the Franke surface. Subtracting the model from the reconstructed surface and subtracting a constant offset from these deviations leads

to the deviations shown in Figure 4.20 b). These deviations show a RMS of $538\ \mathrm{nm}$. However, it has to be mentioned that no model-fitting is performed here. The integration constant cannot be reconstructed during integration. This can lead to a shift of the points of Intersection I_i during the rotation of the reconstructed surface into the CS $\mathcal{S}$.

As shown in Figure 4.6, the discretization of the model function leads to curls in the discrete gradient field. It has been described before that enforcing the integrability can lead to a gradient field, different from the gradient field of the model. To show the influence of the integrability enforcement, it has been performed once before integrating the gradient field. The reconstructed surface and the deviation from the model function from this evaluation are shown in Figure 4.21.

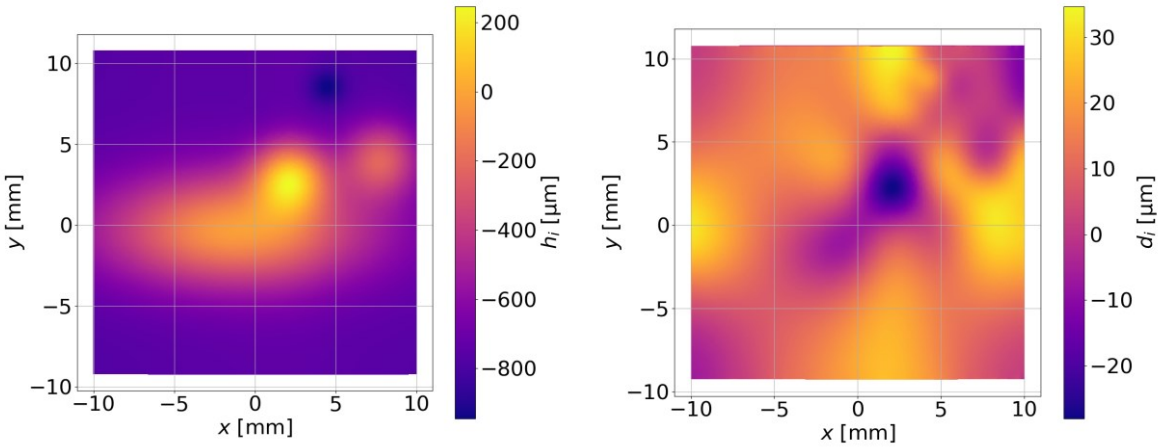

a) b)

Figure 4.21: Plots presenting a) the reconstructed surface from the simulation using the Franke surface. In this evaluation the integrability has been enforced before integration. b) shows the deviation from the model of the reconstructed surface. From the deviation, a constant offset has been subtracted.

Comparing Figure 4.21 b) with Figure 4.20 b), one can clearly see the difference in the determined deviations from the model function. The RMS of the deviations including the integrability enforcement is $15.311\ \mu\mathrm{m}$. This is much larger that the RMS of the deviations without integrability enforcement. This shows that the enforcement of the integrability is not always meaningful. In addition, it points out the ability of the RBF integration to reconstruct surfaces from non-curl-free discrete gradient fields, due to discretization.

4.3 Calibration

In this chapter, the calibration methods are tested by introducing misalignments in the simulation model that are expected to be detected. This is not an analysis on the accuracy or repeatability of these methods. This investigation is presented in Chapter 6. Here, the basic functionality of the methods is shown.

SUT position determination

The first method that is checked is technically not a calibration method, but it is also used in the evaluation of the data. It is the determination of the SUT's position. Regarding Figure 2.2 one can see that in an ideal case, the rotation vector $\boldsymbol{\gamma}_{\mathcal{M}}^{\mathcal{S}} = \left(\alpha_{\mathcal{M}}^{\mathcal{S}}, \beta_{\mathcal{M}}^{\mathcal{S}}, \gamma_{\mathcal{M}}^{\mathcal{S}}\right) = (0°, 180°, 0°)$. If the SUT is positioned perfectly in the center of the CS $\mathcal{M}$, the translation vector is expected to be $\boldsymbol{t}_{\mathcal{M}}^{\mathcal{S}} = \left(\Delta\tilde{x}_{\mathcal{M}}^{\mathcal{S}}, \Delta\tilde{y}_{\mathcal{M}}^{\mathcal{S}}, \Delta\tilde{z}_{\mathcal{M}}^{\mathcal{S}}\right) = (0\ \mathrm{mm}, 0\ \mathrm{mm}, 0\ \mathrm{mm})$. To check the functionality of the SUT position

determination, arbitrary misalignments are introduced, so that the rotation vector $\boldsymbol{\gamma}_{\mathcal{M}}^{\mathcal{S}} = (-0.6°, 179.3°, -0.8°)$ and the translation vector $\boldsymbol{t}_{\mathcal{M}}^{\mathcal{S}} = (1.1\ \text{mm}, 1.2\ \text{mm}, 0\ \text{mm})$ are expected to be determined. Performing the simulation, one can already see the influence of the misalignments in the detected positions $\boldsymbol{C}_i$ and $\boldsymbol{D}_i$ shown in Figure 4.22. Especially, comparing these positions with the positions determined without the misalignments shown in Figure 4.17.

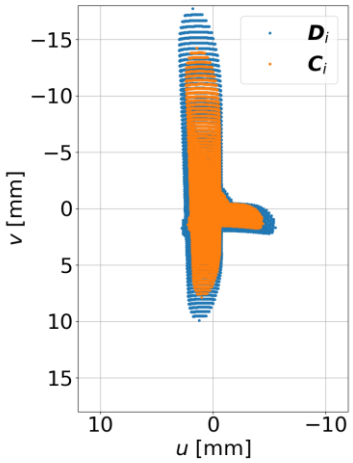

Figure 4.22: Determined positions $\boldsymbol{C}_i$, with $w = 100\ \text{mm}$, and $\boldsymbol{D}_i$, with $w = 90\ \text{mm}$, performing the simulation using the polynomial freeform 1 as SUT including an intended decenter and misalignment of the SUT.

To determine the position of the SUT, the cost function described in Equation (3.39) is minimized by optimizing the parameter $\alpha_{\mathcal{M}}^{\mathcal{S}}, \beta_{\mathcal{M}}^{\mathcal{S}}, \gamma_{\mathcal{M}}^{\mathcal{S}}, \Delta\tilde{x}_{\mathcal{M}}^{\mathcal{S}}$ and $\Delta\tilde{y}_{\mathcal{M}}^{\mathcal{S}}$. As initial values, the ideal values $\alpha_{\mathcal{M}}^{\mathcal{S}} = 0°, \beta_{\mathcal{M}}^{\mathcal{S}} = 180°, \gamma_{\mathcal{M}}^{\mathcal{S}} = 0°, \Delta\tilde{x}_{\mathcal{M}}^{\mathcal{S}} = 0\ \text{mm}$ and $\Delta\tilde{y}_{\mathcal{M}}^{\mathcal{S}} = 0\ \text{mm}$ are chosen. Performing the determination of the SUT's position, the values shown in Table 4.2 are derived.

Table 4.2: Derived angles and decenter from the SUT's position determination and their comparison to the angles and decenter set in the simulation model.

	$\alpha_{\mathcal{M}}^{\mathcal{S}}$ [°]	$\beta_{\mathcal{M}}^{\mathcal{S}}$ [°]	$\gamma_{\mathcal{M}}^{\mathcal{S}}$ [°]	$\Delta\tilde{x}_{\mathcal{M}}^{\mathcal{S}}$ [mm]	$\Delta\tilde{y}_{\mathcal{M}}^{\mathcal{S}}$ [mm]
expected	-0.6	179.3	-0.8	1.1	1.2
derived	-0.60000004	179.30000012	-0.79999894	1.09999997	1.20000019
deviation	$-0.04 \cdot 10^{-6}$	$0.12 \cdot 10^{-6}$	$1.06 \cdot 10^{-6}$	$0.03 \cdot 10^{-6}$	$0.19 \cdot 10^{-6}$

The deviations presented in Table 4.2 show that the expected values have been derived up to a very small deviation. The deviations are in the range of $0.003''$ respectively below $0.2\ \text{nm}$. Thus, one can say that the position of the SUT can be derived from simulation data. The results from the surface reconstruction with this determined SUT position is shown in Figure 4.23.

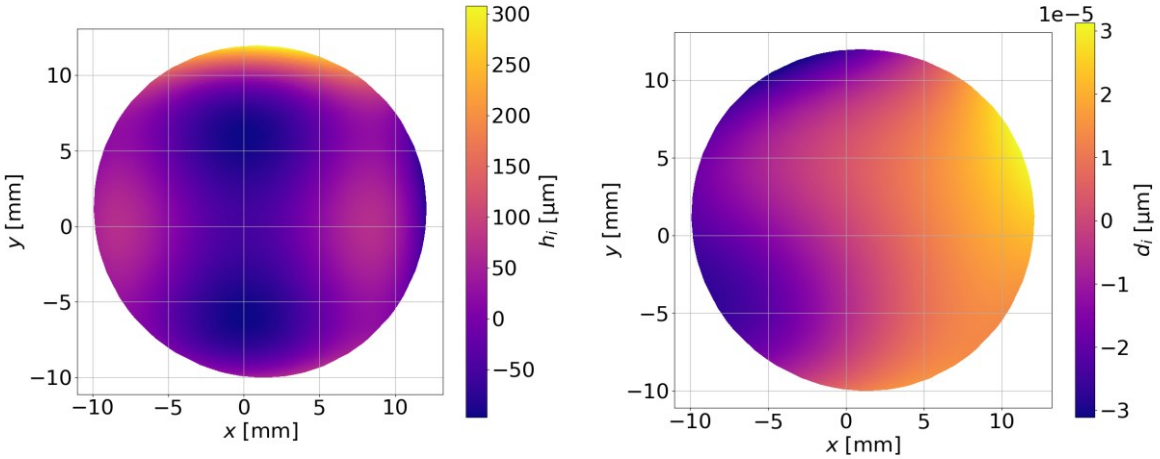

a) b)

Figure 4.23: Plots presenting a) the reconstructed surface from the simulation using the polynomial freeform 1 and b) its deviation from the model. In the simulation the SUT was tilted and misaligned as described before. The set and determined values are shown in Table 4.2.

Combined calibration including camera rotation

The process of this calibration method is described in Chapter 3.6.1. For the simulation, the polynomial freeform 1 sample has been used as SUT, as this sample is also used for the calibration in the experimental setup. This calibration method calibrates 5 values in parallel: the angles $\alpha_{\mathcal{C}}^{\mathcal{I}}$, $\beta_{\mathcal{C}}^{\mathcal{I}}$, $\alpha_{\mathcal{C}}^{\mathcal{M}}$, $\beta_{\mathcal{C}}^{\mathcal{M}}$ and $\gamma_{\mathcal{C}}^{\mathcal{C}}$.

To see if the calibration method is able to determine the angles correctly, the simulation setup has been altered to introduce known misalignments. Regarding the simulation setup described in Chapter 4.1.1, one can see that the angles $\alpha_{\mathcal{C}}^{\mathcal{I}}$ and $\beta_{\mathcal{C}}^{\mathcal{I}}$ are not only dependent on one coordinate break element, but two: surface 1 and surface 9 as described in Table 4.1. Since two combined combinations of transformations are most likely not a simple addition of the given rotation angles, the given angles shown in Table 4.3 lead to the expected angles shown in Table 4.4.

Performing the simulation with the introduced misalignments using the polynomial freeform 1 as SUT leads to the determined positions $\boldsymbol{C}_i$ and $\boldsymbol{D}_i$ shown in Figure 4.24.

Comparing the determined reflected ray positions shown in Figure 4.24 with the positions shown in Figure 4.17, one identifies only minor deviations. In Figure 4.24, a slight shift of all positions to the negative u-direction and a slightly higher deflection of the reflected rays in negative u-direction can be determined. From these small deviations, the calibration method derives the misalignments as presented in Table 4.4. Regarding the deviations in Table 4.4, one can see that the calibration method is able to determine the correct angles up to a minor deviation. Using these derived values to perform an evaluation of the given reflected ray positions the surface shown in Figure 4.25 is reconstructed.

The deviation of the reconstruction shown in Figure 4.25 b) has a RMS value of $239\ \mathrm{fm}$.

Table 4.3: Rotation angles for the coordinate break surfaces in OpticStudio as shown in Table 4.1 and Figure 4.3. The misalignments introduced by these rotation angles are used to test the abilities of the combined setup calibration including the camera rotation.

id	rotation x [°]	rotation y [°]	rotation z [°]
1	45.1	0.015	0.0
2	−0.1	0.075	0.0
8	0.1	−0.075	0.0
9	45.0	0.0	0.0
10	0.0	0.0	−0.13

Table 4.4: Derived angles from the combined calibration and their deviation from the expected angles set in the simulation model.

	$\alpha_{\mathcal{C}}^{\mathcal{I}}$ [°]	$\beta_{\mathcal{C}}^{\mathcal{I}}$ [°]	$\alpha_{\mathcal{C}}^{\mathcal{M}}$ [°]	$\beta_{\mathcal{C}}^{\mathcal{M}}$ [°]	$\gamma_{\mathcal{C}}^{\mathcal{C}}$ [°]
expected	90.10009817	0.10588067	45.1	−0.075	−0.13
derived	90.10009821	0.10588084	45.10000002	−0.07499988	−0.12999991
deviation	$0.04 \cdot 10^{-6}$	$0.17 \cdot 10^{-6}$	$0.02 \cdot 10^{-6}$	$0.12 \cdot 10^{-6}$	$0.09 \cdot 10^{-6}$

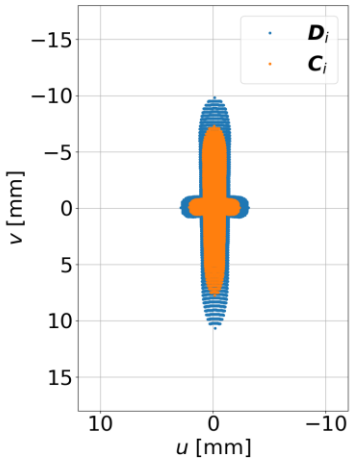

Figure 4.24: Determined positions $\boldsymbol{C}_i$, with $w = 100\,\mathrm{mm}$, and $\boldsymbol{D}_i$, with $w = 90\,\mathrm{mm}$, performing the simulation using the polynomial freeform 1 as SUT including the intended misalignments defined in Table 4.3.

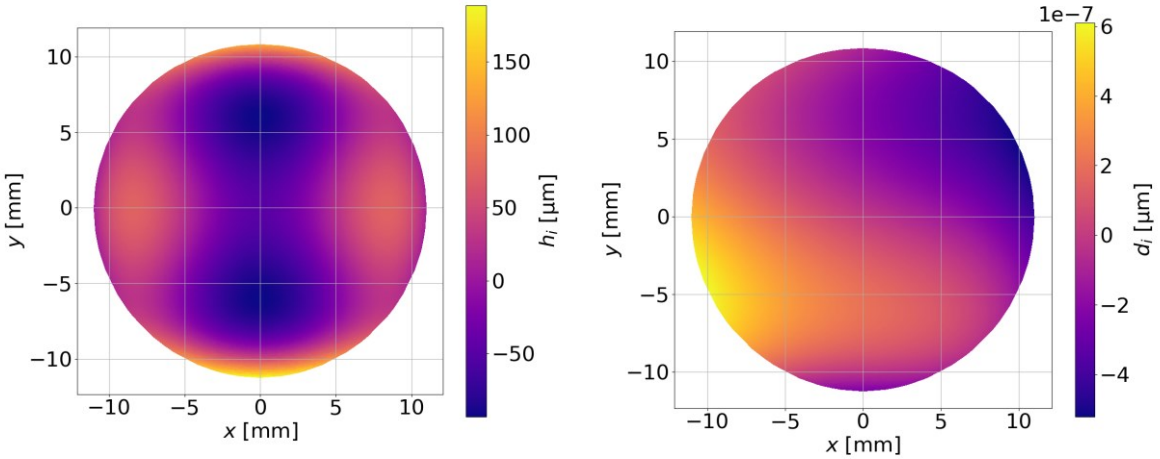

a) b)

Figure 4.25: Plots presenting a) the reconstructed surface from the simulation using the polynomial freeform 1 and b) its deviation from the model. In the simulation the model was misaligned as described in Table 4.3. The expected and determined values are shown in Table 4.4.

4.4 Conclusion

The simulations and their results proof the fundamental functionality of the measurement principle that has theoretically been described before. Additionally, the results show that the calibration methods are able to detect the desired parameters correctly and the evaluation is able to use these parameters meaningful.

In Chapter 3.3.2, it has been described that the enforcement of the integrability may introduce deviations if the suppressed curls are introduced by discretization. This theory has also been substantiated by integrating a discrete gradient field with and without enforcing the integrability.

The simulations are not perfectly error-free. The introduced errors are introduced by numerical limits or limits of the minimization processes. However, these errors are negligible in relation to the errors introduced by the experimental setup as shown later.

5. Experiments and Results

5.1 Experimental setup and procedure

The experimental setup has been built up according to the sketch of the measurement setup shown in Figure 2.2. The experimental setup is shown in Figure 5.1

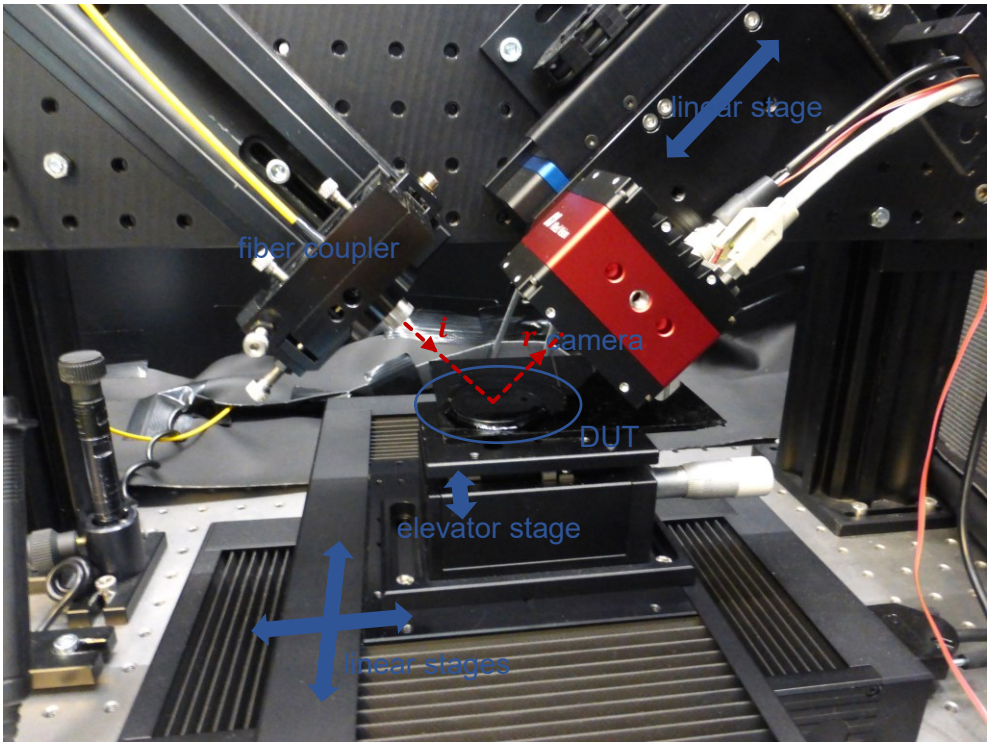

Figure 5.1: Photo of the experimental setup built up according to the sketch shown in Figure 2.2. Selected components and the path of the test beam are illustrated.

The components, used in the setup, are described in the order along the light's path. As single rays do not exist in reality, a narrow light beam represents the incident ray in the experimental setup. The light source for this light beam is a fiber coupled laser diode. Roithner Lasertechnik GmbH distributes the used laser diode *RLCS-S63*. It emits light at a wavelength of $635\ \mathrm{nm}$ and has a maximum output power of $2\ \mathrm{mW}$. The datasheet of the laser diode can be found in Appendix C. The emitted light is guided into the setup using a single mode fiber. This fiber can be seen in Figure 5.1 as the yellow covered fiber coming from the top left corner. To get a narrow collimated light beam after coupling out the light from the fiber, an adjustable aspheric collimator *CFC2-A,* manufactured by Thorlabs Inc., is used [108]. This collimator creates an output beam waist diameter of $0.36\ \mathrm{mm}$ ($\frac{1}{e^2}$ width) at a maximum distance of $203\ \mathrm{mm}$ [109]. The technical drawing of the collimator, provided by Thorlabs Inc., can be found in the Appendix D. In the experimental setup, the collimator has been adjusted to have the waist on the SUT. The beam waist diameter of $0.36\ \mathrm{mm}$ as $\frac{1}{e^2}$ width is equal to a waist diameter of

$0.212\ \mathrm{mm}$ as full width half maximum (FWHM). May the model of the Gaussian beam be applied to this beam, the Rayleigh length of

$$\frac{\pi(0.212\ \mathrm{mm})^2}{635\ \mathrm{nm}} \approx 222\ \mathrm{mm} \tag{5.1}$$

can be determined [1]. As the height deviations of the investigated SUTs are much smaller than the Rayleigh length, the beam diameter can be assumed to be constant. To adjust the position and direction of the beam, the collimator is mounted into the fiber positioner *FAPO 65*, manufactured by OWIS GmbH [110].

After being coupled-out of the fiber and collimation, the light propagates towards the DUT. The DUTs used in this work are made of material transparent to the light emitted by the laser diode. Thus, the light is partially refracted into DUT itself and may be reflected at the lower surface of the DUT. If this light is once again refracted at the SUT, it may disturb the correct detection of the reflected rays position $\boldsymbol{C}$ and $\boldsymbol{D}$. To suppress these reflections at the lower side of the DUT, the DUT itself is placed onto a piece of black glass. The gap in between the DUT and the black glass is closed using index matching liquid. Therewith, the light refracted into the DUT is transmitted into and absorbed by the black glass.

To adjust the height of the DUT in the setup, the elevator stage *HV 60N*, manufactured by OWIS GmbH, is used. Regarding Figure 2.2 and Figure 5.1, one can see that the height positioning of the DUT has an influence on the detected positions $\boldsymbol{C}$ and $\boldsymbol{D}$. With a lower positioning of the DUT, the positions are shifted in positive v-direction. With a higher positioning of the DUT, the positions are shifted in negative v-direction. In Figure 5.1, one can see that a vertical breadboard is used to mount the fiber and the detector (camera). Thus, a height adjustment can also be achieved by moving this breadboard. However, moving the breadboard leads to a realignment of the setup, especially in terms of the calibrated angles $\alpha_C^{\mathcal{M}}$ and $\beta_C^{\mathcal{M}}$. Thus, using the elevator stage overcomes in most cases the movement of the breadboard and therewith does not require a recalibration.

The positioning of the DUT to the desired positions $\tilde{\boldsymbol{x}}_i$ is performed by two linear stages that are orthogonally aligned. The two linear stages are of type *PMT160-100-DC-L-B*, manufactured by Steinmeyer Mechatronik GmbH [111]. The stages have a travel length of $100\ \mathrm{mm}$ and are screw-driven by DC motors. A linear position feedback system with a $100\ \mathrm{nm}$ resolution is integrated. To control the stages a *Galil DMC2133* controller assembled by Steinmeyer Mechatronik GmbH is used. This controller offers a position sensitive output (PSO). Therewith, an electronic signal can be send if predefined positions are reached. The manufacturer has tested the stages before delivery. The general datasheet as well as the test protocols of the stages can be found in the Appendix E.

To detect the reflected beams position in two parallel planes, as intended by the measurement method, a camera on a linear stage is used. The camera used is of type *Prosilica GT4907*, manufactured by Allied Vision Technologies GmbH. The datasheet for the camera can be found in Appendix F. The built-in sensor is a *KAI-16070* monochrome CCD image sensor manufactured by Semiconductor Components Industries, LLC [112]. This sensor has an active image size of $36\ \mathrm{mm}$ by $24\ \mathrm{mm}$ with 4864 by 3232 active pixels, resulting in a number of pixels of $15\ 720\ 448$. The pixel size is $7.4\ \mu\mathrm{m}$ by $7.4\ \mu\mathrm{m}$ and no microlenses are implemented. With these large dimensions, the sensor offers a large area to detect the reflected beam's position. Limited by the chip's size and due to other mechanical limitations, the range of detectable surface angles with this camera can be considered to be within $\pm 10°$. The maximum frame rate of the camera is $7.6\ \mathrm{fps}$. The camera transfers the data to the controlling computer using an Ethernet connection and the GigE protocol. Additionally, the camera has a *Hirose*

HR10A-10R-12PB connector. On the one hand, this connector is used for power supply of the camera, on the other hand, this connector can be used to transmit an external trigger signal to the camera. The trigger input is electronically connected to the PSO of the controller of the DUT's positioning stages. Therewith, a continuous movement of the DUT can be performed, sending triggers to the camera when predefined positions are reached. The determination of the beams position on the camera is achieved by applying a centroid detection algorithm on the camera image [113]. The centroid of a beam propagates in a straight line, even if the intensity distribution is not symmetrical [89, 114].

May $\hat{u}_g$ be the column index and $\hat{v}_g$ be the row index of the g-th pixel with the value B_g, then

$$\bar{u} = \frac{\sum_g \hat{u}_g B_g}{\sum_g B_g} 7.4\ \mu\mathrm{m} \tag{5.2}$$

and

$$\bar{v} = \frac{\sum_g \hat{v}_g B_g}{\sum_g B_g} 7.4\ \mu\mathrm{m} \tag{5.3}$$

define the centroid of the image, when $\hat{u}_g = 0$ defines the center column and $\hat{v}_g = 0$ defines the center row of the sensor. Having the centroid position $\bar{u}_i$ and $\bar{v}_i$ determined for the i-th sample point, one can define the vector

$$\boldsymbol{C}_i = \begin{pmatrix} \bar{u}_i \\ \bar{v}_i \\ w \\ 1 \end{pmatrix} \tag{5.4}$$

for the first detector position. The same is accordingly valid for the position vectors $\boldsymbol{D}_i$ for the second detector position. To overcome noise in the camera image outside of the reflected beam's spot area, an offset can be applied to the whole image data before performing the centroid determination.

To move the detector to the two different positions along the w-axis, a linear stage is used. This linear stage is of type *PLT100-100-SM-L-B* and has been manufactured by Steinmeyer Mechatronik GmbH. The travel distance of the linear stage is $100\ \mathrm{mm}$. The DC motor moves the carriage using a screw. An integrated linear position feedback returns the stage's position with a resolution of $100\ \mathrm{nm}$. Since this stage has to be stable at one position for a long time during the measurement process, a break is included. The general datasheet as well as the test protocol of the stage used in the experimental setup can be found in Appendix G.

The setup has been aligned using the breadboards used for mounting. With these alignments the angles of $\alpha_{\mathcal{C}}^{\mathcal{I}} = 90°$, $\beta_{\mathcal{C}}^{\mathcal{I}} = 0°$, $\alpha_{\mathcal{C}}^{\mathcal{M}} = 45°$, $\beta_{\mathcal{C}}^{\mathcal{M}} = 0°$ and $\gamma_{\mathcal{C}}^{\mathcal{C}} = 0°$ are targeted. Since errors are expected to be in the breadboard accuracy as well as in the alignment, these angles are expected not to be perfectly achieved in the setup. Thus, the calibration methods described before are used to determine the correct values of these angles.

The measurement process has been defined to achieve minimum measurement time. A stop-and-go movement of the DUT positioning, as performed in the simulation, has been avoided. Alternatively, a continuous movement of the DUT positioning is implemented using the PSO of the $\tilde{x}\tilde{y}$-stages controller. Having an even square grid of sample points as shown in Figure 5.2 a), a Meander track is defined using linear movements parallel to the $\tilde{y}$-axis.

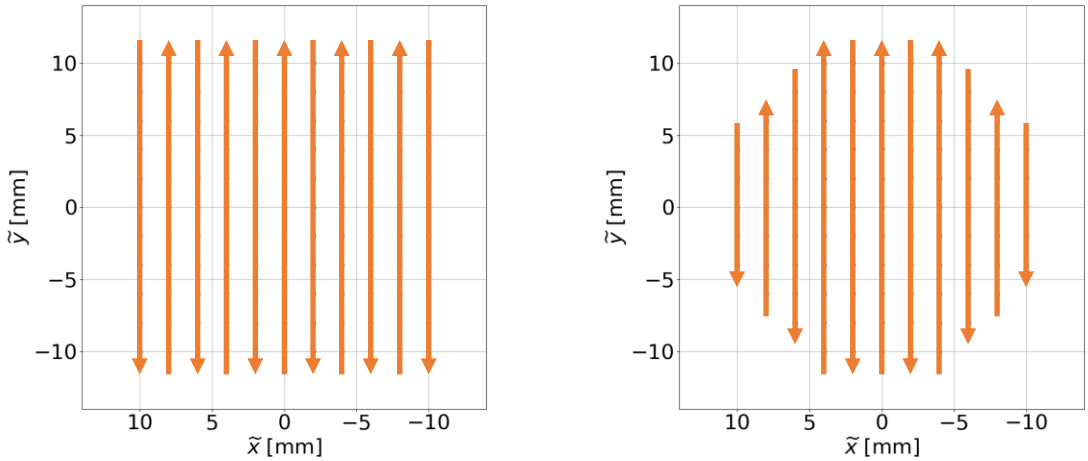

Figure 5.2: Example for a) an even square grid and b) an even circular grid. The blue dots represent the intended sample points. The orange arrows represent the Meander track used for the PSO of the $\tilde{x}\tilde{y}$-stage position.

Along the lines shown in Figure 5.2, the PSO is activated, while the $\tilde{x}$-position is constant. The traveling speed of the stage can be defined from the sample distance to achieve the maximum frame rate of $7.6\ \mathrm{fps}$ of the camera. The same is also applied to circular grids, while the length of the lines parallel to the $\tilde{y}$-axis is varied according to the number of sample points in the line, as shown in Figure 5.2 b). Using the PSO in $\tilde{y}$-direction is useful to perform cross-section measurement along this axis. Performing the cross-section measurements parallel to the $\tilde{x}$-axis leads to a shift of the sample points in $\tilde{y}$-direction when changes in the SUT's sag occur as described in Chapter 2.3.1. This leads to a non-straight line of actually investigated positions on the SUT.

5.2 Calibration

Determination of the $\tilde{x}\tilde{y}$-stages pitch

To determine the pitch of the $\tilde{x}\tilde{y}$-stages the method described in Chapter 3.6.2 is used. Therefore, the experimental setup is altered to represent a setup according to the sketch shown in Figure 3.11. This setup is shown in Figure 5.3.

Moving the $\tilde{x}\tilde{y}$-stages, leads to a direct repositioning of the reflected beams position on the camera chip. Thus, the camera chip is the limiting factor for the maximum detectable area for this investigation. Checking the maximum range possible leads to an even square sample grid with $20\ \mathrm{mm}$ length and width. The sample distance has been set to $250\ \mu\mathrm{m}$. With these parameters the positions $\boldsymbol{C}_i$ and $\boldsymbol{D}_i$ as shown in Figure 5.4 are determined.

The positions shown in Figure 5.4 only show one measurement. To suppress deviations introduced by noise, the measurement has been repeated 50 times. For every investigated stage carriage position $\tilde{\boldsymbol{x}}_i$, the mean ray vector $\bar{\boldsymbol{r}}_i$ is calculated.

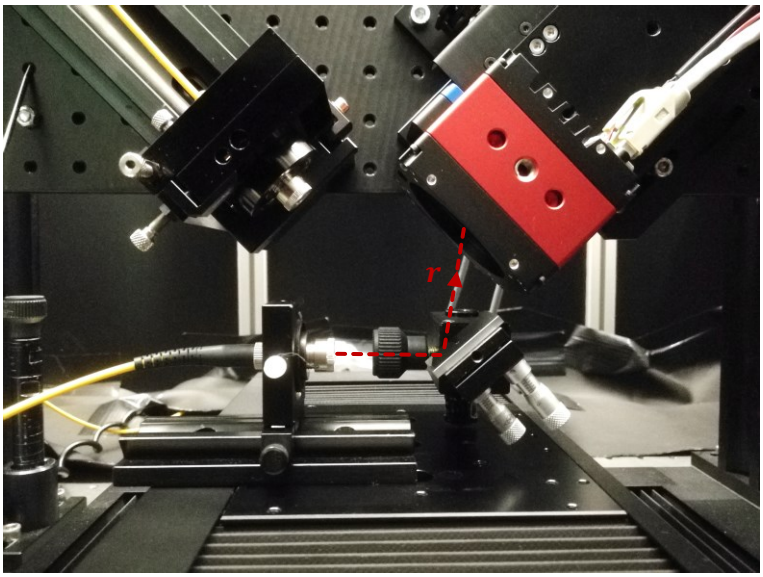

Figure 5.3: Photo of the setup to detect the pitch of the $\tilde{x}\tilde{y}$-positioning stages.

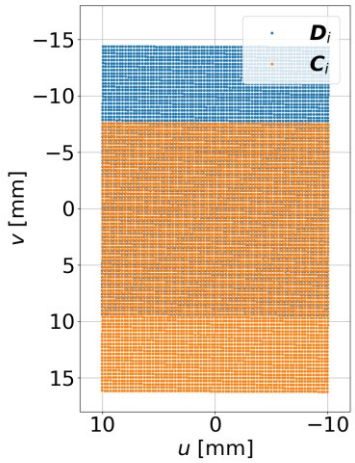

Figure 5.4: Positions $\boldsymbol{C}_i$ and $\boldsymbol{D}_i$ detected from the measurement using the setup to determine the pitch of the $\tilde{x}\tilde{y}$-positioning stages, shown in Figure 5.3.

As described in Chapter 3.6.2 only the change of these mean ray vectors is important. Therefore, the vectors are transferred into slopes

$$\tilde{p}_i = -\frac{\bar{r}_{x,i}}{\bar{r}_{z,i}} \tag{5.5}$$

and

$$\tilde{q}_i = -\frac{\bar{r}_{y,i}}{\bar{r}_{z,i}}. \tag{5.6}$$

Using Equation (3.49) and (3.50), the changes $\hat{p}_i$ and $\hat{q}_i$ of these slope data can be determined. The slope values determined from the experimental measurement for this calibration are shown in Figure 5.5.

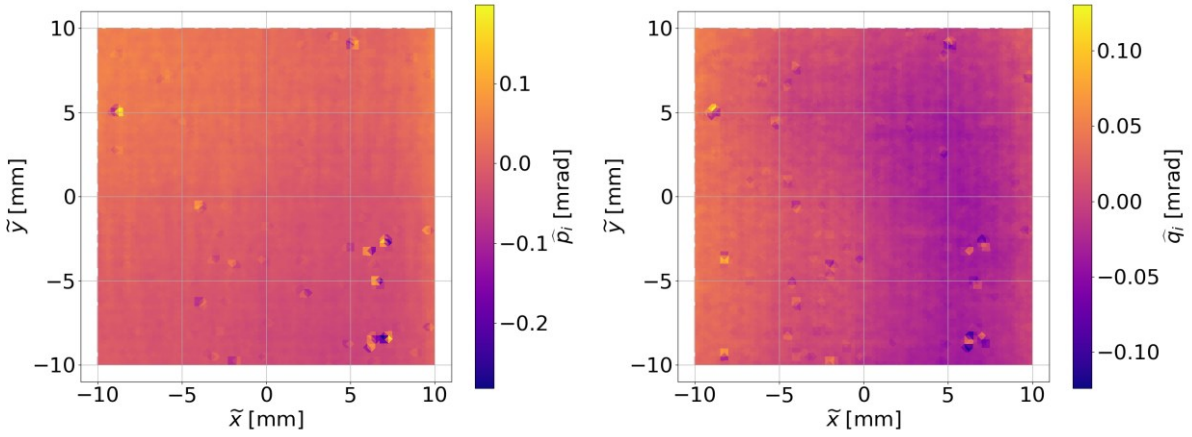

Figure 5.5: Plots showing the slopes $\hat{p}_i$ and $\hat{q}_i$ determined from the measurement performed to calibrate the $\tilde{x}\tilde{y}$-stages pitch.

Performing the fit of the first 36 Zernike polynomials in the slope domain according to Equation (3.51), the Zernike coefficient for these polynomials are derived. Using these coefficient values to reconstruct a surface according to Equation (3.34), a virtual reference surface shown in Figure 5.6 can be determined.

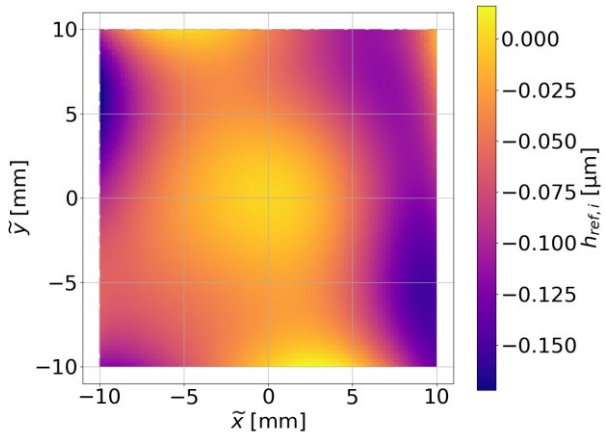

Figure 5.6: Virtual reference surface integrated from the fitted Zernike coefficients from the $\tilde{x}\tilde{y}$-stages pitch.

One could imagine to simply subtract the virtual reference surface shown in Figure 5.6 from the reconstructed surface. But, these values are not defined in the height domain initially, but in the slope domain. Corrections on the slope data to compensate the $\tilde{x}\tilde{y}$-stages pitch, also influence the determination of the SUT position in the setup. Thus, the correction of the determined slopes using the calibration data shown in Figure 5.5, is implemented after the surface normals are determined as shown in Figure 3.12 and Figure 3.13.

Combined calibration including camera rotation

The process of this calibration is described in Chapter 3.6.1. According to this process, a known surface has to be chosen to perform the combined calibration. As already said in the simulation, the DUT with the surface model according to of the polynomial freeform 1 is used here. Equivalent to the simulation, the sample has been investigated over a circular aperture

with a sample distance of $100\ \mu\mathrm{m}$ in $\tilde{x}$- and $\tilde{y}$-direction. The determined positions $\boldsymbol{C}_i$ and $\boldsymbol{D}_i$ are shown in Figure 5.22. From the calibration, the values shown in Table 5.1 are determined. These values will be used throughout all experimental measurement evaluations within this work.

Table 5.1: Determined angles derived from the combined calibration using the polynomial freeform 1 as SUT in the experimental setup.

	$\alpha_{\mathcal{C}}^{\mathcal{I}}$ [°]	$\beta_{\mathcal{C}}^{\mathcal{I}}$ [°]	$\alpha_{\mathcal{C}}^{\mathcal{M}}$ [°]	$\beta_{\mathcal{C}}^{\mathcal{M}}$ [°]	$\gamma_{\mathcal{C}}^{\mathcal{C}}$ [°]
derived	90.301519	−0.065185	45.196817	0.015259	0.299291

5.3 Description of samples and measurement parameters

5.3.1 Sample 1 – “flat surface”

As a flat surface, an aluminum wafer is used. This wafer is highly specular and is expected to have minor local height deviations, while global deviations can be expected due to stress in the material itself. A photo of this sample is shown in Figure 5.7.

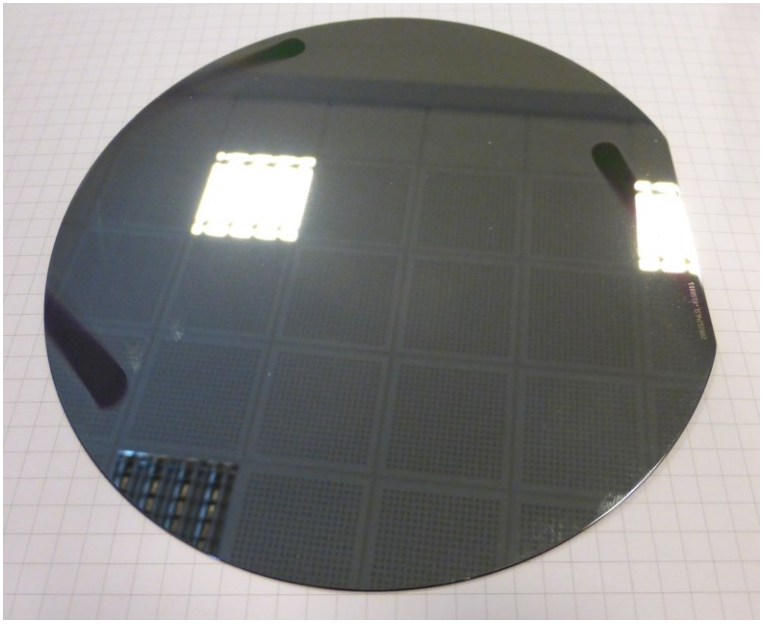

Figure 5.7: Photo of the sample “flat surface”, which is represented by a flat aluminum wafer.

This sample is the largest sample investigated here. This makes it an appropriate sample to show the ability of the proposed measurement method to investigate even large samples. It has been investigated over an even square grid of $90\ \mathrm{mm}$ by $90\ \mathrm{mm}$ size. The sample distance has been set to $1\ \mathrm{mm}$ to observe mainly the global structure of this sample.

The expected surface function

$$s(\boldsymbol{x}) = 0 \tag{5.7}$$

is rather simple. Thus, presenting the model function, as well as the model function slopes in diagrams is skipped. Unfortunately, for this sample no comparison measurement is available.

5.3.2 Sample 2 – “cylinder surface”

The cylinder surface has already been introduced in Chapter 4.1.3 for the simulation. The model function, as well as the design radius $\hat{R} = 206.7\,\mathrm{mm}$ are equivalent to the model described for the simulation. The sample used is a stock product offered by Thorlabs Inc. [115]. The sample is made of N-BK7, is uncoated and has a design focal length of $400\,\mathrm{mm}$. A photo of the sample is shown in Figure 5.8.

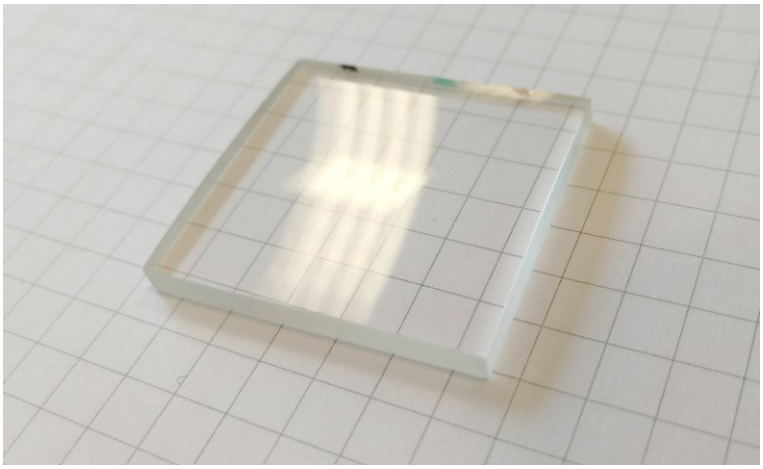

Figure 5.8: Photo of the sample “cylinder surface”.

A technical drawing and the datasheet for this sample provided by Thorlabs Inc. are available in the Appendix H.

For this sample, a comparison measurement is available. The measurement has been performed by BLF Optik Teknoloji Sanayi A.Ş. using a *MarSurf LD 260 Aspheric* manufactured by Mahr GmbH [25]. This measurement machine is a tactile surface profiler, which has been used to perform a cross-section measurement of the samples surface. The documentation of the comparison measurement can be found in Appendix I.

5.3.3 Sample 3 – “polynomial freeform 1”

Equivalent to the cylinder surface, the polynomial freeform 1 has already been described before for the simulation. The surface description can be found in Chapter 4.1.4. The sample for the experimental measurements has been manufactured by Trionplas Technologies GmbH using Atmospheric Plasma Jet Machining [116, 117]. It is made out of fused silica and is uncoated. A photo of the sample is shown in Figure 5.9.

The documentation provided by Trionplas Technologies GmbH can be found in Appendix J. In the SUT of this sample, three fiducials have been implemented. These fiducials have a diameter of approximately $1\,\mathrm{mm}$ and a depth of approximately $500\,\mathrm{nm}$. The fiducials have been implemented at three different positions in the surface as shown in Figure 5.10.

These fiducials help to orient the measurement results when comparing the measurement results from different measurements. For this sample, a comparison measurement is available. Trionplas Technologies GmbH used a *CT 300* by cyberTECHNOLOGIES GmbH to perform this comparison measurement [30]. The *CT 300* has a white light distance sensor and scans the surface with this sensor. Therewith it is categorized a non-contact surface profiler. The scan is performed in lines following a Meander path. The results of this comparison measurement can also be found in Appendix J.

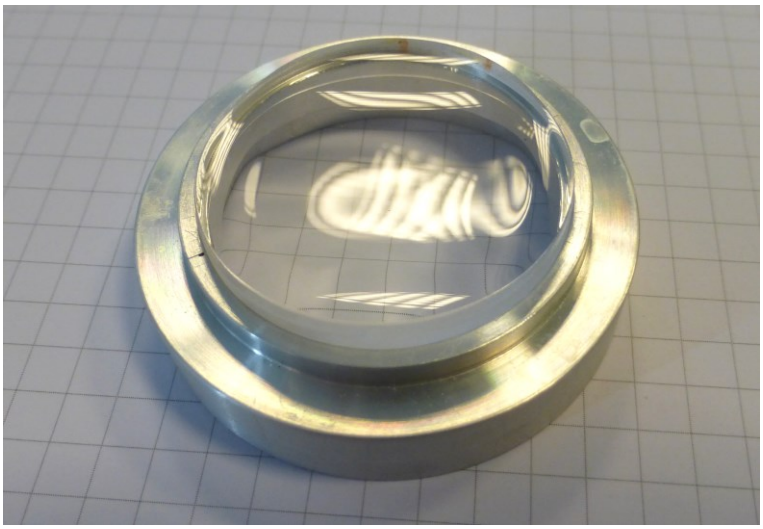

Figure 5.9: Photo of the sample “polynomial freeform 1”.

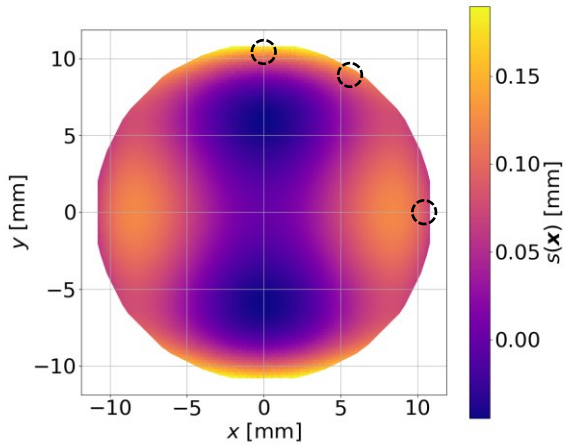

Figure 5.10: The dashed circles mark the positions of the three fiducials implemented in the SUT of the polynomial freeform 1 for the experimental measurements.

5.3.4 Sample 4 – “polynomial freeform 2”

This sample has not been described before. Equivalent to the polynomial freeform 1, this sample follows a polynomial model function. However, the model function of this sample

$$s(\boldsymbol{x}) = 2.5 \cdot 10^{-3}x^2 + 2.5 \cdot 10^{-3}y^2 - 15 \cdot 10^{-5}x^4 - 1.5 \cdot 10^{-5}y^4 \tag{5.8}$$

shows a symmetry with respect to both axis, while the function profile along both axis is also equivalent. Additionally, the surface peak-to-valley (PV) value and the maximum slope is smaller compared to the polynomial freeform 1. The surface model function and the model slopes are shown in Figure 5.11. Following the parameters of the polynomial freeform 1, this sample is also investigated over a circular aperture of $22\,\mathrm{mm}$ with a sample distance of $100\,\mu\mathrm{m}$.

The gradient field derived from the slopes, shown in Figure 5.11 c) and d), is shown in Figure 5.12.

Deriving the curl and the curl height from the discrete gradient field, the values presented in Figure 5.13 are determined.

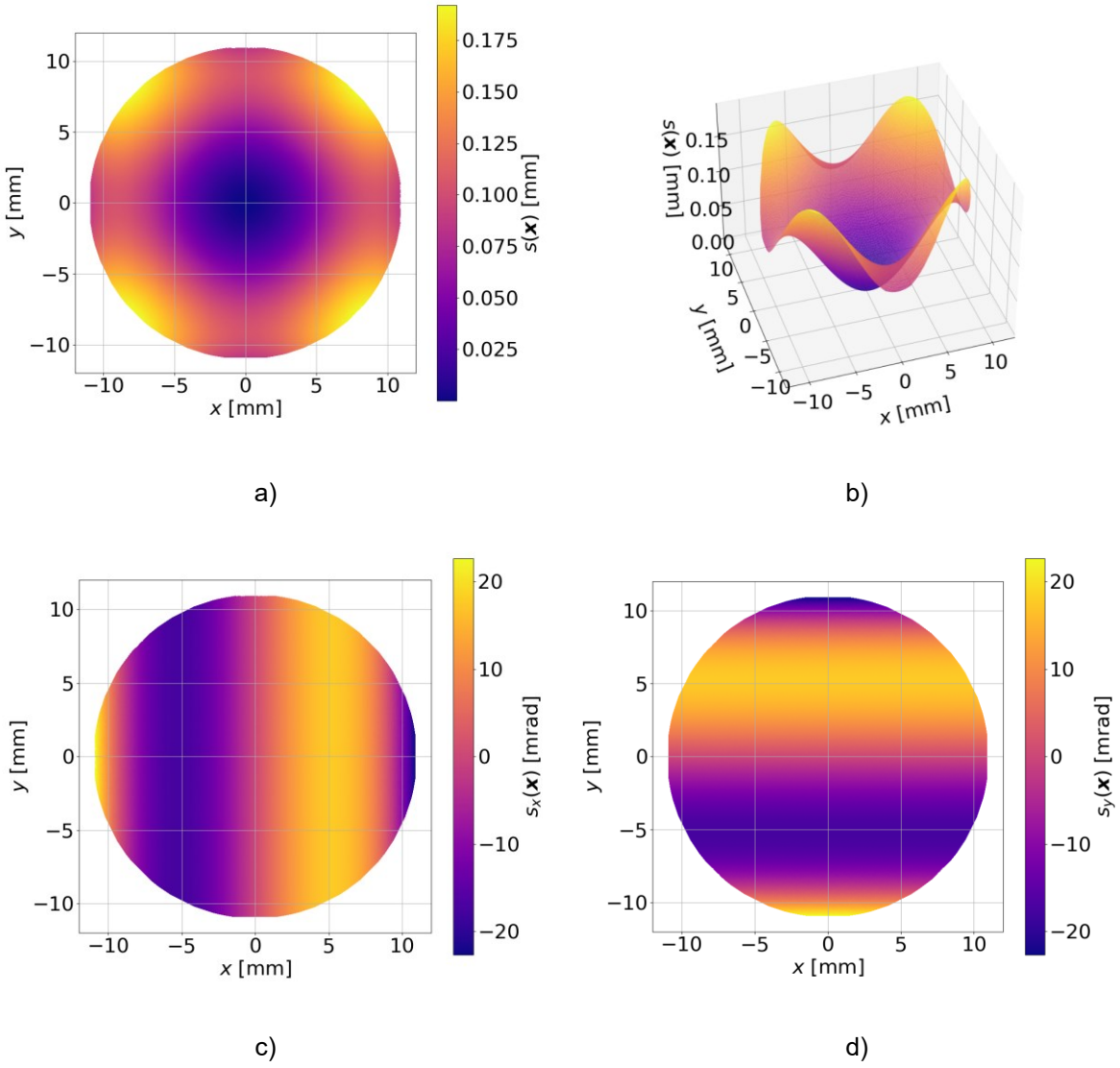

Figure 5.11: Plots presenting the polynomial freeform 2 surface. a) and b) show the surface sag in 2D and 3D. c) and d) show the surface slopes in x- and y-direction.

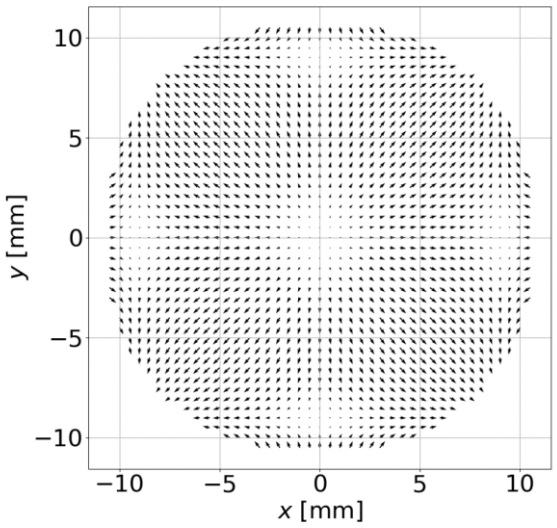

Figure 5.12: Gradient field $\boldsymbol{\zeta}(\boldsymbol{x})$ of the polynomial freeform 2.

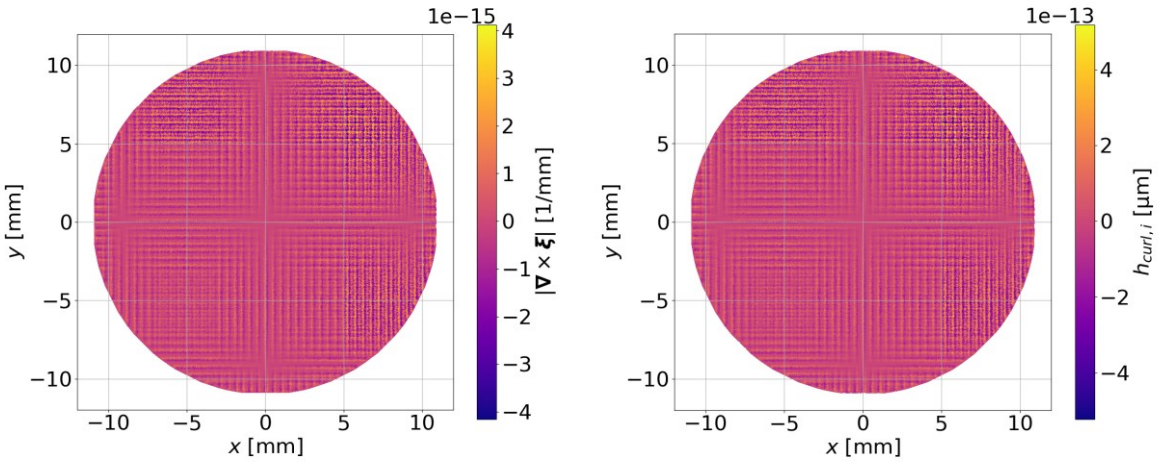

Figure 5.13: Plots presenting a) the curl and b) the curl height of the polynomial freeform 2 sampled discrete at desired positions $\tilde{\boldsymbol{x}}_i$.

Following the polynomial freeform 1, the curl height values, introduced by the discrete sampling of the surface model function, of the polynomial freeform 2 are negligibly small.

The sample for the experimental measurement has also been manufactured by Trionplas Technologies GmbH using Atmospheric Plasma Jet Manufacturing. It is also made of fused silica and is uncoated. A photo of the sample is shown in Figure 5.14.

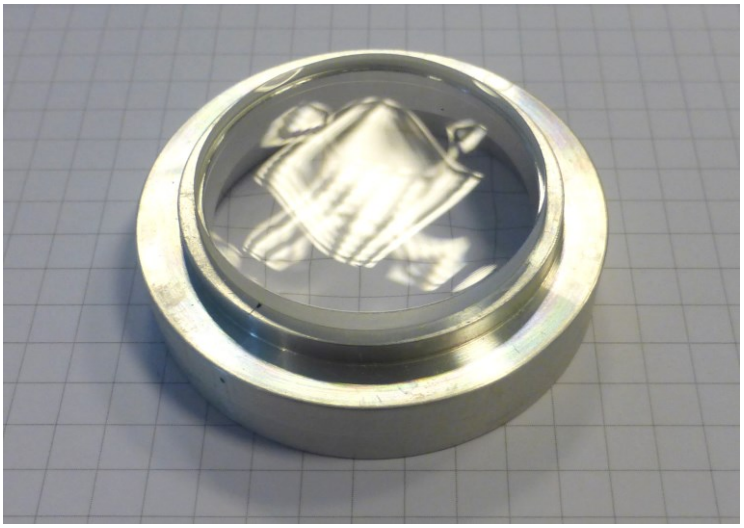

Figure 5.14: Photo of the sample “polynomial freeform 2”.

For this sample, a comparison measurement is available. This comparison measurement has been performed by Trionplas Technologies GmbH using a *LuphoScan 260 HD* manufactured by AMETEK Inc. [29]. The documentation of the sample’s manufacturer as well as the results from the comparison measurement can be found in Appendix K.

5.4 Measurement Results

The samples described before have been measured according to the procedure described in Chapter 5.1. The results of the measurements and the evaluation are presented in the following subchapters.

5.4.1 Sample 1 – “flat surface”

The flat surface, in contrast to the other samples, has been measured with an extended sample distance of $1\ \mathrm{mm}$ and an extended measurement area of $90\ \mathrm{mm}$ by $90\ \mathrm{mm}$. Since this area is much larger than the area used for the calibration of the $\tilde{x}\tilde{y}$-stages pitch, the calibration data is not used to correct the measurement data determined from this measurement. For the evaluation here it is considered that no $\tilde{x}\tilde{y}$-stages pitch exists. Except from this, the evaluation is performed according to the process for the evaluation of known surfaces described in Chapter 3.4.

The positions $\boldsymbol{C}_i$ and $\boldsymbol{D}_i$ determined from the measurement are shown in Figure 5.15. Due to limitations in the experimental setup, the positions of the detector have been set to $90\ \mathrm{mm}$ and $80\ \mathrm{mm}$.

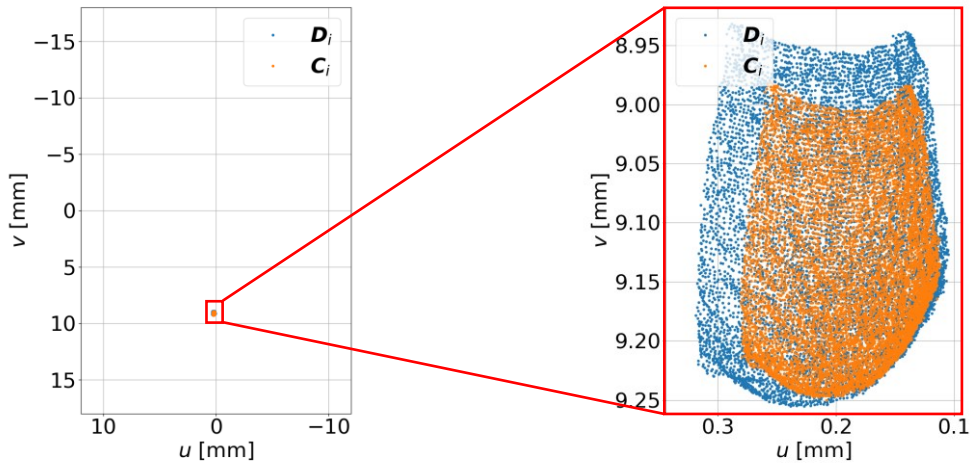

Figure 5.15: Determined positions $\boldsymbol{C}_i$, with $w = 90\ \mathrm{mm}$, and $\boldsymbol{D}_i$, with $w = 80\ \mathrm{mm}$, performing the simulation using the flat surface as SUT. The size of the diagram on the left hand side represents the dimensions of the camera chip.

Regarding Figure 5.15, one can already see that the sample has an almost flat surface, as the measured centroid positions are all close to each other. Additionally, the alignment of the setup can be considered well, as the positions $\boldsymbol{C}_i$ and $\boldsymbol{D}_i$ almost cover up completely. However, these conclusions are only made on visual observations of the centroids and only give a first impression. They cannot be taken as relevant estimations about the alignment, calibration or SUT’s surface profile.

From the determined centroid positions, the SUT’s position within the setup has be determined according to the description given in Chapter 3.4. The values derived from this determination are shown in Table 5.2. Since the sample is flat, the rotation $\gamma_{\mathcal{M}}^{\mathcal{S}}$ and the decenter $\Delta\tilde{x}_{\mathcal{M}}^{\mathcal{S}}$ and $\Delta\tilde{y}_{\mathcal{M}}^{\mathcal{S}}$ are unnecessary. Therefore, these parameters are considered ideal.

Table 5.2: Determined angles and decenter of the flat surface in the experimental setup.

	$\alpha_{\mathcal{M}}^{\mathcal{S}}$ [°]	$\beta_{\mathcal{M}}^{\mathcal{S}}$ [°]	$\gamma_{\mathcal{M}}^{\mathcal{S}}$ [°]	$\Delta\tilde{x}_{\mathcal{M}}^{\mathcal{S}}$ [mm]	$\Delta\tilde{y}_{\mathcal{M}}^{\mathcal{S}}$ [mm]
derived	0.020	180.012	0.0	0.0	0.0

Using this SUT’s position, the surface has been reconstructed. The reconstructed surface and the deviation from the model are shown in Figure 5.16.

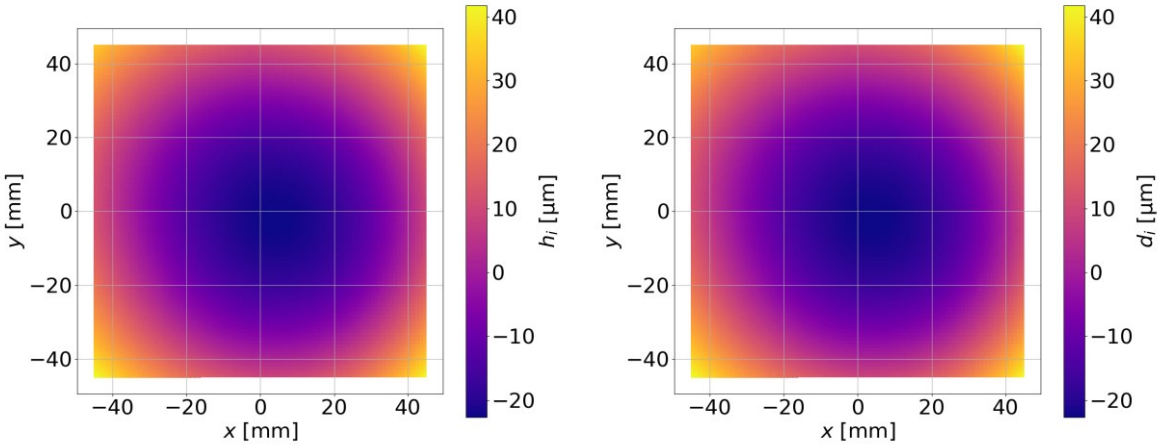

Figure 5.16: Plots presenting a) the reconstructed surface and b) its deviation from the surface model from measurement of the flat surface. For the evaluation, the surface model has been considered as known.

Regarding Figure 5.16, one can see that the two plots are identical. This is due to the surface model being flat, according to Equation (5.7). The deviations shown in Figure 5.16 have a RMS_t of $14.058\ \mu m$, where RMS_t describes the RMS of the total deviation [94]. Regarding Figure 5.16, one can see that a spherically shaped structure can be found in the surface. This structure may be introduced by stress in the aluminum wafer resulting in spherical shaped deformations [118]. Subtracting the best-fit-sphere (BFS) from these deviations leads to the value RMS_i, describing the irregularity of the determined deviation [94, 119]. From the deviations shown in Figure 5.16 b), a BFS with a radius of $31.391\ m$ is derived in a least-squares sense. Subtracting this BFS from the deviations leads to the irregularity deviations shown in Figure 5.17 a).

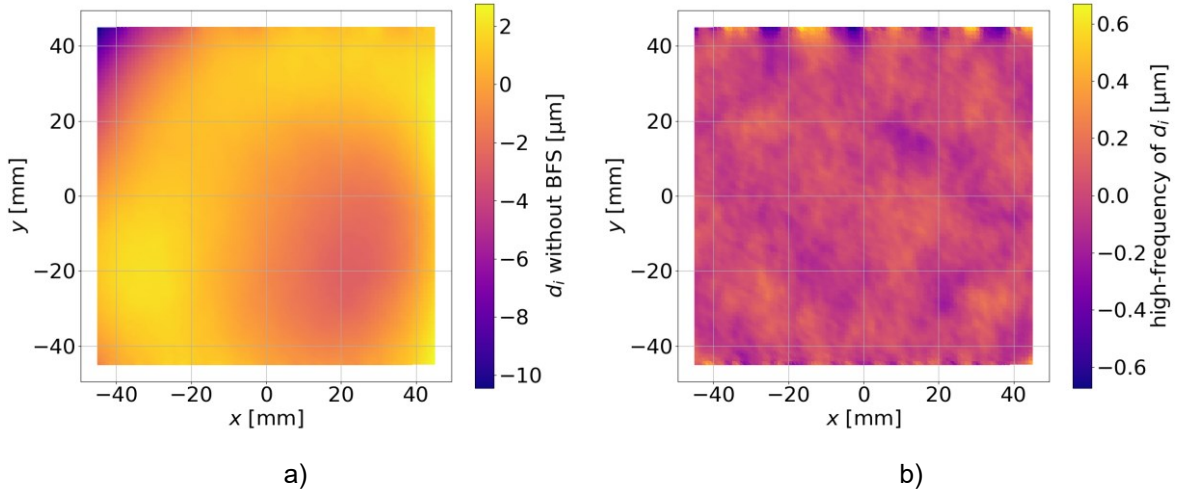

Figure 5.17: Plots presenting a) the deviations shown in Figure 5.16 b) minus a BFS with a radius of $31.391\ m$. b) shows the deviations without BFS, shown in a) minus a fit of the first 36 Zernike polynomials to subtract global deviations.

Subtracting the BFS from the determined deviations leads to a RMS_i of $1.589\ \mu m$. As described in Chapter 3.3.3, subtracting the first 36 Zernike polynomials frees the given deviations from

global structures. Fitting the first 36 Zernike polynomials in a least-squares sense to the deviations shown in Figure 5.17 a), according to Equation (3.34), leads to a set of coefficients. Subtracting the sum of the polynomials multiplied with their coefficients, leads to the high-frequency deviations shown in Figure 5.17 b). These high-frequency deviations have a RMS_{hf} of $92.5\ \mathrm{nm}$, where RMS_{hf} is the RMS of the high-frequency structures.

Since no comparison measurement is available for this sample, the results cannot be compared and discussed critically.

5.4.2 Sample 2 – "cylinder surface"

As described before, the cylinder surface is investigated performing a cross-section measurement along the fast axis of the lens. The investigated sample points $\tilde{\boldsymbol{x}}_i$ are positioned along the $\tilde{y}$-axis at $\tilde{x} = 0\ \mathrm{mm}$. The range of the cross-section is $28\ \mathrm{mm}$ and the sample distance is set to $100\ \mu\mathrm{m}$. The camera is positioned to $w = 90\ \mathrm{mm}$ and $w = 80\ \mathrm{mm}$. The determined centroid positions from this measurement are presented in Figure 5.18.

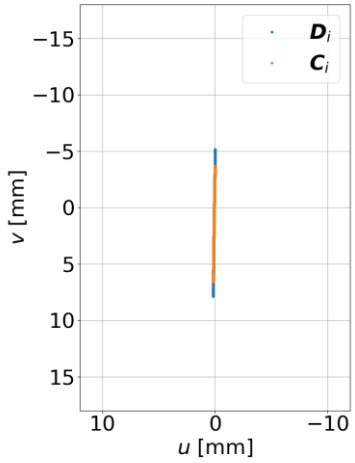

Figure 5.18: Determined positions $\boldsymbol{C}_i$, with $w = 90\ \mathrm{mm}$, and $\boldsymbol{D}_i$, with $w = 80\ \mathrm{mm}$, from the measurement of the cylinder surface. The size of the diagram represents the dimensions of the camera chip.

As described in Chapter 4.2.2, the determination of finding the position of the cylinder surface in the experimental setup reduces to the parameter $\alpha_{\mathcal{M}}^{\mathcal{S}}$ for a cross-section measurement. The other parameters are expected to be ideal. The values, to define the SUT's position determined from the positions presented in Figure 5.18, are presented in Table 5.3.

Table 5.3: Angles and decenter to define the position of the cylinder surface in the experimental setup.

	$\alpha_{\mathcal{M}}^{\mathcal{S}}$ [°]	$\beta_{\mathcal{M}}^{\mathcal{S}}$ [°]	$\gamma_{\mathcal{M}}^{\mathcal{S}}$ [°]	$\Delta\tilde{x}_{\mathcal{M}}^{\mathcal{S}}$ [mm]	$\Delta\tilde{y}_{\mathcal{M}}^{\mathcal{S}}$ [mm]
derived	0.317	180.0	0.0	0.0	0.0

With the parameters presented in Table 5.3, the surface has been reconstructed. The reconstructed surface and its deviation from the model are shown in Figure 5.19.

The deviations shown in Figure 5.19 b) have a RMS_t of $222.4\ \mathrm{nm}$. Regarding the plot in this figure, one can observe a parabolic structure on the determined deviations. This parabolic structure may be due to a deviation of the actual surface's radius from the model's radius. To determine the measured surface radius, a BFS is fitted to the reconstructed surface [119]. Fitting a BFS directly to the reconstructed surface and not to the determined deviation offers

the possibility to compare its radius to the design radius used for the model. The fit of the BFS is performed in a least-squares sense to the deviation between the BFS and the reconstructed surface. The radius determined for the BFS is $206.416\ \mathrm{mm}$. The deviation between the BFS and the reconstructed surface is shown in Figure 5.20.

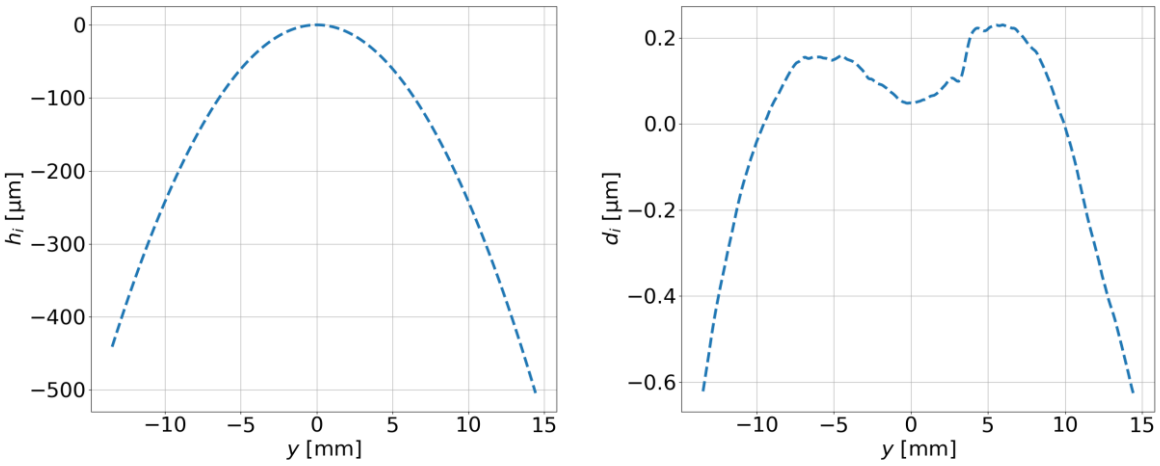

a) b)

Figure 5.19: Plots presenting a) the reconstructed surface and b) the deviation from the model for the cross-section measurement of the cylinder surface.

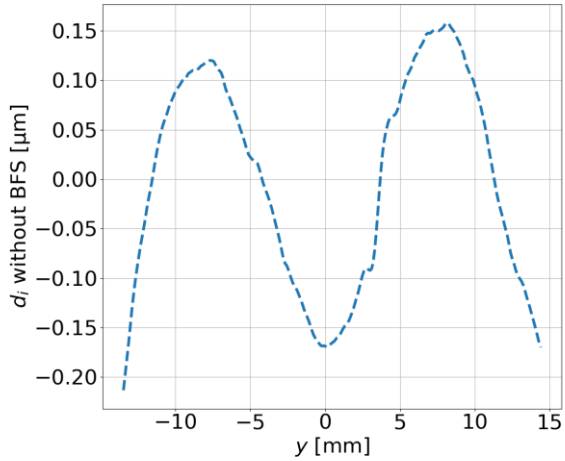

Figure 5.20: Deviation between the reconstructed surface from the cross-section measurement of the cylinder surface and the fitted BFS with a radius of $206.416\ \mathrm{mm}$.

The deviations shown in Figure 5.20 show a $\mathrm{RMS_i}$ of $107.2\ \mathrm{nm}$. As said before in Chapter 5.3.2, a comparison measurement from a tactile surface profiler is available for this sample. This comparison measurement is given as surface sag data. To compare the two measurement results, a BFS is fitted to this comparison measurement, too. This BFS has an radius of $206.497\ \mathrm{mm}$. After subtracting the BFS, the comparison measurement and the results from the proposed measurement technique are both plotted in the same diagram in Figure 5.21 a). Figure 5.21 b) shows the deviation between the proposed measurement technique and the comparison measurement.

Regarding Figure 5.21 a), one can clearly see the agreement between the measurement results. The difference shown in Figure 5.21 b) shows a RMS value of only $19.0\ \mathrm{nm}$. In combination with the agreement of the determined BFS radii, this shows that the results from

the proposed measurement technique are comparable to the results of a commercially available measurement machine performing cross-section measurements.

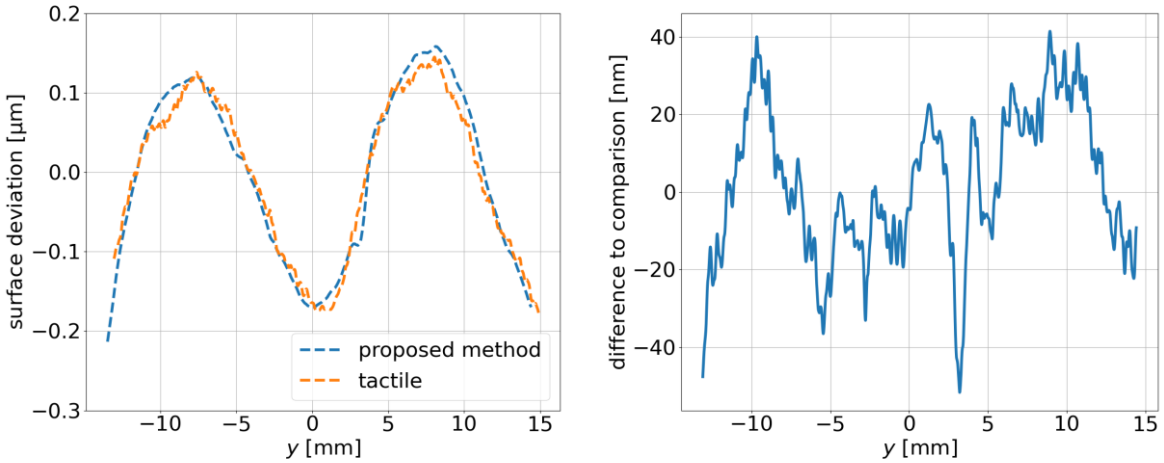

a) b)

Figure 5.21: a) Plot of the determined deviations from the proposed measurement method and the comparison measurement for the cylinder surface. b) Plot of the difference between the determined deviations shown in a).

5.4.3 Sample 3 – “polynomial freeform 1”

The measurement of the polynomial freeform 1 has been performed using an even sample grid with a sample distance of $100\,\mu\mathrm{m}$ on a circular aperture. Due to limitations by the mechanical dimensions in the experimental setup, the camera has been position to $w = 90\,\mathrm{mm}$ to determine the positions $\boldsymbol{C}_i$ and to $w = 80\,\mathrm{mm}$ to determine the positions $\boldsymbol{D}_i$. These measured centroid positions are illustrated in Figure 5.22.

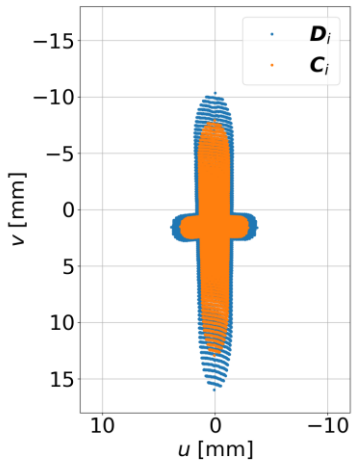

Figure 5.22: Determined positions $\boldsymbol{C}_i$, with $w = 90\,\mathrm{mm}$, and $\boldsymbol{D}_i$, with $w = 80\,\mathrm{mm}$, determined from the measurement of the polynomial freeform 1. The size of the diagram represents the dimensions of the camera chip.

Comparing the positions shown in Figure 5.22 with the positions determined from the simulations, as shown in Figure 4.17, one can see that the basic pattern can be recognized. However, misalignments in the setup and the positioning of the SUT in the experimental setup leads to deformations of this pattern. The SUT’s position determined from these positions is presented in Table 5.4.

Table 5.4: Determined angles and decenter of the polynomial freeform 1 in the experimental setup.

	$\alpha_{\mathcal{M}}^{\mathcal{S}}$ [°]	$\beta_{\mathcal{M}}^{\mathcal{S}}$ [°]	$\gamma_{\mathcal{M}}^{\mathcal{S}}$ [°]	$\Delta\tilde{x}_{\mathcal{M}}^{\mathcal{S}}$ [mm]	$\Delta\tilde{y}_{\mathcal{M}}^{\mathcal{S}}$ [mm]
derived	-0.014	180.013	-1.218	-0.004	-0.103

With this determined position and alignment of the polynomial freeform 1, the reconstructed surface and its deviation from the surface model, as shown in Figure 5.23, are derived. The deviation of the reconstructed surface from the model function has a RMS_t of $92.1\ \mathrm{nm}$.

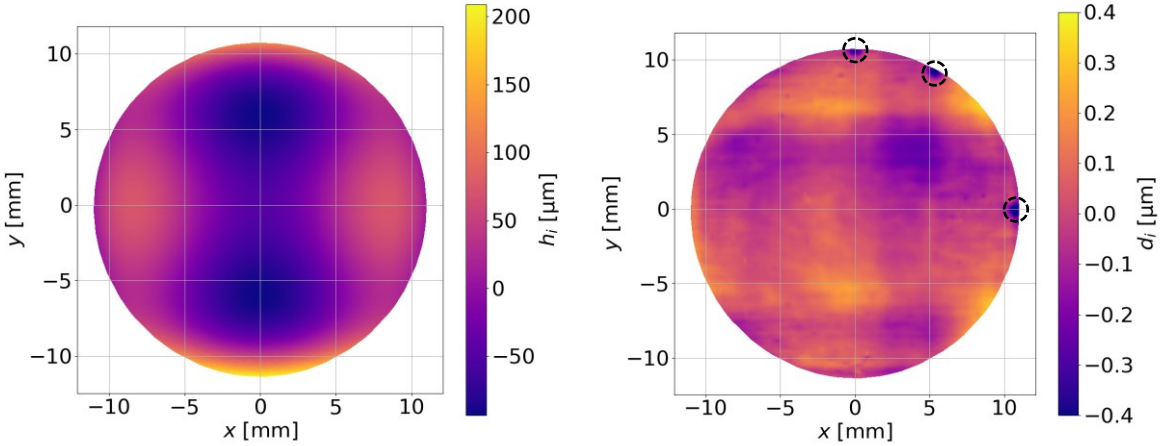

a) b)

Figure 5.23: Plots presenting a) the reconstructed surface of the polynomial freeform 1 and b) its deviation from the surface model. The implemented fiducials are marked with dashed circles and can be recognized clearly.

As described in Chapter 5.3.3, a comparison measurement of this sample is available. To compare the results from the comparison measurement with the results from the measurement performed with the proposed measurement technique, the results of the comparison measurement are linearly interpolated at the actual sample positions $\boldsymbol{I}_i$ from the proposed technique. The surface deviation determined from the comparison measurement $d_{comp,i}$ and the difference between this surface deviation and the surface deviation determined with the proposed technique are shown in Figure 5.24.

The deviations determined with the comparison measurement shown in Figure 5.24 a) has a RMS_t of $64.0\ \mathrm{nm}$. Regarding Figure 5.24 a), one can also clearly see the implemented fiducials. Also, one can recognize that these fiducials almost completely disappear in the differences plotted in Figure 5.24 b).

Regarding the Plots shown in Figure 5.23 b) and Figure 5.24 a), one can recognize the obvious horizontal deviations that can also clearly be recognized in Figure 5.24 b). However, one can also recognize the basic pattern of dips in the deviations that are represented in both plots.

Extracting the high-frequency structures from the deviations shown in Figure 5.23 b) and Figure 5.24 b) by fitting and subtracting the first 36 Zernike polynomials from the given deviations, the high-frequency deviations shown in Figure 5.25 are derived.

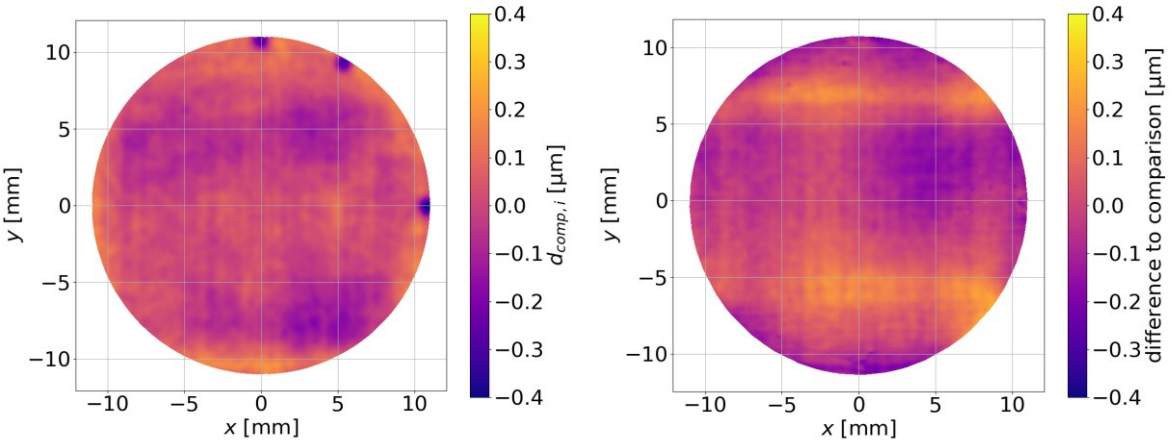

Figure 5.24: a) Plot of the deviation of the polynomial freeform 1 from the surface model, determined by the comparison measurement. b) difference between the deviation determined by the proposed measurement technique, shown in Figure 5.23 b), and the deviations shown in a).

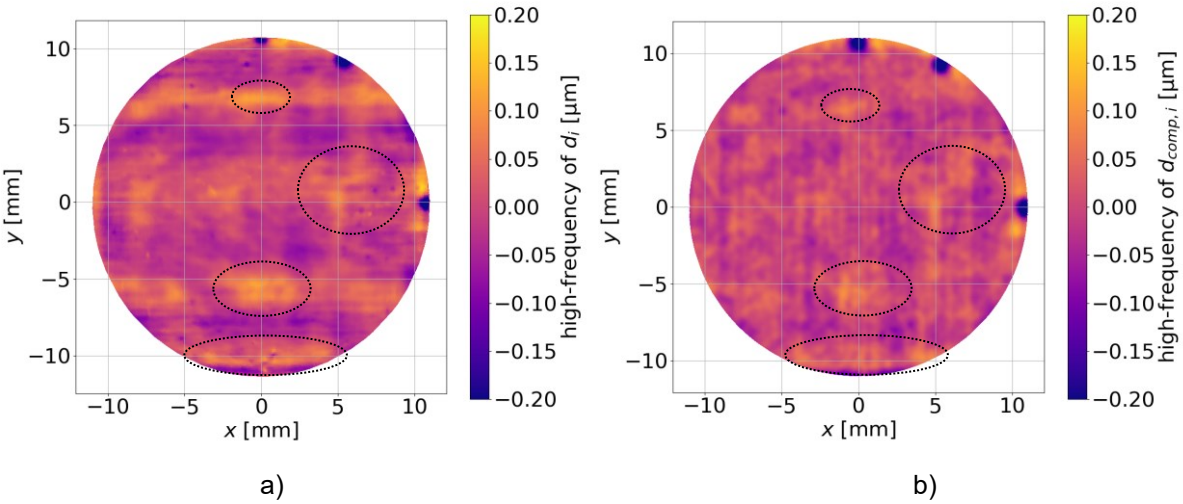

Figure 5.25: Plots presenting the high-frequency deviations of the polynomial freeform 1 from the model function a) determined with the proposed measurement technique and b) determined from the comparison measurement. The dotted circles highlight areas referenced in the text.

On the first glance, the two plots presented in Figure 5.25 seem very different. But, having a closer look offers many fine structured similarities. The four marked areas show heights that can be found in both plots, while the magnitude of these heights is higher in the plot in Figure 5.25 a). Additionally, in the plot in Figure 5.25 a), a fine arrow-like structure can be found pointing to the left parallel to the x-axis at $y = 0$ mm. This structure can only partly be found in the plot in Figure b). Overall, it can be said that both plots show similar structures, while the magnitude of these structures is larger with the proposed measurement method.

5.4.4 Sample 4 – “polynomial freeform 2”

The sample with this SUT, manufactured following the polynomial freeform 2 model function, is closely related to the polynomial freeform 1. Thus, it has been measured using the same

sample points $\tilde{\boldsymbol{x}}_i$ being defined over a circular even grid with $22\,\mathrm{mm}$ diameter and a sample distance of $100\,\mu\mathrm{m}$. Equivalently the camera has been positioned to $w = 90\,\mathrm{mm}$ and $w = 80\,\mathrm{mm}$, too. The positions $\boldsymbol{C}_i$ and $\boldsymbol{D}_i$ detected within the measurement are shown in Figure 5.26.

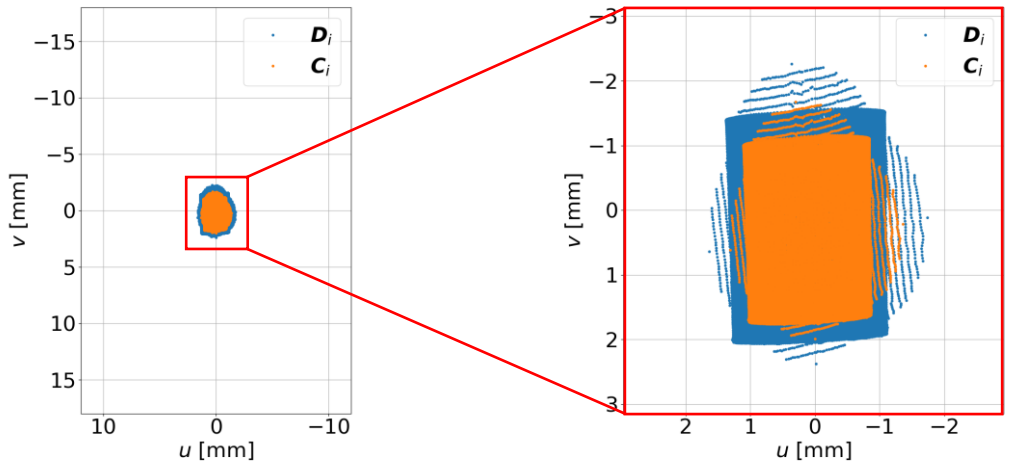

Figure 5.26: Determined positions $\boldsymbol{C}_i$, with $w = 90\,\mathrm{mm}$, and $\boldsymbol{D}_i$, with $w = 80\,\mathrm{mm}$, determined from the measurement of the polynomial freeform 2. The size of the diagram on the left hand side represents the dimensions of the camera chip.

From these detected centroid positions, the orientation and position of the SUT in the experimental setup has been determined to be as shown in Table 5.5.

Table 5.5: Determined angles and decenter of the polynomial freeform 2 in the experimental setup.

	$\alpha_{\mathcal{M}}^{\mathcal{S}}$ [°]	$\beta_{\mathcal{M}}^{\mathcal{S}}$ [°]	$\gamma_{\mathcal{M}}^{\mathcal{S}}$ [°]	$\Delta\tilde{x}_{\mathcal{M}}^{\mathcal{S}}$ [mm]	$\Delta y_{\mathcal{M}}^{\mathcal{S}}$ [mm]
derived	0.117	180.029	−2.143	0.136	−0.067

The deviation of $\gamma_{\mathcal{M}}^{\mathcal{S}}$, shown in Table 5.5, from the expected value is relatively large in comparison to the deviation of $\alpha_{\mathcal{M}}^{\mathcal{S}}$ and $\beta_{\mathcal{M}}^{\mathcal{S}}$ from their expected values. The influence of $\gamma_{\mathcal{M}}^{\mathcal{S}}$ can already be seen regarding the zoomed cutout in Figure 5.26. The tilted lines of determined positions are due to the tilt of the SUT in the experimental setup. With the determined position and orientation, the surface has been reconstructed. The reconstructed surface itself is shown in Figure 5.27 a). The deviation from the expected surface model is shown in Figure 5.27 b).

The deviation of the reconstructed surface from the surface model, as shown in Figure 5.27 b), has a $\mathrm{RMS_t}$ of $76.4\,\mathrm{nm}$.

Equivalently to the polynomial freeform 1, a comparison measurement of the surface from a commercially available measurement machine is available. Details about the measurement machine can be found in Chapter 5.3.4. This comparison measurement has been performed on a different sample grid with smaller sample distance than the measurement performed with the proposed measurement technique. To make the two measurement results comparable, a linear interpolation has been performed over the comparison measurement. The deviation from the model function determined within the comparison measurement is shown in Figure 5.28 a). These deviations show a $\mathrm{RMS_t}$ of $42.5\,\mathrm{nm}$.

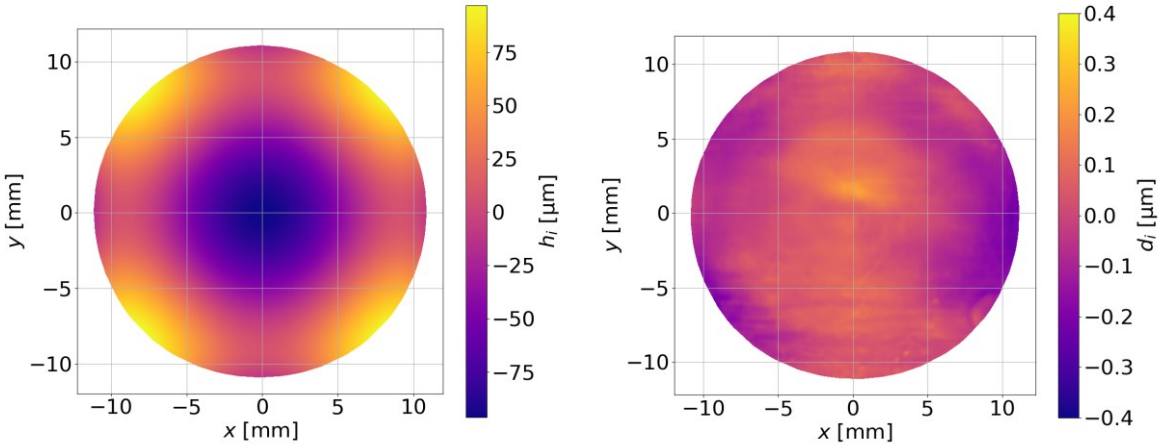

a) b)

Figure 5.27: Plots presenting a) the surface of the polynomial freeform 2, reconstructed with the proposed measurement technique, and b) its deviation from the surface model.

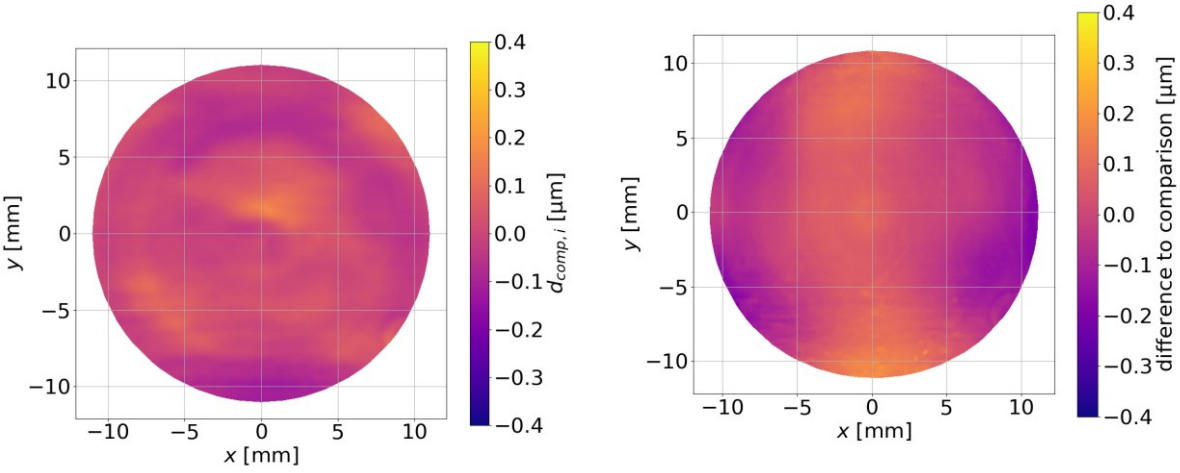

a) b)

Figure 5.28: a) Plot of the deviation of the polynomial freeform 2 from the surface model, determined by the comparison measurement. b) difference between the deviation determined by the proposed measurement technique, shown in Figure 5.27 b), and the deviations shown in a).

Regarding the difference between the surface deviations determined with the proposed measurement technique and the comparison measurement, shown in Figure 5.28 b), one can observe a global height along the y-axis. This height has been determined with the proposed measurement technique, but not with the comparison measurement. This difference lead to the deviation of the RMS_t-values. However, one can also see similar deviations in both results. For example, the striking peak in the middle of the sample has been detected by both measurement techniques and therewith disappears in the comparison.

To observe the high-frequency deviations of the deviations shown in Figure 5.27 b) and Figure 5.28 b), the fit of the first 36 Zernike polynomials is subtracted from these deviations separately. These high-frequency deviations are shown in Figure 5.29.

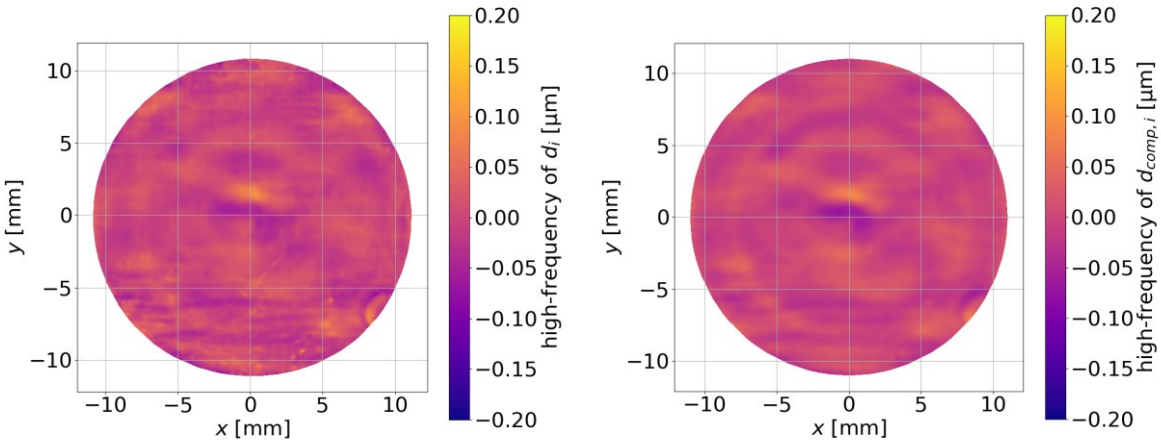

Figure 5.29: Plots presenting a) the high-frequency deviations of the polynomial freeform 2 from the model function determined with the proposed measurement technique and b) the high-frequency deviations of the same sample determined from the comparison measurement.

Comparing the two plots shown in Figure 5.29, one can see many similarities in the high-frequency deviations determined with both measurement techniques. It can be recognized that the deviations from the comparison measurement, shown in Figure 5.29 b), seems to be blurred. This may be due to filters applied to the measurement results. However, to observe the differences in the high-frequency deviations, the two results are subtracted from each other. The remaining differences are shown in Figure 5.30.

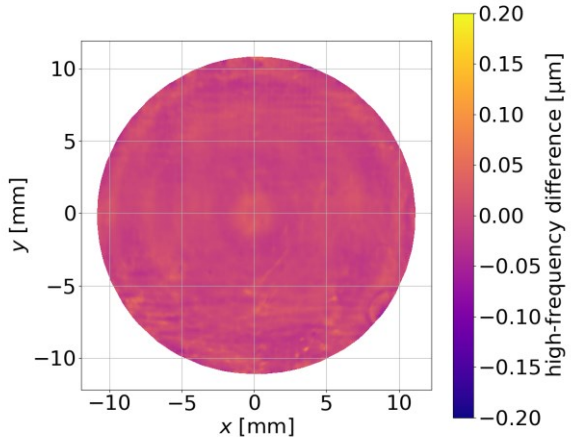

Figure 5.30: Difference of the high-frequency deviations between the results of the proposed measurement technique and the comparison measurement for the polynomial freeform 2.

Regarding the differences shown in Figure 5.30, one can observe that many of the structures shown in both plots in Figure 5.29 disappeared. This shows that the detected high-frequency structures determined from both measurement techniques are very similar. This can also be seen, regarding the RMS of the high-frequency difference shown in Figure 5.30, which is only 10.0 nm.

5.4.5 Analysis on integration parameter ρ

In Chapter 3.3.1, the 2D integration using RBFs according to Ettl et al. has been described [88]. This integration method uses the Wendland function as basis function, which has a limited support radius ρ. This radius defines the “width” of the RBF. With a larger ρ-value one RBF covers more sample points, with a smaller ρ-value it covers less sample points. Therewith, with smaller ρ-values, more local details can be reconstructed, while larger ρ-values lead to a more stable reconstruction when noisy slope data are expected [87]. However, certain limits in both directions exist. If the ρ-value is reduced too far, the interpolation matrix $\mathbf{A}$ defined in Equation (3.18) becomes an identity matrix and the reconstructed surface consists of narrow peaks at the given sample points. If the ρ-value is increased too far, the matrix $\mathbf{A}$ becomes singular showing similar values for each element.

To observe the stability of the reconstruction method, one reconstruction has been performed multiple times with varying ρ-values. Therefore, the dataset of the experimental measurement of the polynomial freeform 1 has been used exemplarily. To observe the influence of the ρ-value on the reconstruction, the value of ρ has been changed from $\rho = 2.0\,\mathrm{mm}$ to $\rho = 40.0\,\mathrm{mm}$ in steps of $1.0\,\mathrm{mm}$. As indicator of the influence of the ρ-value on the reconstruction, the RMS_t-value of each reconstructed surface is observed. The determined RMS_t-values from the reconstruction with different ρ-values are shown in Figure 5.31.

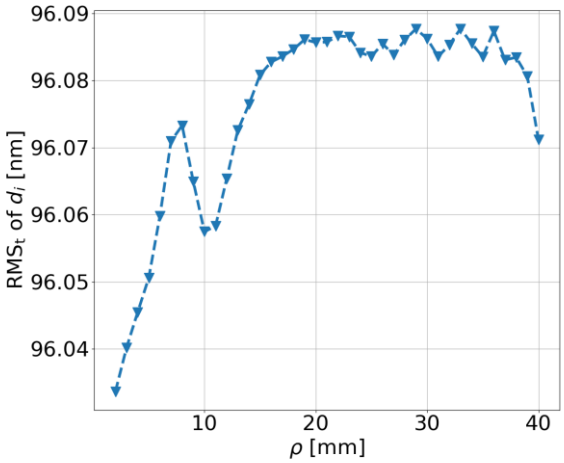

Figure 5.31: Plot of the determined RMS surface deviations for the reconstruction of the polynomial freeform 1 from the experimental measurement. Different values of ρ for the RBF reconstruction method are used.

Regarding Figure 5.31, one can observe two regions of different instabilities. In the region below $\rho = 16.0\,\mathrm{mm}$, the RMS_t-value changes fast, when small changes in the ρ-value are made. In the region above $\rho = 23.0\,\mathrm{mm}$ an oscillating instability of the RMS_t-value can be observed. Although, these changes and oscillations are within a range of only about $50\,\mathrm{pm}$, this observation led to the definition of $\rho = 20.0\,\mathrm{mm}$ for the reconstruction in the simulations and the experimental measurements.

5.5 Performance analysis

5.5.1 Instrument Transfer Function

One of the parameters to define measurement techniques is the instrument transfer function (ITF) [120]. The ITF describes the response of the measurement technique to different spatial wavelengths on the investigated surface. It is defined as the relation between the detected measurement value to the given ground truth. This relation is investigated for varying spatial

wavelengths. The ITF is therewith closely related to the well-known optical transfer function (OTF) and modulation transfer function (MTF) in the field of imaging optics [121].

In terms of the proposed measurement technique, the ITF is defined as the relation between the determined surface slope at a certain position, over the given surface slope of a sinusoidal surface topography with a the spatial wavelength λ_s. To determine this relation, simulations are used. The simulations performed before have used single ray tracing to determine the surface slope. However, this includes the assumption of the beam having an infinitely small diameter. With this, the slope at a certain position will always be detectable perfectly. Thus, another approach has to be found to determine the ITF.

The simulation setup to determine the ITF is shown in Figure 5.32.

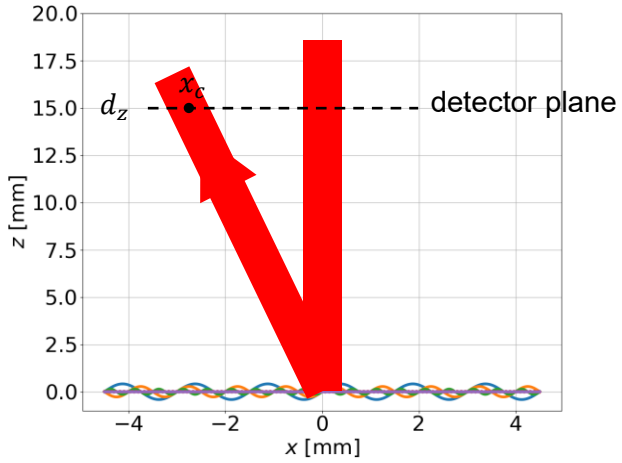

Figure 5.32: Sketch of simulation setup for the determination of the ITF. The red lines represent the incident and the reflected beam. The reflected beam's centroid position on the detector plane is illustrated by x_c. Sinusoidal surface topographies are illustrated at $z = 0$ with different spatial wavelengths. The surfaces shown in the sketch are exemplary and not scaled.

Regarding the sketch shown in Figure 5.32, one can recognize a beam propagating onto the SUT vertically. The SUT follows a sinusoidal function

$$s(x) = \frac{\hat{A}}{2} \sin\left(\frac{x \cdot 2 \cdot \pi}{\lambda_s}\right), \tag{5.9}$$

where λ_s represents the spatial wavelength and

$$\hat{A} = \frac{\hat{m}\lambda_s}{\pi} \tag{5.10}$$

defines the amplitude of the surface, so that its slope

$$\left.\frac{\partial s(x)}{\partial x}\right|_{x=0} = \hat{m} \tag{5.11}$$

at the center position can be set by the parameter $\hat{m}$. In the simulations performed here, this parameter is set to be $\hat{m} = \tan\left(\frac{\pi}{180}\right)$ and is therewith the equivalent of a surface angle of $1°$. Using Equation (5.10) and (5.9), the surface can now be defined for any spatial frequency with a constant surface angle of $1°$ at $x = 0$.

To perform the simulation, Fourier optics is applied. Instead of a single ray representing a beam, it is now defined by intensity and phase distribution [1]. Using a nearfield propagation

algorithm, this intensity and phase distribution can be propagated along a certain axis [122]. As expected from a reflection, the beam's phase is set to $2s(x)$ at $z = 0$. The intensity distribution is considered Gaussian with a half width $\hat{w}_0$. Initially, this half width is set to $\hat{w}_0 = 0.106\ \mathrm{mm}$ as this is the expected beam's half width on the SUT as described in Chapter 5.1. This beam is now propagated along the z-axis to the detector plane at $d_z = 15.0\ \mathrm{mm}$ as shown in Figure 5.32. At the detector plane, the centroid position x_c of the determined intensity distribution is calculated [113]. From this centroid position, the surface slope

$$m = \tan\left(\frac{\arctan\left(\frac{x_c}{d_z}\right)}{2}\right) \tag{5.12}$$

can be determined. Having the slope value $m(\lambda_s)$ determined for a certain spatial wavelength, the

$$ITF(\lambda_s) = \frac{m(\lambda_s)}{\hat{m}} \tag{5.13}$$

can now be defined as the relation between the determined slope value and the expected slope value. Performing the simulation for multiple spatial wavelengths between $10\ \mu\mathrm{m}$ and $100\ \mathrm{mm}$, the ITFs for different beam half widths $\hat{w}_0$, shown in Figure 5.33, are determined.

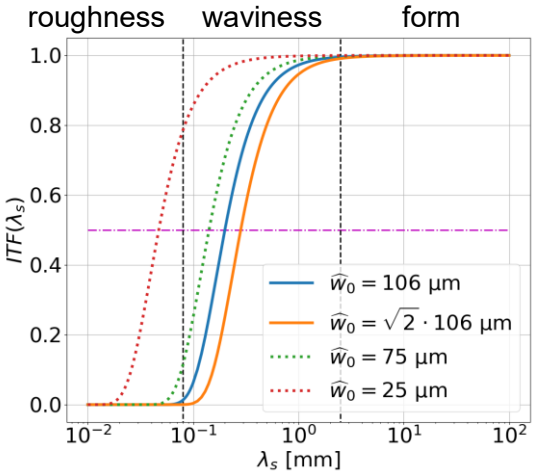

Figure 5.33: ITF's determined for different beam half widths $\hat{w}_0$ over spatial wavelengths between $0.01\ \mathrm{mm}$ and $100\ \mathrm{mm}$. Vertical dashed lines separate the three different surface characteristics roughness, waviness and form. To determine the cutoff wavelength, a horizontal dashed and dotted line is drawn at $ITF = 0.5$.

In Figure 5.33, multiple ITFs are shown. The first ITF depicted by the blue continuous line, shows the ITF for the expected beam half width of $\hat{w}_0 = 106\ \mu\mathrm{m}$. However, regarding Figure 5.32, one can see that the incident beam is here simulated perpendicular on the SUT. In the experimental setup, this is valid for the beam regarded in $\tilde{x}$-direction. Regarding the beam's $\tilde{y}$-direction, the beam is coming under an angle of $45°$. Thus, its beam width on the SUT is increased by the factor of $\sqrt{2}$. Therefore, the orange continuous line with a beam half width $\hat{w}_0 = \sqrt{2} \cdot 106\ \mu\mathrm{m}$ is shown, representing the ITF in $\tilde{y}$-direction. Regarding these two graphs, one can see that they are both almost at $ITF = 1.0$ within the spatial bandwidth of the form. Within the bandwidth of the waviness, both graphs drop to almost $ITF = 0$, where they stay also with the bandwidth of the roughness. This shows that form deviations can be reconstructed, while roughness is not detectable with the given incident beam. The explanation for this can be found in the width $\hat{w}_0$. While the beam only covers the rising slope of the

sinusoidal surface topography for large spatial wavelengths, it covers more and more of the whole period of the sinusoidal structure with decreasing spatial wavelength. When the beam even covers multiple periods of the sinusoidal structure, it is almost orthogonally reflected. According to DIN EN ISO 25178-604, the cutoff-wavelength is defined at the point, where the ITF reaches $50\ \%$ [120]. This means that wavelengths shorter than this cutoff-wavelength are considered not to be detectable. In Figure 5.33 a horizontal line is drawn at $ITF = 50\ \%$. Determining the cutoff frequency for the four beam half widths shown in the Figure, the cutoff-wavelengths presented in Table 5.6 are determined.

Table 5.6: Determined cutoff-wavelengths of the ITF for the different beam half widths presented in Figure 5.33.

$\hat{w}_0$ [µm]	cutoff-wavelength [µm]
106	200.2
$\sqrt{2} \cdot 106$	282.4
75	141.5
25	47.1

Regarding the values presented in Table 5.6, one can see that the shortest wavelength to be detectable with the given setup is $200.2\ \mu\mathrm{m}$. The sample distance used in the experimental measurements (except for the flat surface) is $100\ \mu\mathrm{m}$. Thus, the Nyquist theorem for spatial wavelengths at the cutoff-wavelength is satisfied [123].

Additionally, two more exemplary beam half widths are presented in Figure 5.33 and Table 5.6. In Figure 5.33, the green dotted line shows the ITF of a beam with a half width of $\hat{w}_0 = 75\ \mu\mathrm{m}$. The red dotted line shows the ITF of a beam with $\hat{w}_0 = 25\ \mu\mathrm{m}$. Regarding the graphs in Figure 5.33 and the determined cutoff-wavelengths in Table 5.6, one can see that a decrease of the beam width, leads to more spatial wavelengths to be detectable. For a beam half width of $\hat{w}_0 = 25\ \mu\mathrm{m}$, the cutoff-wavelengths has even been determined to be in the bandwidth of roughness.

5.5.2 Measurement time

The measurement time is a crucial factor for the commercial compatibility of a measurement machine. Thus, a short measurement time has to be achieved. To observe different measurement procedures, a simple sample grid as shown in Figure 5.34 is observed.

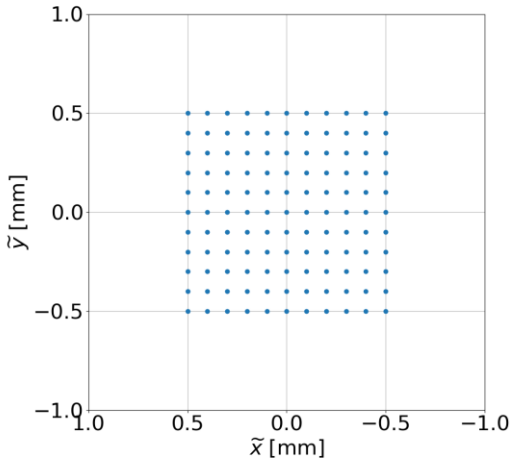

Figure 5.34: Sample grid used for the evaluation of the measurement speed of different measurement processes.

The sample grid is an even square grid with a sample distance of $100\ \mu\mathrm{m}$ and a aperture of $1\ \mathrm{mm}$. It contains 121 sample points distributed over 11 rows and 11 columns. To gather all necessary data for the evaluation for each sample point $\tilde{\boldsymbol{x}}_i$ the position $\boldsymbol{C}_i$ and $\boldsymbol{D}_i$ has to be detected. Three different processes to gather these data are compared here.

The first process is the one described in the flowchart presented in Figure 4.11. It includes the positioning of the SUT at the positions $\tilde{\boldsymbol{x}}_i$ one by one to determine the positions $\boldsymbol{C}_i$. After moving the detector to the second position, once again the SUT is positioned to the positions $\tilde{\boldsymbol{x}}_i$, to determine the positions $\boldsymbol{D}_i$.

The second process to evaluate is closely related to the first process, but instead of determining the positions $\boldsymbol{C}_i$ and $\boldsymbol{D}_i$ serially, they are determined in parallel. Moving to the SUT to a position $\tilde{\boldsymbol{x}}_i$ both positions $\boldsymbol{C}_i$ and $\boldsymbol{D}_i$ are determined by staying at the position $\tilde{\boldsymbol{x}}_i$ and moving the detector.

The third evaluated process is the one used for the experimental measurements. It uses the PSO of the $\tilde{x}\tilde{y}$-stage's controller to trigger the camera, while moving the SUT continuously as described in Chapter 5.1.

To evaluate the different processes, the following values for the needed times are determined. Moving the SUT by a distance of $100\ \mu\mathrm{m}$ and stop takes $1.0\ \mathrm{s}$. Taking a single image takes $0.5\ \mathrm{s}$. Moving the camera by a distance of $10\ \mathrm{mm}$ and stop takes $2.5\ \mathrm{s}$. Moving the SUT continuously while using the PSO to trigger the camera a framerate of $7\ \mathrm{fps}$ can be achieved.

The movement of all stage to reach the initial position is neglected. The determined times needed for the measurement of the given sample grid with the different processes are presented in Table 5.7.

Table 5.7: Measurement times determined for the three different measurement process types described before.

process type	time needed [s]
1	365.5
2	484.0
3	62.2

Regarding the values in Table 5.7, one can clearly see that using the PSO and moving the SUT continuously, achieves the lowest measurement time. This is due to the long time needed for the stop-and-go sampling used in the other two process types. However, even the measurement time of the process type 3 can be improved. The most time consuming element here is the low framerate of the camera. Improving this, even lower measurement times can be achieved.

6. Error analysis

6.1 Error Sources

In contrast to simulations, experimental setups have limited accuracy and stability due to imperfections, misalignments and noise. The impact of these influences are generally donated as measurement errors [124]. To estimate these measurement errors and their influence on the measurement results, the following error sources are investigated:

- centroid uncertainty and drift
- positioning uncertainty of the w-stage
- pitch and yaw of the w-stage
- straightness and flatness of the w-stage
- positioning uncertainty of the $\tilde{x}\tilde{y}$-stages
- pitch and yaw of the $\tilde{x}\tilde{y}$-stages
- straightness and flatness of the $\tilde{x}\tilde{y}$-stages
- calibration errors due to SUT deviations

Error sources that are not investigated, as no information is available about these error sources, are:

- roll of w-stage
- roll of the $\tilde{x}\tilde{y}$-stages
- non-orthogonality of the $\tilde{x}\tilde{y}$-stages
- inaccuracies of the camera chip

The information about the magnitude of the error sources defined above either is taken from datasheets or test protocols or is measured in the measurement setup itself. The error sources and, if available their magnitude, will be described in the following subchapters.

Centroid uncertainty and drift

The centroid stability and drift are two different error sources both influencing the centroid position. The centroid uncertainty is the expected stochastic change of the centroid position due to noise. Dark current, shot noise and centroid instability of the incident beam are included in this noise [125]. Additionally, fluctuations in the air in the measurement setup, as well as vibrations can also influence the centroid uncertainty. The centroid uncertainty can be interpreted as a high frequency change of the centroid position. It will be donated by the two values σ_u and σ_v describing the standard deviation of the centroid uncertainty in u- and v-direction in the camera chip as shown in Figure 6.1.

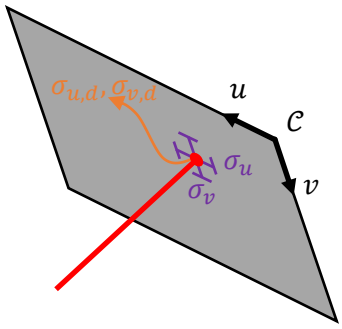

Figure 6.1: Sketch to illustrate the centroid uncertainty and drift. The uncertainty bars at the point, where the incident ray intersects with the detector plane, illustrate the centroid uncertainty σ_u and σ_v. The orange arrow illustrates the centroid drift $\sigma_{u,d}$ and $\sigma_{v,d}$.

The drift of the centroid in u- and v-direction will be donated as $\sigma_{u,d}$ and $\sigma_{v,d}$. This drift is mostly caused by environmental influences. Temperature changes stretch and contract the elements in the setup. The drift will not be given as an uncertainty, but as a change over time [126]. Both uncertainty and drift values are determined experimentally as presented in Chapter 6.2.

Positioning uncertainty of the w-stage

The positing of the detector along the w-axis underlies the uncertainty of the positioning of the w-stage. Although, the w-stage is equipped with a feedback system, the actual positioning has a certain uncertainty. This uncertainty applies to both detector positions. Its magnitude is donated σ_w. The uncertainty is illustrated in Figure 6.2.

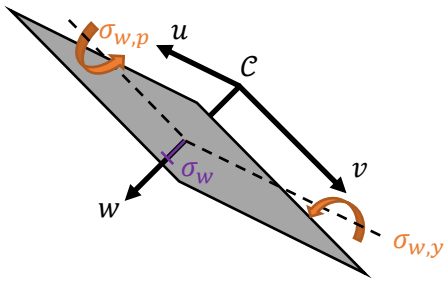

Figure 6.2: Sketch to illustrate the influence of the positioning uncertainty σ_w, the pitch $\sigma_{w,p}$ and the yaw $\sigma_{w,y}$ of the w-stage on the detector plane.

The magnitude of the positioning uncertainty is given as $\sigma_w = \pm 1{,}0\ \mu\mathrm{m}$ according to the test protocol shown in Appendix G. Since an actually targeted position is known and σ_w gives the maximum deviation in positive and negative direction, the error is considered stochastic with a distribution of the deviation between the targeted and the actual position that is assumed to be triangular [127, 128].

Pitch and yaw of the w-stage

The pitch and yaw of the w-stage is directly assignable to the pitch and yaw of the detector plane. Therewith, it has an influence on the detected centroid position of the reflected beams. The magnitude of the pitch and yaw of the w-stage are donated $\sigma_{w,p}$ and $\sigma_{w,y}$. Their influence on the detector plane is illustrated in Figure 6.2.

The magnitudes of the pitch and yaw according to the test protocol given in Appendix G are $\sigma_{w,p} = \pm 17.791\ \mu\mathrm{rad}$ and $\sigma_{w,y} = \pm 12.643\ \mu\mathrm{rad}$. Although, these values are given for the whole travel length of the w-stage, they are assumed to appear also in the same magnitude if the stage is used in shorter ranges. These errors are assumed to be systematical.

Straightness and flatness of the w-stage

The straightness and flatness given for the w-stage will be donate $\sigma_{w,s}$ and $\sigma_{w,f}$. They describe an elevation or shift of the stages carriage during movement as presented in Figure 6.3.

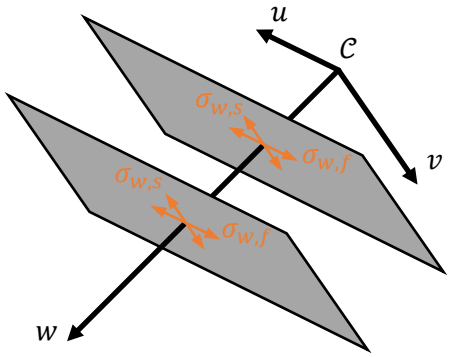

Figure 6.3: Sketch to illustrate the influence of the straightness and flatness of the w-stage on the detector plane's position.

The magnitude of the straightness and flatness error is given as $\sigma_{w,s} = \pm 1.926\,\mu\text{m}$ and $\sigma_{w,f} = \pm 2.286\,\mu\text{m}$ according to the test protocol given in Appendix G. Although, the straightness and flatness influences presented in Figure 6.3 directly indicate the influence on the detector plane, they can also be interpreted differently. Therefore, one has to recall that the detector plane is only positioned at two different w-positions within one measurement. Thus, one can always draw a line between the two center points of the detector plane in the two positions. Assuming that this line is the ideally straight and flat movement of the w-stage, the straightness error turns into a constant yaw error and the flatness turns into a constant pitch error. This is only due to a change of the point of view. To point this out, the change of the point of view is illustrated in Figure 6.4.

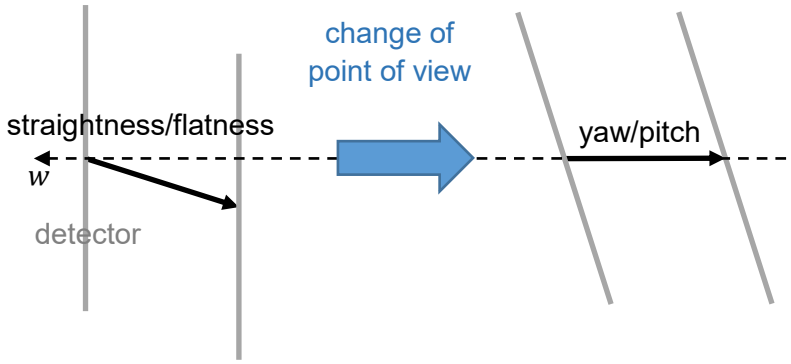

Figure 6.4: Sketch to illustrate change from the straightness and flatness error of the w-stage to a yaw and pitch error of the detector, when the movement of the center of the detector is assumed to be ideally along the w-axis.

May the intended movement along the w-axis be Δw, the constant yaw

$$\sigma_{w,cy} = \sin\left(\frac{\pm\sigma_{w,s}}{\Delta w}\right) \tag{6.1}$$

and the constant pitch

$$\sigma_{w,cp} = \sin\left(\frac{\pm\sigma_{w,f}}{\Delta w}\right) \tag{6.2}$$

can be calculated from the straightness and flatness error. Having $\Delta w = 10\,\text{mm}$, as it is used in the experimental measurements presented in Chapter 5, the constant yaw and pitch can be

calculated to be $\sigma_{w,cy} = \pm 192.6\,\mu\text{rad}$ and $\sigma_{w,cp} = \pm 228.6\,\mu\text{rad}$. These errors are also considered systematical.

Positioning uncertainty of the $\tilde{x}\tilde{y}$-stages

Equivalently to the positioning uncertainty of the w-stage, a positioning uncertainty exists for the $\tilde{x}$- and $\tilde{y}$-stage. These uncertainties are donated $\sigma_{\tilde{x}}$ and $\sigma_{\tilde{y}}$ and they both have a direct influence on the actually investigated position $\boldsymbol{I}$ on the SUT. However, since the SUT is positioned to the sample positions $\tilde{\boldsymbol{x}}_i$, the uncertainty has to be considered in this positioning as illustrated in Figure 6.5.

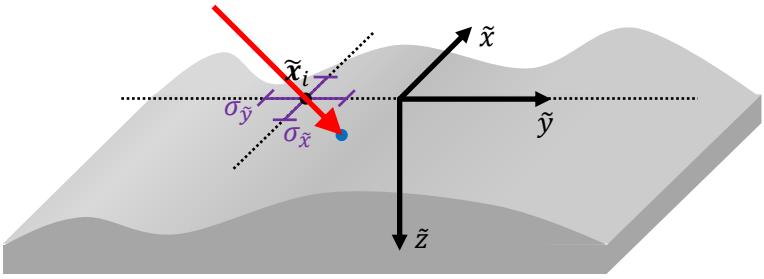

Figure 6.5: Sketch to illustrate the influence of the positioning errors $\sigma_{\tilde{x}}$ and $\sigma_{\tilde{y}}$ of the $\tilde{x}$- and $\tilde{y}$-stages on the sample position $\tilde{\boldsymbol{x}}_i$.

According to the test protocol given in Appendix E, the positioning errors are $\sigma_{\tilde{x}} = \pm 0.627\,\mu\text{m}$ and $\sigma_{\tilde{y}} = \pm 0.517\,\mu\text{m}$. As already assumed for the positioning accuracy of the w-stage, the error is considered stochastic with a triangular distribution of the deviation from the actually targeted position.

Pitch, roll and yaw of the $\tilde{x}\tilde{y}$-stages

The pitch and roll of the $\tilde{x}$- and $\tilde{y}$-stages is crucial to the correct measurement of the surface gradient, as an error in one of these parameters has a direct impact on the surface normal. However, since the two stages are mounted orthogonal to each other, the roll of one stage is equivalent to a pitch of the other and vice versa. Although the roll of the $\tilde{x}\tilde{y}$-stages is listed as not considered error source, it can be assumed to be included in the pitch error of the $\tilde{x}\tilde{y}$-stages. Regarding this pitch error, it comes back in mind that this error is considered in the calibration of the pitch of the DUT positioning described in Chapter 3.6.2 and 5.2. Thus, the influence of the pitch and roll error of the $\tilde{x}\tilde{y}$-stage is considered known and manageable and therewith is not considered in this error analysis.

In contrast to the pitch and roll error of the $\tilde{x}\tilde{y}$-stages, their yaw error is not detected in the experimental setup. Thus, it has to be included in the error analysis. The yaw errors of the two stages are donated $\sigma_{\tilde{x},y}$ and $\sigma_{\tilde{y},y}$ and are expected to be systematical. Their impact on the DUT orientation in the experimental is illustrated in Figure 6.6.

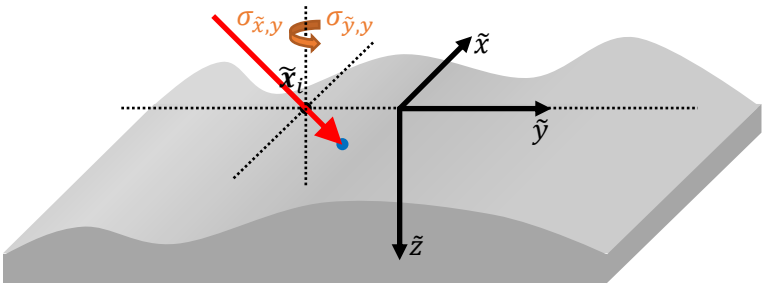

Figure 6.6: Sketch to illustrate the influence of the yaw errors $\sigma_{\tilde{x},y}$ and $\sigma_{\tilde{y},y}$ of the $\tilde{x}$- and $\tilde{y}$-stages on the DUT orientation.

According to the test protocol given in Appendix E, their magnitudes are $\sigma_{\tilde{x},y} = \pm 6.368\ \mu\text{rad}$ and $\sigma_{\tilde{y},y} = \pm 16.662\ \mu\text{rad}$. Both yaw errors have the same influence on the DUT orientation as shown in Figure 6.6. Thus, they will be connected in the error analysis. Additionally, it has to be mentioned that this yaw error has no influence on the sample position $\tilde{\boldsymbol{x}}_i$, but only on the orientation at the sample position itself. The DUT is positioned to $\tilde{\boldsymbol{x}}_i$ before the yaw error is applied. Otherwise the yaw error also had an influence on the position $\tilde{\boldsymbol{x}}_i$.

Straightness and flatness of the $\tilde{x}\tilde{y}$-stages

As described before for the w-stage, the straightness describes a shift and the flatness an elevation of the stage's carriage during movement. The straightness errors of the two stages are donated $\sigma_{\tilde{x},s}$ and $\sigma_{\tilde{y},s}$, while the flatness errors are donated $\sigma_{\tilde{x},f}$ and $\sigma_{\tilde{y},f}$. Their influence on the positioning of the DUT is illustrated in Figure 6.7.

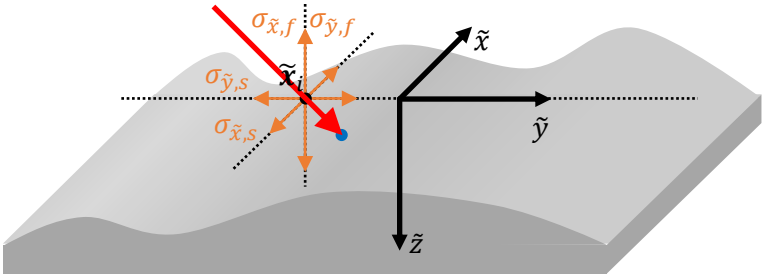

Figure 6.7: Sketch to illustrate the influence of the straightness errors $\sigma_{\tilde{x},s}$ and $\sigma_{\tilde{y},s}$ and the flatness errors $\sigma_{\tilde{x},f}$ and $\sigma_{\tilde{y},f}$ of the $\tilde{x}\tilde{y}$-stages on the DUT position.

Equivalently to the yaw errors, the flatness errors $\sigma_{\tilde{x},f}$ and $\sigma_{\tilde{y},f}$ have the same influence on the DUT position and will later have to be combined. The magnitudes given for the errors described before are $\sigma_{\tilde{x},s} = \pm 0.282\ \mu\text{m}$, $\sigma_{\tilde{y},s} = \pm 0.285\ \mu\text{m}$, $\sigma_{\tilde{x},f} = \pm 0.235\ \mu\text{m}$ and $\sigma_{\tilde{y},f} = \pm 0.260\ \mu\text{m}$ according to the test protocol given in Appendix E. These errors are not considered stochastic, but systematical, as they are a result of the mechanical bearing of the stage carriages. This differentiates the straightness errors $\sigma_{\tilde{x},s}$ and $\sigma_{\tilde{y},s}$ from the positioning errors $\sigma_{\tilde{x}}$ and $\sigma_{\tilde{y}}$, as these errors are considered stochastic.

Calibration errors due to SUT deviations

The combined calibration described in Chapter 3.6.1 and 4.3 assumes that the investigated SUT is free of deviations from the expected surface model. However, this assumption is not valid in experimental measurements, as deviations from the model cannot be prevented. Thus, deviations in the calibrated values have to be expected. These deviations will be donate $\sigma_{\alpha_C^{\mathcal{I}}}$, $\sigma_{\beta_C^{\mathcal{I}}}$, $\sigma_{\alpha_C^{\mathcal{M}}}$, $\sigma_{\beta_C^{\mathcal{M}}}$ and $\sigma_{\gamma_C^{\mathcal{C}}}$, for the uncertainties of the values $\alpha_C^{\mathcal{I}}$, $\beta_C^{\mathcal{I}}$, $\alpha_C^{\mathcal{M}}$, $\beta_C^{\mathcal{M}}$ and $\gamma_C^{\mathcal{C}}$.

6.2 Experimental error determination

The error sources determined experimentally are the centroid uncertainty and the centroid drift. To determine the magnitudes of these values, a flat mirror is used as DUT. The camera is positioned to $w = 90\ \text{mm}$ and without any movement in the setup, a series of images are taken. Determining the centroid for every image, the centroid uncertainty and drift can be derived. To have a significant series of images, $40\,000$ images have been taken and evaluated over a duration of 5.5 hours. The centroid positions determined from this series of images are shown in Figure 6.8.

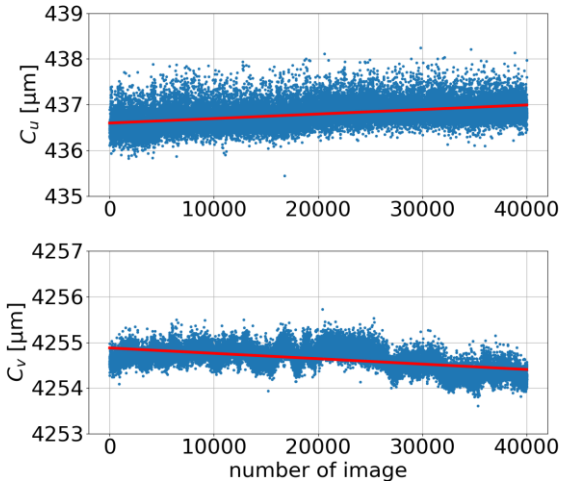

Figure 6.8: Determined centroid positions C_u and C_v to determine the centroid uncertainty and drift. The red line shows a linear fit to the given centroid data, representing the drift of the centroid values.

These centroid positions shown in Figure 6.8 include both, the drift and the stochastic uncertainty. To investigate the two parameters for both directions independently, a linear fit, representing the slow drift, has been performed over the given centroid positions [129]. This fit for each direction is shown by the red lines in in Figure 6.8. Over the full $40\,000$ images this fit indicates a drift of the centroid in u-direction of $395\ \mathrm{nm}$ and in v-direction of $-471\ \mathrm{nm}$. To set this drift in relation to the time the $40\,000$ images have been taken over, one can determine the drift errors

$$\sigma_{u,d} = \frac{|395\ \mathrm{nm}|}{5.5\ \mathrm{h}} = 71.8\frac{\mathrm{nm}}{\mathrm{h}} \tag{6.3}$$

and

$$\sigma_{v,d} = \frac{|-471\ \mathrm{nm}|}{11\ \mathrm{h}} = 85.6\frac{\mathrm{nm}}{\mathrm{h}}. \tag{6.4}$$

After subtracting the drift from the determined centroid positions, the position $\hat{C}_u$ and $\hat{C}_u$ as shown in Figure 6.9 are determined.

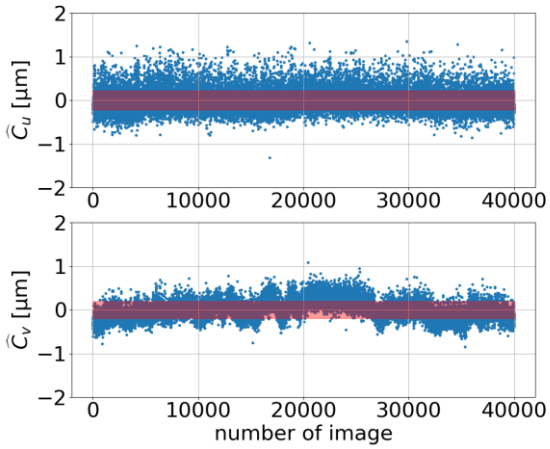

Figure 6.9: Determined centroid positions $\hat{C}_u$ and $\hat{C}_v$ after subtracting the linear drift. The red bars represent the standard deviation.

Regarding the values of $\hat{C}_v$ in Figure 6.9, one can recognize that a systematic structure besides the stochastic fluctuation exists. Since the frequency of this structure is too high to be considered a drift, it is taken into account in the centroid uncertainty evaluation. To determine the centroid uncertainty in u- and v-direction, the standard deviation of the given centroid positions is determined [129]. Although, the standard deviation only is fully trustable if an infinite number of samples are evaluated, the $40\,000$ samples taken into account here are expected to give a trustable assumption of the centroid position uncertainty. From the data presented in Figure 6.9 the standard deviations and therewith the centroid uncertainties $\sigma_u = 219\ \mathrm{nm}$ and $\sigma_v = 196\ \mathrm{nm}$ are determined. These values are also presented in Figure 6.9 by the red bars.

6.3 Uncertainty of ray direction measurement

To investigate the uncertainty of the ray direction measurement, a single sample point is investigated. Therefore, no drift is considered, as drift only occurs over time. The uncertainties and systematic errors that are taken into account here are the centroid uncertainty, the w-stage positioning uncertainty and the w-stage pitch, yaw, straightness and flatness. Additionally, an estimation about the surface slope determination uncertainty and their influence on the integration is given. Therefore, the incident ray direction is considered ideally known.

Centroid uncertainty

For the considerations given in the following, the simplified 2D sketch of the measurement setup shown in Figure 6.10 is used. Additionally, all explanations are only given in 2D for better understandability and readability. If differences to these considerations apply in 3D, they will be pointed out explicitly.

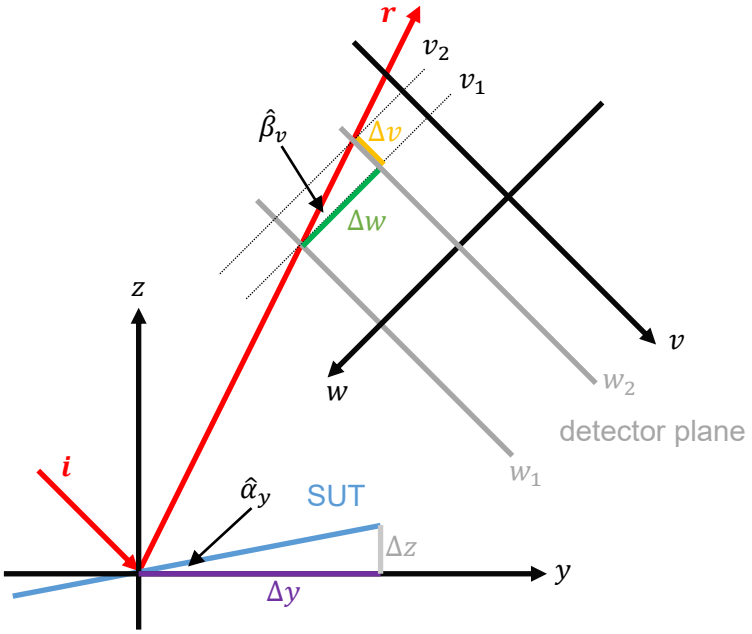

Figure 6.10: Simplified 2D sketch of the measurement setup with the incident ray $\boldsymbol{i}$, the reflected ray $\boldsymbol{r}$, the surface angle $\hat{\alpha}_y$, the surface slope defined by $\frac{\Delta z}{\Delta y}$, the reflected ray angle $\hat{\beta}_v$ and the reflected ray slope $\frac{\Delta v}{\Delta w}$. The reflected ray's position is defined by the two detector planes positions w_1 and w_2 and the determined positions v_1 and v_2.

In the sketch in Figure 6.10, the incident ray is reflected by the SUT, which has a surface angle $\hat{\alpha}_y$ in reference to the y-axis. The surface angle can also be represented by the surface slope

$$s_y = \frac{\Delta z}{\Delta y} = \tan(\hat{\alpha}_y). \tag{6.5}$$

From the law of reflection one can determine $\hat{\beta}_v = 2\hat{\alpha}_y$. While $\hat{\beta}_v$ represents the angle between the reflected ray direction and the w-axis. According to the surface slope, one can also define the ray slope

$$T_v = \frac{\Delta v}{\Delta w} = \frac{v_2 - v_1}{w_2 - w_1} = \tan(\hat{\beta}_v) = \tan(2\hat{\alpha}_y). \tag{6.6}$$

To investigate the influence of the centroid uncertainty on the ray slope uncertainty σ_{T_v}, Equation (6.6) is expanded to

$$T_v \pm \sigma_{T_v} = \frac{(v_2 \pm \sigma_v) - (v_1 \pm \sigma_v)}{w_2 - w_1} = \frac{\Delta v \pm (\sqrt{2} \cdot \sigma_v)}{\Delta w} = \frac{\Delta v}{\Delta w} \pm \frac{(\sqrt{2} \cdot \sigma_v)}{\Delta w}, \tag{6.7}$$

applying Gaussian error propagation [129]. Regarding Equation (6.7) one can see that the σ_{T_v} here is inversely proportional to Δw [130]. This can also be seen regarding Figure 6.11, where the values of σ_{T_v} and σ_{T_u}, which is the ray slope uncertainty in u-direction, are shown dependent on the distance Δw.

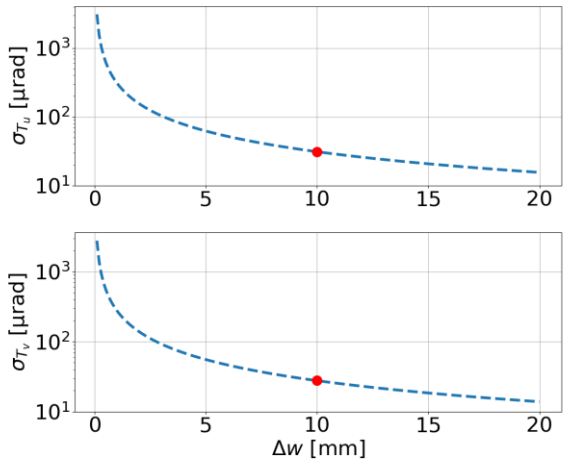

Figure 6.11: Plot to show the influence of the distance Δw on the ray slope detection uncertainties σ_{T_u} and σ_{T_v} including the centroid uncertainties σ_u and σ_v. The red markers indicate the position of $\Delta w = 10\ \text{mm}$ as chosen in the experimental measurements.

In the experimental measurements, a distance of $\Delta w = 10\ \text{mm}$ has been chosen. Although one can see that σ_{T_v} and σ_{T_u} still decrease with $\Delta w > 10\ \text{mm}$, it has also be considered that the first detector position is chosen as close as possible to the DUT, limited by mechanical dimensions. Thus, increasing Δw leads to an increase of the distance between the DUT and the second detector position. Since all reflected beams have to intersect with the optically active area of the camera chip at both positions w_1 and w_2, this directly leads to a decrease of the range of detectable surface angles. The determined uncertainties for $\Delta w = 10\ \text{mm}$ under the influence of the centroid uncertainties are $\sigma_{T_u} = 31.0\ \mu\text{rad}$ and $\sigma_{T_v} = 27.7\ \mu\text{rad}$.

Errors induced by the w-stage

Considering the w-stage positioning uncertainty σ_w, Equation (6.6) is now extended in the denominator leading to

$$T_v \pm \sigma_{T_v} = \frac{\Delta v}{(w_2 \pm \sigma_w) - (w_1 \pm \sigma_w)}. \tag{6.8}$$

Equation (6.8) indicates a dependency of σ_{T_v} on Δv, which is dependent on the surface angle $\hat{\alpha}_y$. Using Equation (6.6), the values of Δv for $\Delta w = 10\,\mathrm{mm}$ and $\hat{\alpha} = -12.0°, -11.9°, \ldots, 11.9°, 12.0°$ are calculated. To derive σ_{T_v} from Equation (6.8), Gaussian error propagation cannot be applied, since the distribution of σ_w is expected to be triangular. Thus, a Monte-Carlo-Simulation (MCS) with $1\,000\,000$ iterations is performed to determine the magnitude of σ_{T_v} numerically [131, 132]. This MCS leads to the standard deviations σ_{T_v} dependent on $\hat{\alpha}_y$ as shown in Figure 6.12.

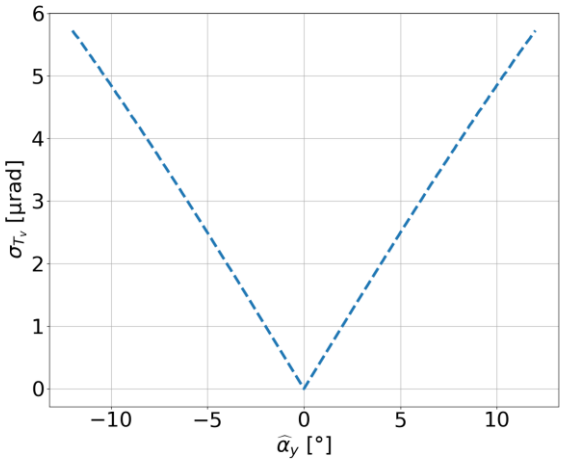

Figure 6.12: Determined values for σ_{T_v} over $\hat{\alpha}_y$ including the w-stage positioning uncertainty σ_w.

It has to be pointed out that this uncertainty is only valid for a single surface slope determination. In an experimental measurement, the error of the w-stage positioning is not stochastic for every sample point, but an unknown systematic error for the determination of all $\boldsymbol{C}_i$ and $\boldsymbol{D}_i$ separately, as the camera is only repositioned once within a measurement.

According to the simplification in 2D, only the yaw error $\sigma_{w,y}$ and the constant yaw error $\sigma_{w,cy}$ resulting from the straightness of the w-stage are considered. To determine the influence of a yaw of the detector on the detected position, the situation illustrated in Figure 6.13 is considered.

In Figure 6.13 the detector plane is tilted by $\hat{\gamma}_v$, which is considered the yaw of the detector plane. Therewith, instead of the correct position v_1, the erroneous position $\hat{v}_1$ is detected. Using the sine rule, one can determine the erroneous position

$$\hat{v}_1 = v_1 \frac{\cos(\hat{\beta}_v)}{\cos(-\hat{\gamma}_v - \hat{\beta}_v)} \tag{6.9}$$

from the correct position and the given angles [79]. One can see that a dependency on the investigated surface angle $\hat{\alpha}_y$ exists, too, since $\hat{\alpha}_y$ directly influences the position v_1. Thus, the uncertainty of the surface slope detection has to be investigated dependent on $\hat{\alpha}_y$. For further investigations, the following assumptions are made. The distance between the intersecting point of the incident ray with the SUT and the first detector position is $28\,\mathrm{mm}$. For the detector position w_1, the tilt angle $\hat{\gamma}_v$ is set to $\sigma_{w,cy} - \sigma_{w,y}$. For the detector position w_2 it is set to $\sigma_{w,cy} + \sigma_{w,y}$. Respectively for the u-direction, the tilt angle $\hat{\gamma}_u$ is set to $\sigma_{w,cp} - \sigma_{w,p}$ for the first

position and $\sigma_{w,cp} + \sigma_{w,p}$ for the second detector position. Therewith, the full range of the given errors is taken into account. Applying this to the same surface angles $\hat{\alpha}_x$ and $\hat{\alpha}_y$, as used for the stochastic error evaluation, erroneous ray slope values $\tilde{T}_u$ and $\tilde{T}_v$ are determined. The deviation from the correct ray slopes T_u and T_v are shown in Figure 6.14.

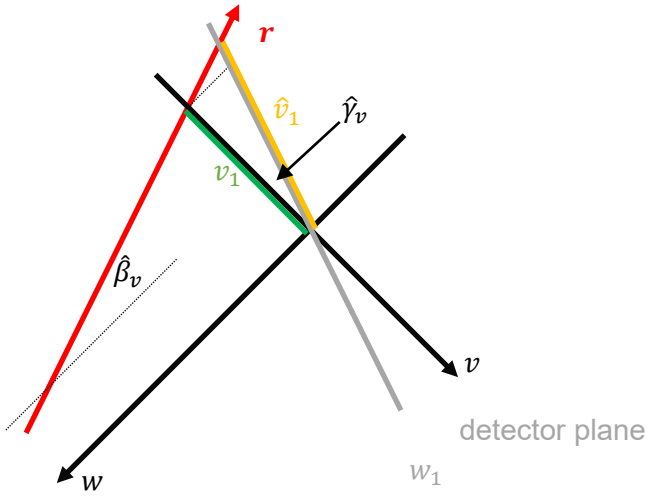

Figure 6.13: Simplified 2D sketch to show the influence of a detector tilted by $\hat{\gamma}_v$ on the determined position v_1 dependent on the reflected beams angle $\hat{\beta}_v$.

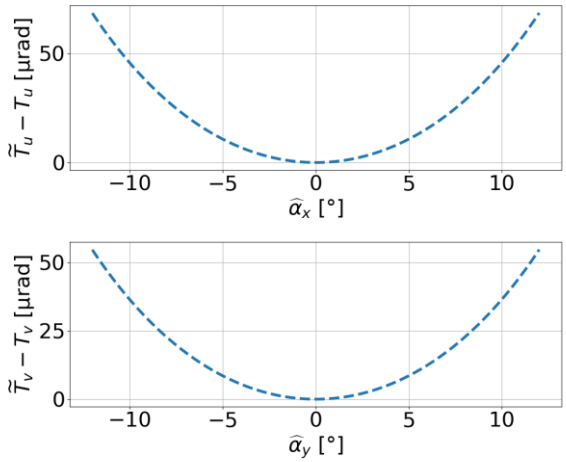

Figure 6.14: Determined values for $\tilde{T}_u - T_u$ and $\tilde{T}_v - T_v$ dependent on the surface angles $\hat{\alpha}_x$ and $\hat{\alpha}_y$ including the w-stage pitch and yaw errors and the w-stage flatness and straightness errors.

Combining centroid uncertainty and w-stage errors

To get an overall assumption about the uncertainty of the ray slope determination, the error sources described before are combined in one MCS of $1\,000\,000$ iterations [132]. The simulation has been performed for the same range of $\hat{\alpha}$ and for $\Delta w = 10.0\,\mathrm{mm}$. The determined uncertainty in terms of the standard deviation is shown in Figure 6.15.

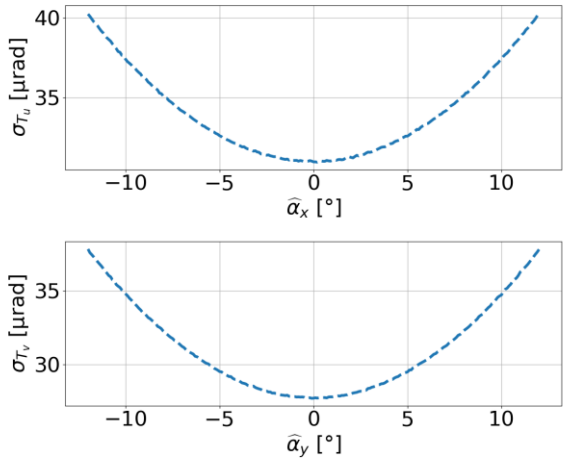

Figure 6.15: Determined for σ_{T_u} and σ_{T_v} dependent on the surface angle $\hat{\alpha}$ including the centroid uncertainty, the w-stage positioning uncertainty, the w-stage pitch and yaw errors and the w-stage flatness and straightness errors.

To transfer the ray slope uncertainties into surface slope uncertainties, Equation (6.6) is extended to determine the surface angle

$$2\left(\hat{\alpha}_y \pm \sigma_{\hat{\alpha}_y}\right) = \arctan\left(T_v \pm \sigma_{T_v}\right) \tag{6.10}$$

including its uncertainty $\sigma_{\hat{\alpha}_y}$. From Gaussian error propagation, Equation (6.10) is solved for

$$\hat{\alpha}_y \pm \sigma_{\hat{\alpha}_y} = \frac{1}{2}\left(\arctan(T_v) \pm \frac{\partial \arctan(T_v)}{\partial T_v}\sigma_{T_v}\right). \tag{6.11}$$

Solving the differentiation, leads to

$$\hat{\alpha}_y \pm \sigma_{\hat{\alpha}_y} = \frac{\arctan(T_v)}{2} \pm \frac{1}{2(1+T_v^2)}\sigma_{T_v} \tag{6.12}$$

for the definition of the surface angle [79]. Applying Equation (6.5), the surface slope

$$q \pm \sigma_q = \tan(\hat{\alpha}_y \pm \sigma_{\hat{\alpha}_y}) \tag{6.13}$$

with the surface slope uncertainty σ_q, is determined from the surface angle. Once again Gaussian error propagation is applied, leading to

$$q \pm \sigma_q = \tan\left(\hat{\alpha}_y\right) \pm \frac{\partial \tan\left(\hat{\alpha}_y\right)}{\partial \hat{\alpha}_y}\sigma_{\hat{\alpha}_y} = \tan\left(\hat{\alpha}_y\right) \pm \frac{1}{\cos^2\left(\hat{\alpha}_y\right)}\sigma_{\hat{\alpha}_y}. \tag{6.14}$$

To transfer this surface slope uncertainty into a surface height uncertainty, the sample distance $\Delta\tilde{y} = \Delta y$ has to be considered. Unfortunately, as described in Chapter 2.3.1, the actual distance between the sample points is dependent on the surface height. Assuming a flat surface in between the sample points as shown in Figure 6.16, one can determine the actual sample distance

$$\widetilde{\Delta y} = \frac{\Delta y}{\tan\left(\hat{\alpha}_y\right) + 1} \tag{6.15}$$

from surface angle $\hat{\alpha}_y$ and the given sample distance Δy for an angle of $45°$ between the incident ray and the z-axis.

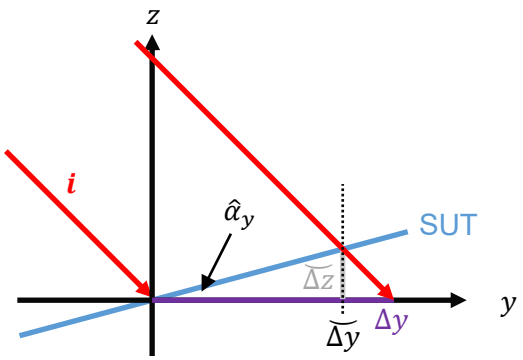

Figure 6.16: Sketch to illustrate the dependency of the actual sample distance $\widetilde{\Delta y}$ on the surface angle $\hat{\alpha}_y$, the initial sample distance Δy and the incident beam direction $\boldsymbol{i}$.

To consider this situation in x-direction, the actual sample distance

$$\widetilde{\Delta x} = \Delta x \tag{6.16}$$

is set equal to Δx as the angle between the incident beam and the z-axis is $0°$. Regarding Figure 6.16, one can derive the relation

$$\sigma_{\widetilde{\Delta z}} = \sigma_q \widetilde{\Delta y} \tag{6.17}$$

to determine the surface height uncertainty $\sigma_{\widetilde{\Delta z}}$. To determine the surface height uncertainty for different given parameters, it is evaluated for x- and y-direction separately for the same surface angle range as considered before and for sample distances of Δx and Δy in a range from $25\ \mu\text{m}$ until $1.0\ \text{mm}$ in steps of $25\ \mu\text{m}$. The results from these considerations are shown in Figure 6.17.

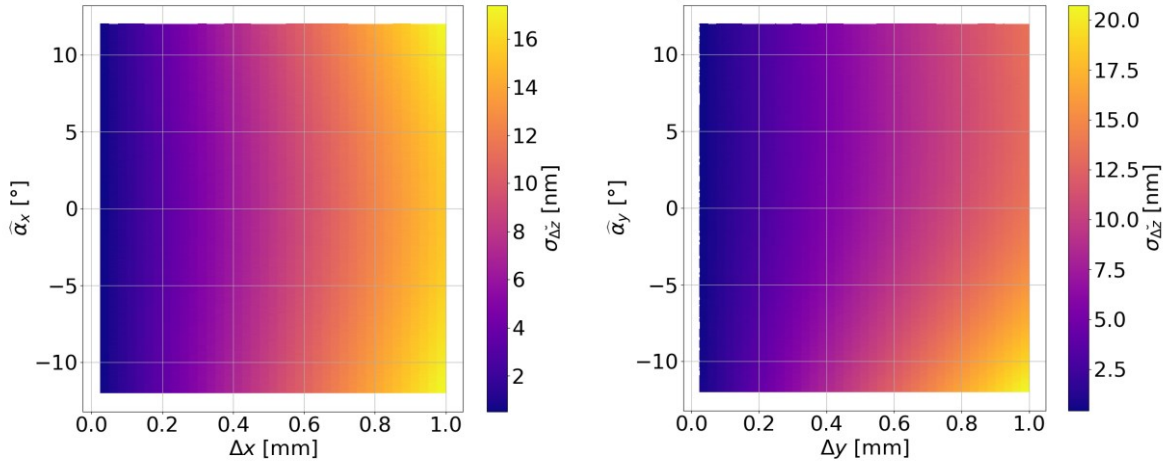

a) b)

Figure 6.17: Plots presenting the single point surface height determination uncertainty in a) x- and b) y-direction dependent on the given sample distances Δx and Δy and the surface angle $\hat{\alpha}_x$ in x- and $\hat{\alpha}_y$ in y-direction.

Analyzing the data presented in Figure 6.17, one can see that the height uncertainty is increasing with the given sample distance Δx and Δy, as expected from Equation (6.17). Additionally, one can recognize that the surface angle has a higher impact on $\sigma_{\widetilde{\Delta z}}$ in y-direction, than it has in x-direction. This is due to the incident ray having an angle of $45°$ to the z-axis in y-direction in contrast to an angle of $0°$ in x-direction. Focusing on the two sample distances used in the experimental measurements, one can derive a maximum value for

$\sigma_{\overline{\Delta z}}$ of $2.1\ \mathrm{nm}$ for a sample distance of $0.1\ \mathrm{mm}$ and a maximum value for $\sigma_{\overline{\Delta z}}$ of $21\ \mathrm{nm}$ for a sample distance of $1.0\ \mathrm{mm}$.

6.4 Calibration uncertainty

Due to the deviations of the SUT from its model, used for the combined calibration of the incident beam direction, the xy-stages orientation and the camera rotation, an uncertainty of the derived calibration data occurs. To derive this uncertainty, the simulation described in Chapter 4.3, to present the basic abilities of the calibration method, has been performed with an expected non-ideal SUT model. In Chapter 5.4.3, the experimental measurement results using the polynomial freeform 1 are shown. From the presented deviations d_i, the first 36 Zernike polynomials have been subtracted to obtain the high-frequency deviations of d_i. Thus, the sum of the first 36 Zernike polynomials describe the low-frequency deviations of d_i, shown in Figure 6.18.

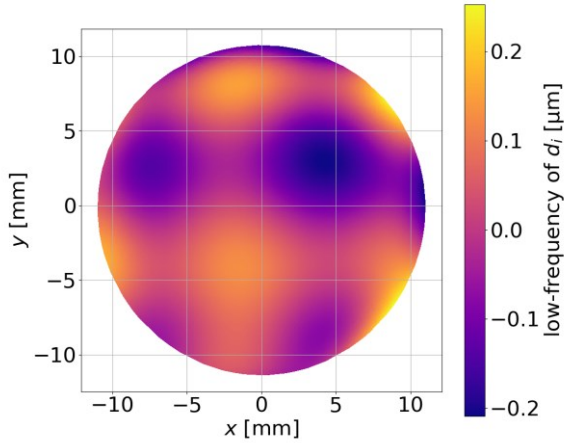

Figure 6.18: Low-frequency deviations of the experimentally determined deviation d_i of the polynomial freeform 1 from its model as shown in Figure 5.23 b). The low-frequency deviations are determined by a fit of the first 36 Zernike polynomials to d_i.

These deviations have been added to the expected SUT model and the calibration has been performed. The derived values and their deviation from the expected values are shown in Table 6.1.

Table 6.1: Derived angles from the combined calibration performed on simulation data, while using a SUT model including expected low-frequency deviations to determine the uncertainty of the calibration method.

	$\alpha_{\mathcal{C}}^{\mathcal{I}}$ [°]	$\beta_{\mathcal{C}}^{\mathcal{I}}$ [°]	$\alpha_{\mathcal{C}}^{\mathcal{M}}$ [°]	$\beta_{\mathcal{C}}^{\mathcal{M}}$ [°]	$\gamma_{\mathcal{C}}^{\mathcal{C}}$ [°]
expected	90.10009817	0.10588067	45.1	−0.075	−0.13
derived	90.11788401	0.26661099	45.10864360	0.01355140	−0.04216675
deviation	0.01778584	0.16073032	0.00864360	0.08855140	0.08783325

The deviations presented in Table 6.1 show the deviations for this exact sample. Since the calibration method is complex, a direct traceability of the deviations to a certain surface structure is not possible. Thus, for further considerations, the deviation values presented in Table 6.1 are take into account as the maximum deviation of these angles, while the deviations are considered distributed uniform.

6.5 Monte-Carlo-Simulation with full measurement model

To derive the uncertainty of the measurement technique, two MCSs have been performed including all considered error sources [132]. One MCS has been performed with an areal measurement using the polynomial freeform 1 as SUT. The second simulation has been performed as a cross-section simulation using the cylinder surface. The model used for the simulation is described in Chapter 4.2.1, while the evaluation has been performed considering the model to be known according to the description in Chapter 3.4.

MCS using polynomial freeform 1

For the first MCS, the polynomial freeform 1 is used as SUT. The sample area is of circular shape with a diameter of $22\ \mathrm{mm}$ and a sample distance of $100\ \mu\mathrm{m}$. Therewith, the simulation can directly be compared to the experimental measurement shown in Chapter 5.4.3.

The centroid uncertainty, the w-stage positioning of the w-stage, the pitch and yaw of the w-stage, the straightness and flatness of the w-stage, the positioning uncertainty of the $\tilde{x}\tilde{y}$-stages as well as the calibration errors are considered as described before.

To determine the centroid drift, a measurement time t_m has to be set. This measurement time is approx. $4{,}5\ \mathrm{h}$ for the experimental measurement of the polynomial freeform as described in Chapter 5.4.3. With this, the expected drifts

$$\hat{\sigma}_{u,d} = \sigma_{u,d} t_m = 323.1\ \mathrm{nm} \tag{6.18}$$

and

$$\hat{\sigma}_{v,d} = \sigma_{v,d} t_m = 385.2\ \mathrm{nm} \tag{6.19}$$

within one measurement can be determined. To model the drift in the uncertainty evaluation here it is now considered normal distributed with the standard deviations $\hat{\sigma}_{u,d}$ and $\hat{\sigma}_{v,d}$ [133]. Thus, one can sum up the centroid uncertainties and drifts to a normal distributed uncertainty with the standard deviation of

$$\hat{\sigma}_u = \sqrt{\sigma_u^2 + \hat{\sigma}_{u,d}^2} \tag{6.20}$$

and

$$\hat{\sigma}_v = \sqrt{\sigma_v^2 + \hat{\sigma}_{v,d}^2}, \tag{6.21}$$

according to Gaussian error propagation [129].

The yaw errors of the $\tilde{x}$- and $\tilde{y}$-stages is considered to be of full range within the considered SUT area. Thus for the sample points at $\tilde{x} = -11\ \mathrm{mm}$ the yaw of the $\tilde{x}$-stage is considered to be $-\sigma_{\tilde{x},y}$, while at the sample points at $\tilde{x} = 11\ \mathrm{mm}$ the yaw is considered to be $\sigma_{\tilde{x},y}$. The evolution in between is considered linear. The same applies for the $\tilde{y}$-stage with $\sigma_{\tilde{y},y}$. Since only one yaw error can be applied to the SUT, the yaw errors are added for each sample point.

Equivalently to the yaw errors, the flatness and straightness errors are taken into account. At the sample positions $\tilde{x} = -11\ \mathrm{mm}$, the flatness of the $\tilde{x}$-stage is considered $-\sigma_{\tilde{x},f}$ while the straightness is considered $-\sigma_{\tilde{x},s}$ at the sample points $\tilde{x} = 11\ \mathrm{mm}$, the flatness is considered $\sigma_{\tilde{x},f}$ while the straightness is considered $\sigma_{\tilde{x},s}$. The evolution in between is considered linear. The same applies equivalently for the $\tilde{y}$-stage with the corresponding error magnitudes. While the straightness can be applied separately on the positioning of the SUT, the flatness of the stages has a correlating influence on the SUT. Thus, the errors of the two stages are added.

With these error sources, one simulation in OpticStudio is performed including the systematic errors of the pitch and yaw of the w-stage, the straightness and flatness of the w-stage, the yaw of the $\tilde{x}\tilde{y}$-stages and the straightness and flatness of the $\tilde{x}\tilde{y}$-stages. In the evaluation, the stochastic errors of the centroid uncertainty and drift, the positioning uncertainty of the w-stage, the positioning uncertainty of the $\tilde{x}\tilde{y}$-stages and the calibration errors are included. The evaluation is performed 500 times. Exemplary, one of the 500 surface deviations is shown in Figure 6.19 a), while Figure 6.19 b) shows the standard deviation for each sample point.

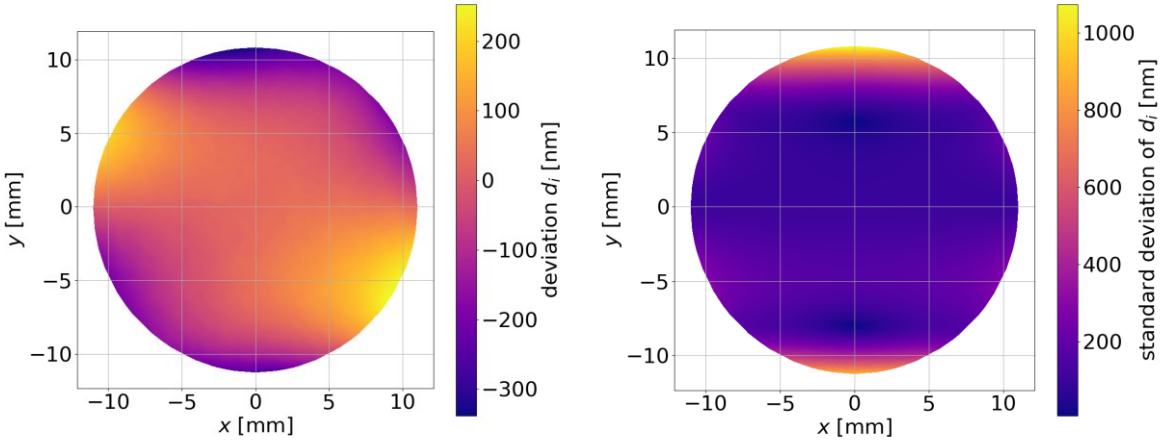

a) b)

Figure 6.19: a) Exemplary plot of the determined surface deviation from one evaluation in the MCS using the polynomial freeform 1. b) Plot of the standard deviation determined for each sample point over all iterations of the MCS using the polynomial freeform 1.

The RMS of the deviations d_i shown in Figure 6.19 a) is $94.5\,\mathrm{nm}$. Regarding Figure 6.19 b), one can recognize that the standard deviation per sample point correlates with the absolute value of the surface slope shown in Figure 4.8 d). This is also in accordance with the expected ray direction uncertainty dependent on the surface angle shown in Figure 6.15. The low number of 500 iterations performed in the MCS has been chosen due to long calculation times needed in the evaluation. However, regarding the RMS surface deviation values determined for each iteration in Figure 6.20 a) and the evolution of the mean value of the RMS value shown in Figure 6.20 b), one can see that the mean value approaches a constant value.

The mean value of all RMS surface deviations shown in Figure 6.20 a) is $215.0\,\mathrm{nm}$ with a standard deviation of $97.6\,\mathrm{nm}$.

These values shown in Figure 6.19 and Figure 6.20 indicate a very high single point and overall RMS surface deviation uncertainty. However, it has to be considered that for multiple uncertainties, worst-case scenarios have been deployed. For example the values for straightness, flatness, pitch and yaw of the w-stage have been deployed over a distance of $10\,\mathrm{mm}$, although the given values for these errors have been determined over the full travel length of $100\,\mathrm{mm}$. The same applies for the yaw of the $\tilde{x}\tilde{y}$-stages. The values for these errors have been determined over the full travel length of $100\,\mathrm{mm}$, but have been deployed in the simulations on a distance of $22\,\mathrm{mm}$. Thus, it can be expected that the standard deviation and the mean value of the RMS surface deviation is smaller than determined in this MCS.

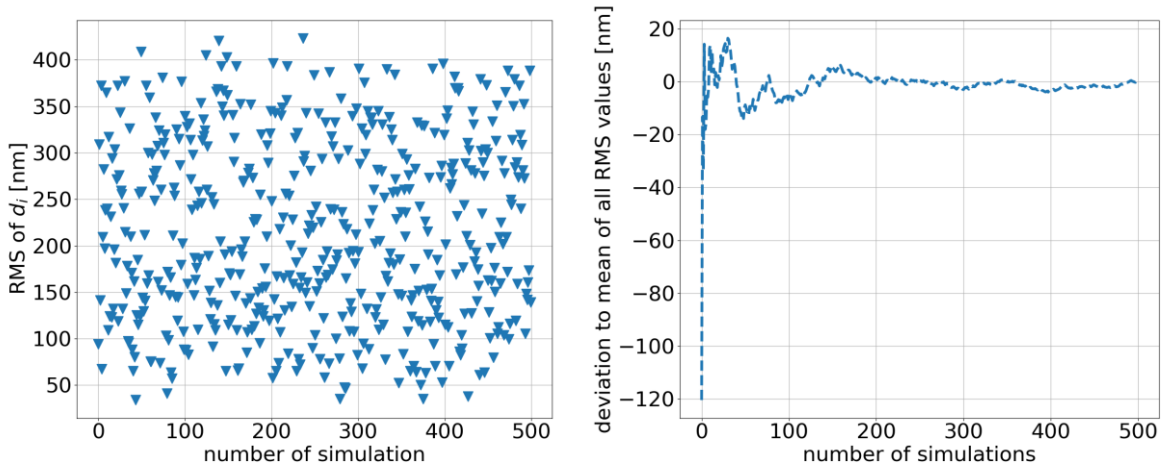

a) b)

Figure 6.20: Plots evaluating the RMS surface deviation values determined in the MCS using the polynomial freeform 1. a) shows the RMS surface deviation for each iteration. b) shows the evolution of the difference of the mean RMS value with increasing number of iterations to the mean RMS value of $215.0\ \mathrm{nm}$ considering all iterations.

MCS using cylinder surface

To perform the MCS using the cylinder surface, the same SUT and parameters have been used as described for the simulation of the cylinder surface in Chapter 4.1.3. The evaluation is performed considering the surface to be known. Regarding the drift considered for this measurement, a measurement time of $t_m = 2{:}25\ \mathrm{min}$ is considered. According to Equation (6.18) and (6.19), an uncertainty induced by the centroid drift of $\hat{\sigma}_{u,d} = 2.7\ \mathrm{nm}$ and $\hat{\sigma}_{v,d} = 3.2\ \mathrm{nm}$ is taken into account. With Equation (6.20) and (6.21), a standard deviation for the centroid of $\hat{\sigma}_u = 219\ \mathrm{nm}$ and $\hat{\sigma}_v = 196$ is considered. These values are almost similar to the centroid uncertainties determined experimentally. This shows that the centroid drift has almost no influence on the cross section measurement due to the short measurement time.

Since the evaluation of the cross-section simulation is very fast in comparison to the evaluation of the full areal simulation, the number of iterations performed is increased to $10\ 000$. For each iteration, a BFS has been fitted to the reconstructed surface. Figure 6.21 a) shows the determined deviations to the BFS, while Figure 6.21 b) shows the standard deviation of the deviation for each sample point.

The determined radii of the BFS are shown in Figure 6.22 a). The mean radius of all determine BFSs is $206.692\ \mathrm{mm}$. The standard deviation of these radii is $186\ \mu\mathrm{m}$ with a PV of $740\ \mu\mathrm{m}$. The evolution of the mean radius as deviation to $206.692\ \mathrm{mm}$ is presented in Figure 6.22 b). One can clearly recognize the approximation of the evaluation towards a constant value.

Regarding the RMS surface deviation determined for each iteration as the RMS of the deviations between the reconstructed surface and the BFS, one can determine values mostly in the range of single-digit nanometer. The RMS surface deviation for each iteration is presented in Figure 6.23 a). The mean RMS value, including all iterations, is $5.2\ \mathrm{nm}$, the according standard deviation is $1.6\ \mathrm{nm}$. The evolution of the mean RMS value with increasing number of iterations in deviation to the mean RMS value including all iterations is shown in Figure 6.23 b). An approach towards a constant mean value can be recognized.

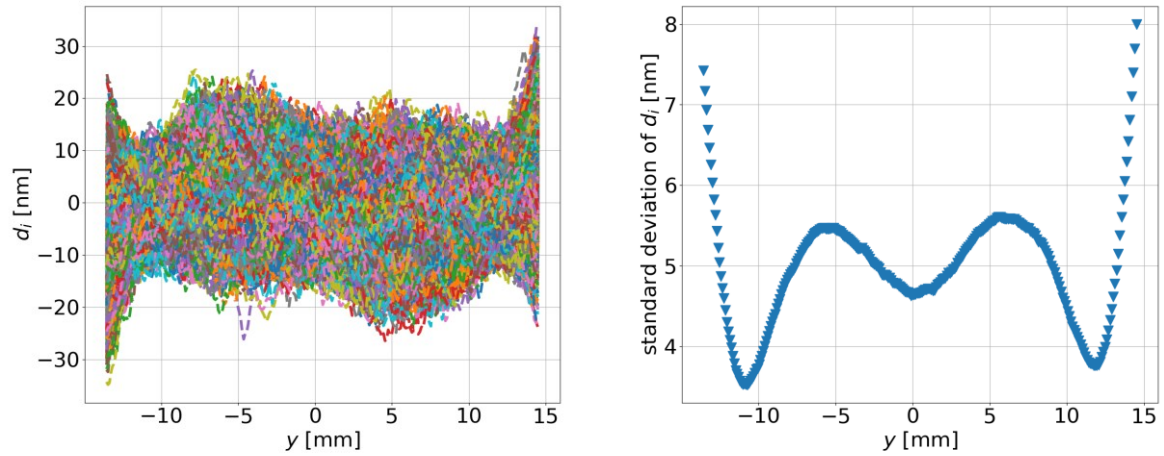

a) b)

Figure 6.21: Results from the MCS using the cylinder surface. a) shows the determined deviation to the BFS for each iteration. b) shows the standard deviation of the deviation to the BFS for each sample point over all iterations of the MCS.

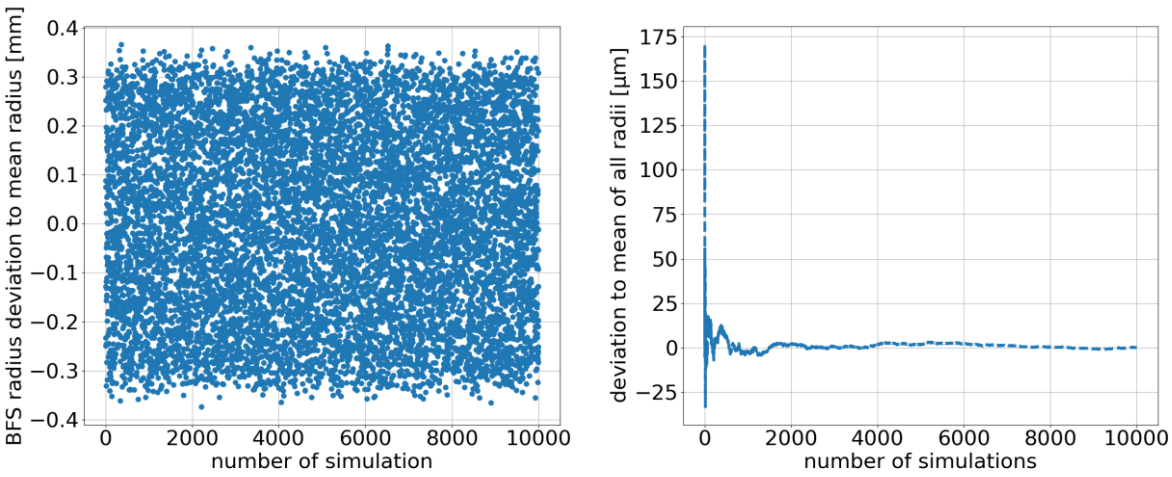

a) b)

Figure 6.22: a) shows the deviation of each BFS radius for the different iterations of the MCS using the cylinder surface in comparison to the mean BFS radius. b) shows the deviation of the mean BFS radius with in creasing number of iterations to the mean BFS radius considering all iterations.

To investigate the influence of different error sources on the presented results from the MCS, histograms of the determined results from the multiple iterations are determined. Figure 6.24 a) shows a histogram of the determined BFS radius deviations to the mean BFS radius presented in Figure 6.22 a). In Figure 6.24 b), the histogram of the determined RMS surface deviations presented in Figure 6.23 a) is shown.

Regarding the histogram presented in Figure 6.24 a), one can recognize an uniform pattern of the distribution of the BFS radii values. As the only error sources considered uniform distributed are the errors in the parameters from the calibration, it can be considered that these errors manly influence the radius of the BFS. Regarding the histogram presented in Figure 6.24 b), one can recognize a gamma distribution. This may be due to a constant RMS deviation

introduced by systematic errors, while the stochastic errors add up to the constant RMS deviation to create the determined gamma distribution.

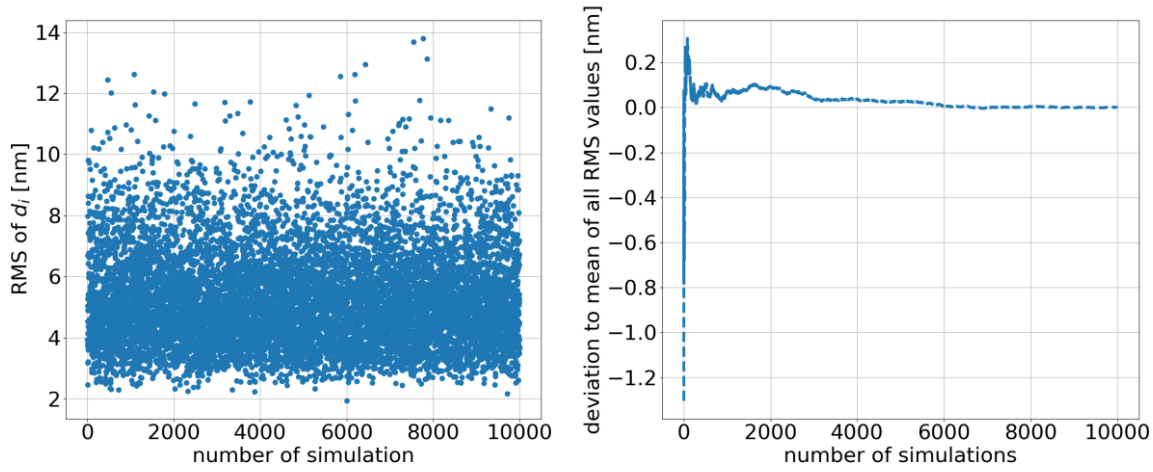

a) b)

Figure 6.23: a) shows the RMS surface deviation to the BFS for each iteration of the MCS using the cylinder surface. b) shows the deviation of the mean RMS surface deviation with in creasing number of iterations to the mean RMS surface deviation considering all iterations.

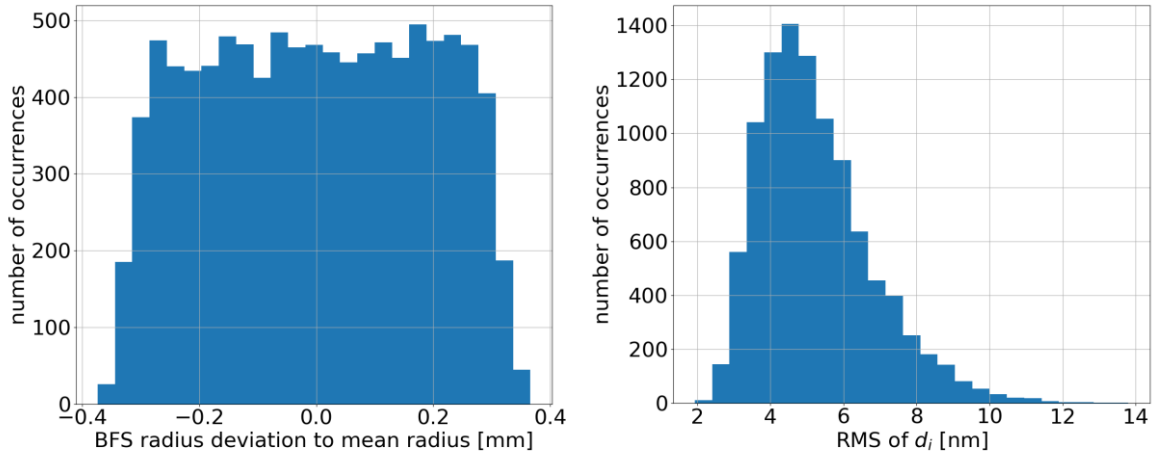

a) b)

Figure 6.24: a) shows the histogram of the determined deviation of the BFS radii from the mean BFS radius as presented in Figure 6.22 a). b) shows the histogram of the determined RMS surface deviation to the BFS for each iteration as presented in Figure 6.23 a).

6.6 Experimental repeatability determination

To evaluate the determined conclusions from the MCS, the measurement of the cylinder surface presented in Chapter 5.3.2 has been repeated 200 times. The determined deviations from these measurements as well as the standard deviation for each sample point are shown in Figure 6.25.

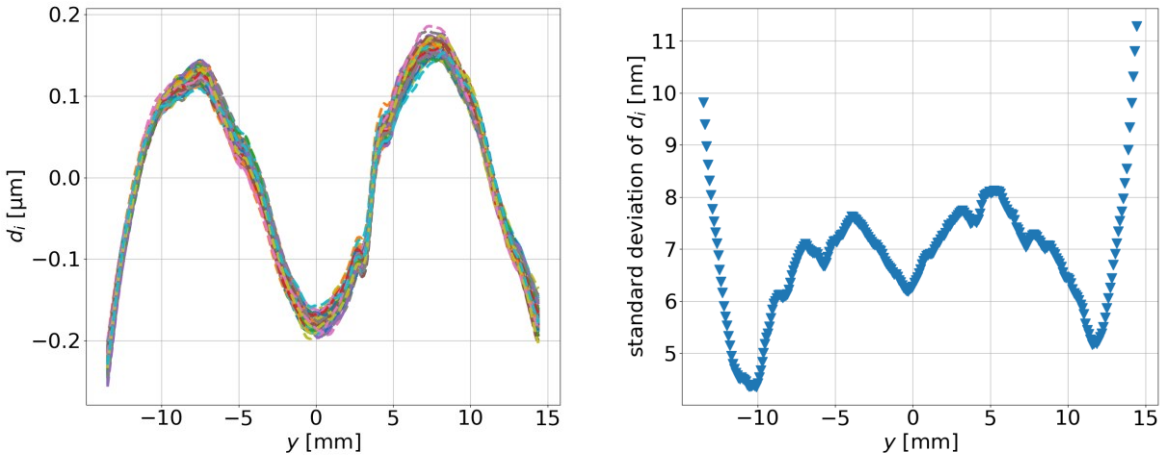

a) b)

Figure 6.25: Results from repeatability measurement using the cylinder surface. a) shows the determined deviation to the BFS for each iteration. b) shows the standard deviation of the deviation to the BFS for each sample point over all iterations.

Regarding Figure 6.25 a), one can see that a certain M-shaped structure dominates the deviations of the reconstructed surfaces from the fitted BFSs. This deviation is expected to be the actual surface deviation from the model, as the structure is in good accordance with the comparison measurement as presented in Chapter 5.4.2. Regarding Figure 6.25 b), a certain systematic structure can here be recognized, too. This structure can also be determined in the MCS as presented in Figure 6.21 b). Therewith, it can be assumed that the model used for the MCS is in accordance with the error sources in the experimental measurements. Regarding the magnitudes of the standard deviations from the MCS and the repeatability measurements, one can recognize slightly higher values determined with the repeatability measurements. On the one hand, it has to be considered that due to the lower number of iterations in the repeatability measurements the determined values are less reliable. On the other hand, since there are still error sources that have not been investigated in the MCS, these error sources can also explain the slightly higher values in the repeatability measurements.

In Figure 6.26 a), the determined BFS radii are presented. The mean radius from all iterations is $206.421\ \mathrm{mm}$. In Figure 6.26 b), the deviation of the mean radius with increasing number of considered iterations from the mean radius considering all iterations is presented.

Regarding Figure 6.26 b), one can see that the mean value is not approaching a constant value. Thus, the determined mean value cannot be considered reliable. However, it has to be mentioned that the scale of the change of the mean value is only in the range of single digit $\mu\mathrm{m}$. The PV of all BFS radii presented in Figure 6.26 a) is less than $70\ \mu\mathrm{m}$, which is only $0.034\ \%$ of the determined mean radius. Comparing this to the PV of the radii determined with the MCS, one can see that the PV determined from the repeatability measurement is smaller by a factor of 10. This underlines the assumption that the high deviations in the radii determined from the MCS is introduced by the uncertainties of the calibration. In the repeatability measurement, the calibration parameter are not varied, but kept constant over all iterations.

Regarding the determine RMS surface deviation values of all iterations of the repeatability measurement, presented in Figure 6.27 a), one can clearly determine the offset of approx. $112\ \mathrm{nm}$ applied to all RMS values. This offset is due to the actual deviation of the reconstructed

surfaces from the BFSs as shown in Figure 6.25 a). The determined mean RMS surface deviation over all iterations is $112.0\ \mathrm{nm}$.

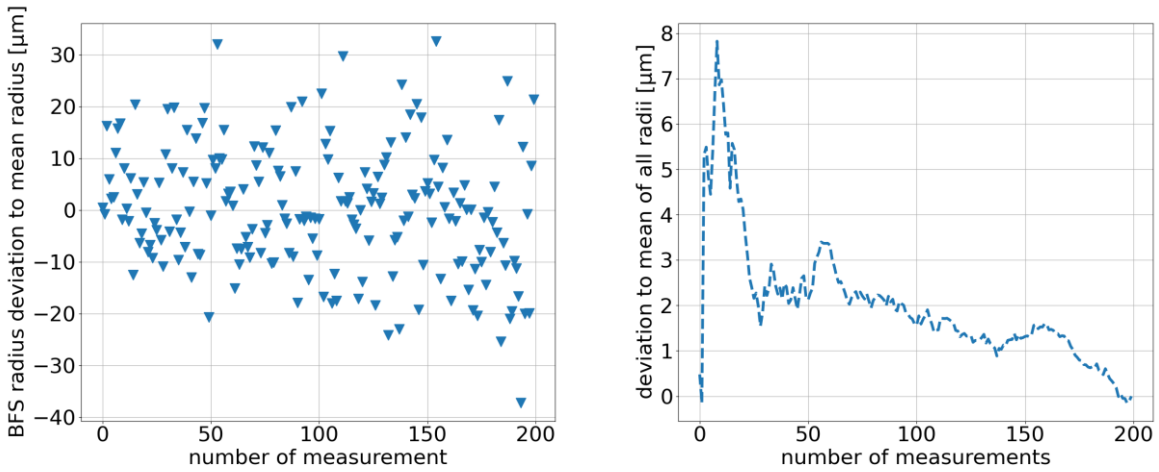

a) b)

Figure 6.26: a) shows the deviation of each BFS radius for the different measurements in the repeatability measurement with the cylinder surface in comparison to the mean BFS radius. b) shows the deviation of the mean BFS radius with in creasing number of measurements to the mean BFS radius considering all measurements.

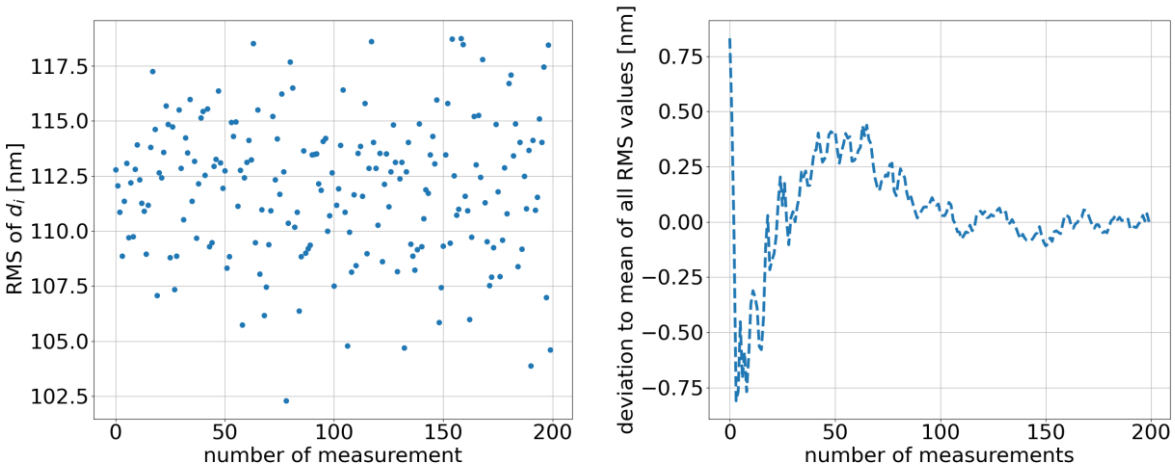

a) b)

Figure 6.27: a) shows the RMS surface deviation to the BFS for each iteration of the repeatability measurement using the cylinder surface. b) shows the deviation of the mean RMS surface deviation with in creasing number of iterations to the mean RMS surface deviation considering all iterations.

Figure 6.27 b) shows the evolution of the difference of the mean RMS surface deviation with increasing number of considered iterations from the mean RMS surface deviation considering all iterations. Regarding this, one can recognize an approach towards a constant value, although the number of iterations is not very high. The standard deviation of the RMS surface deviations shown in Figure 6.27 a) is $3.1\ \mathrm{nm}$. This value is higher than the determined standard deviation from the MCS, which is in accordance to the standard deviation for each sample point presented before.

7. Discussion

The theoretical considerations presented in Chapter 2 and 3, have been confirmed by the simulations presented in Chapter 4. The deviations determined in these simulations are negligible in relation to the expected uncertainties in the experimental setup.

In the experimental measurements, four different samples have been investigated. For three of these samples a comparison measurement exists, while each of these comparison measurements have been performed with a different type of measurement technique. The cross section measurement of a cylinder surface shows a very good agreement with the comparison in the surface deviation as well as in the determined surface radius.

Comparing the deviations of the polynomial freeform 1 sample from the expected surface model determined with the proposed measurement technique with the deviations from the comparison measurement, similar structures can be observed. However, there are also significant structures determined with the proposed method that cannot be seen in the comparison measurement. Since no further comparison measurement of this sample exists, it cannot be said, if these structures exist on the sample or if they are artefacts introduced by the proposed measurement technique. For better orientation of the results, this sample has been provided with three fiducials. These fiducials were determined by both, the proposed and the comparison measurement, with the same magnitude.

The deviation of the reconstructed surface from the expected surface model of the polynomial freeform 2 do not show the artifacts determined in the measurement of the polynomial freeform 1. The surface deviations determined for the polynomial freeform 2 show a slight global shape and many smaller local structures. These local structures are in good agreement with the comparison measurement. Especially regarding the high-frequency deviations determined from the proposed measurement technique and the comparison measurement, many similarities can be observed. The difference of these high-frequency deviations shows a RMS of only $10.0\,\mathrm{nm}$.

For all three comparison measurements, it has to be said that the measurement results determined with the proposed measurement technique are comparable with the results from the comparison measurements. The deviations to the comparison measurements are in the sub-$\mu\mathrm{m}$ range, but still larger than the determined deviations from a round-robin measurement of freeform samples [17]. However, different samples and different measurement machines have been used in the round-robin measurement than have been used to provide the comparison measurements in this work.

In the error analysis, multiple error sources have been investigated. Some error sources were not taken into account, as their magnitude is not known. From the error analysis, one can recognize that the uncertainty of a sample point's height information determined from the surface reconstruction is dependent on the surface's slope at this position. This is due to the integration and the measurement setup with the incident beam not perpendicular to the plane defined by the movement of the $\tilde{x}\tilde{y}$-stages. Considering the uncertainties related to the

determination of the reflected beams direction, a standard deviation of $\sigma_{\widetilde{\Delta z}} = \pm 2.1\ \mathrm{nm}$ for a surface angle of $0°$ and a sample distance of $0.1\ \mathrm{mm}$ is determined. Since the proposed measurement technique is a gradient-based measurement technique, an absolute measurement accuracy cannot be defined for the surface sag. Having the standard deviation $\sigma_{\widetilde{\Delta z}}$, one can expect this to be the standard deviation of the determined surface sag between two neighboring points with the same ground truth. In relation to this, the *LuphosScan 260 HD*, which has been used to perform the comparison measurement for the polynomial freeform 2, is defined with an accuracy of less than $\pm 50\ \mathrm{nm}\ (3\sigma)$ [29]. Therewith, two neighbored points with the same ground truth can deviate with a standard deviation of approximately $\pm 16\ \mathrm{nm}$. However, it has to be mentioned that this standard deviation is not only valid for two neighbored points, but for the overall measurement and for the full surface angle range.

From the MCS simulating an areal measurement using the polynomial freeform 1, a large standard deviation per sample point of up to $1\ \mu\mathrm{m}$ had been determined. This high standard deviation occurred in areas of high local slope of the SUT. Additionally, uncertainties in the calibration had been included in the MCS. Therewith, a conclusion about the repeatability from this MCS is not reliable. For the second MCS, using the cylinder surface, a comparison to a repeatability measurement from the experimental setup is available. Although the repeatability measurement has only been performed over 200 iterations, conclusions about the performance of the experimental setup can be drawn. The pattern of the standard deviation for each sample predicted by the MCS was confirmed by the repeatability measurement. Therewith, a basic accordance of the simulation model with the experimental setup can be confirmed. However, the standard deviation for each sample point as well as for the RMS surface deviation from the BFS show slightly higher values in the experimental repeatability measurement than in the MCS. This may be due to not considered error sources in the MCS. However, since the calibration data is varied in the experimental repeatability measurement, but in the MCS, a much smaller distribution of the determined BFS radii has been determined in the experimental repeatability measurement. The MCS predict an almost uniform uncertainty of up to $\pm 300\ \mu\mathrm{m}$ for the BFS radius, the determined mean radius of the experimental repeatability measurement deviates from the radius determined by the comparison measurement by only $\pm 38\ \mu\mathrm{m}$.

The MCS model considered multiple error sources in their maximum expected magnitude, although this magnitude might not occur in the experimental setup. For more exact conclusions from the MCS, further investigation on the error sources and their magnitude has to be done. Additionally, a more expressive investigation on the influence of measurement errors on the calibration procedure has to be performed. However, the error analysis provides a good model of the experimental setup to investigate the error sources.

8. Conclusion and outlook

In this work, a novel measurement technique for the characterization of specular freeform surfaces has been proposed. It provides the measurement of freeform specular surfaces deviation from a flat while utilizing the advantages of gradient-based measurement, which is not available in this combination yet. The measurement technique is a variation of laser deflectometry and combines a reflective laser scanning approach with the beam direction determination from a technique called Experimental Ray Tracing. A narrow beam is targeted onto the surface under test with a non-perpendicular angle. The reflected beam follows a direction, dependent on the incident beam and the surface angle. Having the incident beam direction and the reflected beam direction, conclusions about the surface angle can be drawn. With this, the measurement technique determines the gradient field of a surface under test. To reconstruct the surface from the gradient-field an integration method based on radial bases functions is applied, since this integration method is capable of handling non-even sample grids. The evaluation of the determined data is implemented using homogeneous coordinates. With geometrical optics used as optical model, advantages of the homogeneous coordinate representation of points and directions can be applied.

To confirm the essential functionality of the measurement principle, a simulation model has been implemented in Zemax OpticStudio. Using this simulation model, multiple different surface types have been investigated to proof the ability of this measurement technique to handle these surface types. Additionally, the proposed methods for the calibration have been confirmed using simulations.

An experimental measurement setup has been built up according to the proposed measurement principle and in correspondence with the simulation model. With the experimental setup, four different surfaces have been measured and evaluated. The determined results from the surface's reconstruction were compared to the expected surface model. For three of the samples, comparison measurements are available. Comparing the deviations from the model determined with the proposed method with the deviations determined from the comparison measurements show good agreements, but also deviations. However, the determined deviations are in the sub-μm range. Therewith the practical abilities of the measurement technique are proven.

In the error analysis multiple error sources are investigated. The results from the error analysis show relatively high deviations, which are higher than expected from the comparison of the results from the experimental measurements with the comparison measurements. However, it has to be taken into account that the error analysis handled multiple error sources as a worst-case scenario, even if it may be expected that they have minor magnitudes. A repeatability measurement of a cylinder lens has been performed, which can directly be compared to a Monte-Carlo-Simulation using the model function of the cylinder lens. The comparison revealed slightly higher uncertainties in the experimental repeatability measurement than predicted from the Monte-Carlo-Simulation, but also proved a good repeatability of the measurement technique for the performed cross-section measurement.

Comparing the results from the proposed measurement technique with the results from the comparison measurements and considering the experimental error analysis, it can be said that the proposed measurement technique is comparable with other available measurement techniques. Therewith, it offers a measurement technique to manufacturers, which is gradient-based and able to measure freeform surfaces. Especially in the field of freeform surface deviating from a flat basic shape, the available measurement techniques are exceeding their limits fast. This is overcome with the proposed measurement technique.

As all scanning measurement techniques, the proposed measurement technique also needs to scan with a high speed to be comparable with non-scanning measurement techniques. Thus, a fast beam position detector is needed. In the experimental setup proposed in this work, a CCD camera chip with a high resolution is used that only provides $7.6\ \mathrm{fps}$ defining the sample frequency. Using a position sensitive detector instead of a camera chip can improve the sample frequency drastically. However, these detectors have a higher centroid uncertainty and are more prone to environmental influences.

Another possibility to improve the measurement speed is to overcome the scanning of the two parallel detector planes serially. Using two cameras and a beamsplitter, the two camera positions can be realized in parallel. Using an integrated beam direction detector in one camera may also implement this improvement.

References

[1] E. Hecht, *Optik,* 7. Auflage, De Gruyter.

[2] K. P. Thompson and J. P. Rolland, *Freeform optical surfaces: a revolution in imaging optical design,* Opt. Photon. News 23, 30–35, 2012.

[3] K. Fuerschbach, *Freeform, φ-Polynomial Optical Surfaces: Optical Design, Fabrication and Assembly,* University of Rochester, 2014.

[4] A. Brömel, *Development and evaluation of freeform surface descriptions,* Friedrich–Schiller-Universität Jena, 2018.

[5] DIN Deutsches Institut für Normung, *Optics and photonics – Preparation of drawings for optical elements and systems – Part 12: Aspheric surfaces (ISO 10110-12:2007 + Amd 1:2013),* Beuth Verlag, 2016.

[6] DIN Deutsches Institut für Normung, *Optics and photonics – Preparation of drawings for optical elements and systems – Part 19: General description of surfaces and components (ISO 10110-19:2015),* Beuth Verlag, 2016.

[7] F. Z. Fang, X. D. Zhang, A. Weckenmann, G. X. Zhang and C. Evans, *Manufacturing and measurement of freeform optics,* CIRP Annals, Volume 62, Issue 2, 823-846, 2013.

[8] M. Beier, *Fertigung und Kompensation von metalloptischen Hochleistungsspiegelsystemen für den visuellen Spektralbereich,* Fraunhofer Verlag, Fraunhofer-Institut für angewandte Optik und Feinmechanik IOF, 2017.

[9] M. Khreishi, R. G. Ohl, J. M. Howard, J. .. Papa, R. McClelland, C. Hovis, T. Hadjimichael, P. Thompson, K. Ranson, R. Liang and N. Gorius, *Enabling precision coordinate metrology for universal optical testing and alignment applications,* Opt. Eng. 60(3). 035106, 2021.

[10] O. Cakmakci, S. Vo, S. Vogl, R. Spindelbalker, F. A. and J. P. Rolland, *Optical free-form surfaces in off-axis head-worn display design,* 7th IEEE/ACM International Symposium on Mixed and Augmented Reality, pp. 29-32, 2008.

[11] M. Essameldin, T. Binkele, F. Fleischmann, T. Henning and W. Lang, *Functional concept for the source independent beam-shaping of LED light,* OSA Continuum, Vol. 2, No. 3, 759-766, 2019.

[12] J. C. Minano, P. Benitez and A. Santamaria, *Free-Form Optics for Illumination,* Optical review Vol. 16, No. 2, 99–102, 2009.

[13] F. Chen, K. Wang, Z. Y. Liu, X. B. Luo and L. S., *Freeform lens for application-specific LED packaging,* Proc. International Conference on Electronic Packaging Technology & High Density Packaging (ICEPT-HDP), 443–447, 2009.

[14] P. Benitez and J. C. Minano, *Freeform optics for Photovoltaic Concentration,* EOS OSJ, 2012.

[15] W. Osten, *Optical metrology: the long and unstoppable way to become an outstanding measuring tool,* Proc. SPIE 10834, Speckle 2018: VII International Conference on Speckle Metrology, 1083402, 2018.

[16] S. R. Kiontke and U. Fuchs, *Analyzing and mitigating mid-spatial frequency errors,* Design and Fabrication Congress 2019 (Freeform, OFT), OSA, 2019.

[17] I. Fortmeier, R. Schachtschneider, V. Ledl, O. Matousek, J. Siepmann, A. Harsch, R. Beisswanger, Y. Bitou, Y. Kondo, M. Schulz and C. Elster, *Round robin comparison study on the form measurement of optical freeform surfaces,* J. Eur. Opt. Soc.-Rapid Publ. 16, 2, 2020.

[18] R. Schachtschneider, I. Fortmeier, M. Stavridis, J. Asfour, G. Berger, R. B. Bergmann, A. Beutler, T. Blümel, H. Klawitter, K. Kubo, J. Liebl, F. Löffler, R. Meeß, C. Pruss, D. Ramm, M. Sandner, G. Schneider, M. Wendel, I. Widdershoven, M. Schulz and C. Elster, *Interlaboratory comparison measurements of aspheres,* Meas. Sci. Technol. 29 055010, 2018.

[19] S. Lowitzsch, J. Kaminski and G. Häusler, *Shape reconstruction of 3D objects from noisy slope data,* DGaO-Proceedings 2005 – A22, 2005.

[20] C. Wagner and G. Häusler, *Information theoretical optimization for optical range sensors,* Applied Optics, Vol. 42, No. 27, 5418-5426, 2003.

[21] S. Ettl, J. Kaminski, M. C. Knauer and G. Häusler, *Shape reconstruction from gradient data,* Applied Optics 47, 2091-2097, 2008.

[22] D. Malacara, *Optical Shop Testing,* Second edition, John Wiley & Sons, Inc., 1992.

[23] Panasonic Corporation, "Ultrahigh Accurate 3-D Profilometer UA3P," [Online]. Available: https://www.panasonic.com/global/business/ua3p/specification.html. [Accessed 22nd June 2021].

[24] IBS Precision Engineering, "ISARA 400 KMG," [Online]. Available: https://www.ibspe.com/de/messsysteme/koordinatenmessmaschine-isara-400. [Accessed 22nd June 2021].

[25] Mahr GmbH, "MarSurf LD 130 / 260 Aspheric 2D und 3D," [Online]. Available: https://metrology.mahr.com/de/produkte/artikel/6850887-asphaerenmessplatz-marsurf-ld-130-260-aspheric-2d-und-3d. [Accessed 3rd June 2021].

[26] C. Pruss, G. B. Baer, J. Schindler and W. Osten, *Measuring aspheres quickly: tilted wave interferometry,* Opt. Eng. 56(11), 111713, 2017.

[27] R. Leach, *Optical Measurement of Surface Topography,* Springer-Verlag, 2011.

[28] A. Beutler, *Shape measurement of freeform optics,* Proc. SPIE 10692, Optical Fabrication, Testing, and Metrology VI, 106920O, 2018.

[29] AMETEK Inc., "LUPHOScan HD," [Online]. Available: https://www.taylor-hobson.com.de/products/ber%C3%BChrungslose-optische-3d-profilometer/luphos/luphoscan-260-420-hd. [Accessed 3rd June 2021].

[30] cyberTECHNOLOGIES GmbH, "CT 300," [Online]. Available: https://www.cybertechnologies.com/de/produkte/ct-300-hochauflosendes-und-beruhrungslos-arbeitendes-oberflachenmesssystem-fur-grose-flachen/. [Accessed 22nd June 2021].

[31] Mahr GmbH, "MarForm MFU 200 Aspheric 3D Hochgenauer 3D-Messplatz," [Online]. Available: https://www.mahr.de/de-ch/Leistungen/Fertigungsmesstechnik/Produkte/MarOpto---Messger%C3%A4te-f%C3%BCr-die-Optikindustrie/MarForm-MFU-200-Aspheric-3D/. [Accessed 22nd June 2021].

[32] Dutch United Instruments, "NMF Products," [Online]. Available: https://dutchunitedinstruments.com/form-metrology-products/#nmfproducts. [Accessed 22nd June 2021].

[33] M. Born and E. Wolf, *Principles of Optics,* 7th anniversary edition, Cambridge University Press, 2019.

[34] AMETEK Germany GmbH, "Verifire Produktreihe - Interferometer Systeme," [Online]. Available: https://zygo.de/?/de/met/interferometers/verifire/. [Accessed 23rd June 2021].

[35] L. Allen, R. Angel, J. D. Mangus, G. A. Rodney, R. R. Shannon and C. P. Spoelhof, *The Hubble space telescope - optical systems failure report,* NASA - National Aeronautics and Space Administration, 1990.

[36] P. E. Murphy, G. Forbes, J. Fleig, P. Dumas and M. Tricard, *Stitching Interferometry: A Flexible Solution for Surface Metrology,* Optics & Photonics News 14(5), 38-43, 2003.

[37] P. E. Murphy and C. Supranowitz, *Freeform testability considerations for subaperture stitching interferometry,* Proc. SPIE 11175, Optifab 2019, 111750Z, 2019.

[38] QED Technologies International, Inc., "ASI(Q)," [Online]. Available: https://qedmrf.com/en/ssimetrology/ssi-products/asiq. [Accessed 23rd June 2021].

[39] J. C. Wyant and V. P. Bennett, *Using Computer Generated Holograms to Test Aspheric Wavefronts,* Appl. Opt. 11, 2833-2839, 1972.

[40] J.-M. Asfour and A. G. Poleshchuk, *Asphere testing with a Fizeau interferometer based on a combined computer-generated hologram,* J. Opt. Soc. Am. A, Vol. 23, No. 1, 172-178, 2006.

[41] C. Pruss, S. Reichelt, H. J. Tiziani and W. Osten, *Computer-generated holograms in interferometric testing,* Opt. Eng. 43(11), 2004.

[42] P. Su, J. Ma, Q. Tan, G. Kang, Y. Liu and G. Jin, *Computer generated hologram null test of a freeform optical surface with rectangular aperture,* Opt. Eng. 51(2) 025801, 2021.

[43] DIOPTIC GmbH, "CGH Asphärenprüfung: Diffraktive Optiken für die Messtechnik von Asphären, Sphären, Zylindern und Freiformflächen," [Online]. Available: https://www.dioptic.de/diffraktive-optik/asphaerenpruefung/. [Accessed 23rd June 2021].

[44] A. Harsch, C. Pruss, A. Haberl and W. Osten, *Tilted wave interferometry for testing large surfaces,* Proc. SPIE 10829, Fifth European Seminar on Precision Optics Manufacturing, 1082908, 2018.

[45] Mahr GmbH, "MarOpto TWI 60 Tilted Wave Interferometer," [Online]. Available: https://www.mahr.de/en-us/Services/Production-metrology/Products/MarOpto---Measuring-Devices-for-Optics-Industry/MarOpto-TWI-60/. [Accessed 23rd June 2021].

[46] J. Hartmann, *Objektivuntersuchungen,* Zeitschrift für Intrumentenkunde 24, 1-21, 1904.

[47] D. R. Burada, K. K. Pant, V. Mishra, M. Bichra, G. S. Khan, S. Sinzinger and C. Shakher, *Development of metrology for freeform optics in reflection mode,* Proc. SPIE 10329, Optical Measurement Systems for Industrial Inspection X, 103291K, 2017.

[48] OPTOCRAFT GmbH , "OPTOCRAFT: Ihr Partner für optische Messtechnik," [Online]. Available: https://www.optocraft.de/de/home/. [Accessed 23rd June 2021].

[49] OPTOCRAFT GmbH, "SHSCam – Sensor head overview," [Online]. Available: https://www.optocraft.de/fileadmin/Download/TS_SHSCam_Sensor_Head _Overview_WWW_210525.pdf. [Accessed 23rd June 2021].

[50] M. V. R. K. Murty, *The Use of a Single Plane Parallel Plate as a Lateral Shearing Interferometer with a VisibleGas Laser Source,* Appl. Opt. 3, 531-534, 1964.

[51] P. Bon, G. Maucort, B. Wattellier and S. Monneret, *Quadriwave lateral shearing interferometry for quantitative phase microscopy of living cells,* Opt. Express 17, 13080-13094, 2009.

[52] PHASICS S.A, "SID4-HR," [Online]. Available: https://www.phasics.com/en/product/sid4-hr-wavefront-sensor/. [Accessed 23rd June 2021].

[53] C. Faber, E. Olesch, R. Krobot and G. Häusler, *Deflectometry challenges interferometry: the competition gets tougher!,* Proc. SPIE 8493, Interferometry XVI: Techniques and Analysis, 84930R, 2012.

[54] Z. Zhang, C. Chang, X. Liu, Z. Li, Y. Shi, N. Gao and Z. Meng, *Phase measuring deflectometry for obtaining 3D shape of specular surface: a review of the state-of-the-art,* Opt. Eng. 60(2) 020903, 2021.

[55] M. C. Knauer, J. Kaminski and G. Häusler, *Phase measuring deflectometry: a new approach to measure specular free-form surfaces,* Proc. SPIE 5457, Optical Metrology in Production Engineering, 2004.

[56] G. Häusler, C. Faber, E. Olesch and E. S., *Deflectometry vs. Interferometry,* Proc. SPIE 8788, Optical Measurement Systems for Industrial Inspection VIII, 87881C, 2013.

[57] ISRA VISION AG, " SpecGAGE3D-curved," [Online]. Available: https://www.isravision.com/en/ready-to-use/surface-inspection/surface-defects/specgage3d-curved/. [Accessed 24th June 2021].

[58] S. Krey, W. D. van Amstel, K. Szwedowicz, J. Campos, A. Moreno and E. J. Lous, *A fast optical scanning deflectometer for measuring the topography of large silicon wafers,* Proc. SPIE 5523, Current Developments in Lens Design and Optical Engineering V, 2004.

[59] M. Schulz, G. Ehret and A. Fitzenreiter, *Scanning deflectometric form measurement avoiding path-dependent angle measurement errors,* Journal of the European Optical Society - Rapid publications, Europe, v. 5, 2010.

[60] E. Hofbauer and R. Rascher, *Deflectometric Acquisition of Large Optical Surfaces DaOS,* Optik & Photonik, 11, 40-44, 2016.

[61] I. Weingaertner, M. Schulz and C. Elster, *Novel scanning technique for ultraprecise measurement of topography,* Proc. SPIE 3782, Optical Manufacturing and Testing III, 1999.

[62] M. Rosete-Aguilar and R. Díaz-Uribe, *Profile testing of spherical surfaces by laser deflectometry,* Appl. Opt. 32, 4690-4697, 1993.

[63] S. Krey, I. Erichsen, I. Mahns, W. D. van Amstel and K. Vielhaber, *A deflectometric sensor for the on-machine surface form measurement and adaptive manufacturing,* Proc. SPIE 7718, Optical Micro- and Nanometrology III, 77180C, 2010.

[64] A. Miks, J. Novak and P. Novak, *Method for reconstruction of shape of specular surfaces using scanning beam deflectometry,* Optics and Lasers in Engineering, Volume 51, Issue 7, 2013.

[65] Q. Hao, Q. Zhu and Y. Wang, *Deflectometer with synthetically generated reference circle for aspheric surface testing,* Optics & Laser Technology, Volume 37, Issue 5, 2005.

[66] T. Rindfleisch, *Photometric Method For Lunar Topography,* Photogrammetric Eng., vol. 32, pp. 262-276, 1966.

[67] J.-F. Hu, W.-S. Zheng, X. Xie and J. Lai, *Sparse transfer for facial shape-from-shading,* Pattern Recognition, Vol. 68, 2017.

[68] S. Ordones, M. Servin, M. Padilla, I. Choque, J. L. Flores and A. Muñoz, *Shape defect measurement by fringe projection profilometry and phaseshifting algorithms,* Opt. Eng. 59(1), 014107, 2020.

[69] H. Yuan, G. Feng, H. Li, L. Cui and Z. Bao, *Phase-shifting coding method for absolute phase retrieval,* Opt. Eng. 58(10), 104103, 2019.

[70] A. Dickins, T. Widjanarko, D. Sims-Waterhouse, A. Thompson, S. Lawes, N. Senin and R. Leach, *Multi-view fringe projection system for surface topography measurement during metal powder bed fusion,* J. Opt. Soc. Am. A 37, B93-B105, 2020.

[71] T. Kishimoto and M. Fujigakia, *Development of Handy Type Full-color and Real-time 3D Measurement System Using Linear LED Device,* Optics & Photonics International Congress 2019, OPTM-3-02, 2019.

[72] G. Häusler and G. Schneider, *Testing optics by experimental ray tracing with a lateral effect photodiode,* OSA - Applied Optics, Vol. 27, No. 24, 1988.

[73] J. E. Greivenkamp, *Field Guide to Geometrical Optics,* SPIE Field Guides Volume FG01, SPIE Press, 2004.

[74] G. H. Spencer and M. V. R. K. Murty, *General Ray-Tracing Procedure†,* J. Opt. Soc. Am. 52, 672-678, 1962.

[75] D. Marsh, *Applied Geometry for Computer Graphics and CAD,* 2nd edition, Springer, 2005.

[76] A. Miks and P. Novak, *Determination of unit normal vectors of aspherical surfaces given unit directional vectors of incoming and outgoing rays: comment,* J. Opt. Soc. Am. A 29, 1356-1357, 2012.

[77] J. Bloomenthal und J. Rokne, *Homogeneous coordinates,* The Visual Computer (1994) 11:15-26, Springer-Verlag, 1994.

[78] H. Meschkowski, D. Laugwitz, M. Hengst and D. Müller, *Meyers Handbuch über Mathematik,* Bibliographisches Insititut, Mannheim, 1967.

[79] I. N. Bronstein and K. A. Semendjajew, *Taschenbuch der Mathematik,* 19. Völlig überarbeitete Auflage, Verlag Harri Deutsch, Thun, 1980.

[80] G. Rill and T. Schaeffer, *Grundlagen und Methodik der Mehrkörpersimulation,* 3. Auflage, Springer Vieweg, 2017.

[81] J. Ho, J. Lim, M.-H. Yang und D. Kriegman, *Integrating Surface Normal Vectors Using Fast Marching Method,* ECCV 2006, Part III, LNCS 3953, pp. 239-250, 2006.

[82] U. Ceyhan, T. Henning, F. Fleischmann, D. Hilbig and D. Knipp, *Measurements of aberrations of aspherical lenses using experimental ray tracing,* Proc. SPIE 8082, Optical Measurement Systems for Industrial Inspection VII, 2011.

[83] R. Szeliski, *Computer Vision: Algorithms and Applications,* Springer, 2011.

[84] A. M. J. Campos and L. P. Yaroslavsky, *Frequency response of five integration methods to obtain the profile from its slope,* Optical engineering 44(3), 033604, 2005.

[85] W. Southwell, *Wave-front estimation from wave-front slope measurements,* J. Opt. Soc. Am., Vol. 70, No.8, 1980.

[86] H. Wendland, *Piecewise polynomial, positive definite and compactly supported radial functions of minimal degree,* Advances in Computational Mathematics 4, 389-396, 1994.

[87] S. Lowitzsch, J. Kaminski, M. C. Knauer and G. Häusler, *Vision and Modeling of Specular Surfaces,* Proc. VMV, 479-486, 2005.

[88] S. Ettl, J. Kaminski and G. Häusler, *Generalized hermite interpolation with radial basis functions considering only gradient data,* Curve Surf. Fitting: Avignon 2006, 141–149, 2007.

[89] T. Binkele, *Evaluation of a method for shape reconstruction from gradient data,* Hochschule Bremen, 2017.

[90] W. H. Press, S. A. Teukolsky, W. T. Vetterling and B. P. Flannery, *Numerical Recipes - The Art of Scientific Computing,* Third Edition, Cambringe University Press, 2007.

[91] L. Huang, I. Mourad, Z. Chao, K. Kaznatcheev, L. Zhou and A. Asundi, *Comparison of two-dimensional integration methods for shape reconstruction from gradient data,* Optics and Lasers in Engineering, Vol. 64, 1-11, 2015.

[92] A. Agrawal, R. Chellappa and R. Ramesh, *An algebraic approach to surface reconstruction from gradient fields,* Tenth IEEE International Conference on Computer Vision (ICCV'05), Volume 1, 174-181, 2005.

[93] H. Ng, T. Wu and C. Tang, *Surface-from-Gradients without Discrete Integrability Enforcement: A Gaussian Kernel Approach,* IEEE Transactions on Pattern Analysis and Machine Intelligence, vol. 32, no. 11, pp. 2085-2099, 2010.

[94] DIN Deutsches Institut für Normung, *Optics and photonics – Preparation of drawings for optical elements and systems – Part 5: Surface form tolerances (ISO 10110-5:2015),* Beuth Verlag, 2016.

[95] DIN Deutsches Institut für Normung, *Optics and photonics – Preparation of drawings for optical elements and systems – Part 8: Surface texture; roughness and waviness (ISO 10110-8:2010),* Beuth Verlag, 2012.

[96] J. E. Harvey and A. Kotha Thompson, *Scattering effects from residual optical fabrication errors,* Proc. SPIE 2576, International Conference on, 1995.

[97] I. Kaya, *Mathamatical and computational methods for freeform optical shape description,* Dissertation, College of Engineering and Computer Science, University of Central Florida, 2013.

[98] F. Zernike, *Beugungstheorie des Schneidenverfahrens und seiner verbesserten Form, der Phasenkontrastmethode,* Physica, Volume 1, Issues 7–12, 689-704, 1934.

[99] V. N. Mahajan, Optical imaging and aberrations - Part II: Wave diffraction optics, Society of Photo-Optical Instrumentation Engineers, 2011.

[100] D. Hilbig, *Characterization of shape and functionality of optical components by gradient based transmission test,* Dissertation, Jacobs Unversity Bremen, University of Applied Sciences Bremen, 2015.

[101] Z. Hosseinimakarem und A. D. E. C. J. Davies, *Zernike polynomials for mid-spatial frequency representation on optical surfaces,* Proc. SPIE 9961, Reflection, Scattering, and Diffraction from Surfaces V, 99610P, 2016.

[102] M. J. D. Powell, *An efficient method for finding the minimum of a function of several variables without calculating derivatives,* The Computer Journal, Volume 7, Issue 2, 155–162, 1964.

[103] Zemax LLC, *OpticStudio,* Version 21.1.2, 2021.

[104] Zemax LLC, *OpticStudio - User Manual,* Version 21.1, January 2021, 2021.

[105] Team Anaconda, *Anaconda,* Edition 2020.11 with Python 3.8.5, 2020.

[106] R. Franke, *A critical comparison of some methods for interpolation of scattered data,* Naval Postgraduate School, Monterey, California, 1979.

[107] M. Mongillo, *Choosing Basis Functions and Shape Parameters for Radial Basis Function Methods,* SIAM undergraduate research online, 2011.

[108] Thorlabs Inc., "CFC2-A - Adjustable Fiber Collimator," [Online]. Available: https://www.thorlabs.com/thorproduct.cfm?partnumber=CFC2-A. [Accessed 2nd June 2021].

[109] Thorlabs Inc., "Adjustable Aspheric FC/PC and FC/APC Collimators," [Online]. Available: https://www.thorlabs.com/newgrouppage9.cfm?objectgroup_id=4353#. [Accessed 2nd June 2021].

[110] OWIS GmbH, "Product information FAPO 65," [Online]. Available: https://www.owis.eu/fileadmin/user_upload/owis.eu/products/ pdf/pi_fapo_65.pdf. [Accessed 2nd June 2021].

[111] Steinmeyer Mechatronik GmbH, "PMT160-DC - Lineartische," [Online]. Available: https://www.steinmeyer-mechatronik.de/positioniersysteme/standardsysteme/lineartische/pmt160-dc/. [Accessed 2nd June 2021].

[112] Semiconductor Components Industries, LLC, 2, "KAI-16070 - Interline CCD Image Sensor," [Online]. Available: https://www.onsemi.com/pdf/datasheet/kai-16070-d.pdf. [Accessed 2nd June 2021].

[113] M.-K. Hu, *Visual Pattern Recognition by Moment Invariants,* IRE Transactions on Information Theory, vol. 8, no. 2, pp. 179-187, 1962.

[114] X. Ji, Y. Baykal and X. Jia, *Changes of the centroid position of laser beams propagating through an optical system in turbulent atmosphere,* Optics & Laser Technology, 54, 199-207, 2013.

[115] Thorlabs Inc., "LJ1363L1 - N-BK7 Plano-Convex Cylindrical Lens, Uncoated," [Online]. Available: https://www.thorlabs.com/thorproduct.cfm?partnumber=LJ1363L1. [Accessed 3rd June 2021].

[116] T. Arnold, G. Böhm and H. Paetzelt, *Ultra-Precision Surface Machining with Reactive Plasma Jets,* Contrib. Plasma Phys., 54, 145-154, 2014.

[117] H. Paetzelt, G. Böhm and T. Arnold, *Etching of silicon surfaces using atmospheric plasma jets,* Plasma Sources Sci., 2015.

[118] M. A. Brown, *Measuring stress in thin film-substrate systems featuring spatial nonuniformities of film thickness and/or misfit strain,* Dissertation, California Institute of Technology, Pasadena, 2007.

[119] DIN Deutsches Institut für Normung, *Optik und Photonik – Interferometrische Messung von optischen Elementen und Systemen – Teil 4: Interpretation und Beurteilung der Toleranzen nach ISO 10110,* Beuth Verlag, 2016.

[120] DIN Deutsches Institut für Normung, *Geometrische Produktspezifikation (GPS) – Oberflächenbeschaffenheit: Flächenhaft – Teil 604: Merkmale von berührungslos messenden Geräten (Weißlicht-Interferometrie) (ISO 25178-604:2013),* Beuth Verlag, 2013.

[121] X. C. de Lega and P. J. de Groot, *Lateral resolution and instrument transfer function as criteria for selecting surface metrology instruments,* Imaging and Applied Optics Technical Papers, OSA Technical Digest, 2012.

[122] J. W. Goodman, *Introduction to Fourier Optics,* Third edition, Roberts & Company Publishers, 2005.

[123] R. Scheithauer, *Signale und Systeme,* B. G. Teubner Stuttgart, 1998.

[124] Joint Committee for Guides in Metrology, *Evaluation of measurement data - Guide to the expression of uncertainty in measurement,* JCGM 100:2008 - GUM 1995 with minor corrections, 2008.

[125] European Machine Vision Association, *EMVA Standard 1288: Standard for Characterization of Image Sensors and Cameras,* 2016.

[126] Z. Yusheng, Z. Zhifeng, L. Yang, L. Dongdong, L. Jintao, C. Yinhang, Y. S., L. Wenlong and W. Xinjie, *Experimental Study of Laser Beam Drift,* International Conference on Optoelectronics and Microelectronics, pp. 107, 2015.

[127] N. Schiering, *Die richtige Wahl von Verteilungen,* 277. PTB-Seminar Berechnung der Messunsicherheit – Empfehlungen für die Praxis, PTB Berlin, 2014.

[128] DKD-Fachausschuss Messunsicherheit, *Praxisgerechte Ermittlung der Messunsicherheit - Grundlagen und Vorgehensweisen für einfache Modelle ohne Korrelation,* Version 5.3, 2012.

[129] P. Profos and T. Pfeifer, *Grundlagen der Meßtechnik,* 5., überarbeitete Auflage, R. Oldenbourg Verlag, 1997.

[130] U. Ceyhan, *Characterization of aspherical lenses by experimental ray tracing,* Jacobs University, Bremen, School of Engineering and Science, 2003.

[131] I. Lira, *Evaluating the measurement uncertainty - Fundamentals and practical guidance,* IOP - Institute of Physics Publishing, 2002.

[132] Joint Committee for Guides in Metrology, *Evaluation of measurement data - Supplement 1 to the "Guide to the expression of uncertainty in measurement" - Propagation of distributions using a Monte Carlo method,* JCGM 101:2008 - First edition 2008, 2008.

[133] imc Test & Measurement GmbH, "Messunsicherheitsbestimmung in imc FAMOS–Die Monte-Carlo-Methode," [Online]. Available: https://www.imc-tm.de/fileadmin/Public/Downloads/ Whitepapers/WP_DE_MonteCarloMethode.pdf. [Accessed 13th June 2021].

Publications

[A] T. Binkele, D. Hilbig, F. Fleischmann, T. Henning, *Determination of the paraxial focal length according to its definition by the German DIN standard in measurements*, DGaO-Proceedings 2016 - P086, ISSN: 1614-8436 (2016)

[B] D. Hilbig, U. Ceyhan, T. Binkele, G. Gutierrez, T. Henning, F. Fleischmann, D. Knipp, *Experimental ray tracing for characterization of optical components*, DGaO-Proceedings 2016 – P011, ISSN: 1614-8436 (2016)

[C] T. Binkele, D. Hilbig, F. Fleischmann, T. Henning, *Determination of the paraxial focal length of strong focusing lenses using Zernike polynomials in simulation and measurement*, Proc. SPIE 9960, Interferometry XVIII, 99600N; doi:10.1117/12.2238059 (2016)

[D] T. Binkele, D. Hilbig, T. Henning, F. Fleischmann, *Determination of the paraxial focal length using Zernike polynomials over different apertures*, Proc. SPIE 10110, Photonic Instrumentation Engineering IV, 1011008; doi:10.1117/12.2251442 (2017)

[E] T. Binkele, D. Hilbig, F. Fleischmann, T. Henning, *Calibration of the incident beam in a reflective topography measurement from an unknown surface*, Proc. SPIE 10329, Optical Measurement Systems for Industrial Inspection X, 103291S; doi: 10.1117/12.2270291 (2017)

[F] T. Binkele, D. Vassmer, D. Hilbig, F. Fleischmann, T. Henning, *Shape measurement of freeform surfaces using experimental ray tracing*, Proc. SPIE 10448, Optifab 2017, 1044816; doi: 10.1117/12.2279797 (2017)

[G] T. Binkele, D. Hilbig, F. Fleischmann, T. Henning, *Measurement of spherical, aspherical and freeform specular surfaces using experimental raytracing in simulation and measurement*, Proc. SPIE 10695, Optical Instrument Science, Technology, and Applications, 106950F; doi: 10.1117/12.2314924 (2018)

[H] T. Binkele, D. Hilbig, T. Henning, F. Fleischmann, *Freeform surface measurement as an example for the advantages of the use of databases in measurement setups*, DGaO-Proceedings 2018 - P006, ISSN: 1614-8436 (2018)

[I] T. Binkele, D. Hilbig, F. Fleischmann, T. Henning, *Using computer vision methods for the measurement of freeform surfaces with experimental ray tracing*, Imaging and Applied Optics 2018 (3D, AO, AIO, COSI, DH, IS, LACSEA, LS&C, MATH, pcAOP), The Optical Society (Optical Society of America), paper JW4A.23 (2018)

[J] T. Binkele, D. Hilbig, U. Ceyhan, G. Gutierrez, M. Essameldin, T. Henning, F. Fleischmann, *Experimental Ray Tracing – from simulation to reality*, Frontiers in Optics / Laser Science, OSA Technical Digest (Optical Society of America), paper JW4A.8 (2018)

[K] T. Binkele, D. Hilbig, M. Essameldin, T. Henning, F. Fleischmann, *Measurement of freeform specular surfaces in a multilanguage data analysis environment*, EOSAM 2018 Proceedings, The European Optical Society Biennial Meeting 2018 (2018)

[L] T. Binkele, R. Dylla-Spears, M. A. Johnson, D. Hilbig, M. Essameldin, T. Henning, F. Fleischmann, *Characterization of gradient index optical components using experimental ray tracing*, Proc. SPIE 10925, Photonic Instrumentation Engineering VI, 109250D (2019)

[M] M. Essameldin, T. Binkele, F. Fleischmann, T. Henning, W. Lang, *Functional concept for the source independent beam-shaping of LED light*, OSA Continuum 2, 759-766 (2019)

[N] T. Binkele, D. Hilbig, M. Essameldin, T. Henning, and F. Fleischmann, *Freeform Surface Measurement with Experimental Ray Tracing – Refraction vs. Reflection*, Optical Design and Fabrication 2019 (Freeform, OFT), OSA Technical Digest (Optical Society of America), paper JT5A.13 (2019)

[O] T. Binkele, D. Hilbig, M. Essameldin, J. Rase, T. Henning, F. Fleischmann, *Hochpräzise Messung flacher spiegelnder Freiform-Oberflächen mit Experimental Ray Tracing*, DGaO-Proceedings 2019 – P005, ISSN: 1614-8436 (2019)

[P] T. Binkele, D. Hilbig, M. Essameldin, T. Henning, F. Fleischmann, W. Lang, *Precise measurement of known and unknown freeform surfaces using Experimental Ray Tracing*, Proc. SPIE 11056, Optical Measurement Systems for Industrial Inspection XI, 110561N (2019)

[Q] T. Binkele, D. Hilbig, M. Essameldin, T. Henning, F. Fleischmann, *Component-level Test of Complex Beam Shaping Optics for Quasi-point Sources*, Frontiers in Optics + Laser Science APS/DLS, OSA Technical Digest (Optical Society of America), paper JW3A.1 (2019)

[R] T. Binkele, D. Hilbig, M. Essameldin, F. Fleischmann, T. Henning, W. Lang, *Measurement of form and mid-spatial-frequency errors of specular freeform surfaces*, Proc. SPIE 11175, Optifab 2019, 1117513 (2019)

[S] T. Binkele, D. Hilbig, M. Essameldin, T. Henning, F. Fleischmann, *Fast measurement of optical components using a PSD for experimental ray tracing*, Proc. SPIE 11287, Photonic Instrumentation Engineering VII, 112870V (2020)

[T] T. Binkele, D. Hilbig, M. Essameldin, T. Henning, F. Fleischmann, *Form and Mid-Spatial-Frequency Measurement of Unknown Freeform Surfaces*, SMSI Conference – Sensor and Measurement Science International (2020)

[U] M. Essameldin, T. Binkele, F. Fleischmann, T. Henning, W. Lang, *Design and evaluation of a freeform lens-array for a structured light illumination*, OSA Continuum 4, 774-782 (2021)

[V] T. Binkele, D. Hilbig, M. Essameldin, T. Henning, F. Fleischmann, W. Lang, *Characterization of Specular Freeform Surfaces from Reflected Ray Directions using Experimental Ray Tracing*, J. Sens. Sens. Syst., 10, 261-270 (2021)

Appendix

A. First and second order derivatives of the Wendland's function

$$\frac{\partial\psi}{\partial x}=\frac{2x\left(\rho-\sqrt{x^2+y^2}\right)^5}{3\rho^8\sqrt{x^2+y^2}}\Big(-9\rho^2-54\rho\sqrt{x^2+y^2}-105x^2-105y^2 + \left(\rho-\sqrt{x^2+y^2}\right)\left(9\rho+35\sqrt{x^2+y^2}\right)\Big)$$

$$\frac{\partial\psi}{\partial y}=\frac{2y\left(\rho-\sqrt{x^2+y^2}\right)^5}{3\rho^8\sqrt{x^2+y^2}}\Big(-9\rho^2-54\rho\sqrt{x^2+y^2}-105x^2-105y^2 + \left(\rho-\sqrt{x^2+y^2}\right)\left(9\rho+35\sqrt{x^2+y^2}\right)\Big)$$

$$\frac{\partial^2\psi}{\partial x^2}=\frac{1}{3\rho^8}\Big(-56\rho^6+2520\rho^4x^2+840\rho^4y^2-8960\rho^3x^2\sqrt{x^2+y^2}-2240\rho^3y^2\sqrt{x^2+y^2} + 12600\rho^2x^4+15120\rho^2x^2y^2+250\rho^2y^4-8064\rho x^4\sqrt{x^2+y^2} - 9408\rho x^2y^2\sqrt{x^2+y^2}-1344\rho y^4\sqrt{x^2+y^2}+1960x^6+4200x^4y^2+2520x^2y^4 + 280y^6\Big)$$

$$\frac{\partial^2\psi}{\partial x\partial y}=\frac{\partial^2\psi}{\partial y\partial x}=\frac{560xy}{\rho^8}\Big(\rho^4-4\rho^3\sqrt{x^2+y^2}+6\rho^2x^2+6\rho^2y^2-4\rho x^2\sqrt{x^2+y^2}-4\rho y^2\sqrt{x^2+y^2} + x^4+2x^2y^2+y^4\Big)$$

$$\frac{\partial^2\psi}{\partial y^2}=\frac{1}{3\rho^8}\Big(-56\rho^6+840\rho^4x^2+2520\rho^4y^2-2240\rho^3x^2\sqrt{x^2+y^2}-8960\rho^3y^2\sqrt{x^2+y^2} + 2520\rho^2x^4+15120\rho^2x^2y^2+12600\rho^2y^4-1344\rho x^4\sqrt{x^2+y^2} - 9408\rho x^2y^2\sqrt{x^2+y^2}-8064\rho y^4\sqrt{x^2+y^2}+280x^6+2520x^4y^2+4200x^2y^4 + 1960y^6\Big)$$

B. First order derivatives of the surface model functions

Franke surface

May $s(\boldsymbol{x})$ be the Franke surface as defined in Equation (4.2), its first order derivatives are

$$\frac{\partial s(\boldsymbol{x})}{\partial x}=-0.3375(-2+0.9x)e^{-0.25(-2+0.9x)^2-0.25(-2+0.9y)^2}-\frac{13.5}{490}(1+0.9x)e^{-\frac{(1+0.9y)^2}{49}-\frac{(1+0.9y)^2}{10}} - 0.225(-7+0.9x)e^{-0.25(-7+0.9x)^2-0.25\cdot(-3+0.9y)^2} + 0.36(-4+0.9x)e^{-(-7+0.9y)^2-(-4+0.9x)^2}$$

and

$$\frac{\partial s(\boldsymbol{x})}{\partial y}=-0.3375(-2+0.9y)e^{-0.25(-2+0.9x)^2-0.25(-2+0.9y)^2}-\frac{6.75}{50}(1+0.9y)e^{-\frac{(1+0.9y)^2}{49}-\frac{(1+0.9y)^2}{10}} - 0.225(-3+0.9y)e^{-0.25(-7+0.9x)^2-0.25(-3+0.9y)^2} + 0.36(-4+0.9y)e^{-(-7+0.9y)^2-(-4+0.9x)^2}.$$

Cylinder surface

May $s(\boldsymbol{x})$ be the cylinder surface as defined in Equation (4.3), its first order derivatives in y-direciton is

$$\frac{\partial s(\boldsymbol{x})}{\partial y} = \begin{cases} -\dfrac{y}{\sqrt{\hat{R}^2 - y^2}} & \text{for } \hat{R} > 0 \\ \dfrac{y}{\sqrt{\hat{R}^2 - y^2}} & \text{for } \hat{R} < 0 \end{cases}$$

for $\hat{R} \neq 0$.

Polynomial freeform 1

May $s(\boldsymbol{x})$ be the polynomial freeform 1 as defined in Equation (4.4), its first order derivatives are

$$\frac{\partial s(\boldsymbol{x})}{\partial x} = 7.0 \cdot 10^{-3} x - 10^{-4} x^3$$

and

$$\frac{\partial s(\boldsymbol{x})}{\partial y} = -5.0 \cdot 10^{-3} y + 1.4 \cdot 10^{-4} y^3.$$

Polynomial freeform 2

May $s(\boldsymbol{x})$ be the polynomial freeform 2 as defined in Equation (5.8), its first order derivatives are

$$\frac{\partial s(\boldsymbol{x})}{\partial x} = 0.005x - 6 \cdot 10^{-5} x^3$$

and

$$\frac{\partial s(\boldsymbol{x})}{\partial y} = 0.005y - 6 \cdot 10^{-5} y^3.$$

C. Datasheet of the laser diode

ROITHNER LASERTECHNIK
Wiedner Hauptstraße 76, A-1040 Vienna, Austria
Tel.: ++43 1 586 52 43-0, Fax -44, office@roithner-laser.com

635nm Pigtailed Modules with Single-mode Beam

Features:

- Single-mode beam
- 4µm core fiber with N.A.0.11
- FC/ST/SMA 905 connector available
- Pigtail output

Applications:

- Medical
- Industrial

Absolute Maximum Ratings

Parameter	Symbol	Value	Unit
Reverse Voltage	V_r	2.0	V
Operating Temperature	T_{op}	+10~+30	°C
Storage Temperature	T_{stg}	-20 ~ +80	°C
Lead Soldering Temperature (10 sec.)	T_{ls}	260	°C

Specifications	RLCD-S63
Peak Wavelength @25℃	635±10nm
Output Power (Typ.)	1/2/10/20mW
Spectral Width (FWHM)	≤3nm
Temperature Coefficient of Wavelength	0.2nm / °C
Threshold Current	<30mA
Operating Current	<50mA
Operating Voltage (Typ.)	2V
Fiber core Diameter	4µm
Fiber Numerical Aperture	0.11
Fiber Length (Typ.)	70cm
Connector Type	SMA905 / ST / FC
Package Type	Coaxial

ROITHNER LASERTECHNIK
Wiedner Hauptstraße 76, A-1040 Vienna, Austria
Tel.: ++43 1 586 52 43-0, Fax -44, office@roithner-laser.com

Coaxial Package View

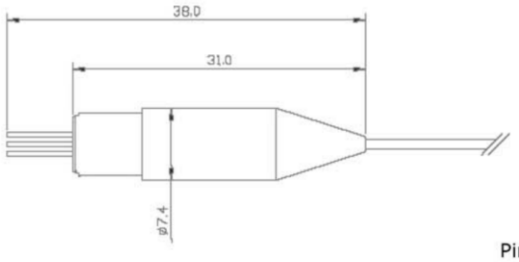

Pin Layout
1. LD Cathode (-)
2. LD Anode (+), PD Cathode (-), Case
3. PD Anode (+)

OPERATIONAL PRECAUTIONS

Laser Safety

Laser light emitted from this laser diode is harmful to the human. Avoid looking directly into the module aperture or the fiber end when the device is in operation.

ESD Caution

Handle laser diodes and modules with extreme care to prevent electrostatic discharge (ESD), which is the main cause of unexpected diode failure.
Always wear wrist straps, work on grounded anti-static mats, and follow extremely rigorous anti-static procedures. If a laser diode is handled carelessly, it may be destroyed instantly by ESD from a human body. When not in use, shorten the leads of laser diodes to protect against ESD.

Operation Caution

Prevention of current surge

Laser diodes are of fast response devices. Use surge-protected outlets to prevent the possibilities of large momentary transients from switches, power supply and other high current devices such as soldering irons, vacuum pumps, fluorescent lamps, etc.

Soldering

- Keep the solder iron (30W) tip temperature less than 260°C.
- Apply solder promptly once the connections are brought in place.
- Grounded the metal part of the solder iron tip if solder iron is used more than 5 min.

Cutting leads

- Perform the work over conductive mats.
- Wear grounded anti-static wrist bands.
- Do not use air nippers as they are a source of static electricity.

Handling

ROITHNER LASERTECHNIK
Wiedner Hauptstraße 76, A-1040 Vienna, Austria
Tel.: ++43 1 586 52 43-0, Fax -44, office@roithner-laser.com

- Do not directly touch the leads of laser diodes or modules.
- Do not touch the window glass of a laser diode or a finer emitting end with bare hands.
- Use care to prevent damage to the window glass by tools or other objects.
- When dust deposited on the window glass, be sure to remove with an air gun.

Fiber Caution

The bending diameter of fiber should be larger than 4cm for short term storage and larger than 8cm for long term storage.

Operation Procedure

a) Connect the electrodes of a laser diode or module correctly according to the supplied pin layout.
b) Set the current or voltage to zero before switching on the power supply.
c) Increase the current or voltage gradually to the required value; never exceed the rated value.
d) Suggest to put the modules on a heat sink when operation.
e) Decrease the current or voltage gradually to zero when finish.
f) Disconnect the module.
g) Turn off the power supply.

Electrically shorten LD module and store in non-extreme conditions.
Suggest using the constant current power supply.

D. Technical drawing of the adjustable aspheric collimator CFC2-A

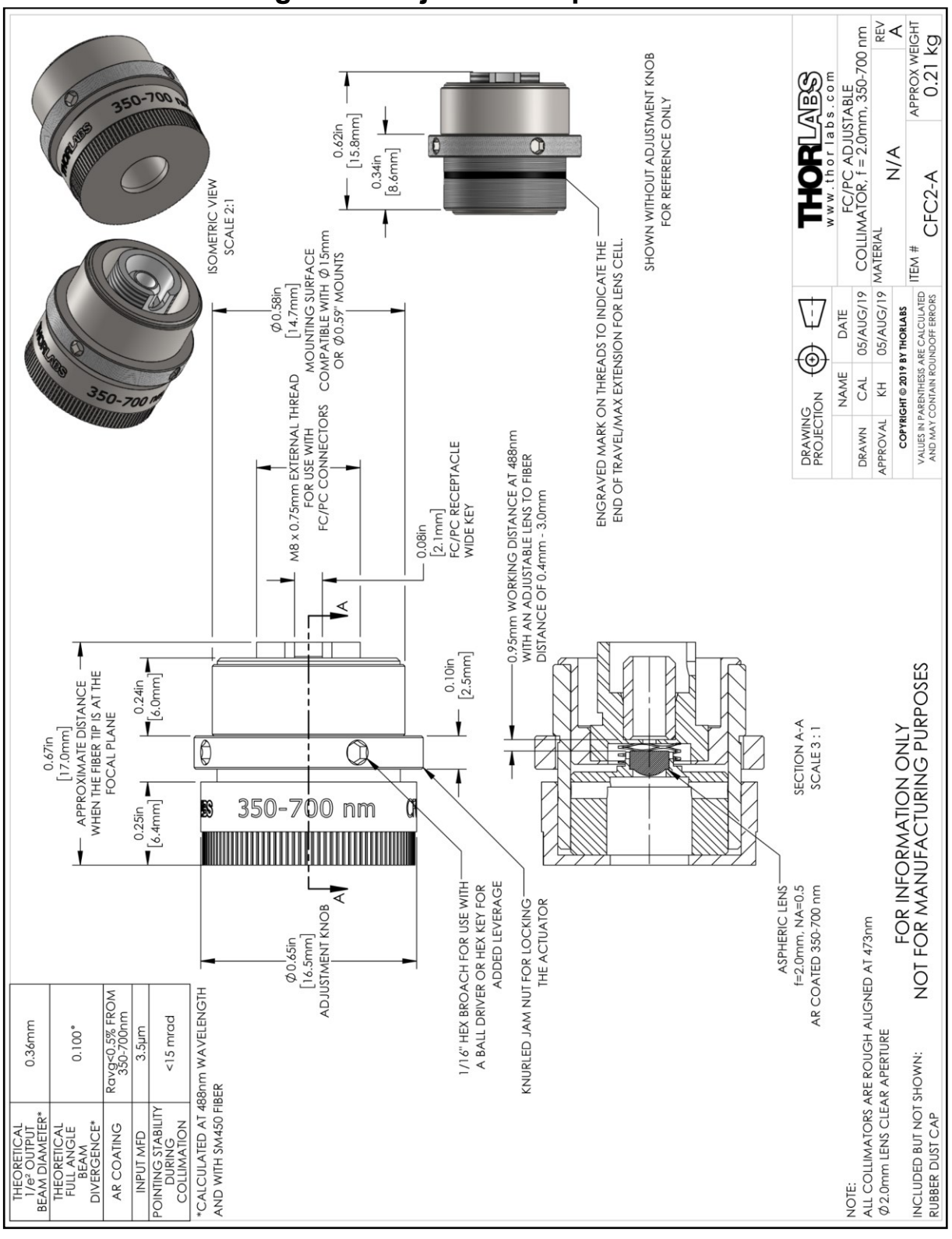

Lineartische | Linear Stages
PMT160-DC

Mehr Informationen | more information: **www.steinmeyer.com**

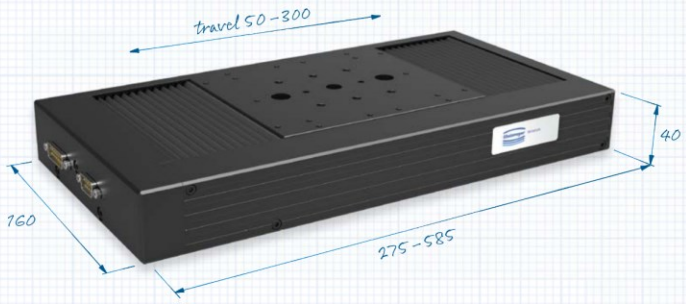

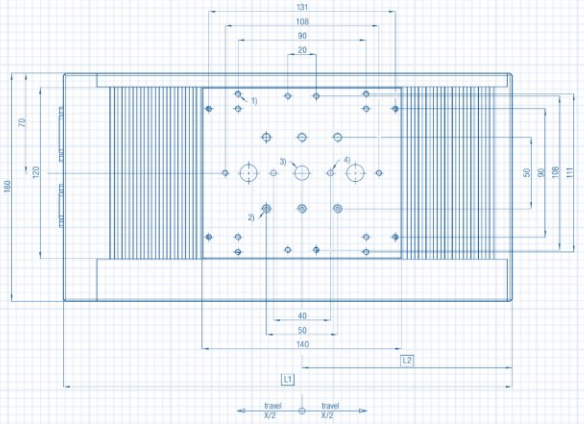

1) M 4; depth 7 (18×)
2) M 6; depth 8 (6×)
3) Ø 10 H11
4) Ø 4 H7; depth 6 (2×)

DC R KR DC L KR

Hochpräziser Messtisch
Der PMT160 mit DC-Motor ist ein Präzisionsmesstisch, der über hervorragende Ablaufwerte verfügt. Zudem garantiert eine vorgespannte Kugelgewindespindel hohe Steifigkeit und ein minimales Umkehrspiel.

Schnell und einfach kombinierbar
Der PMT160 mit DC-Motor erreicht in Kombination mit einem linearen Wegmesssystem kleinste Schrittweiten bei vergleichsweise hohen Positioniergeschwindigkeiten. Er ist leicht zum 2-Achs-System kombinierbar oder lässt sich, optional mit elektromagnetischer Bremse, ideal als vertikale Achse einsetzen.

Für dynamische Anwendungen
Der hochpräzise Lineartisch eignet sich für alle Anwendungen, die perfekte Ebenheit, kleinste Toleranzen für Nicken und Gieren sowie ein gleichmäßiges Ablaufverhalten benötigen. Zum Einsatz kommt der PMT160-DC deshalb vor allem in der Messtechnik, der Mikrobearbeitung oder in der Optik.

High precision measurement stage
The PMT160 with DC motor is a precision measurement stage that has outstanding operational parameters. A preloaded ball screw ensures high stiffness and minimum backlash.

Quick and easy to combine
The PMT160 with DC motor, in combination with a linear distance measuring system, achieves very small adjustment increments at high positioning speeds. It is easily combined to create a two axis system or, when equipped with an electromagnetic brake, is ideal for use as a vertical axis.

For highly dynamic applications
The high precision linear stage is suitable for all applications that require excellent flatness, very small tolerances for pitch and yaw as well as smooth movement. The PMT160-DC is therefore primarily used in measurement engineering, micromachining or in optics.

Modelle und Spezifikationen | Models and specifications

PMT160	-DC-R					-DC-L				
	-50-	-100-	-150-	-200-	-300-	-50-	-100-	-150-	-200-	-270-
Verfahrweg | Travel [mm]	50	100	150	200	300	50	100	150	200	270
Wiederholgenauigkeit unidirektional | Repeatability unidirectional [µm]	±1.7	±1.7	±1.7	±1.7	±1.7	±0.3	±0.3	±0.3	±0.3	±0.3
Wiederholgenauigkeit bidirektional | Repeatability bidirectional [µm]	±2.2	±2.2	±2.2	±2.2	±2.2	±0.4	±0.4	±0.4	±0.4	±0.4
Positioniergenauigkeit | Accuracy [µm]	±4.5	±6.6	±8.5	±10.4	±14.2	±0.9	±1.1	±1.3	±1.5	±1.7
Ebenheitsabweichung | Flatness [µm]	±0.5	±1	±1.5	±2	±3	±0.5	±1	±1.5	±2	±2.7
Geradheitsabweichung | Straightness [µm]	±0.4	±0.7	±1.1	±1.4	±2.2	±0.4	±0.7	±1.1	±1.4	±1.9
Positioniergeschwindigkeit | Positioning speed [mm/s]	30	30	30	30	30	30	30	30	30	30
Max. Beschleunigung | Max. acceleration [m/s²]	0.5	0.5	0.5	0.5	0.5	0.5	0.5	0.5	0.5	0.5
Max. Last | Max. load F_x [N]	45	45	45	45	45	45	45	45	45	45
Max. Last | Max. load F_y [N]	150	150	150	150	150	150	150	150	150	150
Max. Last | Max. load F_z [N]	150	150	150	150	150	150	150	150	150	150
L1 [mm]	275	315	385	460	585	275	315	385	460	585
L2 [mm]	127.5	147.5	182.5	220	282.5	127.5	147.5	182.5	220	282.5

Steinmeyer Mechatronik GmbH
Fritz Schreiter Str. 32
D - 01259 Dresden
Tel.: (+49) 0351 / 885 85-0
Fax: (+49) 0351 / 885 85-25
http://www.steinmeyer.com

Steinmeyer
Mechatronik

PRÜFPROTOKOLL / TEST PROTOCOL

Kunde / Customer		Hochschule Bremen		
Auftragsnummer / Order no.		021794		
Bezeichnung / Specification				
Typ / Type		XY-System		
Teilenr. / Part no.		782300:236.26		
Serienr. / Serial no.		051703_081716		
Baujahr / Year of construction		2018		
Verdrahtungsplan / Wiring diagram		48		
Prüfergebnisse / Test result		X	Y	
Verfahrweg / Travel		100,96	101,05	mm
Positioniergenauigkeit absolut / Accuracy absolute	+/-	1,582	1,084	µm
Positioniergenauigkeit 1D komp. / Accuracy 1D comp.		0,627	0,517	µm
Kompensationsdatei / Compensation file		#KORA.dmc	#KORB.dmc	
Wiederholgenauigkeit (bidirektional) / Repeatability (bidirectional)	+/-	0,240	0,219	µm
Ebenheit / Flatness	+/-	0,235	0,260	µm
Geradheit / Straightness	+/-	0,282	0,285	µm
Nicken / Pitch	+/-	18,000	12,354	µrad
Gieren / Yaw	+/-	6,368	16,662	µrad
max. Geschwindigkeit / max. speed		30,00	30,00	mm/s
max. Beschleunigung / max. acceleration		500,00	500,00	mm/s²
für Bremsrampen-Berechnung / for brake ramp calculation				
Weg zwischen Endschalter-Schaltpunkt und mechanischer Begrenzung Travel between limit switching point and mechanical limit				
negativer Endschalter / negative limit switch		2,22	2,42	mm
positiver Endschalter / positive limit switch		2,34	2,23	mm

Funktionskontrolle / Functional check
Sichtkontrolle / Visual check

Steinmeyer
Mechatronik

Steinmeyer Mechatronik GmbH
Fritz-Schreiter-Straße 32
[redacted]

Datum / Date 23.02.2018

Produkte mit Sollwertabweichungen werden nur mit Sonderfreigabe des Kunden geliefert.
Falls zutreffend, ist die Sonderfreigabe diesem Dokument beigefügt.

Products with setpoint deviations are only delivered with special release of the customer.
If applicable, the special release is attached to this document.

Prüfprotokoll_782300_236_26_051703_081716_0 - Erstelldatum 28.02.2018 09:57

Original-Einbauerklärung
im Sinne der Maschinenrichtlinie 2006/42/EG Anhang II 1B

Steinmeyer
Mechatronik

Hersteller:	Steinmeyer Mechatronik GmbH Fritz-Schreiter-Str. 32 01259 Dresden Deutschland
Bevollmächtigter für die Zusammenstellung der relevanten technischen Unterlagen:	Steinmeyer Mechatronik GmbH Fritz-Schreiter-Str. 32 01259 Dresden Deutschland
Produktbezeichnung:	XY-System
Modell:	PMT160
Typ:	DC
Teile-Nr.:	782300:236.26

Der Hersteller erklärt, dass das oben genannte Produkt eine unvollständige Maschine im Sinne der Maschinenrichtlinie ist. Das Produkt ist ausschließlich zum Einbau in eine Maschine oder unvollständige Maschine vorgesehen und entspricht daher noch nicht allen Anforderungen der Maschinenrichtlinie.

Folgende grundlegenden Anforderungen der Maschinenrichtlinie wurden angewandt und eingehalten:

1.1.2; 1.1.5; 1.3.2; 1.3.4; 1.5.1; 1.5.5; 1.5.8; 1.5.9; 1.7.3; 1.7.4

Die speziellen technischen Unterlagen gemäß Anhang VII Teil B wurden erstellt. Der Bevollmächtigte für das Zusammenstellen der technischen Unterlagen verpflichtet sich, die Unterlagen auf begründetes Verlangen an die einzelstaatlichen Stellen zu übermitteln. Die Übermittlung erfolgt postalisch in Papierform oder auf elektronischem Datenträger.

Die Inbetriebnahme des Produkts ist so lange untersagt, bis festgestellt wurde, dass die Maschine, in die das oben genannte Produkt eingebaut wird, allen grundlegenden Anforderungen der Maschinenrichtlinie entspricht.

Es wurden folgende harmonisierte Normen angewandt:

- DIN EN ISO 12100:2011 – Sicherheit von Maschinen - Allgemeine Gestaltungsleitsätze – Risikobeurteilung
- DIN EN 82079-1:2013 – Erstellen von Anleitungen - Gliederung, Inhalt und Darstellung
- DIN ISO 3864-1:2012 – Graphische Symbole - Sicherheitsfarben und Sicherheitszeichen
- DIN ISO 3864-2:2011 – Graphische Symbole - Sicherheitsfarben und Sicherheitszeichen
- VDI 4500:2006 – Technische Dokumentation, Benutzerinformation

Dresden, 06.02.2018

F. Datasheet of the camera

Allied Vision

GiGE VISION

Prosilica GT

4907

- Weiter Temperaturbereich für extreme Umgebungen
- IEEE 1588 PTP
- PoE
- 7.6 fps @ 15.7 Megapixel

Beschreibung

15.7 Megapixel **CD Kamera für extreme Umgebungen - GigE Vision**

Die Prosilica GT4907/GT4907C ist eine 15.7 Megapixel Kamera mit Gigabit Ethernet Interface (GigE Vision). Die Prosilica GT4907/GT4907C ist eine besonders robuste Kamera für extreme Umgebungen. Sie ist mit dem OnSemi KAI-16070 CCD Sensor ausgestattet, der eine hervorragende Bildqualität für Monochrom- und Farbkameras bietet.

Optionen:

- Diverse IR Cut/Pass Filter
- Class 1 Sensor
- Diverse Objektivanschlüsse

Spezifikationen

Prosilica GT	**4907**
Interface	IEEE 802.3 1000BASE-T, IEEE 802.3af (PoE)
Auflösung	4864 (H) × 3232 (V)
Sensor	ON Semi KAI-16070
Sensortyp	CCD Progressive
Zellgröße	7.4 µm x 7.4 µm
Objektivanschluss	F-Mount
Maximale Framerate bei voller Auflösung	7.6 fps
ADC	14 bit
Bildzwischenspeicher (RAM)	128 MByte
Output	
Bit-Tiefe	14 (monochrome); 12 (color) bit

Allied Vision

Prosilica GT	4907
Mono Modi	Mono8, Mono12, Mono12Packed, Mono14
Farbmodi YUV	YUV411Packed, YUV422Packed, YUV444Packed
Farbmodi RGB	RGB8Packed, BGR8Packed, RGBA8Packed, BGRA8Packed
Raw Modi	BayerGR8, BayerGR12, BayerRG12Packed
General purpose Inputs/Outputs (GPIOs)	
TTL I/Os	1 input, 2 outputs
Optogekoppelte I/Os	1 input, 2 outputs
RS-232	1
Betriebsbedingungen/Abmessungen	
Betriebstemperatur	-20 °C to +50 °C ambient (without condensation)
Spannungsversorgung	7 to 25 VDC; PoE
Leistungsaufnahme (@12 V)	7.7 W @ 12 VDC; 9.5 W PoE
Masse	372 g
Abmessungen (L × B × H in mm)	96 × 66 × 53.3 mm (inkl. Anschlüsse)
Konformität	CE, RoHS, REACH, WEEE, FCC, ICES

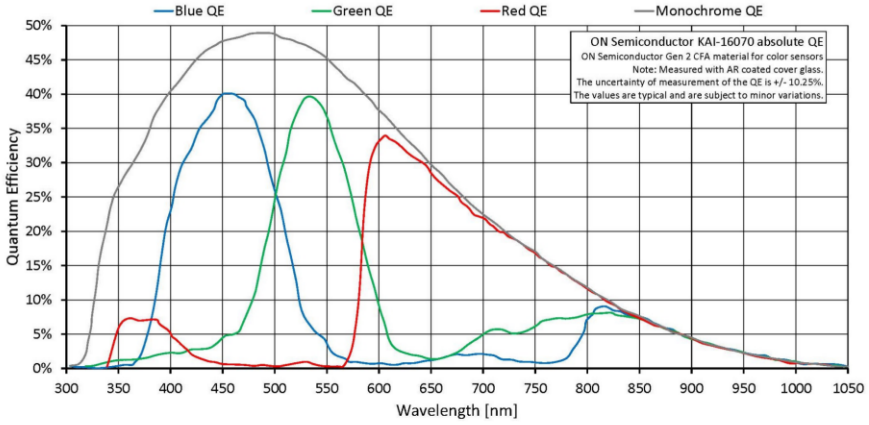

Features

Features zur Bildoptimierung:

- Auto Gain (manuelle Gainsteuerung: 0 bis 32 dB)

Allied Vision

- Auto Belichtung (manuelle Belichtung: 35 µs bis 26,8 s)
- Auto Weißabgleich (Color-Modelle)
- Binning
- Decimation
- Farbton, Sättigung, Farbkorrektur (Color-Modelle)
- Spaltendefekt-Maskierung
- Gamma
- LUTs (Look-Up Tables)
- Region of interest (ROI), separates ROI für Auto Features
- Bildspiegelung (X/Y)

Kamerakontroll-Features:

- EF-Objektivsteuerung (Atikelnummer -18)
- Event Channel
- Chunk Daten
- IEEE 1588 Precision Time Protocol (PTP)
- RS232
- Speicherbare Benutzereinstellungen
- StreamBytesPerSecond (einfache Bandbreitenkontrolle)
- Stream Hold
- Sync out Modi: Trigger ready, input, exposing, readout, imaging, strobe, GPO
- Tap Modus umschaltbar (four-tap, one-tap)
- Kameratemperatur-Überwachung (Mainboard und Sensorboard)
- Trigger over Ethernet (ToE) Action Commands

Allied Vision

Technische Zeichnung

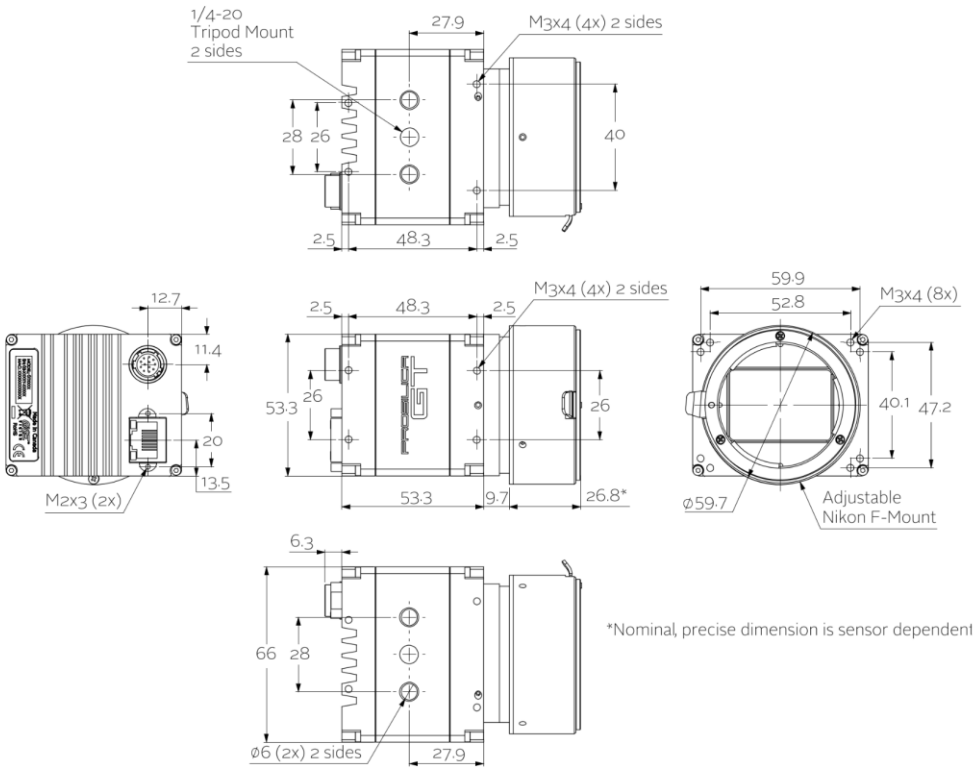

*Nominal, precise dimension is sensor dependent

Allied Vision

Applikationen

Prosilica GT4907/GT4907C eignet sich ideal für viele Applikationen einschließlich:

- Outdoor Bildverarbeitung
- Verkehrsüberwachung / Intelligent Traffic Systems (ITS)
- Öffentliche Sicherheit und Überwachung
- Industrielle Inspektion
- Machine Vision
- Militär und Raumfahrt

G. Datasheet and test protocol of the *w*-stage

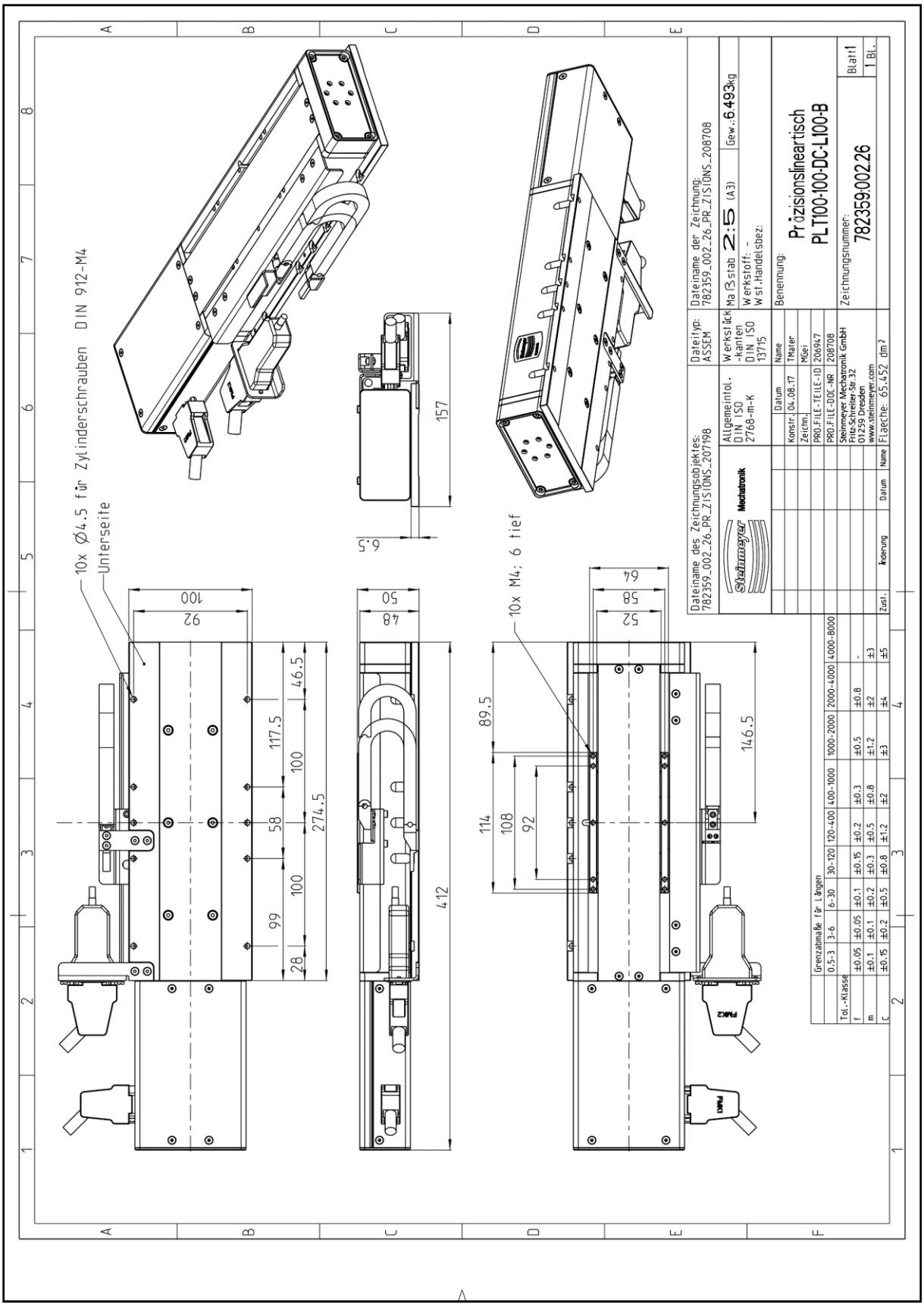

Steinmeyer Mechatronik GmbH
Fritz Schreiter Str. 32
D - 01259 Dresden
Tel.: (+49) 0351 / 885 85-0
Fax: (+49) 0351 / 885 85-25
http://www.steinmeyer.com

Steinmeyer
Mechatronik

PRÜFPROTOKOLL / TEST PROTOCOL

Kunde / Customer		Hochschule Bremen	
Auftragsnummer / Order no.		021794	
Bezeichnung / Specification			
Typ / Type		PLT100-100-DC-R-L-B	
Teilenr. / Part no.		782359:002.26	
Serienr. / Serial no.		021801	
Baujahr / Year of construction		2018	
Verdrahtungsplan / Wiring diagram		299	
Prüfergebnisse / Test result			
Verfahrweg / Travel		100,00	mm
Positioniergenauigkeit / Accuracy	+/-	1,000	µm
Kompensationsfaktor / Compensation factor		0,999953	
Umkehrspiel / Backlash	+/-	xxx	µm
Ebenheit / Flatness	+/-	2,286	µm
Geradheit / Straightness	+/-	1,926	µm
Nicken / Pitch	+/-	17,791	µrad
Gieren / Yaw	+/-	12,643	µrad
max. Geschwindigkeit / max. speed		0,00	mm/s
max. Beschleunigung / max. acceleration		0,00	mm/s²
für Bremsrampen-Berechnung / for brake ramp calculation			
Weg zwischen Endschalter-Schaltpunkt und mechanischer Begrenzung Travel between limit switching point and mechanical limit			
negativer Endschalter / negative limit switch		5,50	mm
positiver Endschalter / positive limit switch		5,50	mm
Funktionskontrolle / Functional check Sichtkontrolle / Visual check		[redacted]	
Datum / Date		28.02.208	

Produkte mit Sollwertabweichungen werden nur mit Sonderfreigabe des Kunden geliefert.
Falls zutreffend, ist die Sonderfreigabe diesem Dokument beigefügt.

Products with setpoint deviations are only delivered with special release of the customer.
If applicable, the special release is attached to this document.

Steinmeyer
Mechatronik

Steinmeyer Mechatronik GmbH
Fritz-Schreiter-Straße 32
01259
Pho[redacted] 8585-0
Fax 88585-25

Prüfprotokoll_782359_002_26_021801_0 - Erstelldatum 28.02.2018 11:41

Original-Einbauerklärung
im Sinne der Maschinenrichtlinie 2006/42/EG Anhang II 1B

Steinmeyer
Mechatronik

Hersteller:	Steinmeyer Mechatronik GmbH Fritz-Schreiter-Str. 32 01259 Dresden Deutschland
Bevollmächtigter für die Zusammenstellung der relevanten technischen Unterlagen:	Steinmeyer Mechatronik GmbH Fritz-Schreiter-Str. 32 01259 Dresden Deutschland
Produktbezeichnung:	PLT100
FMD Teilenr.:	782359:xxx.26

Der Hersteller erklärt, dass das oben genannte Produkt eine unvollständige Maschine im Sinne der Maschinenrichtlinie ist. Das Produkt ist ausschließlich zum Einbau in eine Maschine oder unvollständige Maschine vorgesehen und entspricht daher noch nicht allen Anforderungen der Maschinenrichtlinie.

Folgende grundlegenden Anforderungen der Maschinenrichtlinie wurden angewandt und eingehalten:

1.1.2; 1.1.3; 1.1.5; 1.3.2; 1.3.4; 1.5.1; 1.5.5; 1.5.8; 1.5.9; 1.7.3; 1.7.4

Die speziellen technischen Unterlagen gemäß Anhang VII Teil B wurden erstellt. Der Bevollmächtigte für das Zusammenstellen der technischen Unterlagen verpflichtet sich, die Unterlagen auf begründetes Verlangen an die einzelstaatlichen Stellen zu übermitteln. Die Übermittlung erfolgt postalisch in Papierform oder auf elektronischem Datenträger.

Die Inbetriebnahme des Produkts ist so lange untersagt, bis festgestellt wurde, dass die Maschine, in die das oben genannte Produkt eingebaut wird, allen grundlegenden Anforderungen der Maschinenrichtlinie entspricht.

Es wurden folgende harmonisierte Normen angewandt:

- DIN EN ISO 12100:2011 – Sicherheit von Maschinen - Allgemeine Gestaltungsleitsätze - Risikobeurteilung
- DIN EN 82079-1:2013 – Erstellen von Anleitungen - Gliederung, Inhalt und Darstellung
- DIN ISO 3864-1:2012 – Graphische Symbole - Sicherheitsfarben und Sicherheitszeichen
- VDI 4500:2006 – Technische Dokumentation, Benutzerinformation

Dresden, 28.02.2018

H. Technical drawing of the Sample 2 “cylinder surface”

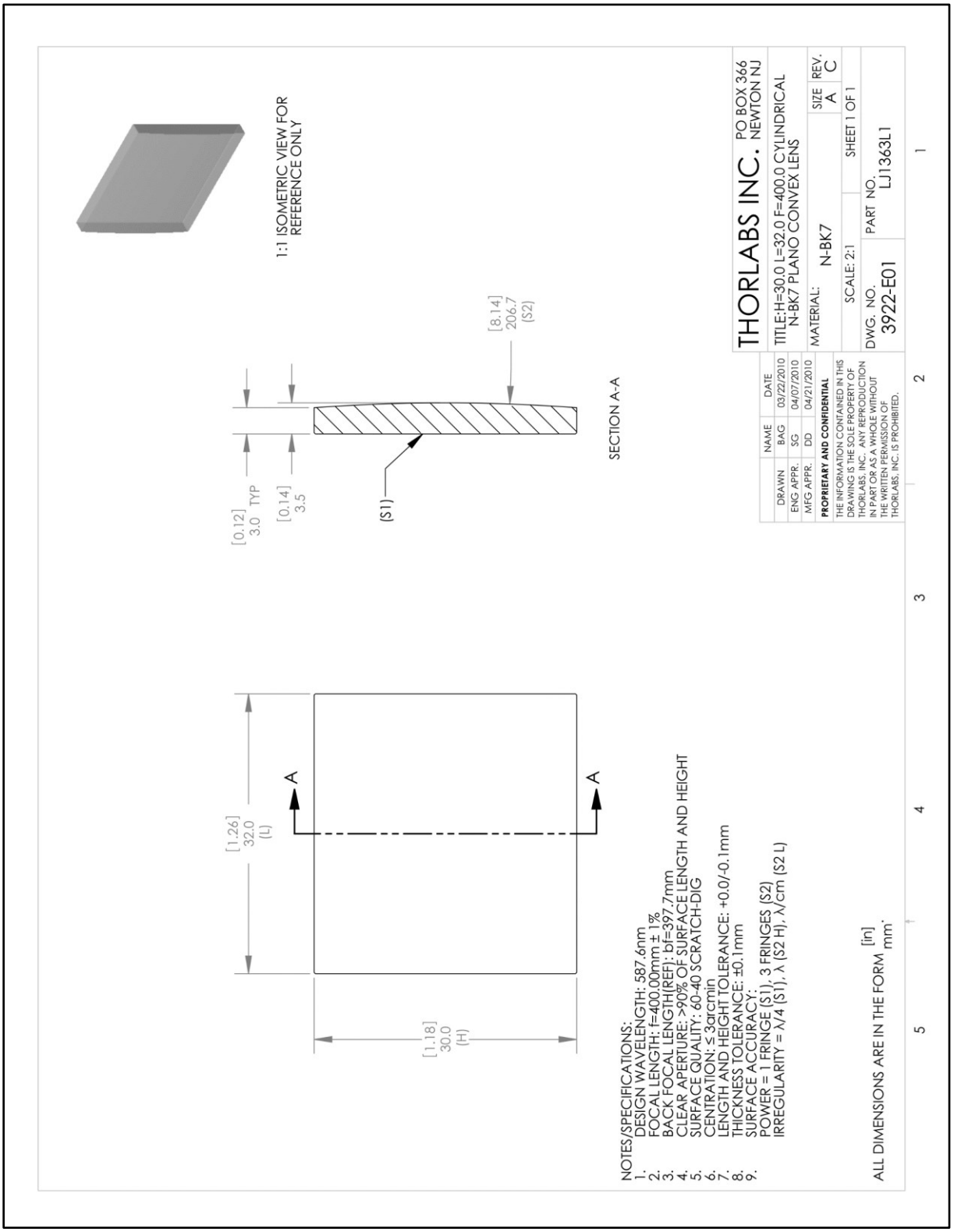

I. Documentation of the comparison measurement of the Sample 2 “cylinder surface” for the experiments

Mahr MarWin 8.00-28	BLF OPTIK **Asphere measurement** Meas. profile and differential profile	**27/10/2017** 1 17:20:43 Inspector: Signature:
Part:	Drawing n°:	Machining operation:
Probe arm LP D 20-10-5_47 1101	**Measuring force 0.5 mN**	
LJ1363L1		**LD260**
Comment:		

K1-2D filter 0,20 mm

Measured profile + Nominal profile

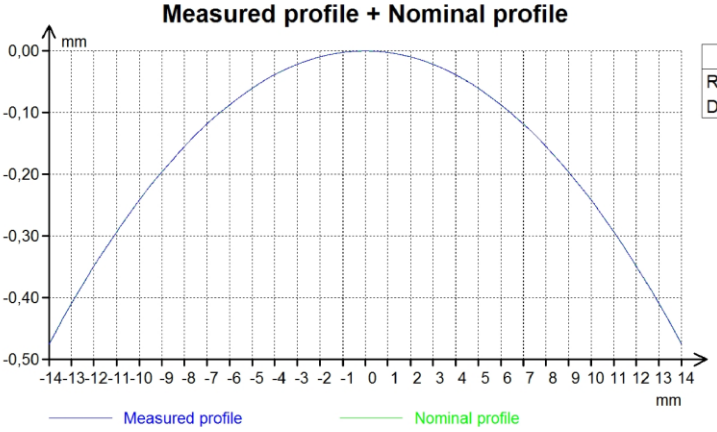

Sphere

	nominal	fitted
R0 [mm]	206.700000	206.497440
D [mm]	28.000000	

Differential curve fit/Measurement

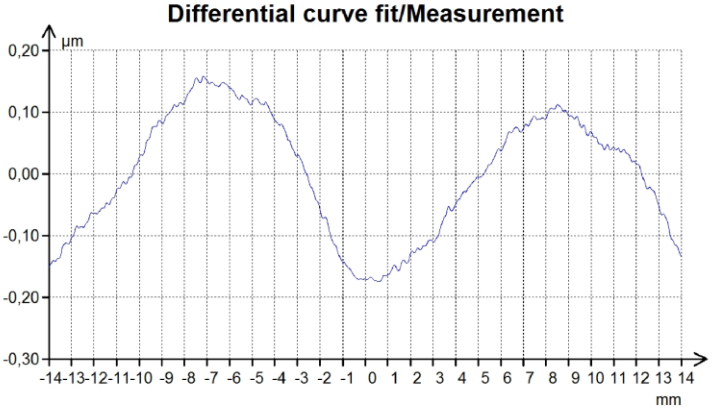

	µm	λ'
PV	0.333	0.526
RMS	0.098	0.155
MIN	-0.174	
MAX	0.159	

Sagitta (Fit)

h (mm)	z(h) (mm)
0,00	0,000000
0,50	0,000605
1,00	0,002421
1,50	0,005448
2,00	0,009686
2,50	0,015134
3,00	0,021793
3,50	0,029664
4,00	0,038745
4,50	0,049038
5,00	0,060542
5,50	0,073258
6,00	0,087187
6,50	0,102327
7,00	0,118680
7,50	0,136245
8,00	0,155024

C:/Mahr/Family/Asphere/Para/THOR LABS Lensleri/LJ1363L1_Y/

[1] λ_{ref} = 632.82 nm - HeNe laser (red)

C:/Mahr/Family/Asphere/MPR/Asphere.mpr

AsphericLib 3.01-36

J. Documentation given by the manufacturer of the Sample 3 for the experiments “polynomial freeform 1”

trionplas technologies

Freiform auf Quarzglas

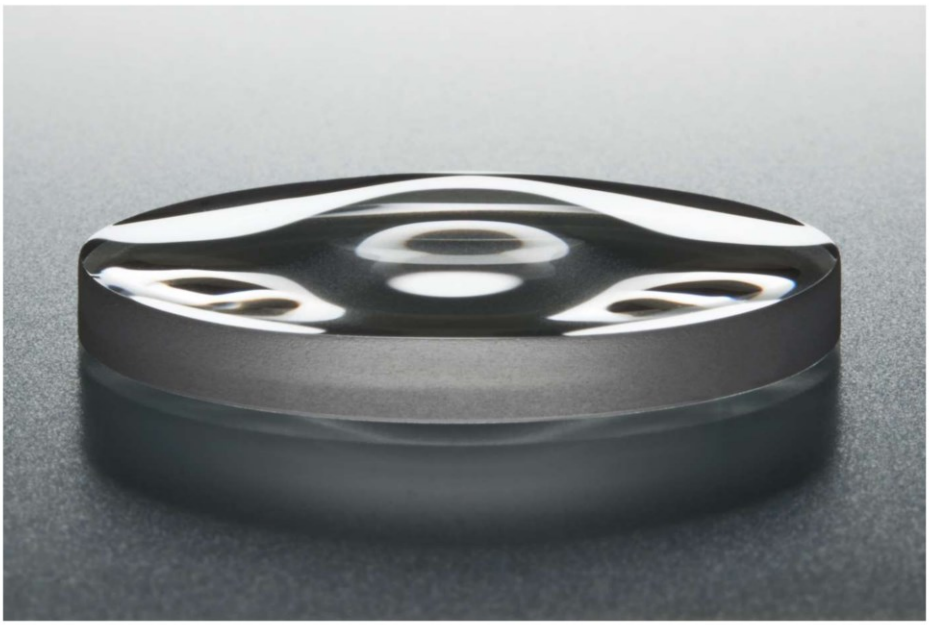

14.06.2019

Freiform auf Quarzglas 2019

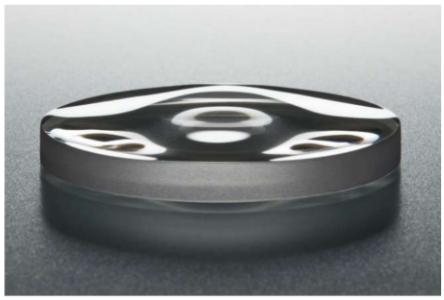

Material: Quarzglas

Durchmesser: 36 mm

Dicke: ca. 4 mm

CA: 26 mm

Mathematische Sollform

SAG(X,Y) = A*X.^2 + B*Y.^2 + C*X.^4 + D*X.^2.*Y.^2 + E*Y.^4 + F*X.^6 + G*X.^4.*Y.^2 + H*X.^2.*Y.^4 +I*Y.^6

A = +3.5000e-03; A = A/1000^1;
B = -2.5000e-03; B = B/1000^1;
C = -2.5000e-05; C = C/1000^3;
D = +0.0000e-01; D = D/1000^3;
E = +3.5000e-05; E = E/1000^3;
F = -0.0000e-01; F = F/1000^5;
G = +0.0000e-01; G = G/1000^5;
H = -0-0000e-01; H = H/1000^5;
I = -0.0000e-01; I = I/1000^5

Max. Sag ~ 670 µm

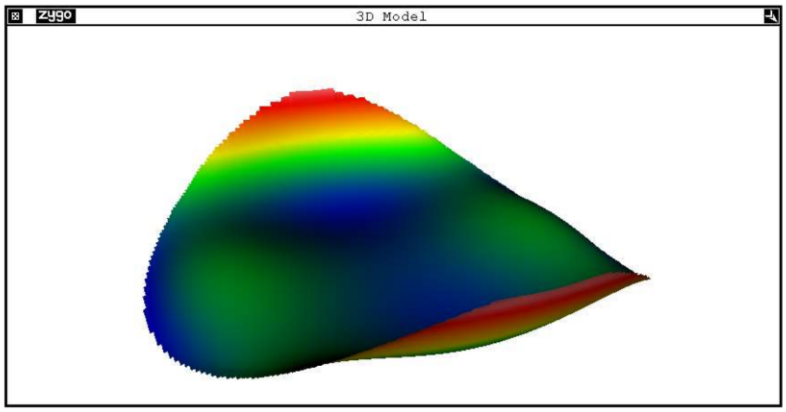

Freiform CA 26 mm

Freiform auf Quarzglas 2019

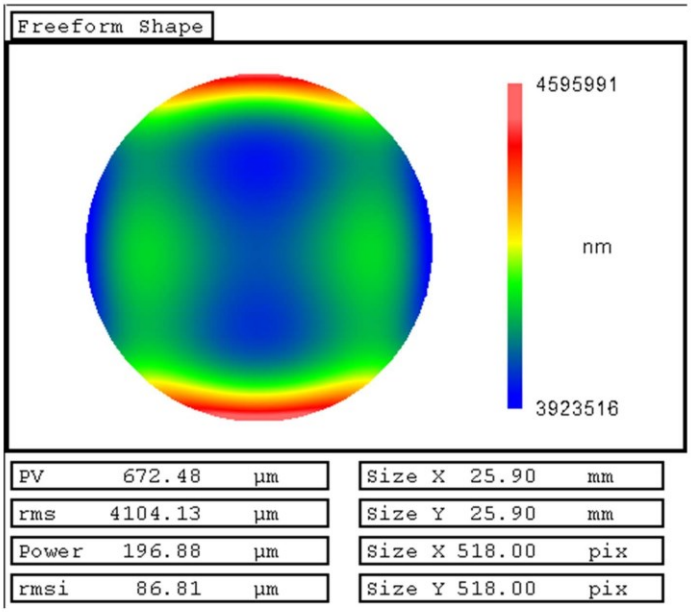

Freiform, PV ~ 670 µm

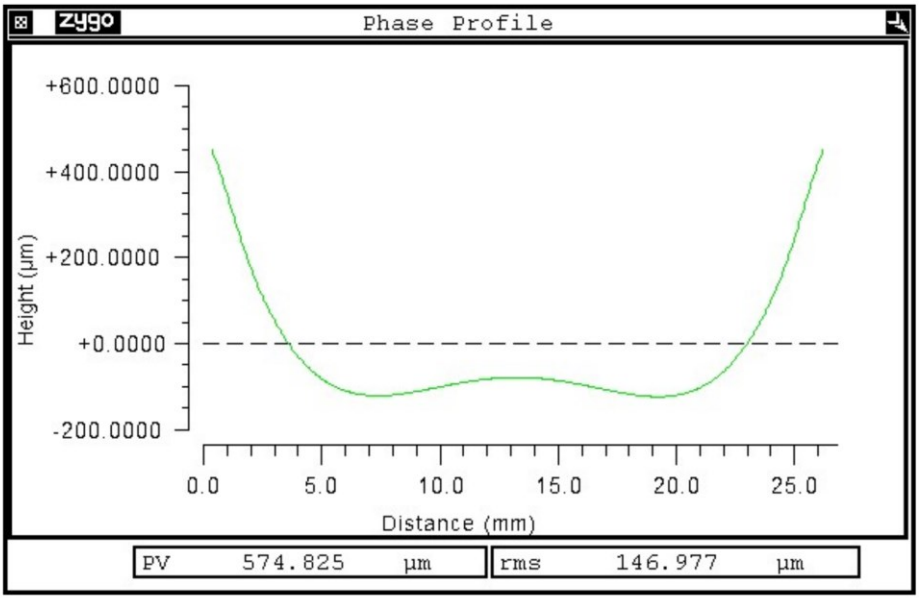

Profil in NS-Richtung

Freiform auf Quarzglas 2019

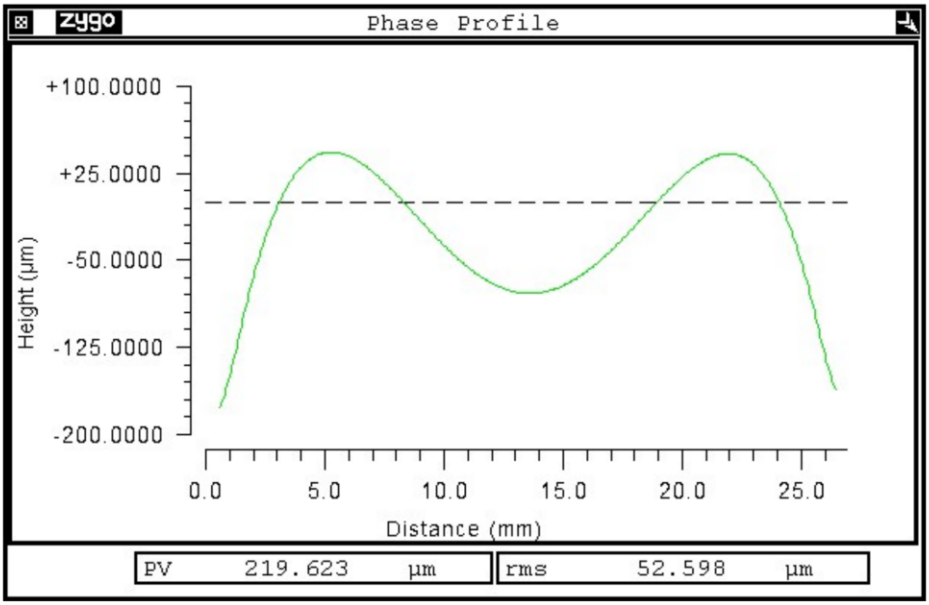

Profil OW-Richtung

Freiform auf Quarzglas 2019

Restfehlermessungen mit CyberScan

Messungen erfolgte mit automatischer Z-Nachfuhr und anschließendem Fit gegen die Sollform mit 100 µm Auflösung in XY.

Messung 01

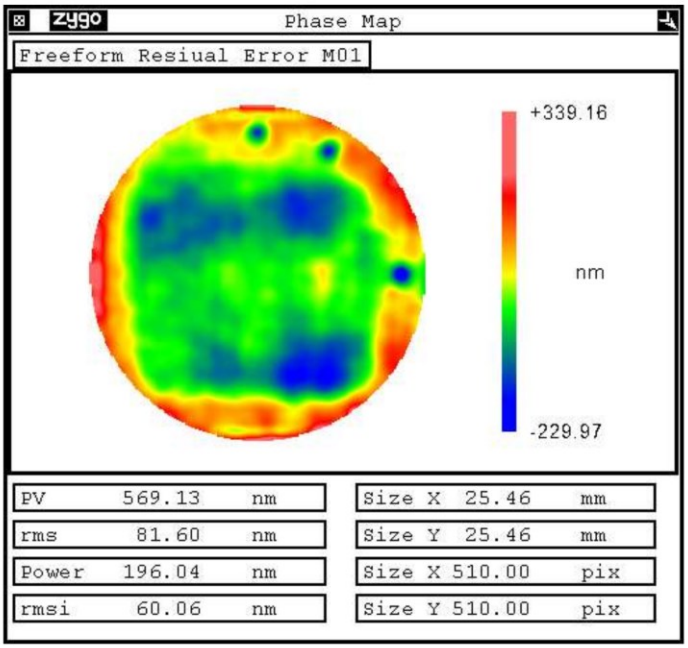

Daten Restfehler:

Daten Freiform\ Freiform Messung 01 Restfehler.ascii

Daten Freiform\ Freiform Messung 01 Restfehler.dat

Daten Freiform\ Freiform Messung 01 Restfehler.xyz

Daten Form:

Daten Freiform\ Freiform Messung 01 Form.ascii

Daten Freiform\ Freiform Messung 01 Form.dat

Daten Freiform\ Freiform Messung 01 Form.xyz

trionplas technologies

K. Documentation given by the manufacturer of the Sample 4 for the experiments “polynomial freeform 2”

trionplas technologies

Kalibrierelement MFF8

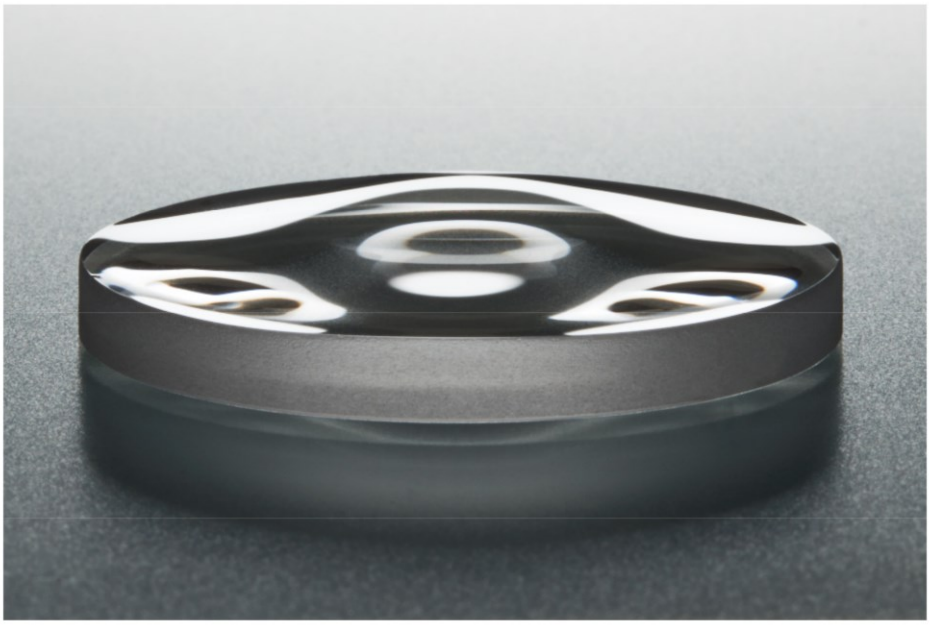

18.06.2018

Kalibrierelement MFF8

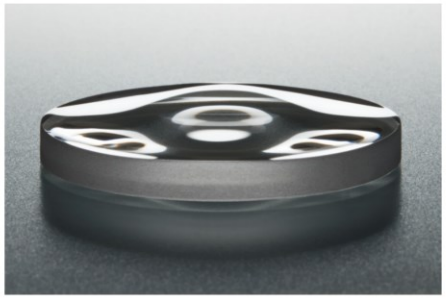

Material: Quarzglas

Durchmesser: 36 mm

Dicke: ca. 4 mm

CA: 26 mm

Mathematische Sollform

SAG(X,Y) = A*X^2 + B*Y^2 + C*X^4 + D*Y^4

A = 2.5E-3

B = 2.5E-3

C = -1.5E-5

D = -1.5E-5

Max. Sag ~ 210 µm

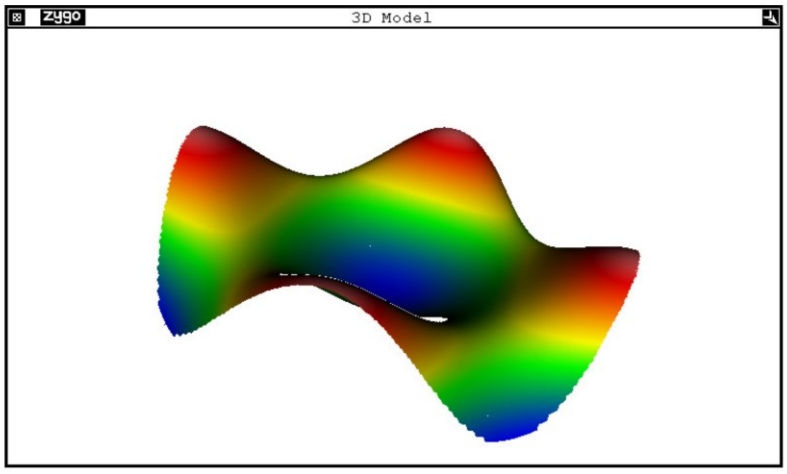

Freiform MFF8 CA 26 mm

trionplas technologies

2

Kalibrierelement MFF8

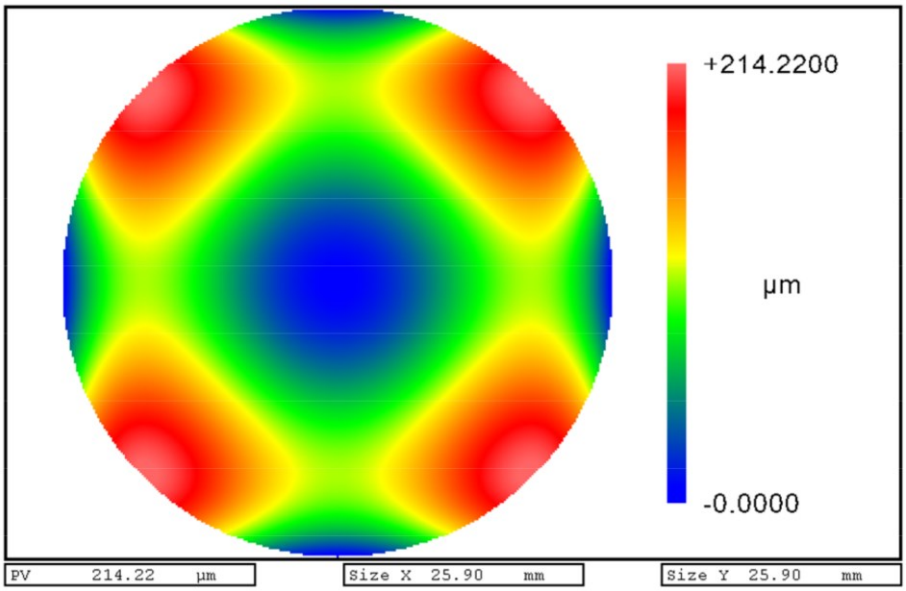

MFF8 SAG(X,Y), PV ~ 214 µm

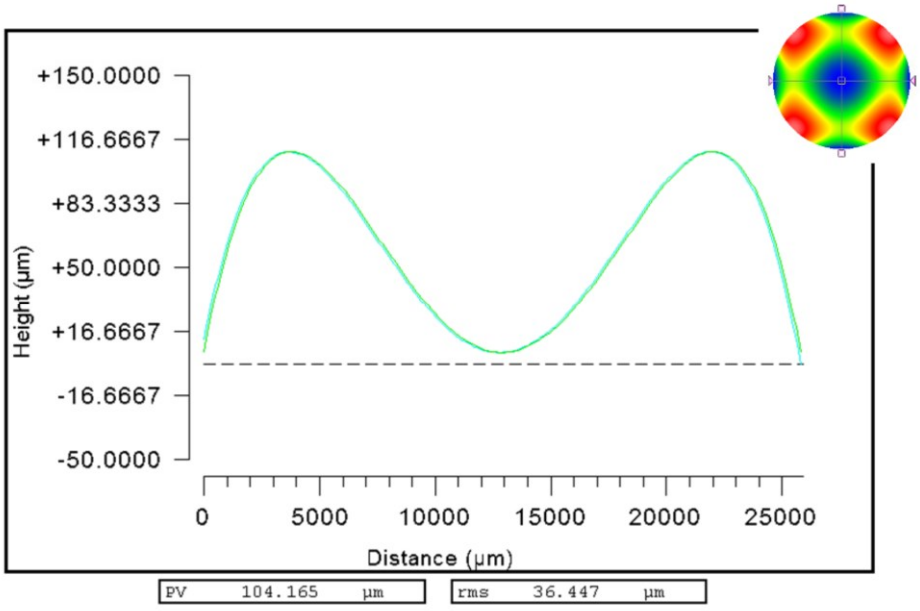

Profil in NS- bzw. OS-Richtung

trionplas technologies

3

Kalibrierelement MFF8

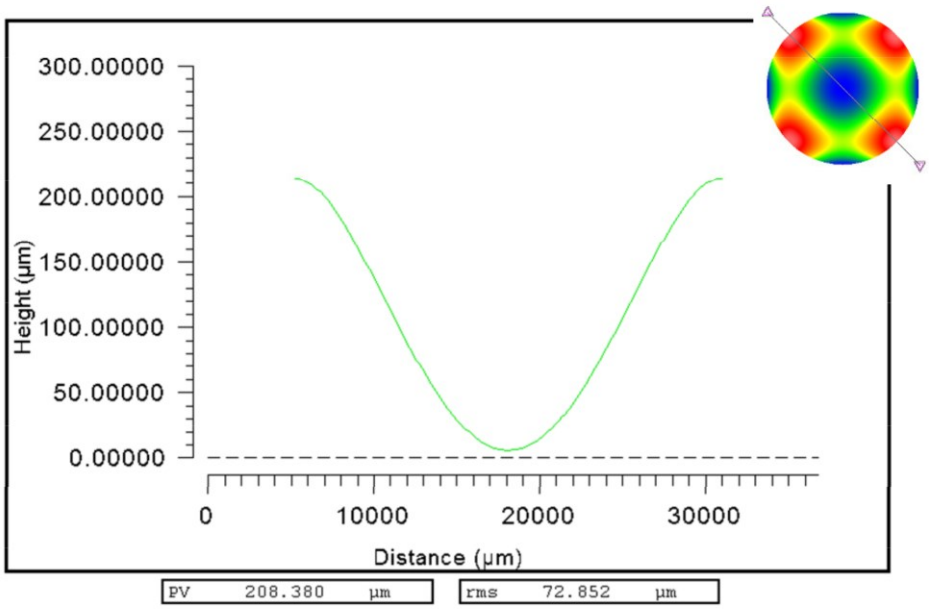

Profil diagonal NW-SO-richtung

Daten:

MFF8_Sollform\MFF8_Sollform.ascii

MFF8_Sollform\MFF8_Sollform_ZYGO.dat

MFF8_Sollform\MFF8_Sollform_ZYGO.xyz

Restfehlermessungen mit LuphoScan 260 HD

Messungen erfolgten gegen Sollform mit 100 µm Auflösung in XY.

Messung 01

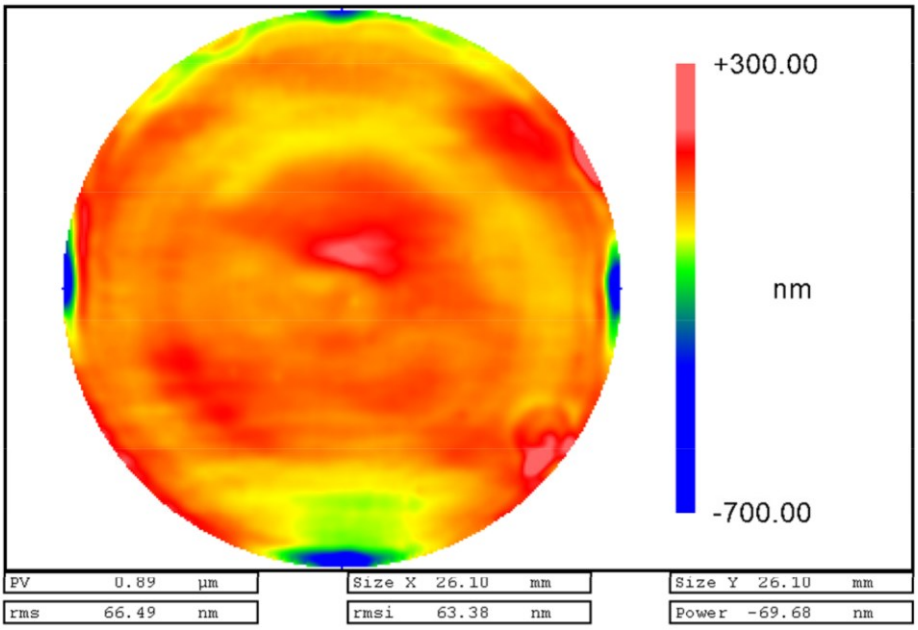

Daten Restfehler:

MFF8_LuphosHD_Messung01\ MFF8_LuphosHD_Messung01_Restfehler.ascii

MFF8_LuphosHD_Messung01\ MFF8_LuphosHD_Messung01_Restfehler_ZYGO.dat

MFF8_LuphosHD_Messung01\ MFF8_LuphosHD_Messung01_Restfehler_ZYGO.xyz

Daten Form:

MFF8_LuphosHD_Messung01\ MFF8_LuphosHD_Messung01_Form.ascii

MFF8_LuphosHD_Messung01\ MFF8_LuphosHD_Messung01_Form_ZYGO.dat

MFF8_LuphosHD_Messung01\ MFF8_LuphosHD_Messung01_Form_ZYGO.xyz